Nondestructive tissue analysis for *ex vivo* and *in vivo* diagnosis of central nervous system tumors

Inaugural-Dissertation

zur Erlangung des Doktorgrades
der Mathematisch-Naturwissenschaftlichen Fakultät
der Heinrich-Heine-Universität Düsseldorf

vorgelegt von

Samira Daali
aus Kandel

Köln, August 2019

aus dem Institut für Pädiatrische Immunologie und Hämostaseologie
der Heinrich-Heine-Universität Düsseldorf

Gedruckt mit der Genehmigung der
Mathematisch-Naturwissenschaftlichen Fakultät der
Heinrich-Heine-Universität Düsseldorf

Berichterstatter:
1. PD. Dr. med. Hans-Jürgen Laws

2. Prof. Dr. Laura Rose

Tag der mündlichen Prüfung: 22.01.2020

Kurzzusammenfassung

Hintergrund. Eine vollständige Tumorentfernung ohne Verletzung lebenswichtiger Gewebe, ist das Hauptziel der onkologischen Neurochirurgie, welches aber oft an der Erkennung invasiver Tumorzellen scheitert. Die Konfokale- Laserendomikroskopie (CLE Abk. vom englischen **C**onfocal **L**aser **E**ndomicrosopy) könnte dieses Ziel erreichen. Sie ist eine neue Technik, die in hoher Auflösung *in vivo* Aufnahmen von zellulären Strukturen in Echtzeit ermöglicht. In der Neurochirurgie wird dieses Verfahren jedoch noch nicht eingesetzt; in erster Linie wegen des Fehlens eines geeigneten Kontrastmittels.

Ziel. Das Hauptziel dieser Arbeit war es, einen fluoreszierenden Farbstoff für CLE zu finden, welches spezifische Tumor-Merkmale hervorhebt, um 1) den Tumor und dessen Grad zu diagnostizieren und von anderen Krankheiten abzugrenzen, 2) eine sichere Entfernung von Tumorgewebe zu gewährleisten, und 3) Tumorprozesse auf einer zellulären Ebene besser zu verstehen.

Materialien/Methoden. Schnell färbende und in der Klinik eingesetzte Kontrastmittel (Acriflavin-Hydrochlorid, Acridinorange, Cresylviolett, Indocyaningrün und Fluorescein-Natrium) wurden an unterschiedlichen Tumoren aus dem zentralen Nervensystem sowie an gesundem Gewebe mit CLE-488 nm und -780 nm (Cellvizio®) untersucht. Darüber hinaus wurden weitere Farbstoffe, die für den Menschen zugelassen sind, z.B. zum Einfärben von Lebensmitteln, analysiert und mit den Färbungen der traditionellen Histologie verglichen. Um CLE für die Neurochirurgie zu evaluieren, wurden des Weiteren im Rattengehirn implantiere C6-Gliome chirurgisch entfernt, mit CLE als Hilfsmittel zur Visualisierung. Ein Standard Operationsmikroskop (OPMI Pentero®) mit 5-Aminolävulinsäure als Kontrastmittel wurde als Kontrolle für die CLE-Technik eingesetzt. Abschließend wurde das Gehirn eines gesunden Schweines mit CLE *in vivo* untersucht, um konfokale Merkmale eines großen gesunden Hirngewebes zu definieren.

Ergebnis. Durch CLE konnte, insbesondere mit Acriflavin-Hydrochlorid und Indocyaningrün als Kontrastmittel, eine hohe Trefferquote (ca. 91%) in der Diagnose von Tumoren erreicht werden. Darüber hinaus ermöglichte *in vivo* CLE eine klare Abgrenzung von neoplastischem und gesundem Gewebe sowie der Tumorgrenzen in Echtzeit. Dies ermöglichte bessere chirurgische Resektionsergebnisse des Tumors als mit dem Visualisierungs-Standard.

Schlussfolgerung. Diese Arbeit zeigt CLE als ein hervorragendes Hilfsmittel, um sowohl Biopsien schnell zu diagnostizieren als auch eine radikale Entfernung des Tumorgewebes zu gewährleisten. In Zukunft könnte CLE durch eine Verbesserung der intraoperativen Entscheidung auch zu einer sicheren erweiterten Resektion von menschlichen Tumoren beitragen. Bevor eine Integration in der Neurochirurgie möglich ist, müssen jedoch diverse technische, klinische und medizinrechtliche Hürden genommen werden.

Abstract

Background. To prevent a loss of brain function, gross total resection of tumors without causing injury to vital tissues is the major aim for neurosurgeons, but it often fails due to limited recognition of infiltrative tumor cells. Confocal laser scanning microscopy (CLSM) is a new promising technology for intraoperative high-resolution, three-dimensional, and real-time imaging on a cellular level, which could fulfill this aim. In the field of neurosurgery, experience with CLSM is rare, primarily due to the lack of a suitable fluorophore to stain human tissue.

Aim. The goal was to identify a suitable fluorophore, which provides satisfactory contrast of specific tumor features 1) to diagnose biopsies and to differentiate between different grades, types and other diseases, 2) to facilitate safe tumor resection, and 3) to aid in understanding tumor processes on a cellular level.

Material/methods. This study investigated the application of CLSM (Cellvizio®) devices at 488 nm and 780 nm excitation in *ex vivo* and *in vivo* imaging of primary central nervous system (CNS) tumors as well as of healthy tissue. Various rapid-staining fluorophores (acriflavine, acridine orange, cresyl violet, indocyanine green, and fluorescein) used in clinical practice were examined for their staining abilities. Furthermore, other permitted fluorescent agents for human application, in particular food dyes, were investigated using the CLSM approach and compared to traditional histology. To evaluate CLSM and the contrast agents for an *in vivo* neurosurgical application, high-grade glioma resection was guided using intraoperative CLSM in rats implanted with C6 glioma cells. Routine surgical wide-field microscopy (OPMI Pentero®) with 5-aminolevulinic acid as contrast agent served as the optical gold standard. Finally, normal brain cytoarchitecture of a pig was examined *in vivo* to define confocal features of a large, healthy brain.

Results. Acriflavine and indocyanine green were identified as suitable for all stated goals. Highlighted with CLSM, they enabled high accuracy (approximately 91%) in the diagnosis of CNS tumors, similar to the corresponding traditional histology. Based on cellular morphological and physiological properties of neoplastic tissue, *in vivo* CLSM imaging provided delineation of borders between tumor and healthy tissue, thus allowing for better surgical resection results than with standard surgical wide-field microscopy.

Conclusion. In conclusion, this study establishes CLSM as a feasible and reliable tool not only to increase the initial diagnosis yield but also to extend the resection borders, thus demonstrating its potential future application in improving intraoperative decisions for a safe extended resection of human tumors. Nonetheless, several technical, clinical, and medico-legal issues have to be resolved before its role in neurosurgery can reach its full potential.

Contents

Abbreviation **xiv**

1 Introduction **1**

1.1 Primary central nervous system tumors 1

1.2 Classification and problematic of primary CNS tumors 4

1.3 Challenge in neurosurgery: Intraoperative tumor assessment 11

1.4 Confocal laser scanning microscopic system 13

1.5 Challenge using CLSM in neurosurgery: contrast agents 15

1.6 Fluorescence in CNS tumor surgery 18

  1.6.1 5-aminolevulinic acid 18

  1.6.2 Fluorescein 19

  1.6.3 Indocyanine green 20

1.7 Aim 21

2 Material and methods **23**

2.1 Chemicals and Reagents 23

2.2 Ethical considerations 27

2.3 Technical considerations 27

  2.3.1 Confocal laser endomicroscopic system 27

2.3.2 Intraoperative wide-field microscopy 31

2.4 *Ex vivo* human studies 31

2.4.1 Statistical analyses of primary CNS tumor distribution 31

2.4.2 Collection and confocal imaging of human tissues 32

2.4.3 Fluorescent agents used *ex vivo* on human tissue 35

2.4.4 Histopathology 38

2.4.5 Statistical analysis of CLSM images 39

2.5 Cell culture 40

2.5.1 Cell culture work 40

2.5.2 Trypan blue viability test 41

2.5.3 Counting of cells 41

2.5.4 Fluorescent agent used in cell culture 42

2.6 Animal *in vivo* studies 42

2.6.1 Rats 42

2.6.2 Fluorescent agents used *in vivo* 43

2.6.3 C6 glioma cell implantation 43

2.6.4 Post-surgical care 44

2.6.5 Craniotomy 44

2.6.6 *In vivo* fluorescence imaging and tumor resection 45

2.6.7 Histopathology 46

2.6.8 Histopathological analysis 47

2.6.9 Studies on pig 50

2.6.10 Pig surgery and CLSM imaging 50

3 Results **52**

3.1 Distribution of primary CNS tumors 52

3.1.1 Distribution by subtype, behavior, and gender 52

3.1.2 Distribution by age and behavior 56

3.2 *Ex vivo* studies using the CLSM device at 488 nm excitation 61

3.2.1 Investigation of different CLSM Miniprobes™ 61

3.2.2 Investigation of incubation times for tumor staining 61

3.2.3 Investigations of contrast agents for tumor staining 66

3.2.4 Investigation of the food dyes 75

3.2.5 Investigation of CLSM in the diagnosis of primary CNS tumors 80

3.2.6 Astrocytoma grading using CLSM and AF 95

3.3 Examination of CNS tissue with ICG using the CLSM device at 780 nm excitation 98

3.4 *In vivo* examination of brain tissue 100

3.4.1 Brain tumor resection assisted by intraoperative CLSM at 488 nm and 780 nm excitation 100

3.4.2 Brain tumor resection assisted by OPMI Pentero® 105

3.4.3 Histopathological analyses of the rat brain and the removed specimen 105

3.4.4 *In vivo* examination of healthy brain tissue using CLSM at 780 nm excitation 111

3.4.5 Artifacts during CLSM imaging 114

4 Discussion **115**

4.1 General aspects 115

4.2 Analyses of primary CNS tumors: *ex vivo* study 116

4.3 Contrast agents evaluated with CLSM 119

4.3.1 5-ALA: *in vivo* study 120

4.3.2 Fluorescein sodium: *in vivo* study 121

4.3.3 Cresyl violet: *ex vivo* study 122

4.3.4 Erythrosine B and other food dyes: *ex vivo* study 122

4.3.5 Acriflavine hydrochloride and acridine orange: *ex vivo* and *in vivo* studies . . . 123
4.3.6 Indocyanine green: *ex vivo* and *in vivo* studies . . . 124
4.4 Grading of astrocytic tumors: *ex vivo* study . . . 125
4.5 Comparison of CLSM and wide-field microscopy: *in vivo* study . . . 127
4.6 Advantages of CLSM . . . 128
4.7 General limitations and caveats of CLSM . . . 130
4.8 Future directions . . . 131
4.9 Conclusions . . . 133

5 References 134

Acknowledgements 157

Erklärung zur Urheberschaft 158

List of Figures

1.1 CNS structures and their basic functions (modified from pixabay.com) . 3

1.2 Primary CNS tumor locations (modified from pixabay.com). 10

1.3 Light pathways in confocal microscopy (source: own representation) . . 14

1.4 Jablonski diagram of fluorescence (source: own representation). 16

2.1 Cellvizio®system (source: own representation) 29

2.2 Laser scanning unit (modified from www.maunakeatech.com) 30

2.3 Pre-CLSM imaging (source: own representation). 32

2.4 *Ex vivo* CLSM imaging (source: own representation) 34

2.5 Example of one entity on the online form (source: own representation) 40

2.6 Rat surgery and allograft tumor (source: own representation). 45

2.7 Setup tumor surgery (source: own representation). 48

2.8 Calculation of the resection volume and the residual tumor ratio (source: own representation). 49

2.9 Setup pig surgery (source: own representation). 51

3.1 Absolute frequency of all examined primary CNS tumors (source: own representation). 53

3.2 Relative frequency of all investigated primary CNS tumors (source: own representation). 54

3.3 Relative frequency of investigated benign primary CNS tumors (source: own representation). 55

3.4 Relative frequency of investigated malignant primary CNS tumors (source: own representation). 55

3.5 Relative frequency of investigated gliomas (source: own representation). 56

3.6 Boxplots regarding ages at diagnosis of a malignant CNS tumor (source: own representation). 58

3.7 Boxplots regarding ages at diagnosis of a benign CNS tumor (source: own representation). 59

3.8 Relative frequency of malignant and benign primary CNS tumors by age (source: own representation). 59

3.9 Age-adjusted frequency of malignant primary CNS tumors (source: own representation). 60

3.10 Age-adjusted frequency of benign primary CNS tumors (source: own representation). 60

3.11 Investigation of CLSM Miniprobes™ (source: own representation). . . . 62

3.12 Incubation times of AF for tumor staining (source: own representation). 63

3.13 Incubation times of AO for tumor staining (source: own representation). 64

3.14 Incubation times of CV for tumor staining (source: own representation). 65

3.15 Analysis of hemangioblastoma (source: own representation). 68

3.16 Analysis of glioblastoma (source: own representation). 69

3.17 Analysis of a brain metastasis of a non-small cell lung adenocarcinoma (source: own representation). 70

3.18 Analysis of epidermoid tumor (source: own representation). 71

3.19 Analysis of WHO grade I meningioma (source: own representation). . . 72

3.20 Analysis of choroid plexus papilloma (source: own representation). . . . 73

3.21 Analyses of pilocytic astrocytoma (source: own representation). 74

3.22 Erythrosine accumulation in fibroblast cells (source: own representation) 75

3.23 Investigation of erythrosine in tumor staining (source: own representation) 77

3.24 Investigation of erythrosine in CNS tumor staining compared to H&E (source: own representation). 78

3.25 CLSM and histopathological examination of healthy cortex tissue (source: own representation). 84

3.26 CLSM and histopathological examination of neuroepithelial tumors (modified from: Daali et al., 2016). 85

3.27 CLSM and histopathological examination of cranial and paraspinal nerve tumors (modified from: Daali et al., 2016). 86

3.28 CLSM and histopathological examination of pituitary adenomas (modified from: Daali et al., 2016). 87

3.29 CLSM and histopathological examination of WHO grade I meningioma subtypes (modified from: Daali et al., 2016). 88

3.30 CLSM and histopathological examination of WHO grade I meningioma subtypes (source: own representation). 89

3.31 CLSM and histopathological examination of WHO grade II meningioma subtypes (source: own representation). 90

3.32 CLSM and histopathological examination of a cavernoma (source: own representation). 90

3.33 CLSM and histopathological examination of an epidermoid tumor (modified from: Daali et al., 2016). 91

3.34 CLSM and histopathological examination of a plasmacytoma (source: own representation). 91

3.35 CLSM and histology of WHO grades I-IV astrocytomas (source: own representation). 96

3.36 CLSM negative imaging of high-grade astrocytomas (source: own representation). 97

3.37 *Ex vivo* examination with ICG and H&E (source: own representation). 99

3.38 *In vivo* CLSM imaging of AF and fluorescein (source: own representation).102

3.39 *In vivo* CLSM imaging of AF + fluorescein and ICG (source: own representation). 103

3.40 Examination of the tumor margin (source: own representation) 104

3.41 H&E stained sections of an incompletely removed tumor (source: own representation). 106

3.42 H&E stained sections of a sufficiently removed tumor (source: own representation). 107

3.43 Resection outcome and resection volume (source: own representation). . 108

3.44 Regression analyses (source: own representation) 110

3.45 *In vivo* CLSM imaging of healthy brain structures (source: own representation). 112

3.46 *In vivo* CLSM imaging of healthy glia cells, nerve cells and nerve fibers (source: own representation). 113

3.47 Artifacts during CLSM examination (source: own representation). . . . 114

List of Tables

1.1 WHO classification and survival statistics for gliomas 7
1.2 Outlook on the experimental approaches 22

2.1 Chemicals and reagents 23
2.3 Laboratory equipment and instruments 24
2.2 Media and Solutions 26
2.4 Technical information of used confocal Miniprobes^{TM} 31
2.5 Origin and number of human tumor samples examined by CLSM . . . 33
2.6 Properties of the contrast agents 36
2.7 Health hazard statements 37
2.8 Paraffin tissue processing 38

3.1 Fluorophores and their fluorescence intensity 79
3.2 Comparison of cell features stained with AF and H&E 92

Abbreviation

3D	three-dimensional
λ_{ex}	Excitation wavelength
λ_{em}	Emission wavelength
5-ALA	5-aminolevulinic acid
AF	Acriflavine hydrochloride
AO	Acridine orange
BBB	Blood-brain barrier
Bw	Body weight
CEA	carcinoembryonic antigen
CNS	Central nervous system
CLE	Confocal laser endomicroscopy
CLIP2	CAP-GLY-domain-containing linker protein 2
CT	Computed tomography
CV	Cresyl violet
DMEM	Dulbecco's Modified Eagle Medium
DMSO	dimethyl sulphoxide
DTI	Diffusion tensor imaging
DWI	Diffusion weighted imaging
EGFR	Epidermal growth factor receptor
EMA	European Medicines Agency

$etCO_2$	end-tidal carbon dioxide
EtOH	Ethanol
FCS	Fetal calf serum
FDA	Food and Drug Administration
Fig.	Figures
FiO_2	Inspired oxygen
FITC	Fluorescein isothiocyanate
GHS	Globally Harmonized System
h	Hours
H&E	Hematoxylin and eosin
HCl	Hydrogen chlorate
HIF-1	Hypoxia-inducible factor 1
ICG	Indocyanine green
IDH	Isocitrate dehydrogenase
IGF-1R	Insulin-like growth factor 1 receptor
IGFBP7	Insulin-like growth factor-binding protein-7
i.p.	Intra-peritoneal
i.d	Internal diameter
JECFA	Joint FAO/WHO Expert Committee on Food Additives
MA	Massachusetts
MAPK	Mitogen-activated protein kinase
min	Minutes
MRI	Magnetic resonance imaging
NADPH	Nicotinamide adenine dinucleotide phosphate
O/N	Over night
PET	Positron emission tomography

PpIX	Protoporphyrin IX
PTPRZ1	protein-tyrosine phosphatase receptor type Z polypeptide 1
(R)-2HG	(R)-2-hydroxyglutarate
ROI	Region of interest
ROS	Reactive oxygen species
rpm	Revolutions per minute
SAPK	stress-activated protein kinase
SCF	Scientific Committee for Food
SPECT	Single photon emission computed tomography
TGF-β	Transforming growth factor-beta
TNF	Tumor necrosis factor
TPA	12-O-tetradecanoyl phorbol acetate
VEGF	Vascular endothelial growth factor
WHO	World Health Organization

1. Introduction

1.1 Primary central nervous system tumors

This study focuses on primary tumors of the central nervous system (CNS), which are abnormal cell formations within the brain and spinal cord. They are comparatively rare, constituting about 2–3% of all human neoplasms, but they account for 7% of cancer-related mortality before the age of 70 years (Buckner et al., 2007). In children (age < 15 years), primary CNS tumors are the most common solid tumors and the most common cause of cancer-related mortality after leukemia (Kaatsch et al., 2001).

In adults, most CNS tumors are metastatic lesions, which are 10 times more common than primary tumors (Kopczak et al., 2014; Langen et al., 2018). Metastatic lesions or secondary tumors are always malignant. They develop from other parts of the body and spread to the CNS through the lymph system and bloodstream (Langen et al., 2018). In contrast, Primary CNS tumors can be either benign (noncancerous) or malignant (cancerous). A malignant tumor is typically life-threatening due to its aggressive and invasive nature, but unlike other types of malignant tumors (e.g., lung, colon, breast), primary CNS tumors rarely spread (metastasize) to distant body sites (Budczies et al., 2014). In comparison, a benign tumor typically has a slow growing rate and well-defined borders, and it remains confined to its original location (Rees, 2011). However, due to their critical location, both benign and malignant CNS tumors are potentially life-threatening and can cause significant neurological morbidity (Langen et al., 2018).

Diagnosis of a CNS tumor is frequently delayed because symptoms are usually nonspecific caused by the pressure of the tumor on the brain or spinal cord, such as headache, difficulty with balance, vomiting, and altered mental status. The symptoms depend on the location, size, growth rate, and histology of the tumor (Rees, 2011). In contrast, specific symptoms (such as hypopituitarism) are directly linked to the location of the tumor, depending on the function controlled by the specific CNS part (Ackerman, 1992) (Fig. 1.1 and 1.2).

In order to locate the tumor and identify its size, both magnetic resonance imaging

(MRI) and computed tomography (CT), with and without administration of contrast media, are the methods of choice. Compared to CT, MRI is more sensitive, due to its superior soft tissue resolution, in detecting the presence of a tumor; however, CT is faster and is therefore regularly used in the clinic for unstable patients (Tsutsumi et al., 2017). More sophisticated imaging techniques, such as functional MRI, diffusion tensor imaging (DTI), diffusion weighted imaging (DWI), positron emission tomography (PET), and single photon emission computed tomography (SPECT), may provide complementary information about the tumor and its anatomic interrelationships within the eloquent area of the brain (Zhang et al., 2018).

The goals of CNS tumor surgery are to obtain pathological diagnosis, provide significant relief from mass effect, and to promote tumor resection. Surgical removal remains the initial treatment for nearly all patients with primary CNS tumors and can be curative for most benign tumors (Adamson et al., 2010). Unfortunately, surgical treatment of CNS tumors is associated with a high risk of collateral damage to the healthy, vital tissue that is essential for motor functions, speech, sensation, hearing, and memory (Baron Nelson et al., 2013). On the other hand, incomplete tumor resection is associated with high recurrence rate of approximately 90% and with decreased survival rate for the patient (Kowalczuk et al., 1997; Weller et al., 2013). Because radical surgical resection is associated with increased life expectancy and decreased morbidity, resection of as much tumor tissue as possible without causing injury to healthy tissues is the major aim for neurosurgeons (Lacroix et al., 2001; Sanai & Berger, 2008).

Today, the gold standards for surgery are stereotactic needle biopsy and open biopsy through craniotomy (including complete tumor removal). Stereotactic biopsy is a minimally invasive procedure, using CT or MRI guidance to obtain tissue with a needle. This procedure is primarily reserved for small and/or deep (i.e., thalamic) lesions in which a resection would cause unacceptable neurologic deficits; for lymphomas, because treatment usually involves radiation therapy and/or chemotherapy; and for metastatic lesions when the origin organ is unknown (Kelly, 1989, Kelly & Hunt, 1994). In the case of surgically accessible tumors, open craniotomy allows for biopsy and gross total resection (excisional open biopsy) simultaneously and is the first-choice method (Parney & Berger, 2012). An open biopsy without gross total resection of the tumor (incisional open biopsy) is usually only performed to confirm the diagnosis in the case that the needle biopsy was not informative (Kelly & Hunt, 1994). After the surgery, the removed specimen is histopathologically evaluated to confirm the first diagnosis (made by MRI/CT or needle biopsy), to differentiate tumor from other tissues, and to determine the type and the grade of the tumor.

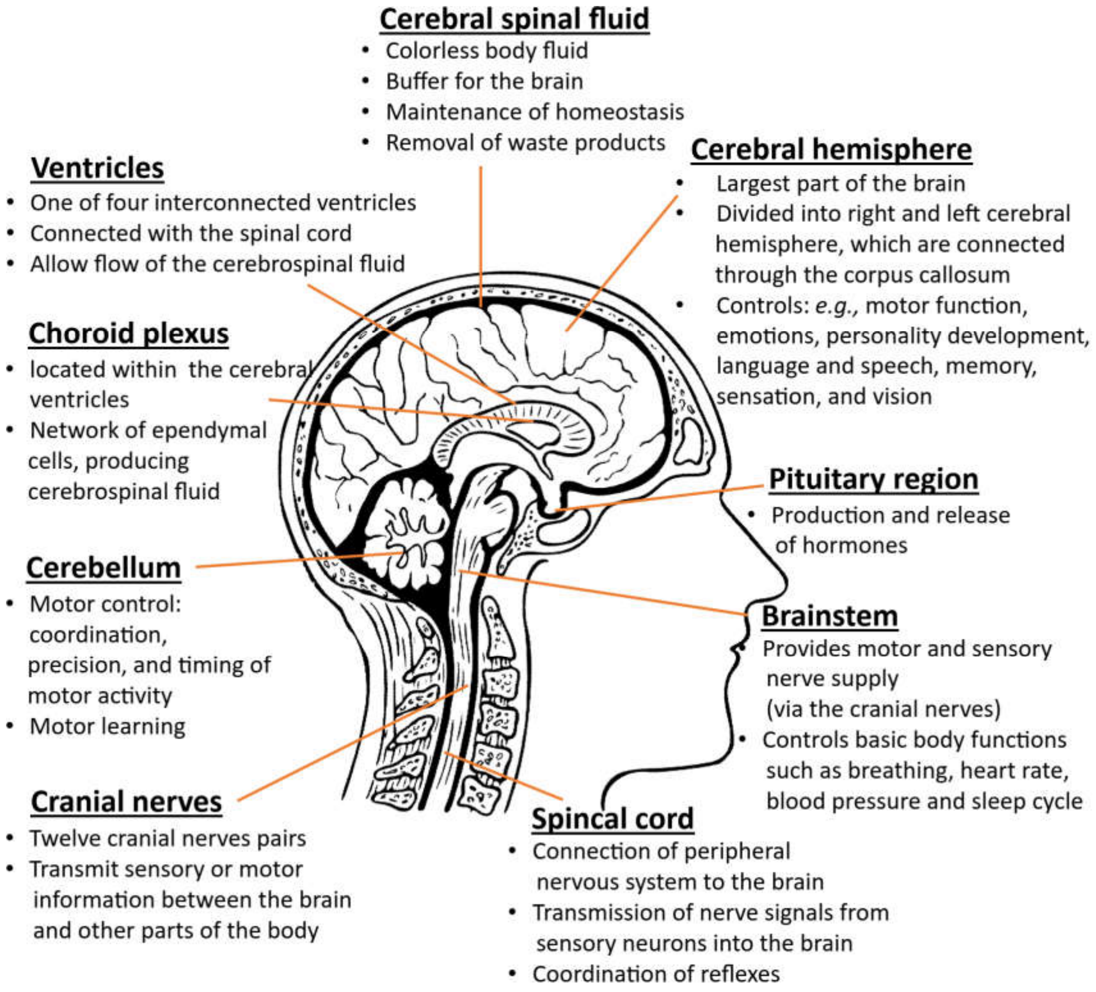

Figure 1.1: CNS locations and their basic functions (modified from pixabay.com). Schematic illustration showing the functions controlled by the specific CNS part. *CNS, central nervous system.*

1.2 Classification and problematic of primary CNS tumors

The World Health Organization (WHO) classification, first published by Zülch and colleagues in 1979, is the most widely accepted system for classifying CNS tumors (Zülch, 1980). The most recent classification, published in 2016, combines traditional histology criteria with an assessment of molecular biomarkers, and it contains more than fifty pathological entities, plus many variants within a subtype (Louis et al., 2016). The most common primary CNS tumor types found are the following:

Gliomas

Gliomas are the most common malignant primary CNS neoplasm (Louis et al., 2016). They are derived from glial cells, the supportive tissue of the brain (Adamson et al., 2010), and subdivided, according to the cells' origin, into ependymomas (ependymal cells), oligodendrogliomas (oligodendrocytes), astrocytomas (astrocytes), and mixed gliomas (oligodendrocytes and astrocytes). The degree of malignancy is characterized by WHO grades I–IV, in which WHO grade I is the least malignant and WHO grade IV is the most malignant glioma (Table 1.1). The grading system is primarily based on the degree of proliferation (mitotic index), the cell morphology, and the presence or absence of necrosis (Louis et al., 2016).

Moreover, variant analysis of isocitrate dehydrogenase (IDH; mutations affecting codon 132 of *idh1* or codon 172 of *idh2*) is an important molecular diagnostic marker for the classification of gliomas. For instance, the majority of primary glioblastomas have no *idh* variation compared to WHO grade II–III gliomas (diffuse astrocytoma, oligodendroglioma, oligoastrocytoma, anaplastic astrocytoma, anaplastic oligodendroglioma, and anaplastic oligoastrocytoma) and to secondary glioblastomas, in which this variation occurs in approximately 80% of cases (Balss et al., 2008). Patients having a glioma with an *idh* variation are associated with a significantly better overall survival prognosis compared to those having gliomas with wild-type *idh* (*idh1* mutation versus wild *idh1*; 31 months versus 15 months with therapy in the case of glioblastomas) (Kaminska et al., 2019).

Ependymomas

Ependymomas are more common in children (age < 15) and usually do not infiltrate surrounding tissue, allowing for curative resection after gross total resection (Allen et al., 1998). This implies that they have not spread along the cerebrospinal fluid; in which case the demand for gross total resection should be weighed against the risk of surgery-induced long-term disability (Buckner et al., 2007). Furthermore, the location of these tumors is an important prognostic factor: on average, posterior fossa ependymomas have a moderate prognosis, while spinal cord ependymomas have a good prognosis (Chai et al., 2017).

Oligodendrogliomas

Oligodendrogliomas are usually found in adults of an average age of 35 years (Mesfin & Al-Dhahir, 2017). These infiltrating tumors typically involve the white matter and cerebral cortex (Fig. 1.2). The prognosis depends on the pathologic grade, either WHO grade II or III (Buckner et al., 2007; Wesseling et al., 2015), with WHO grade III having a shorter median survival rate and higher recurrence rate (Table 1.1).

Oligoastrocytomas

Oligoastrocytomas are diffuse mixed tumors with neoplastic astrocytic and oligodendroglial parts (Louis et al., 2016). They arise most frequently in the frontal and temporal lobes and are divided into oligoastrocytomas (WHO grade II) and anaplastic oligoastrocyotmas (WHO grade III). Prognosis depends on the WHO grade as well as on the amount of neoplastic astrocytic cells (Adamson et al., 2010) (Table 1.1).

Astrocytomas

- WHO grade I astrocytomas (predominantly pilocytic astrocytoma, cerebellar astrocytoma and desmoplastic infantile astrocytoma) arise most commonly in the cerebellar hemispheres and around the third ventricle (Fig. 1.2). They are slow-growing, generally well demarcated, and therefore the most benign glioma (Zülch, 1979; Louis et al., 2016). Pilocytic astrocytomas occur more often in children (age < 15) and may allow surgical cure by gross total resection (Adamson et al., 2010) (Table 1.1).
- WHO grade II astrocytomas (diffuse astrocytoma) arise most commonly in the cerebral hemispheres (Fig. 1.2). They are slow-growing but diffuse infiltrative

gliomas with continuous growth (Preusser et al., 2011) (Table 1.1). Most commonly, diffuse astrocytomas occur in young adults, with a peak frequency in the mid-thirties (Adamson et al., 2010).

As these tumors inevitably progress into higher grade tumors, it is necessary to monitor the tumor closely to adapt the treatment to its growth rate. The most important factors increasing survival include younger age at diagnosis, tumor size of less than 5 cm, and gross total resection of the tumor if possible (Buckner et al., 2007).

- WHO grade III astrocytomas (anaplastic astrocytoma) are diffusely infiltrating, malignant gliomas which occur most frequently in adults around 45 years of age (Grimm & Chamberlain, 2016). They grow at a faster pace and require a more aggressive treatment than WHO grade II gliomas (Ichimura et al., 2009; Sanai & Berger, 2012). The standard initial treatment is maximal surgical tumor resection, without causing or increasing substantial neurologic deficits, followed by radiation therapy. However, even with therapy, the recurrence rate is high and the prognosis poor (Grimm & Chamberlain, 2016) (Table 1.1).
- WHO grade IV astrocytomas (glioblastomas) are the most common malignant primary CNS tumors in adults and children (Kaatsch et al., 2001). Although this tumor is found in all age groups, it presents more frequently in adults between 45 and 75 years of age (Tofte et al., 2014). Prognosis is complicated due to the tumor's diffuse infiltrative nature, including the opposite hemisphere, making surgical extirpation impossible (Sahm et al., 2012). Tumor recurrence occurs in up to 90% of cases within the immediate vicinity of the original location and only in rare cases in remote locations (Roy et al, 2015).

  In most patients, glioblastomas arise *de novo* (90%), without any previous lesion, and are called primary glioblastomas (Ohgaki et al., 2004). In few cases, however, these tumors develop from lower-grade astrocytomas and are then called secondary glioblastomas (10%) (Ohgaki & Kleihues, 2005). Patients with a secondary glioblastoma have a significantly better overall survival prognosis (Preusser et al., 2011) (Table 1.1).

Table 1.1: WHO classification and survival statistics for gliomas.

WHO grade	**Description**[1]	**Tumor type**	**Median survival** [years]
I	• Least malignant • Non-infiltrative; slow growing • Nuclear atypia present	Pilocytic astrocytoma	up to 50 years; cure is possible[2]
II	• Relatively slow growing • Infiltrative • Increased hypercellularity • May recur as higher grade	Diffuse astrocytoma Oligodendroglioma Oligoastrocytoma	6–8* 12* 3–10*
III	• Highly infiltrative • Increased mitotic activity • Tend to recur as higher grade	Anaplastic astrocytoma Anaplastic oligodendroglioma Anaplastic ependymoma	3* 3–4* 3–10*
IV	• Most malignant • Widely infiltrative • Rapid recurrence • With necrosis and/or micro-vascular proliferation • High rates of mitosis	Primary glioblastoma Secondary glioblastoma	1–2* 2–2.5*

WHO, World Health Organizatio; IDH, Isocitrate dehydrogenase.

[1](Louis et al., 2016); [2]in children and young adults; survival decreases with increasing age (Johnson et al., 2012); *with therapy in adults (Vigneswaran et al., 2015; Kaminska et al., 2019; Wu et al., 2016).

Benign CNS tumors

Choroid plexus tumors

Choroid plexus tumors are rare tumors; approximately 2%–4% of intracranial tumors in children and 0.5% in adults (Ozdogan et al., 2015; Jaiswal et al., 2013). They arise from the choroid plexus epithelium, which are characterized by papillary and intraventricular growth. It is of utmost importance for the patient's treatment to discriminate between the benign forms; choroid plexus papilloma (WHO grade I) and atypical choroid plexus papilloma (WHO grade II) and the very rare malignant form; choroid plexus carcinoma (WHO grade III) (Louis et al., 2016).

The treatment of choice for choroid plexus papilloma is gross total surgical resection. However, the surgery is challenging, and surgical complications can occur due to a marked vascularity, the presence of massive hydrocephalus, and/or the high age of the patient (Gopal et al., 2008).

For choroid plexus carcinomas, which primarily occur in children, surgical treatment is even more challenging due to the tumors' infiltrating growth pattern in the contiguous brain parenchyma (Jeibmann et al., 2007). Furthermore, choroid plexus carcinomas may also spread metastases along the cerebrospinal fluid pathways, which further complicates the surgery and promotes a dismal prognosis (Gopal et al., 2008).

Meningiomas

Meningiomas (WHO grade I) arise from arachnoid cap cells and are the most common benign intracranial tumors (Shibuya, 2015). However, a minority progress to malignant forms (WHO grades II and III) (Linsler et al., 2014). Furthermore, irrespective of the grade, some can cause substantial morbidity and can have, depending on their location, lethal consequences (Adamson et al., 2010). Especially, skull-based meningiomas can be challenging in surgery due to their critical location close to vital brain regions (Shaikh et al., 2018).

In the cases of atypical (WHO grade II) and anaplastic (WHO grade III) meningiomas, a complete resection is almost impossible due to their infiltrating growth pattern, which promotes a high recurrence rate (Riemenschneider et al., 2006). The tumor grade and the extent of resection appear to be the two most important prognostic factors regarding tumor recurrence (Hortobagyi et al., 2016).

Schwannomas

Schwannomas arise from Schwann cells and are the most common benign primary tumors of the spine (Seppala et al., 1995). The well-demarcated tumor is mostly diagnosed in the fourth and fifth decade of life and has a favorable prognosis (Jinnai & Koyama, 2005). Nevertheless, schwannomas can suppress the spinal cord, leading to weakness, sensory loss, intestinal and bladder problems (Raj & Lofton, 2013). Schwannomas occurring on the vestibulocochlear nerve near the cerebellum are called vestibular schwannomas, and their pressure can cause hearing loss, tinnitus, and unsteadiness. Here, tumor resection relies on avoiding an injury of the cranial nerves (Jameson et al., 2007). Unfortunately, to avoid postoperative neurological deficits, it is often necessary to leave a tumor residue at the nerves, which leads to an increased recurrence rate (Bloch et al., 2004). Nonetheless, early surgical resection can lead to a promising outcome, with a recurrence rate of only 5% within several years after surgery (Deng et al., 2015; Fehlings et al., 2016).

Pituitary adenomas

Pituitary adenomas are benign tumors in the pituitary gland of the brain (Louis et al., 2016). Approximately 50% are microscopic (< 1 cm) and are not growing or causing problems (Ferlay J, 2018). The remainder are macroadenomas (≥ 1 cm) and giant adenomas (≥ 4 cm), which can cause hypopituitarism or a complete insufficiency of the pituitary gland (Foppiani et al., 2009). Therefore, pituitary adenomas are further clinically classified as functional and nonfunctional adenomas, depending on their ability to produce and secrete excess hormones (most commonly prolactin) (Kopczak et al., 2014). Surgical removal is recommended for either functional or nonfunctional adenomas that threaten the visual pathways, for macroadenomas because of mass effect and\or hypopituitarism, and for prolactinomas when drug treatment was not successful (Ferlay, 2018).

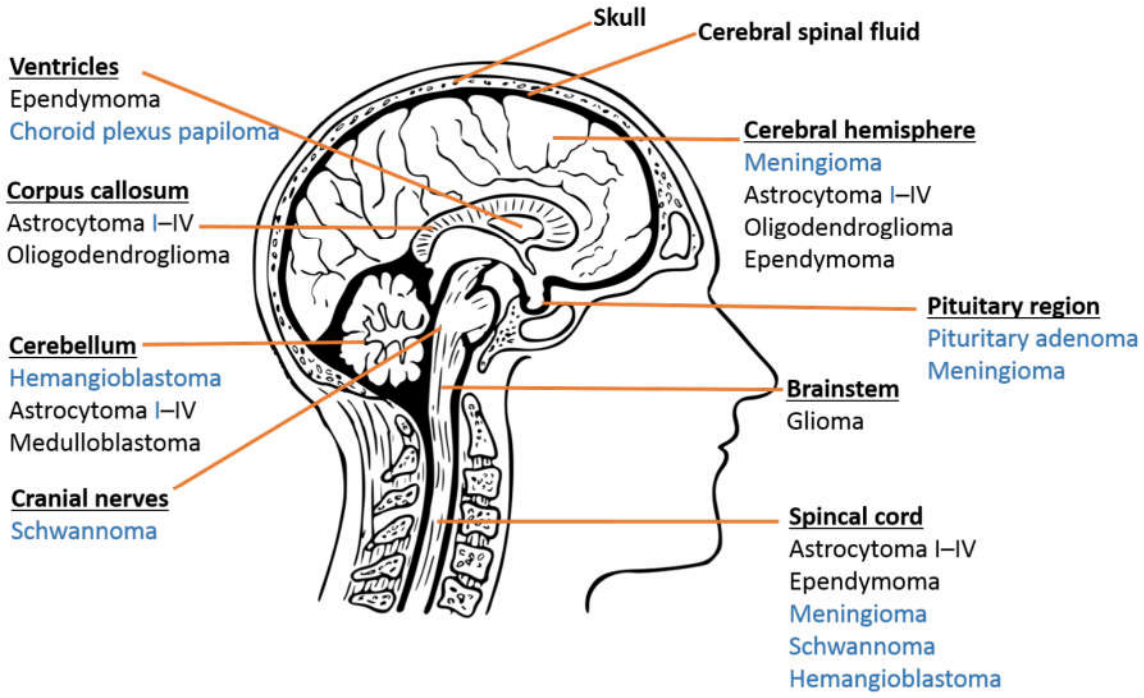

Figure 1.2: Primary CNS tumor locations (modified from https://pixabay.com). Schematic illustration of a brain showing the most common locations of a primary CNS tumor. Blue color marks the benign tumors. Uncolored tumors are malignant primary CNS tumors. *CNS, central nervous system.*

1.3 Challenge in neurosurgery: Intraoperative tumor assessment

In neurosurgery, the risk of collateral damage to vital healthy tissue is a major concern. On the other hand, several studies have shown an association between the extension of surgical tumor removal and prolonged survival (Roth & Elvidge, 1960; Coffey et al., 1988; Franklin, 1992; Devaux et al., 1993; Iacoangeli et al., 1993; Simpson et al., 1993; Senft et al., 2011; Markert, 2012; Chaichana et al., 2014). Thus, surgeons need to take utmost care when removing tumor tissue to prevent a loss of brain function, while at the same time removing as much of the tumor as possible to increase the survival time and decrease intracranial pressure (Markert, 2012). To achieve this goal, several modalities have been developed to provide precise spatial information to neurosurgeons, including surgical wide-field microscopy with 5-aminolevulinic acid (5-ALA; see subsection 1.6.1), navigation devices, ultrasonography, intraoperative MRI and CT, and electrocortical mapping (Fengqiang et al., 2008).

Of these, **neuronavigation** is regularly used in the surgical management of brain tumors, particularly in skull-based surgeries. It helps to accurately localize important anatomic structures, such as the carotid artery or cranial nerves (Fengqiang et al., 2008). However, its utility is limited during the operation process because it is an offline method based on preoperative imaging alone and thereby suffers from brain shift (Mitsui et al., 2011). This intraoperative brain deformation occurs after cerebrospinal fluid loss, cyst decompression, and cerebral edema or sag (Orringer et al., 2012).

Ultrasonography overcomes this problem, as it is a semi-online assessment technique that can be used as often as needed during the surgery process. The 3D (three-dimensional) scanning of the resection cavity allows for both continuous monitoring of resection progress and assessment of brain shift (Machi et al., 2004). The addition of Doppler ultrasonography can be helpful in assessing flow in normal cerebral and spinal vasculatures (Oglat et al., 2018). Major limitations of this system are low signal-to-noise ratios and poor contrast resolution (Machi et al., 2004).

In contrast, intraoperative **CT** and **MRI** are characterized by high contrast resolution and are not affected by brain shifts. Especially MRI-guided surgery provides real-time data on tumor volume and location, with high contrast (Mondal et al., 2014). The assessment of the tumor in a 3D view allows for a safer trajectory planning for tumor access (Mislow et al., 2009; Mondal et al., 2014). Unfortunately, although there are promising reports of improved tumor removal rates through the use of these tools, their regular application in neurosurgery is currently inhibited due to their complexity, their high cost, and a prolonged operative duration (Bayer et al., 2017).

Finally, tumors in critical brain regions can be more radically removed if the surgery is performed while the patient is awake (awake craniotomy). Intraoperative stimulation mapping using **electrocortical mapping** allows the surgeon to map brain cortical regions and their radiating white matter tracts, which helps minimize neurological impairment during the operation (Dziedzic & Bernstein, 2014). Cortical stimulation in language areas of the brain tests the speech ability by talking to the patient during the surgery, thereby providing a significant preservation of speech function compared to surgery with general anesthesia (Ibrahim & Bernstein, 2012). However, this procedure cannot be performed if the patient is claustrophobic or has psychiatric issues such as anxiety or neurocognitive issues such as dementia or mental retardation (Young et al., 2015).

Overall, the major limitation of these approaches is that they are only effective for the localization of the bulk disease and/or preserving eloquent brain regions. The intraoperative procedures are not able to provide tissue detail on a cellular level to achieve complete tumor resection by minimizing the amount of residual tumor cells in tissue with a normal appearance, which often results in tumor recurrence (Fengqiang et al., 2008).

To date, **frozen section analysis** is the only method for intraoperative tissue assessment on a cellular level (Jaafar, 2006). Frozen section analysis is rapid and generally preferred over traditional histology, which is more time-consuming. Unfortunately, intraoperative histopathology also suffers from several drawbacks, including the formation of freezing artifacts, errors in tissue sampling, and a poor resolution of the final slide. Finally, the lack of real-time interactivity with the pathologist and a waiting time of about 40 min for diagnostic evaluation disrupt the surgical work flow (Jaafar, 2006).

Hence, new methods for intraoperative evaluation of tissues are required to improve the diagnostic yield in ongoing surgery. The optimal imaging approach would allow for microscopic detection of infiltrative neoplastic cells and margins in real time to enhance surgical decisions without prolonging the operating times. **Confocal laser scanning microscopy (CLSM)**, initially described in 2004 in gastroenterology, is a promising diagnostic tool fulfilling these requirements as it can achieve *in vivo* high-resolution imaging of histopathological features (Kiesslich et al., 2004). The main advantage of CLSM is the ability to visualize tissues in real time, unaffected by sampling errors. This approach has already been utilized in gastroenterology (Polglase et al., 2005; Meining et al., 2007), pulmonology (Thiberville et al., 2007; Lane et al., 2009), gynecology (Carlson et al., 2005; Tan et al., 2009), urology (Sonn et al., 2009; Wiesner et al., 2011), and dermatology (Schulz et al., 2016). It has enabled real-time examination of several diseases, including Barrett's esophagus (Trovato et al., 2013), inflammatory bowel diseases (Malmstrom et al., 2014), celiac disease (Nguyen & Leong, 2008), and various types of cancer (Buchner & Wallace, 2015). In the field of neurosurgery, experience with CLSM is rare and mostly limited to animal models, with only few human studies (Schlosser et al., 2010; Sanai et al., 2011b; Whitson et al., 2011; Foersch et al., 2012; Wirth et al., 2012; Snuderl et al., 2013; Charalampaki et al., 2015).

1.4 Confocal laser scanning microscopic system

The CLSM system is an extension of a fluorescence microscope. It has integrated fluorescence optics which allow excitation (λ_{ex}) of a fluorophore molecule by an external source, such as a laser, and then detection of the fluorophore's appropriate emission wavelength (λ_{em}) by a detector (Fig. 1.3). The principle of fluorescence is described in Section 1.5. In addition, the concept of CLSM is based on the principle of confocal microscopy, which was invented by Minsky in 1955 (Minsky, 1988). Figure 1.3 illustrates the light pathway of a confocal system.

Firstly, a diffraction-limited laser spot is directed through a pinhole to a dichroic mirror. The dichroic mirrow is a key component of a fluorescence microscope as it reflects the laser light (excitation light, shorter wavelength) to the sample but enables the emitted light (longer wavelength) to pass through to the detector (Fig. 1.3).

Before the laser light reaches the sample, it is focused through an objective lens in a specific focal plane of the sample. The fluorescence emitted by the excited sample is then refocused by the same objective through the dichroic mirror to the detector. Due to a confocal pinhole at the entrance to the detector, only the in-focus fluorescence light of the focal plane can pass. An image is then generated by scanning the light point to point through the area of interest in the sample. In this way, the scanning system provides a clear, in-focus, 3D image of a thin section within a thick tissue (Meining, 2009). In contrast, in conventional wide-field microscopy, a large region of the specimen is illuminated, and the image is generated from in-focus light and out-of-focus background light. The axial resolution and image contrast are decreased, which precludes an appropriate visualization of thick samples (Wolenski & Julich, 2014).

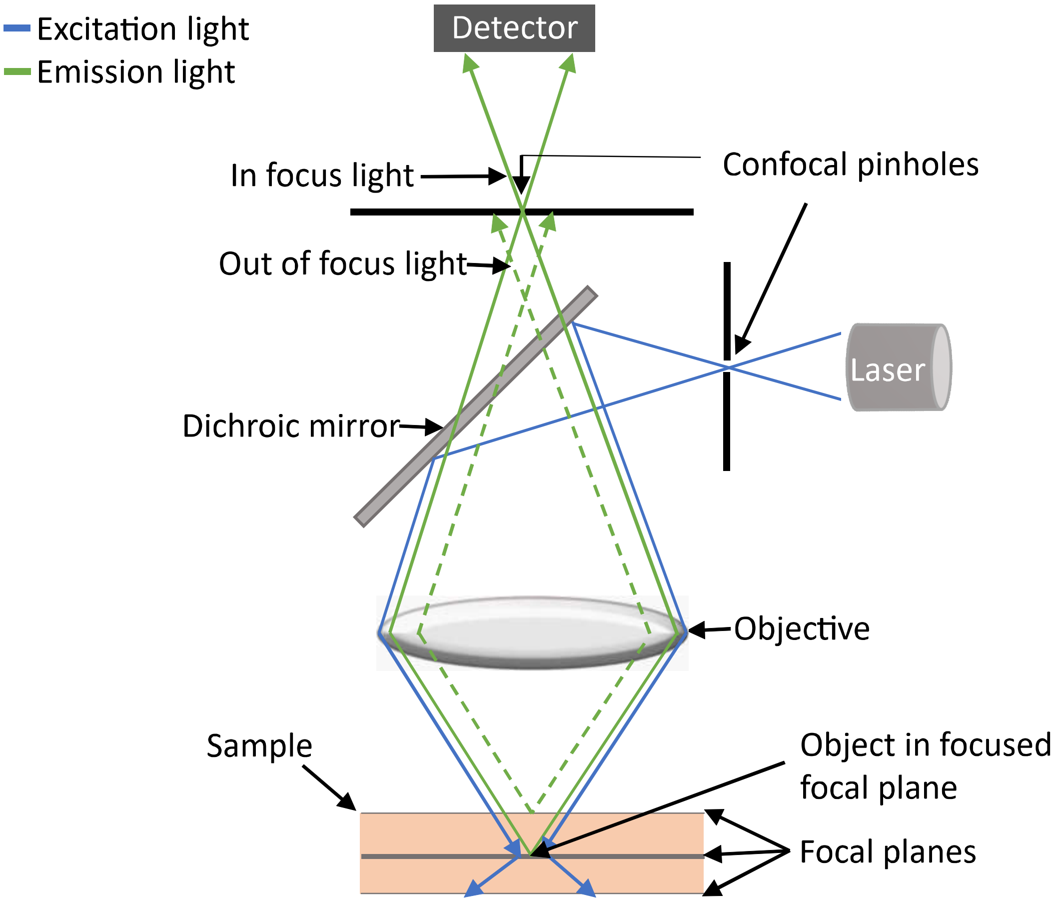

Figure 1.3: Schematic illustration of the light pathways in confocal microscopy (source: own representation). The laser light (excitation light; blue arrow) is directed through a pinhole to a dichroic mirror, which reflects the light to the focus point of the objective onto the specimen. The fluorescence emitted by the excited sample (green arrow) is then collected by the same objective lens and transmitted through the dichroic mirror to the detector. The confocal pinhole at the entrance to the detector allows only the in-focus fluorescence light of the certain focal plane to pass. Fluorescence from excited molecules above and below the focused focal plane (out-of-focus fluorescence; broken green line) are also collected by the objective but not measured by the detector.

Currently, two Food and Drug Administration (FDA) approved CLSM systems are available for clinical practice and research (Meining, 2009): endoscopy-integrated CLSM (Optiscan®; Notting Hill, Victoria, Australia/Pentax; Tokyo, Japan) and probe-based CLSM (Cellvizio®; Mauna Kea Technologies, Paris, France). The endoscopy-integrated CLSM was developed by a collaboration between Pentax (Tokyo, Japan) and Optiscan® (Notting Hill, Victoria, Australia) as a fluorescent-based CLSM device that incorporate a miniaturized confocal microscope into the tip of an ordinary endoscope, thus allowing endoscopy and confocal microscopy to be simultaneously displayed side by side on separate monitors (Cartana et al., 2012). A further advantage of this system is that the depth of imaging can be controlled mechanically by using two buttons on the endoscope (Meining, 2009).

The second CLSM system, Cellvizio®, is a probe-based CLSM system consisting of a range of flexible probes that can be introduced through the working channel of a conventional endoscope or used independently (see subsection 2.3.1) (MaunaKeaTechnologies, 2016). The various probes differ in their field of view, lateral resolution, depth of observation, and length suitable for different clinical indications. Advantages of this system are its greater versatility and the possibility of combining it with other imaging techniques, such as chromoendoscopy and magnification endoscopy (Kolodziej et al., 2016).

1.5 Challenge using CLSM in neurosurgery: contrast agents

Suitable fluorophores to stain human tissue *in vivo* are a limiting factor for using CLSM in neurosurgery and other surgery disciplines (Zehri et al., 2014).
Fluorophores are per definition fluorescent compounds which are capable of emitting light upon excitation (Drummen, 2012). The fluorescence process can be described in a Jablonski diagram (Fig. 1.4), named after the physicist Aleksander Jablonski (Jablonski, 1933). When a fluorophore absorbs light of its absorption spectrum, its electrons are excited from the lowest (ground) electronic state into a higher energy state corresponding to the amount of energy transferred. The absorbance is a very fast process of approximately 10^{-15} seconds. The excited electron then very quickly (10^{-12} seconds) loses energy as kinetic energy, mainly due to vibrational relaxation, a nonradiative process. The vibrational relaxation causes a fall of the electron to a lower vibrational level or from a vibrational level in one electronic state to a vibrational level in a lower electronic state (internal conversion). Nanoseconds later (about 10^{-8} seconds), in the usually slowest process, longer-wavelength light (fluorescence) is emitted when

the electrons return to the ground state. The energy of the fluorescent light (longer wavelength) is lower than that of the absorbed light (shorter wavelength), as energy is "lost" in vibrational relaxation and internal conversion (Fig. 1.4) (Jablonski, 1933). The fluorophore can be excited and detected repeatedly unless it is irreversibly destroyed in the excited state (photobleaching).

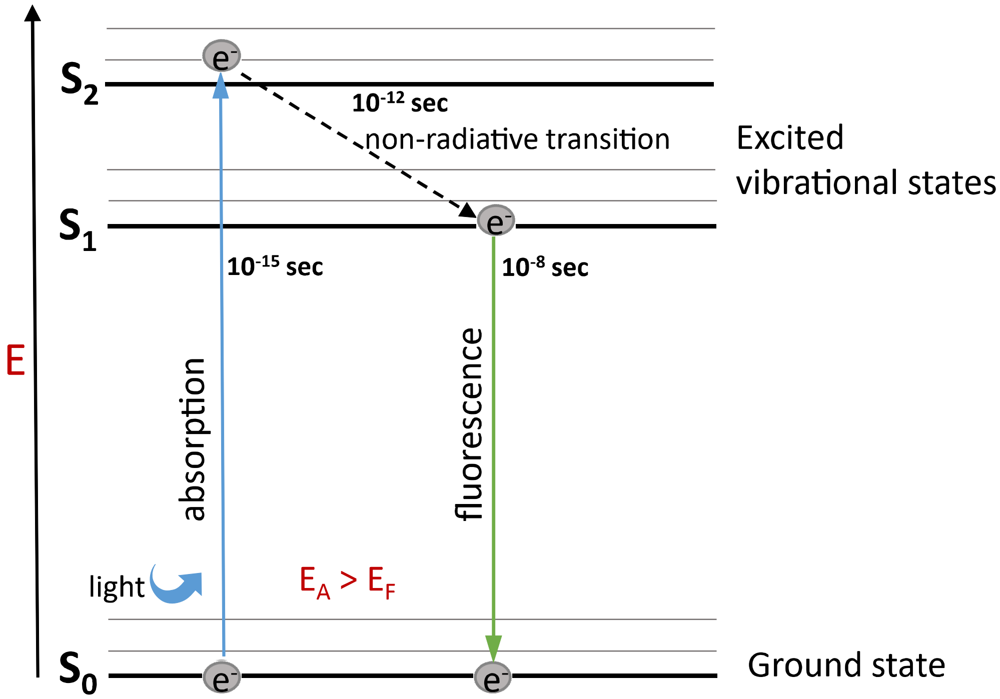

Figure 1.4: Jablonski diagram of fluorescence (source: own representation). The diagram shows electronic states as bold horizontal lines. The thin horizontal lines are the vibrational sublevels. The absorption of light by an electron (indicated by the blue arrow) causes its excitation from the ground state (lowest energy state; S_0) to an excited state (here S_2). This is a very fast process of approximately 10^{-15} seconds. The excited electron loses then very fast ($\approx 10^{-12}$ seconds) energy through vibrational relaxation (internal conversion) and falls to the lowest level of the first excited state (S_1). Finally, the electron returns to the ground state ($\approx 10^{-8}$ seconds) by releasing light (fluorescence; green arrow). Due to the energy loss in internal conversion, the energy of light emitted (E_F) has a lower energy than the light absorbed (E_A). *S, state; E, energy; sec, seconds.*

The difference in wavelength between the maximum of excitation and emission is described as the Stokes shift, named after the physicist George G. Stokes (Stokes, 1852). Each fluorophore has a specific absorption and emission spectrum, depending on its molecular structure (Te Velde et al., 2010). A fluorophore with a large Stokes shift results in more reliable fluorescence detection than a fluorophore with a small Stokes shift (Stokes, 1852).

Furthermore, the optimal fluorescent dye must exhibit low phototoxicity, photobleaching, scattering and signal attenuation (Zehri et al., 2014). Of these, phototoxicity can result from different sources and is closely connected to photobleaching (Sugden, 2004). One main cause of phototoxicity is the production of reactive oxygen species (ROS) during the excitation of a fluorophore (Zehri et al., 2014). In excess, ROS causes the oxidation of the fluorophore and several oxidizable components of the tissue under investigation (Bernas et al., 2004). Thus, inducing photobleaching of the fluorophore as well as damage to the proteins, nucleic acids, lipids and plasma formations of the tissue (Vrouenraets et al., 2003). The occurrence of ROS is primarily dependent on the properties of the fluorescent dye (Sugden, 2004) and the dose of photons absorbed (Bernas et al., 2004).

Scattering of light, signal attenuation, and absorption are limiting factors for the depth of tissue penetration: with increasing wavelength, scattering and absorption decreases. The near infrared spectrum (700–900 nm) is therefore suitable for imaging deeper cell structures (Licha, 2002). Fluorophores with emission wavelengths above 900 nm are not practicable, as water absorbs very strongly at these wavelengths, reducing the light transmission (Osterman et al., 2007).

In addition, a suitable fluorophore for *in vivo* CLSM application should be soluble for administration and safe for human application, and it should have a fast clearance, an optimal wavelength corresponding to available CLSM excitation wavelengths (λ_{ex} of 488 nm and 780 nm, respectively), and a high quantum yield. The fluorescence quantum yield is a measure of the fluorescence process and is defined as the ratio of photon absorption to emission (Schwartz et al., 2002). Accordingly, the highest quantum yield (1.0) is achieved when every absorbed photon is emitted (Te Velde et al., 2010).

Finally, for a neurosurgical application, the fluorophore needs to be able to enter the blood-brain barrier (BBB). The BBB, formed by the cerebral microvascular endothelium, possesses unique properties to strictly control the diffusion of molecules, ions, and cells, allowing only specific small and lipid soluble substances with a molecular weight of < 400 Da to cross between the blood and the brain (Daneman & Prat). This heavily regulated barrier protects the CNS from toxins, pathogens, and inflammation to provide health and proper neuronal function. In several diseases, including brain tumors, the permeability of the BBB is increased, which supports the progression of the disease (Daneman & Prat, 2015). BBB dysfunction also leads to an increased entry of drugs and molecules, such as fluorescent dyes, into the brain, facilitating their use for an enhanced tumor contrast (Banks, 2009).

1.6 Fluorescence in CNS tumor surgery

1.6.1 5-aminolevulinic acid

5-ALA is a body's own non-fluorescent precursor in the hemoglobin biosynthetic pathway formed in the mitochondria (Yang et al., 2015). Its metabolism produces protoporphyrin IX (PpIX), an endogenous fluorophore, which is the last precursor of heme. The final step of the heme biosynthesis, the incorporation of iron into PpIX, requires the catalytic activity of the enzyme ferrochelatase (Pogue et al., 2010).

Thus, PpIX is believed to collect in neoplastic cells due to a reduced activity of the enzyme ferrochelatase in malignant high-grade tumors (Peng et al., 1997; Gibson et al., 1999). Other factors are the breakdown of the BBB, a higher neovascularity, cell proliferative activity, and cellular density (Stummer et al., 1998; Stepp et al., 2007).

It is important to note that the natural occurrence of PpIX is not detectable by fluorescence microscopy; only overloading the natural pathway with exogenous 5-ALA causes fluorescently visible accumulation of PpIX in tumor tissue at a λ_{ex} between 375 and 440 nm and a λ_{en} between 640 and 710 nm (Zehri et al., 2014, Pogue et al., 2010).

Stummer et al. presented the first human trial of PpIX fluorescence of gliomas after 5-ALA application in 1998. The authors were able to show a high accuracy in predicting the presence of malignant tissue due to a strong PpIX fluorescence in tumor tissue and no visible PpIX fluorescence in healthy tissue (Stummer et al., 1998). In a follow-up study, fluorescence-guided resection of glioblastomas using PpIX fluorescence was achieved in 33 of 52 patients (63%) (Stummer et al., 2000). Additionally, Stummer and colleagues conducted a multicenter, randomized phase III trial, which demonstrated better frequency of gross total resections (65% vs. 36%) and 6-month progression-free survival (41% vs. 21.1%) with 5-ALA use compared to conventional white-light surgery (Stummer et al., 2006). Since this trial, 5-ALA has been widely used for the visualization of high-grade gliomas, foremost glioblastomas, under the trademark of Gliolan® (Teixidor et al., 2016).

Gliolan®, which contains 30 mg/ml of the active 5-ALA substance, is the only contrast agent currently approved for the imaging of high-grade gliomas in Europe by the European Medicines Agency (EMA) (Nguyen & Tsien, 2013). In Australia, Canada, and Asia, Gliolan® is also allowed for neurosurgical purposes, while in the US, it is still awaiting approval by the FDA (Martirosyan et al., 2011).

Unfortunately, apart from high-grade gliomas, malignant meningiomas and metastases, the other types of CNS tumors have shown almost no PpIX fluorescence (Gibbs et al., 2006; Valdes et al., 2011). Likewise, Gliolan® cannot be used during pregnancy or in children due to studies suggesting an embryotoxic activity of 5-ALA and to missing studies evaluating the safety of 5-ALA in children and adolescents aged 0 to 18 years, respectively (Teixidor et al., 2016). In adults, however, it has shown a high safety profile, with only minor systemic side effects, such as anemia, nausea, vomiting, hypotension, and an increased sensitivity to sunlight, up to 48 hours after application (Colditz et al., 2012; Stummer & Suero, 2017).

1.6.2 Fluorescein

Fluorescein is a strong yellow contrast agent having a peak λ_{ex} at 490 nm and a λ_{en} between 500 and 550 nm. It is an FDA- and EMA-approved contrast agent for diagnostic angiography of the retina (Nguyen & Tsien, 2013). In ophthalmology, fluorescein has been used since 1960 and has shown a high safety profile with only few reports of severe side effects, such as nausea and vomiting (Behbahaninia et al., 2013).

In neurosurgery, fluorescein is one of the original fluorophores used in surgical treatments for arteriovenous malformations (Feindel et al., 1971), cerebral artery anastomoses (Feindel et al., 1971), aneurysm clipping (Wrobel et al., 1994), and brain tumor contrast (Moore et al., 1948). Following intravenous administration, fluorescein binds to serum albumin in the blood stream and penetrates the disrupted BBB. Thus, fluorescein is not a specific tumor dye, but it often concentrates at the tumor site in regions of compromised neurovasculature, especially in high-grade tumors such as glioblastomas (Stummer, 2015).

In the clinical study carried out by Moore et al., fluorescein contrast facilitated differentiation between tumor and healthy tissue in 95.7% of patients (Moore et al., 1948). Another study, carried out by Shinoda et al., reported an increased gross total resection (84.4%) of glioblastomas with fluorescein contrast obtained by a surgical wide-field microscope; in control patients, the gross total resection of glioblastomas without use of fluorescein was 30.1% (Shinoda et al., 2003). Moreover, Chen et al. achieved an 80% gross total resection rate of glioblastomas and additionally an increased 6-month progression-free survival in patients with low-grade gliomas (Chen et al., 2012). Finally, fluorescein contrast has been used to facilitate tumor resection of different skull base tumors, such as meningiomas, schwannomas, and pituitary adenomas (da Silva et al., 2010). However, fluorescein is not FDA/EMA-approved for brain tumor surgery and is therefore restricted to clinical studies (Nguyen & Tsien, 2013).

1.6.3 Indocyanine green

Indocyanine green (ICG) belongs to the cyanine dyes, which are small cationic molecules with two terminal nitrogen-containing heterocycles connected through a polymethine bridge (Yi et al., 2014). It is a near-infrared fluorophore with an λ_{ex} peak at 760–775 nm and an λ_{em} peak at around 835 nm. Its anionic and amphiphilic properties allow a high affinity to proteins, such as albumin, which increases its hydrodynamic diameter (Behbahaninia et al., 2013). It remains in the vasculature with a plasma half-life of 4 min, after which it is metabolized in the liver (Hanel et al., 2010). For clinical use, ICG is typically administered as an intravenous bolus at the recommended dose of 0.2–0.5 mg/kg with a maximum dose of 5 mg/kg per day (Baek et al., 2015).

The FDA approved ICG in 1975 for use in ophthalmic angiography due to its low negative-reaction profile (Polom et al., 2011). Furthermore, ICG has proven to be a clinically useful fluorophore and is widely used. For example, ICG has been used to map sentinel lymph nodes and to detect various cancers such as breast, anal, liver and gastrointestinal cancers (Ohnishi et al., 2005; Tagaya et al., 2008; Hirche et al., 2010; Kelder et al., 2010). In neurosurgery, intravenously applied ICG has been mainly used for brain video angiography to aid in treating cerebral aneurysms or to define abnormal vascular flow patterns in arteriovenous malformations and dural arteriovenous fistulas (abnormal connections between arteries and dural veins or venous sinuses in the dura) (Youssef et al., 2014). Though 3D intraoperative digital subtraction angiography is still the gold standard in vascular neurosurgery, intraoperative ICG is faster and requires less equipment (Marbacher et al., 2018). Additionally, ICG video angiography has been used during surgery of hemangioblastomas, which are primary CNS tumors with an irregular vascular network (Shinya et al., 2018). Here, ICG has provided a safe tumor resection due to identification of hidden arterial feeders and vessels (Hojo et al., 2014).

Uptake of ICG is increased at the site of the tumor, mainly due to the breakdown of the normal BBB. Thus, like fluorescein, ICG is not a tumor-specific agent, as it provides only nonspecific contrast in regions of compromised neurovasculature (Petrovsky et al., 2003). This phenomenon was first demonstrated in 1993 by Hansen et al. who showed the ability of ICG to macroscopically demarcate gliomas in rats using a wide-field microscope (Hansen et al., 1993). Thereafter, enhanced optical imaging with ICG was also achieved in human gliomas. In nine patients, ICG imaging allowed differentiation between healthy and tumor tissue as well as better assessment of tumor margins in real time (Haglund et al., 1996).

1.7 Aim

The aim of this study was to identify a contrast agent compatible with the CLSM device to conduct a CNS tumor study on a cellular level. Therefore, the fluorescent agents acriflavine (AF), acridine orange (AO), cresyl violet (CV), fluorescein, and ICG were investigated in terms of their staining ability of healthy and neoplastic CNS tissue. The goal was to identify a suitable fluorophore which provides satisfactory contrast of specific tumor features to 1) diagnose biopsies, 2) differentiate between different tumor grades/types and other diseases, and 3) study the tumor on a cellular level. This set of contrast agents was chosen because they are currently used in clinical practice and have been shown to stain the tissue immediately, which would avoid the diagnostic delay between intraoperative tissue examination and histopathological data acquisition. Moreover, other permitted fluorescent agents for human use, such as 5-ALA and food dyes, were investigated in terms of their ability to stain cellular CNS features.

To diagnose CNS lesions correctly, physicians need to be familiar with the CLSM features of neoplastic and healthy tissues. Therefore, CLSM features of 317 different CNS lesions were analyzed, using histology from the same region of interest (ROI) for comparison. Representative images were used for a blinded statistical evaluation by neuropathologists.

Further, the staining ability of the contrast agents in the CLSM approach was investigated in the *in vivo* imaging and guiding of glioma resection in a rat brain tumor model. Therefore, two novel CLSM systems from Cellvizio® (λ_{ex} of 488 nm and 780 nm respectively) with fluorescein, AF, 5-ALA, and ICG were compared with an OPMI Pentero® (λ_{ex} of 400 nm) routine surgical wide-field microscope and 5-ALA as the surgical standard in their resection outcome. The key focus was on the cellular distinction between healthy and neoplastic tissues and on the identification of the transition zone. Traditional histology served as the gold standard for the histopathological evaluation of the resected tissues and of the removed rat brain to examine whether a complete and safe resection of the tumor were achieved. The operating environment, instruments, and operating technique were kept as similar as possible to those used in human surgery. Additionally, normal brain cytoarchitecture of a pig was examined *in vivo* to evaluate a potential use of CLSM for neurosurgical application in general and to define CLSM features of a large brain model.

In particular, the application of CLSM, at λ_{ex} of 488 nm and 780 nm, was investigated for *ex vivo* and *in vivo* imaging of primary CNS tumors and healthy tissues, following fluorescent staining. The goal was to bring surgical cancer therapy to the cellular level and the implementation of CLSM to the neurosurgical operative field. Table 1.2 presents an outlook on all experimental approaches.

Table 1.2: Outlook on the experimental approaches.

	Aim	**Experimental approach**
I	Overview of all examined tumor tissue	• Descriptive statistics of all examined tumor tissue
II	Establishing CLSM for an *ex vivo* CNS application	• The CystoFlex™ UHD, UroFlex™ and the GastroFlex™ probes of the CLSM-488 nm device (Cellvizio®) were compared in their suitability to examine human CNS tumors. • Optimization of incubation times of AF, AO and CV for tumor staining. • Staining ability analysis of other permitted fluorescent agents on fibroblast cells and human CNS samples using the CLSM-488 nm device. • Analysis of 317 different tumor lesions and healthy tissue of the CNS to establish CLSM features. • Establishing CLSM in tumor grading. • CNS tumor examination using a CLSM-780 nm device (Cellvizio®) and ICG. → Traditional histology with H&E served as the gold standard for *ex vivo* tumor imaging.
III	Establishing CLSM for an *in vivo* CNS application	• High-grade glioma resection using intraoperative CLSM devices at 488 and 780 nm excitation for tumor imaging in rats. • Investigation of AF, fluorescein, 5-ALA and ICG for *in vivo* imaging. • CLSM analysis of healthy brain structures in rats and a pig. → Routine surgical wide-field microscopy (OPMI Pentero®) with 5-ALA as contrast agent served as the optical gold standard.

CLSM, confocal laser scanning microscopy; CNS, central nervous system; AF, acriflavine; AO, acridine orange; CV, cresyl violet; ICG, indocyanine green; H&E, hematoxylin and eosin; WHO, World Health Organization; 5-ALA, 5-aminolevulinic acid.

2. Material and methods

2.1 Chemicals and Reagents

Basic chemicals and reagents were purchased from Sigma-Aldrich and Roth. All other suppliers are listed in Table 2.1. To prepare buffers and solutions (Table 2.2), only analytically pure chemicals were used. The main devices used in this study are listed in Table 2.3.

Table 2.1: Chemicals and reagents.

Compound	Supplier
5-aminolevulinic acid	Gliolan, Medac GmbH, Wedel, Germany
Acriflavine hydrochloride	Sigma Aldrich, Melbourne, Australia
Acridine orange	Sigma Aldrich, Melbourne, Australia
Allura Red	Sigma Aldrich, Melbourne, Australia
Bone wax	Ehicon, Norderstedt, Germany
Chlorhexidine	Sigma Aldrich, Melbourne, Australia
Cresyl violet acetate	Sigma Aldrich, Melbourne, Australia
Erythrosine B	Sigma Aldrich, Melbourne, Australia
Ethanol	Sigma Aldrich, Melbourne, Australia
Fetal calf serum	Lonza, Basel, Switzerland
Fluorescein	Alcon Pharma, Freiburg, Germany
Formaldehyde	Roth, Karlsruhe, Germany
Hydrogen chloride	Sigma Aldrich, Melbourne, Australia
Indocyanine green	Sigma Aldrich, Melbourne, Australia
Phosphate buffered saline	Roth, Karlsruhe, Germany

Compound	**Supplier**
Penicillin	Gibco, Life Technologies, Darmstadt, Germany
Piritramid (Dipidolor®)	Janssen-Cilag, Neuss, Germany
Roti® Histokit II	Roth, Karlsruhe, Germany
Saline	Gibco, Life Technologies, Darmstadt, Germany
Streptomycin	Gibco, Life Technologies, Darmstadt, Germany
Thiopental-sodium (Trapanal)	Altana AG, Wesel, Germany
Trypan blue	Sigma Aldrich, Melbourne, Australia
Trypsin-EDTA	Gibco, Life Technologies, Darmstadt, Germany
Xylene	Roth, Karlsruhe, Germany

Table 2.3: Laboratory equipment and instruments.

Device	**Supplier**
Bench-top microscope	Carl Zeiss Microscopy, GmbH, Oberkochen, Germany
Catheter	Dispomed, Gelnhausen, Germany
Centrifuge	Heraeus Megafuge 16 R, Thermo Fisher Scientific, MA, USA
Confocal laser endomicroscopic device	Cellvizio®; Mauna Kea Technologies, Paris, France
Ear bars	David Kopf Instruments, LA, USA
Electric razor	WPI, Sarasota, USA
Endotracheal tube	Super-Safety-Clear, Teleflex, Ruesch, Germany
Fluorescence bench-top microscope	IX70, Olympus, Hamburg, Germany
Hand driller	WPI, Sarasota, USA
Heating pad	Homeothermic Blanket System; Harvard Apparatus, South Natick, MA, USA
Incubator	B5050E, Heraeus, MA, USA
Kopf small-animal stereotaxic instrument	David Kopf Instruments, LA, USA

Device	**Supplier**
Medical monitor	Capnomag Ultima; Datex Engstrom Division, UK
Microscope slide	SARSTEDT, Nuembrecht, Germany
Microtome	Leitz, Wetzlar, Germany
MiniprobesTM	Mauna Kea Technologies, Paris, France
Neubauer Counting Chamber	OptikLabor, Germany
Pipettes	Pipetman, Gilson, Germany
Scalpels	Fine Science Tools, Heidelberg, Germany
Set of surgical forceps	Fine Science Tools, Heidelberg, Germany
Syringe	Hamilton, Babuzen, Switzerland
TABOTAMP®	Ehicon, Norderstedt, Germany
Tissue culture plates (6, 12, 24 and 96 well)	Costar, Corning, New York, USA
Tube 5ml, 75x12mm, PS	Sarstedt, Nuembrecht, Germany
Ventilator	Siemens-Elema AB, Erlangen, Germany
Vortex	Vortex genie, Scientific industries INC, Germany
Water bath	GFL, Burgwedel, Germany
Wide-field surgical microscope	OPMI Pentero® Carl Zeiss Microscopy, GmbH, Oberkochen, Germany

Table 2.2: Media and Solutions.

Media or solution	**Ingredients**
Acid-Ethanol	• 1 mL concentrated hydrogen chlorate (HCI) • 400 mL 70% EtOH in H_2O
DMEM medium	• To 500 mL • 440.5 mL DMEM • 50 mL FCS (10%) • 5 mL 10 x penicillin/streptomycin (1x) • 2.5 mL 12-O-tetradecanoyl phorbol acetate (TPA) from 40 µM stock solution (200 nM) • 2.0 mL cholera toxin from 25 µg/mL stock solution (0.1 µg/mL)
Eosin Y solution	• 10 g Eosin Y • 200 mL ddH_2O • 800 mL 95% EtOH in H_2O
Hematoxylin solution	• 50 g potassium • 1 g hematoxylin • 0.2 g sodium iodate • 1 g citric acid • Add to 1000 mL ddH_2O

2.2 Ethical considerations

Samples of CNS and CNS-associated lesions were collected from patients who had undergone surgery at the Department of Neurosurgery of Merheim Hospital, Cologne, Germany. Use of human biopsy tissues was in compliance with the requirements of the local ethics committee ("Ethikkomission an der Medizinischen Fakultät der HHU"; study number: 5530) and in agreement with the Declaration of Helsinki. Each sample was used with permission of the patient (including written informed consent) if that material was not required for other purposes. All studies involving animals were conducted in accordance with national and international guidelines and were approved by the Governmental Animal Care and Use Committee ("Ethikkomission Koblenz 23-177-070/G 10-1-0500").

2.3 Technical considerations

2.3.1 Confocal laser endomicroscopic system

Two probe-based CLSM systems from Cellvizio® (Mauna Kea Technologies, Paris, France) were used in this study. The Cellvizio® system is composed of a Laser Scanning Unit λ_{ex} of 488 nm and 780 nm, respectively; the Confocal Miniprobe™, which is the link between the scanning device and the sample; and a Confocal Processor™ with the software unit (Fig. 2.1).

Two scanning mirrors, X and Y, mounted onto a galvanometer, enable raster scanning of the laser beam on the object (Fig. 2.2). The frame rate of 12 frames/s makes the acquisition of movie sequences possible. The Cellvizio® system is designed for *in vivo* imaging due to the length and diameter of the Miniprobes™, which are compatible with invasive surgical procedures. The Miniprobes™ are composed of 30,000 optical fibers which transport the scanned laser beam to the site of observation and capture the fluorescent light emitted back from the tissue (Fig. 2.2). Each fiber of the bundle provides only one sampling point on the examined tissue. The confocal principle of the system (Fig. 2.2) results from the size of each fiber core (diameter approximately 2 µm), which serves as a pinhole and allows optical sectioning of the object.

Various Miniprobes™ (GastroFlex™, GastroFlex™ UHD, ColoFlex™, ColoFlex™ UHD, CholangioFlex™, UroFlex™, CystoFlex™, CystoFlex™ UHD, AQ-Flex™;

Mauna Kea Technologies, Paris, France) are available. The Miniprobes$^{\text{TM}}$ differ in their their bundle properties, distal optics as well as in their length, sensitivity, and lateral resolution.

In this study, the Gastroflex$^{\text{TM}}$, CystoFlex$^{\text{TM}}$ UHD, and UroFlex$^{\text{TM}}$ probes were used for the examination, as no specific Miniprobes$^{\text{TM}}$ for CNS application are available. The GastroFlex$^{\text{TM}}$ is 3 m long and has a maximum field of view of Ø 240 µm with a lateral resolution of 1 µm and an imaging plane depth of 55–65 µm. The CystoFlex$^{\text{TM}}$ UHD has a length of 2 m, an optical field of view of Ø 240 µm, an imaging plane depth of 55–65 µm, and a lateral resolution of 1 µm. The UroFlex$^{\text{TM}}$ has a length of 3 m, a maximum field of view of Ø 325 µm, a depth of observation of 40–70 µm, and a lateral resolution of 3.5 µm. Table 2.4 presents the major technical information of the three confocal Miniprobes$^{\text{TM}}$ used in this study. The probes can be disinfected and reused approximately 20 times.

The software unit regulates the system and manages the image data. The Cellvizio® software also allows inversion of the image colors (white to black or to another color, such as green, orange, blue, or red) during CLSM imaging or later after saving. This is especially useful for the examination of small structures.
A foot pedal allows starting and pausing videos, which can then be recorded, commented, and exported with the Cellvizio® software.

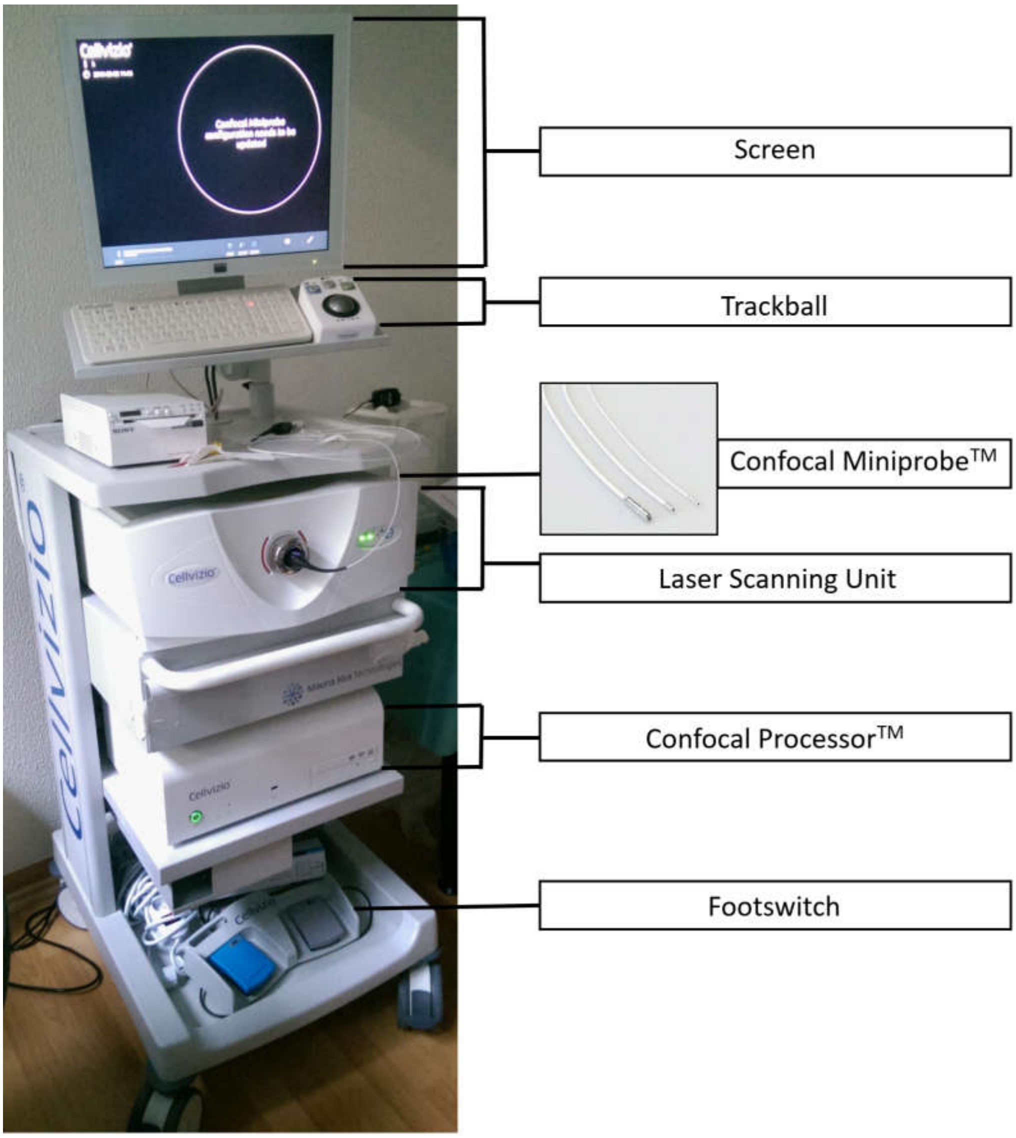

Figure 2.1: Cellvizio® system (source: own representation). The main opto-electronic components are the Laser Scanning Unit, the Confocal Miniprobe™, and the Confocal Processor™ with the Cellvizio® software.

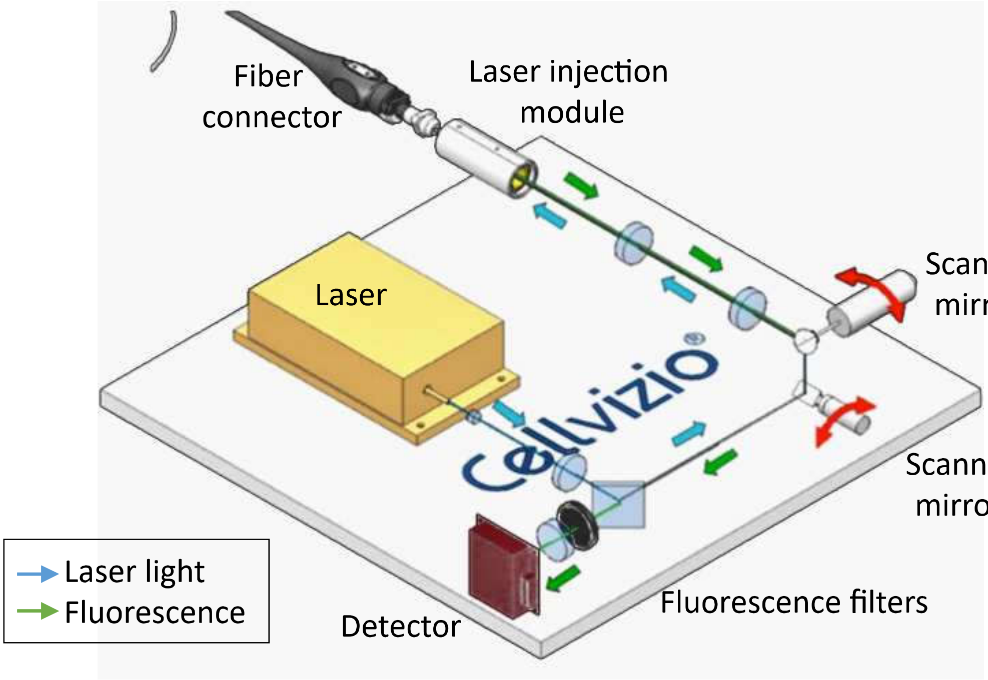

Figure 2.2: Schematic diagram of the laser scanning unit (modified from www.maunakeatech.com). The laser beam (blue arrow) and the emitted fluorescent light (green arrow) are illustrated. The scanning mirrors X and Y are mounted onto a galvanometer, allowing raster scanning of the laser beam on the object. The fluorescence light is collected by a fiber bundle and follows the same pathway back through the scanning mirrors that was used for excitation, resulting in a "de-scanned" emission. Prior to detection, the emitted light passes through fluorescence filters, which eliminate laser backscatter. The diagram is used with permission from Mauna Kea Technologies.

Table 2.4: Technical information of used confocal Miniprobes^{TM}.

Miniprobes^{TM}	**GastroFlex^{TM}**	**CystoFlex^{TM} UHD**	**UroFlex^{TM}**
Length	3 m	2 m	3 m
Maximum field of view	Ø 240 µm	Ø 240 µm	Ø 325 µm
Depth of observation	55–65 µm	55–65 µm	40–60 µm
Lateral resolution	1 µm	1 µm	3,5 µm
Reprocessing	Cleaning & Sterilization	Cleaning & Sterilization	Cleaning & Sterilization
Maximum pressure on fiber	< 1 kg	< 1 kg	< 1 kg
Water tightness of the distal tip	IP 67	IP 67	IP 67
Storage/Operating/ Temperature range	- 10 °C to + 60 °C / + 10 °C to + 35 °C	-10 °C to + 60 °C / + 10 °C to + 35 °C	-10 °C to + 60 °C / + 10 °C to + 35 °C

(MaunaKeaTechnologies, 2016)

2.3.2 Intraoperative wide-field microscopy

A standard surgical wide-field microscope (OPMI Pentero®; Carl Zeiss Microscopy, GmbH, Oberkochen, Germany) with a λ_{ex} of 400 nm was used to reveal PpIX-fluorescence. The PpIX-fluorescence was imaged with a video camera attached to the microscope.

2.4 *Ex vivo* human studies

2.4.1 Statistical analyses of primary CNS tumor distribution

Analyses of primary CNS tumor distribution were based on data from January 2014 – February 2016. All patients underwent biopsy or resection as part of their diagnostic or therapeutic evaluation in the Merheim hospital, Cologne, Germany. Only histopathologically confirmed tumors were included in the statistical analyses (SPSS software). Age, sex, date of diagnosis, and tumor histology were recorded for all patients. The date at the first surgical treatment (to obtain the age at diagnosis) is the date on which the pathological diagnosis was obtained. Pilocytic astrocytomas were considered benign.

2.4.2 Collection and confocal imaging of human tissues

The samples of CNS lesions (Table 2.5) were collected from patients who had undergone surgery (Fig. 2.3) at the Department of Neurosurgery of the Merheim Hospital, Cologne, Germany. Biopsies were examined mostly using CLSM either straight after surgery or after being fixed in 4% formaldehyde (Fig. 2.4), as preliminary tests showed that neither the fixation process nor the preoperative administration of 5-ALA have an effect on CLSM analysis (data not shown). For tissue examination, the confocal Miniprobe™ was placed in gentle contact with the surface of the sample. Biopsy sections were always analyzed (3–5 min) with and without the application of the fluorophore (see subsection 2.4.3).

Confocal images of each patient were stored anonymized in a specific folder. ROI that was examined using CLSM was marked with tissue ink (India ink; Rotring, Germany) so that the exact location could be validated with traditional histology as gold standard. To this end, the samples were placed in 10% formalin and processed for histopathological examination (see subsection 2.4.4).

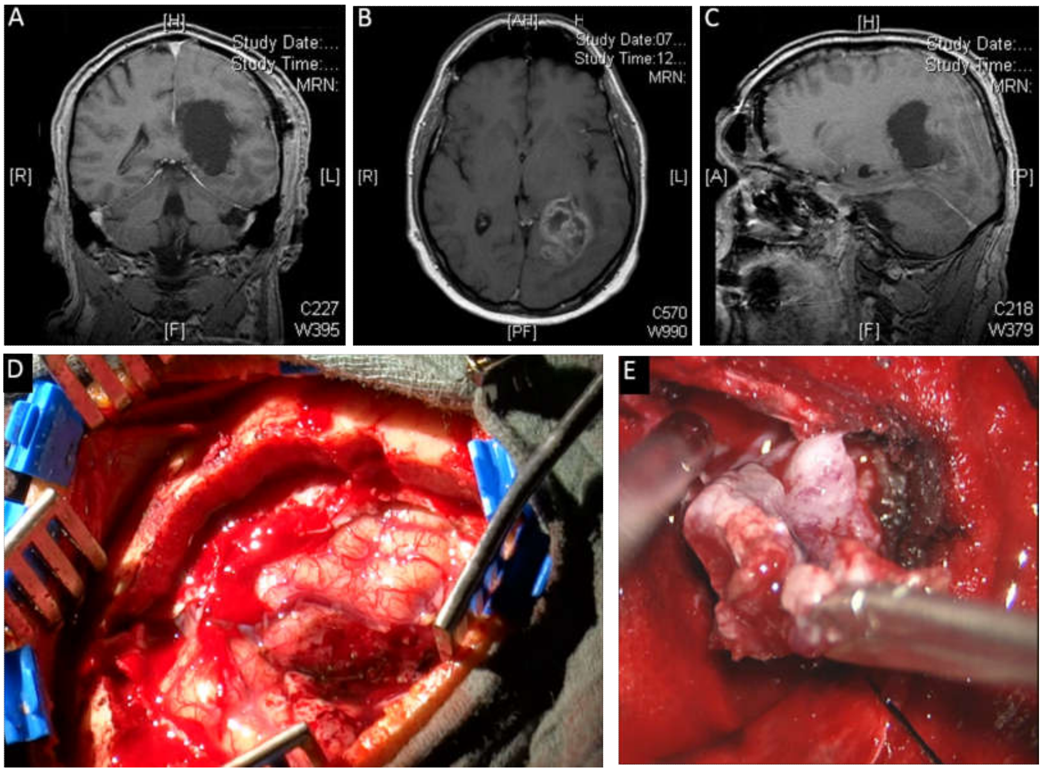

Figure 2.3: Pre-CLSM imaging (source: own representation). Preoperative MRI images (A–C) show the location of the tumor (glioblastoma) in the brain. Resection cavity (D) and tumor resection process (E). MRI images and images of the brain/tumor are used with permission of the patient. *CLSM, confocal laser scanning microscopy; MRI, magnetic resonance imaging.*

Table 2.5: Origin and number of human tumor samples examined by CLSM.

Pathological diagnosis	Number of samples
I. Tumors of neuroepithelial tissue	**122**
WHO grade I astrocytoma	4
WHO grade II astrocytoma	4
WHO grade III astrocytoma	9
WHO grade VI astrocytoma (glioblastoma)	80
Choroid plexus papilloma	4
WHO grade II ependymoma	5
WHO grade III ependymoma	3
WHO grade II oligoastrocytoma	4
WHO grade II oligodendroglioma	6
WHO grade III oligodendroglioma	3
II. Tumors of cranial and paraspinal nerves	**26**
Neurofibroma	3
Schwannoma	23
III. Tumors of the meninges	**134**
Cavernoma (hemangioma)	5
Hemangioblastoma	4
WHO grade I meningioma	101
WHO grade II meningioma	24
IV. Tumors of the hematopoetic system	**7**
Plasmacytoma	7
V. Tumors of the sella region	**22**
Pituitary adenoma	22
VI. Metastatic tumors	**2**
Non-small cell lung adenocarcinoma	2
VII. Cysts and tumor-like lesions	**4**
Epidermoid tumor	4

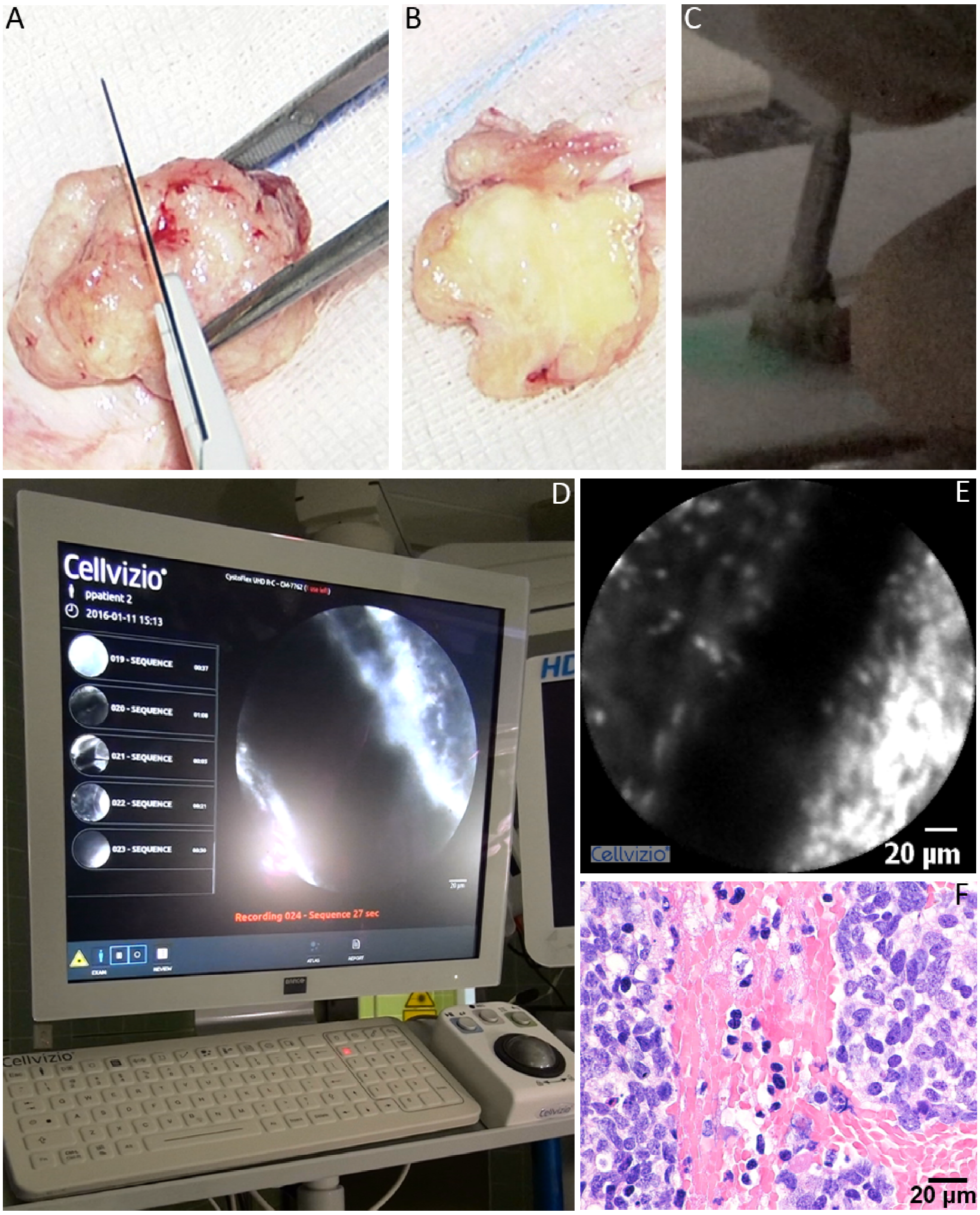

Figure 2.4: *Ex vivo* CLSM imaging (source: own representation). The unfixed removed tumor (A, B) was immediately examined by CLSM (C-E). Traditional histology of the same ROI was performed from each specimen for correlation. Bars = 20 µm. *CLSM, confocal laser scanning microscopy; ROI, region of interest.*

2.4.3 Fluorescent agents used *ex vivo* on human tissue

Biopsy samples were investigated *ex vivo* after topical application of one drop of either 0.01 mg/mL AF (Sigma Aldrich, Melbourne, Australia), 0.01 mg/mL AO (Sigma Aldrich, Melbourne, Australia), 0.02 mg/mL CV (Sigma Aldrich, Melbourne, Australia), or 0.5 mg/mL ICG (Sigma Aldrich, Melbourne, Australia) dissolved in phosphate-buffered saline.

AF (λ_{ex} 505 nm/λ_{em} 585 nm), which is mixture of 3.6-diaminoacridine (proflavine) and 3.6-diamino-10-methylacridinium chloride (trypaflavin), marks the DNA and cell membrane. AO interacts with the DNA and RNA by intercalation or electrostatic attraction. When bound to the DNA, AO reaches a λ_{ex} at 502 nm and a λ_{em} at 525 nm. CV localizes predominantly to the cytoplasm and exhibits a λ_{ex} at 540 nm with a λ_{em} at approximately 614 nm. Near-infrared ICG (λ_{ex} 760–775 nm/λ_{em} 835 nm) stains the cytoplasm and blood vessels. Properties of the fluorophores and routes of administration are summarized in Table 2.6.

Health hazard statements of the Globally Harmonized System of Classification and Labeling of Chemicals (GHS) for all fluorescent agents used are presented in Table 2.7. Hazard statements (H statements), which have replaced the Risk statements (R statements), provide standardized formulations to indicate the hazards of a chemical, including the degree of hazard. The codes have the form Hnxx, where the health hazards start with the letter H (hazard), followed by the number 3 (health hazards), and two more digits (xx) following a sequential numbering scheme.

Imaging using CLSM was performed either without any fluorescent agent, or after different incubation times (0–30 min) of AF, AO and CV. ICG was applied 1 min prior imaging on the sample. For each fluorophore, a part of the same tumor was cut and stained.

Furthermore, the food dyes, erythrosine (Erythrosine B; Sigma Aldrich, Melbourne, Australia), Allura red AC (Sigma Aldrich, Melbourne, Australia), Canthaxanthen (Sigma Aldrich, Melbourne, Australia), Rubixanthin (Sigma Aldrich, Melbourne, Australia), Ponceaux SX (Sigma Aldrich, Melbourne, Australia) were tested in their staining ability on human samples. To this end, different concentrations (0.5, 1.0, and 2.0 mg/mL) with various incubation times (1, 5, and 10 min) were investigated.

Only erythrosine (λ_{ex} 525 nm/λ_{em} 549 nm), also called Eosin B, is known to accumulate in lysosomes and mitochondria (Table 2.6).

The excess dye of the fluorophores was washed off with saline. According to the producer's advice, the contrast agents were stored at 4 °C and kept in a dark place.

Table 2.6: **Properties of the contrast agents.**

Contrast agents	Molecular weight [g/mol]	Excitation [nm]	Emission [nm]	Concentration	Localization	Human use	Brain use
5-aminolevulinic acid ($C_5H_9NO_3$) (PpIX; $C_{34}H_{34}N_4O_4$)	PpIX; 562.6	PpIX; 405 (highest peak), 495, 546, 625	700	200 mg/kg	Cytoplasm; mitochondria	yes	yes
Acridine orange ($C_{17}H_{19}N_3$)	265.36	502	525	0.01 mg/mL	DNA	no	no
Acriflavine ($C_{27}H_{25}ClN_6$)	541.90	505	585	0.01 mg/mL	Membrane; DNA	yes	no
Cresyl violet ($C_{19}H_{18}ClN_3O$)	339.823	540	614	0.02 mg/mL	Cytoplasm	yes	no
Erythrosine ($C_{20}H_6I_4Na_2O_5$)	879.86	525	549	0.5-5 mg/mL	Lysosomes; mitochondria	yes	no
Fluorescein ($C_{20}H_{12}O_5$)	332.31	490	520	0.01 mg/mL	Extracellular matrix; blood vessels (binds to albumin)	yes	no
Indocyanine green ($C_{43}H_{47}N_2NaO_6S_2$)	774.96	760–775	835	0.5 mg/mL	Cytoplasm; blood vessels binds to cellular proteins and albumin	yes	no

**PpIX, protoporphyrin IX*; (Martirosyan et al., 2014).

Table 2.7: Health hazard statements.

5-aminolevulinic acid	"**H315 (100%)**: Causes skin irritation [Warning Skin corrosion/irritation]. **H319 (100%)**: Causes serious eye irritation [Warning Serious eye damage/eye irritation]. **H335 (96.15%)**: May cause respiratory irritation [Warning Specific target organ toxicity, single exposure; Respiratory tract irritation]."
Acridine orange	"**H340 (98.31%)**: May cause genetic defects [Danger Germ cell mutagenicity]."
Acriflavine	"**H302 (100%)**: Harmful if swallowed [Warning Acute toxicity, oral]. **H315 (100%)**: Causes skin irritation [Warning Skin corrosion/irritation]. **H319 (100%)**: Causes serious eye irritation [Warning Serious eye damage/eye irritation]. **H335 (98.39%)**: May cause respiratory irritation [Warning Specific target organ toxicity, single exposure; Respiratory tract irritation]."
Cresyl violet	"**H302 (100%)**: Harmful if swallowed [Warning Acute toxicity, oral]. **H332 (100%)**: Harmful if inhaled. **H315 (85.29%)**: Causes skin irritation [Warning Skin corrosion/irritation]."
Erythrosine B	"**H302 (98.19%)**: Harmful if swallowed [Warning Acute toxicity, oral]."
Fluorescein	"**H315 (82.35%)**: Causes skin irritation [Warning Skin corrosion/irritation]. **H319 (85.29%)**: Causes serious eye irritation [Warning Serious eye damage/eye irritation]."
Indocyanine green	"**H315 (100%)**: Causes skin irritation [Warning Skin corrosion/irritation]. **H319 (100%)**: Causes serious eye irritation [Warning Serious eye damage/eye irritation]. **H335 (96%)**: May cause respiratory irritation [Warning Specific target organ toxicity, single exposure; Respiratory tract irritation]."

(Kim et al., 2016)

2.4.4 Histopathology

- **Paraffin processing of tissue:**

Human specimens were sectioned into 3 mm slices and drop-fixed in a 10% formalin solution (2 mL of formalin per 100 mg of tissue) to preserve tissue structures and protect them against subsequent processing steps. After 48 hours (h) of fixation, the fixed tissues were each transferred to a labeled cassette to segregate them from other specimens. Next, the fixed tissues were dehydrated (wet-fixed tissues cannot be directly penetrated with paraffin) through a series of graded ethanol (EtOH) baths and then infiltrated with wax as described below in Table 2.8.

Table 2.8: Paraffin tissue processing.

Process	Solution	Time
1. Dehydration	70% EtOH in H_2O	1 h
2. Dehydration	95% EtOH and 5% methanol in H_2O	1 h
3. Dehydration	100% EtOH	1 h
4. Dehydration	100% EtOH	1½ h
5. Dehydration	100% EtOH	1½ h
6. Dehydration	100% EtOH	2 h
7. Clearing	Xylene	1 h
8. Clearing	Xylene	1 h
9. Infiltration	First wax (Paraplast X-tra) at 58 °C	1 h
10. Infiltration	Second wax (Paraplast X-tra) at 58 °C	1 h

After the final infiltration, the specimens were removed from the cassette and carefully orientated within a suitably sized metal mold. Next, the mold was filled up with paraffin, covered with a cassette, topped up with more wax to form a block, and finally allowed to cool to 20 °C on a cold plate. Thereafter, the completed blocks were removed from the mold and prepared for tissue sectioning.

- **Tissue sectioning**

The paraffin-embedded tissue blocks were sectioned using a microtome (Leitz, Wetzlar, Germany). First, the blocks were placed face down on an ice block for 10 min and then inserted into the microtome parallel to the cutting blade. After they had been cut at a thickness of 4–5 µm, they were placed onto the surface of a deionized water bath at 40–45 °C. Using a microscope slide (5 µm slice thickness), the sections were picked out of the water bath and stored upright in a slide rack, overnight at 37 °C.

- **Hematoxylin and eosin staining**

For histopathological analysis of the samples, the paraffin sections were stained with hematoxylin and eosin (H&E). Hematoxylin has a deep blue-purple color and stains acidic components (such as nucleic acids), whereas eosin Y is pink and stains basic components (such as proteins) nonspecifically in the cell.

First, the sections were kept for 30 min at 68 °C to deparaffinize the sections. After two times 5 min clearing in xylene (Carl Roth, Karlsruhe, Germany), the paraffin slides were hydrated by being passed through decreasing concentrations of EtOH (100%, 95%, 80% EtOH in H_2O) for 2 min each. Subsequently, the slides were stained in hematoxylin (Table 2.2) for 3 min and washed with running tap water for 5 min to remove excess dye. Then the slides were differentiated with 0.3% acid EtOH (dipped 8–12 times). After the slides were rinsed again for 1 min in running tap water, they were stained with eosin Y (Table 2.2) for 3 to 5 min. Afterwards, the slides were dehydrated through a series of graded EtOH of 30%, 50%, 70%, 85%, 95%, and 100% (3 x 5 min each) and cleared in xylene (3 x 15 min). Following this, glass slides were mounted with Roti® Histokit II (Carl Roth, Karlsruhe, Germany) and allowed to dry prior to observation under a bench-top light microscope (Carl Zeiss Microscopy, GmbH, Oberkochen, Germany).

2.4.5 Statistical analysis of CLSM images

A statistical analysis of the interpretation of CLSM images was performed to establish accuracy and interobserver agreement. For this purpose, CLSM images obtained after AF and ICG staining of different CNS specimens were presented to neuropathologists ($n = 4$). The neuropathologists were blinded to the traditional histopathological findings and inexperienced with the CLSM approach. Each participant received an online survey created from "Google Docs" containing one CLSM image and five answer possibilities for each CNS tumor as demonstrated in Figure 2.5 (no traditional histology was available for the neuropathologists) .

Welcher ZNS Tumor ist als konfokales Bild dargestellt?

○ Oligodendrogliom
○ Epidermoid Tumor
○ Meningeom
○ Glioblastom
○ Antwort nicht vorhanden

Figure 2.5: Example of one entity on the online form (source: own representation).
Translation: Which CNS tumor is presented as a CLSM image?
() Oligodendroglioma
() Epidermoid tumor
() Meningioma
() Glioblastoma
() None of the possible answers
CNS, central nervous system; CLSM, confocal laser scanning microscopy.

2.5 Cell culture

2.5.1 Cell culture work

All experiments were carried out on C6 glioma cells (primary rat glioma cell line) or fibroblasts obtained from the Institute of Neurosurgical Pathophysiology (Medical Center, Johannes Gutenberg University, Mainz, Germany).

Cell work was performed under a sterile hood in sterile conditions. Solutions, glass and plastic ware were autoclaved or sterile filtrated (0.22 µm pore size). The cells were cultivated in Dulbecco's Modified Eagle Medium (DMEM, Gibco Invitrogen^{TM}, Karlsruhe, Germany) supplemented with inactivated 10% fetal calf serum (FCS; Lonza, Basel, Switzerland) at 37 °C and in a humid 5% CO_2 atmosphere.

DMEM contains salts, amino acids, vitamins, and phenol red (pH indicator). The supplemented FCS contains hormones and other nutrients for cell growth as well as 1% penicillin/streptomycin (Gibco-BRL®, Germany) to prevent contaminations by bacteria.

The medium was stored at 4 °C and heated up to 37 °C before use. Medium was changed every 2–3 days and the cell culture was split every 5–6 days. For cell splitting, the cells were detached from the plastic flask, by tapping on the flask, and half of the detached cells were transferred to a new plastic culture flask. Cells were harvested using trypsin-EDTA (0.05%, 0.02% respectively, Gibco Invitrogen™, Germany) and suspended in DMEM without a supplement for implantation. After centrifugation of the cell suspension in a Heraeus Megafuge 16 R (Thermo Fisher Scientific, MA, USA) at 2000 revolutions per min (rpm) for 5 min, the medium was removed, and the cells were re-suspended in DMEM.

Cell viability of implanted C6 tumor cells was never below 94%, as assessed by trypan blue staining (see subsection 2.5.2). The final cell concentration for C6 tumor cell implantation was determined using a cell counting chamber (see subsection 2.5.3). After counting, the cells were centrifuged again and re-suspended in DMEM (without FCS and antibiotics) to a final concentration of 10^6 cells/mL^{-1}.

2.5.2 Trypan blue viability test

The trypan blue cell viability test was performed to differentiate between viable and non-viable cells in the cell suspension. This test is based on the principle that living cells have an intact cell membrane (negatively charged) that excludes the diazo dye trypan blue.

For the viability test, the cell samples were diluted 1:1 in 0.4% trypan blue solution (Sigma Aldrich, Melbourne, Australia), which was followed by incubation for 1–2 min at room temperature. Non-viable cells (blue cytoplasm) and viable cells (clear cytoplasm) were then counted using a cell counting chamber (see subsection 2.5.3). The incubation period never exceeded 30 min, as cell viability decreases from this point due to trypan toxicity.

2.5.3 Counting of cells

Cell counting was achieved by using a Neubauer chamber (Laboroptik, Lancing, UK), a thick crystal slide (30 x 70 mm and 4 mm thickness) with a double chamber providing two counting areas that can be loaded separately. The counting grid is 3 mm^2 in size, divided into 9 large squares each of 1 mm in width. The central square is again divided into 25 squares of 0.2 mm in width, with double or triple lines. Each of the 25 central squares is further divided into 16 small squares with single lines, such that each of the 16 small square has an area of 1/400 mm^2.

The Neubauer chamber was cleaned with 70% EtOH in H_2O before placing the glass cover (a squared glass of width 22 mm) over the central area, allowing 0.1 mm room for the cell suspension. With a pipette, 10 µL of the cell dilution was carefully expelled until the counting chamber was full. The cells were counted beginning from the first counting grid square under a light microscope with 20-fold magnification (Carl Zeiss Microscopy, GmbH, Oberkochen, Germany). Cells touching the upper and left limits of the grid were counted, whereas cells touching the lower and right sides were not considered in the calculation. When the cell density was higher than 200 cells/square, the cell suspension was adjusted to an appropriate dilution factor. A second sample was counted to ensure accuracy.

2.5.4 Fluorescent agent used in cell culture

Erythrosine B (Sigma Aldrich, Melbourne, Australia) was dissolved in dimethyl sulphoxide (DMSO) at 50 mg/mL^{-1}. The uptake of erythrosine in living cells was investigated in fibroblast cells. The uptake was visualized by a bench-top fluorescence microscope (IX70, Olympus, Hamburg, Germany) with blue laser illumination (λ_{ex} 450 nm) after an incubation time of 0, 1, 5, 10, 30, 60, and 300 min and overnight. Properties of erythrosine and routes of administration are summarized in Table 2.6.

2.6 Animal *in vivo* studies

2.6.1 Rats

Laboratory rats (*Rattus norvegicus*) are a traditional animal model, used by scientists for over a hundred years. In this study, rats were preferred to mice because their physiology and circulatory systems are more akin to those of humans. Sprague-Dawley® rats are an outbreed of albino rats used in medical and nutritional research. The main advantage of choosing these rats was easy handling and their calm temperament.

In total, 30 adult male Sprague-Dawley® rats (250 g, approximately 10 weeks of age) were purchased from Charles River (Wiga, Sulzheim, Germany). The rats were bred and kept in environmentally controlled animal facilities (room temperature of max. 25 °C; 12-h light/dark cycle). Food and water were always available.

All animal studies were performed at the Institute for Neurosurgical Pathophysiology (Medical Center, Johannes Gutenberg University, Mainz, Germany).

2.6.2 Fluorescent agents used *in vivo*

AF (Sigma Aldrich, Melbourne, Australia), ICG (Sigma Aldrich, Melbourne, Australia), fluorescein (Alcon Pharma, Freiburg, Germany), and 5-ALA (Gliolan®, Medac GmbH, Wedel, Germany) were used as fluorophores to enhance *in vivo* tissue contrast. 5-ALA (0.5 mL) was intravenously administered via catheter at 200 mg/kg bw dissolved in phosphate-buffered saline 3–5 h before surgery (n = 7). Fluorescein (20 mg/kg) was intravenously injected immediately before surgery (n = 5). One drop of ICG (0.5 mg/mL in NaCl) and of AF (0.1 mL of 0.01% in phosphate-buffered saline) were topically applied to the tissue during surgery (n = 5). Both ICG and AF were washed off with saline after an incubation time of 1 min. A 0.4 mg/kg injection of ICG was also applied intravenously to enhance tissue contrast in a pig.

AF was used alone as well as concomitantly with fluorescein sodium for morphological enhancement, since the fact is well established that a combination of dyes (for example H&E) provides superior contrast between tissue features. ICG is usually administrated intravenously in many clinical areas, such as for ophthalmic angiography. In the rat trial, ICG was applied topically to the tissue because preliminary studies showed higher cellular resolution compared to an intravenous application. Properties of the fluorophores and routes of administration are summarized in Table 2.6.

2.6.3 C6 glioma cell implantation

30 adult male Sprague-Dawley® rats (Charles River Wiga, Sulzfeld, Germany) underwent stereotaxic surgery. Prior to surgery, all instruments and materials were sterilized by autoclaving. The working area and the stereotaxic apparatus were disinfected with a 70% EtOH in H_2O solution.

First, the rats were anesthetized by inhalation of isoflurane gas in a small, ventilated chamber; this was followed by an intra-peritoneal (i.p.) injection of chloral hydrate (36 mg/kg body weight [bw]) and ketamine (0.7 mL/kg bw). For analgesia, tramadol (50 mg/kg bw) was given i.p. After the rat had lost consciousness, it was placed on a heating pad to maintain body temperature at 37 ± 0.5 °C. Next, the incision site was shaved with an electric razor and eye cream applied to avoid dehydration.

To stabilize the animal's head, the rat was placed in a stereotaxic apparatus (David Kopf Instruments, LA, USA), which positions the skull in a precise orientation so that the stereotaxic atlas remain consistent from animal to animal. For this reason, the instrument's ear bars were fixed into the ear canals of the animal, allowing the head to be moved up and down but not side to side. In order to restrict the up and down movement, the teeth of the rat were placed on a bite bar and the nose held in a nose brace. Then, the incision site was disinfected (e.g., chlorhexidine 0.5%) and an anterior-posterior incision of about 2.5 cm on the midline of the scalp was made. Connective tissue was removed with a spatula and the area cleaned to expose the skull surface. The 3D coordinates in the x, y, and z axes were measured by a micromanipulator on the stereotaxic instrument. It was necessary to adjust the incisor bar until the height of lambda and bregma skull points were equal. When this had been assured, a burr hole (trephination 2 mm Ø) was made with a hand driller and 7 µL of the C6 glioma cell suspension (2–6 x 10^6 cells) was implanted with a syringe into the rat's left parietal cortex (Hamilton, Babuzen, Switzerland; needle diameter 0.47 mm).

After surgery, the craniectomy was closed with bone wax (Ethicon, Norderstedt, Germany) and the skin incision sealed with sterile 4-0 suture (Ethicon, Norderstedt, Germany). The rats were removed from the stereotaxic apparatus and placed in a recovery cage at 28 °C for at least 1 h before being returned to their home cages. Tumors were allowed to grow for 7 days.

2.6.4 Post-surgical care

After surgery (C6 glioma cell injection), the recovery of the rat was monitored by daily weight recordings and other observations on the condition of the animal (such as of the surgical wound, eyes, mouth, and ears). Rats that showed obvious signs of pain, wound infection, weight loss, or other signs of discomfort received an additional dose of analgesics. During the study, a total of 3 rats died as a result of the glioma implantation.

2.6.5 Craniotomy

In total, 27 adult male Sprague-Dawley® rats with C6 gliomas underwent microsurgical resection (Fig. 2.6). The rats were anesthetized and sedated as described before (see subsection 2.6.3). A portal venous catheter was placed for the application of fluorescein and 5-ALA. Craniotomy was performed in a stereotaxic frame (David

Kopf Instruments, LA, USA) to remove the skull and gain access to the allograft tumor under a conventional white-light bench-top microscope (Carl Zeiss Microscopy, GmbH, Oberkochen, Germany). After removing the dura, the arachnoid membrane was incised using micro forceps. Brain tumors were identified in the left hemisphere of all rats (Fig. 2.6). Hemostasis was achieved using TABOTAMP® (Ehicon, Norderstedt, Germany).

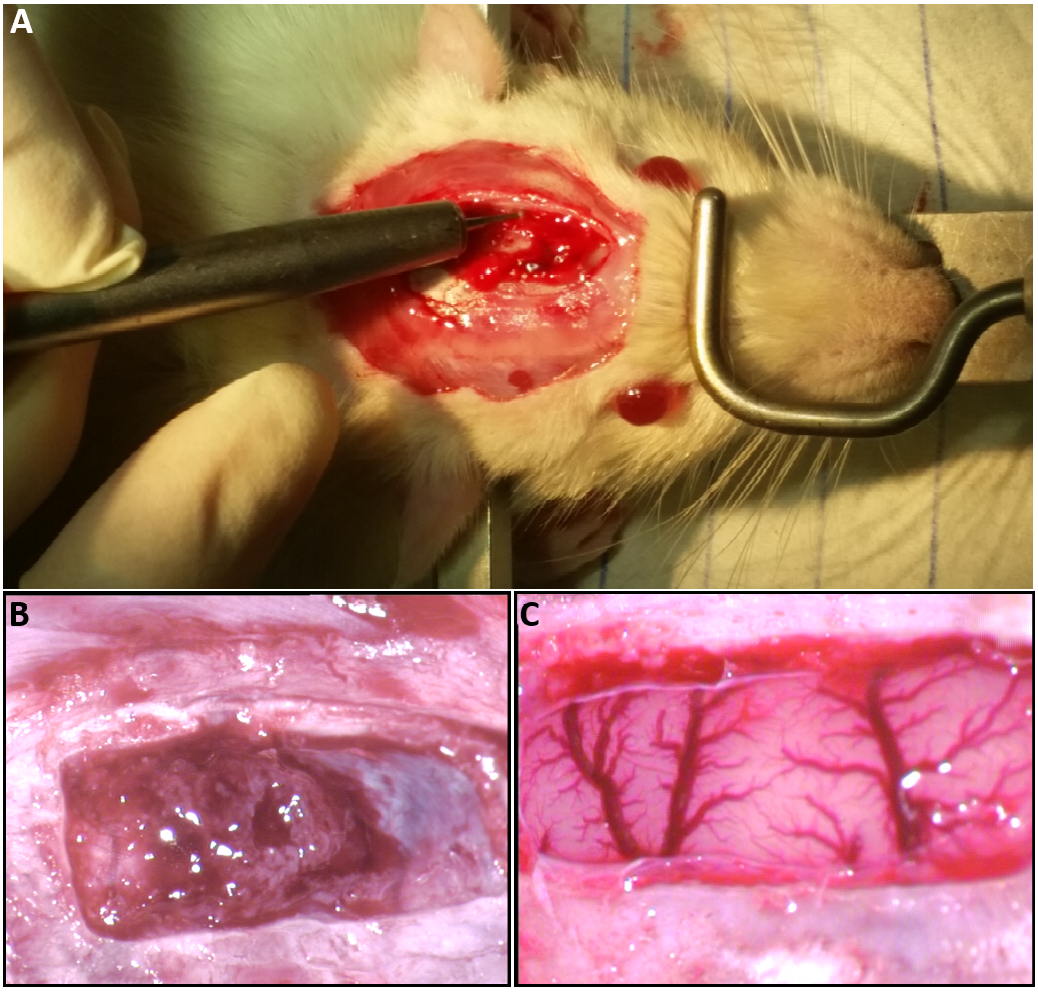

Figure 2.6: Rat surgery (source: own representation). Craniotomy was performed in a stereotaxic frame to remove the skull (A) and gain access to the rat brain (B, C). Brain tumors were localized in the left hemisphere of all rats (B); the right hemisphere comprised mostly healthy brain tissue (C).

2.6.6 *In vivo* fluorescence imaging and tumor resection

Three systems of intraoperative fluorescence microscopy were compared for assessment of *in vivo* high-grade glioma resection: two miniaturized CLSM systems (λ_{ex} of 488 nm and 780 nm) from Cellvizio® (Mauna Kea Technologies, Paris, France) and one OPMI Pentero® (λ_{ex} of 400 nm) routine surgical wide-field microscope (Carl Zeiss Microscopy, GmbH, Oberkochen, Germany).

Brain tissue was stained either with the topical application of ICG (n = 5) or AF (n = 5) alone, with intravenously applied fluorescein alone (n = 5), or with intravenously applied fluorescein and topically applied AF simultaneously (n = 5). Furthermore, intravenous applied 5-ALA was administered to enhance tissue contrast either with CLSM (n = 2), or functioning as control group (n = 5) with wide-field microscopy (OPMI Pentero®-400 nm).

To provide nearly the same conditions, always 4 rats (one for each fluorescent agent; AF, AF + fluorescein, ICG, and 5-ALA as control) received the glioma cell implantation on the same day. Also, these rats were surgically treated (guided by CLSM or OPMI Pentero®) on the same day, to minimize performance differences.

For *in vivo* imaging, the GastroFlex™ probe was placed gently over the target tissue (Fig. 2.7), and video sequences were recorded using the image-capture foot pedal. The entire brain tissue was scanned, and the identified neoplastic tissue was removed using routine surgical instruments (scalpel, applicator, curettes, and dissectors). The surface of the brain was washed with sterile saline to remove erythrocytes.

The resection cavity was then searched again for tumor cells, using one of the fluorescence microscopes to confirm a complete tumor resection (Fig. 2.7). The total imaging time was approximately 10 min/rat. The removed brain and the resected biopsies were fixed in 4% buffered formaldehyde for histopathological evaluation (see subsection 2.6.7).

2.6.7 Histopathology

The tumor specimens removed during surgery were immediately fixed in 4% buffered formaldehyde until histopathological procedure. The rat brains were also prepared for traditional histology. For this purpose, the rats were first anesthetized with chloral hydrate and then transcardially perfusion-fixed using heparinized saline (10 IU/mL) and 4% paraformaldehyde (pH 7.4). Afterwards, the brains were removed and post-fixed in 4% paraformaldehyde for 24 h. Thereafter, the rat brains and the removed specimens were formalin-fixed, PFA-embedded, and processed for H&E staining, as described previously (see subsection 2.4.4).

Four-µm-thick serial sections were prepared at 250 µm intervals and examined under a conventional white-light bench-top microscope (Carl Zeiss Microscopy, GmbH, Oberkochen, Germany). For every slide, a picture was made with a camera (OptixCam, North Carolina, US) attached to the microscope, using 2.5x, 5x, and 40x magnification, respectively.

2.6.8 Histopathological analysis

In total, data pertaining to 25 rats was included in the analysis. Both, the residual tumor tissue in the resection zone and the resection zone volume were determined using the Optima® 6.51 analysis program for image analysis. Therefore, the 4-µm-thick serial sections (250 µm intervals) were examined individually. As the maximal observing depth of the GastroFlex™ is 55–65 µm (Table 2.4), only tumor cells located within this range were included in the measurements. In order to calculate the resection volume, the resection areas were summated and multiplied by 250 µm (Fig. 2.8). The "tumor left ratio" was calculated according to the following formula: [(summated rest tumor * 250 µm)/summated perimeter].

Furthermore, regression analyses were carried out to better compare the resection outcomes assisted by CLSM or by wide-field microscopy. First, the correlation was estimated between the amount of healthy tissue in the biopsies and the remaining tumor in the resection zone for each rat. This correlation was examined to estimate if a safe resection combined with an extensive resection is possible using one of the approaches. Second, the correlation between the amount of remaining tumor in the resection cavity and the resection volume was examined. This regression analysis was carried out to analyze whether more residual tumor tissue was left when the tumor was large.

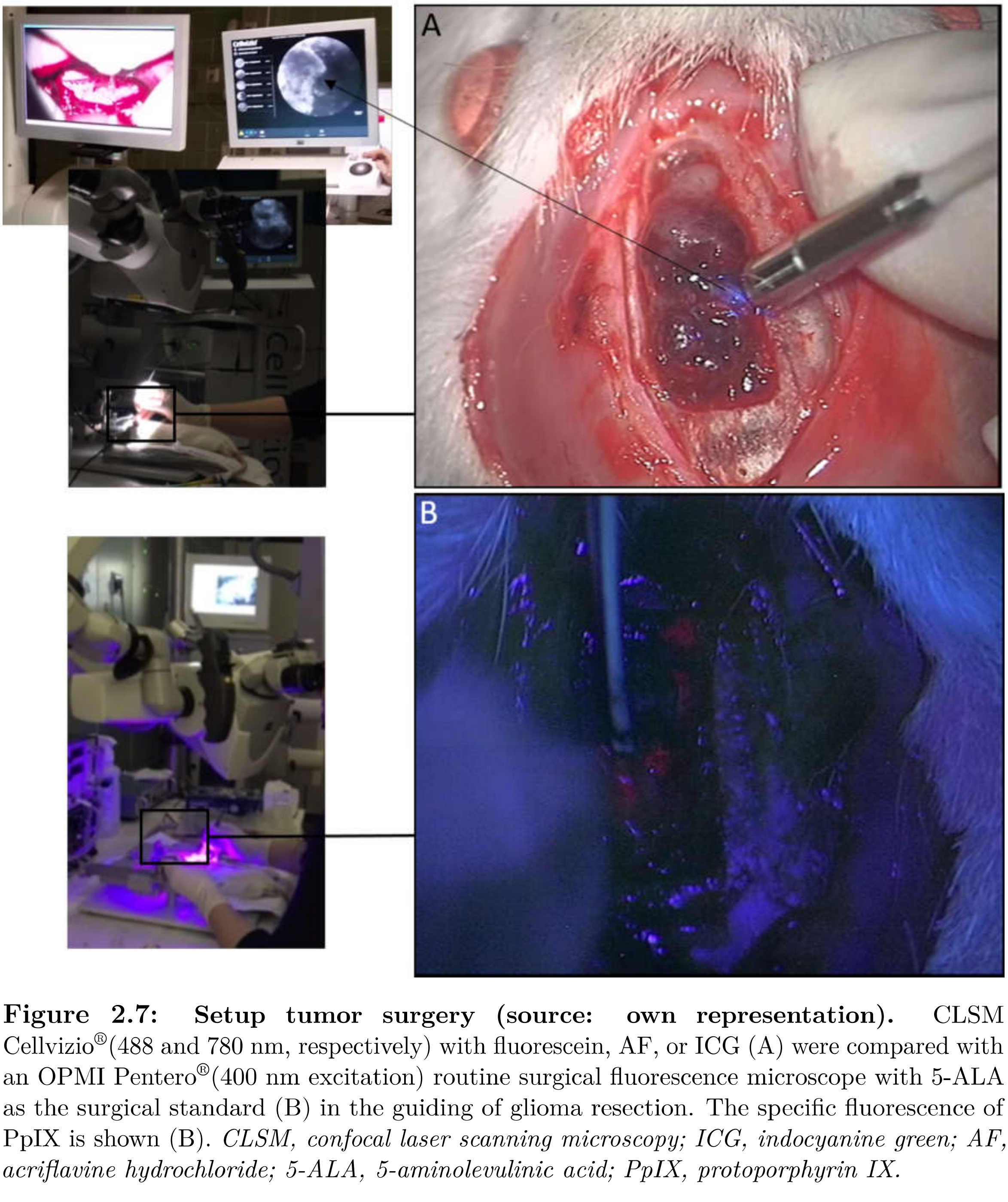

Figure 2.7: Setup tumor surgery (source: own representation). CLSM Cellvizio®(488 and 780 nm, respectively) with fluorescein, AF, or ICG (A) were compared with an OPMI Pentero®(400 nm excitation) routine surgical fluorescence microscope with 5-ALA as the surgical standard (B) in the guiding of glioma resection. The specific fluorescence of PpIX is shown (B). *CLSM, confocal laser scanning microscopy; ICG, indocyanine green; AF, acriflavine hydrochloride; 5-ALA, 5-aminolevulinic acid; PpIX, protoporphyrin IX.*

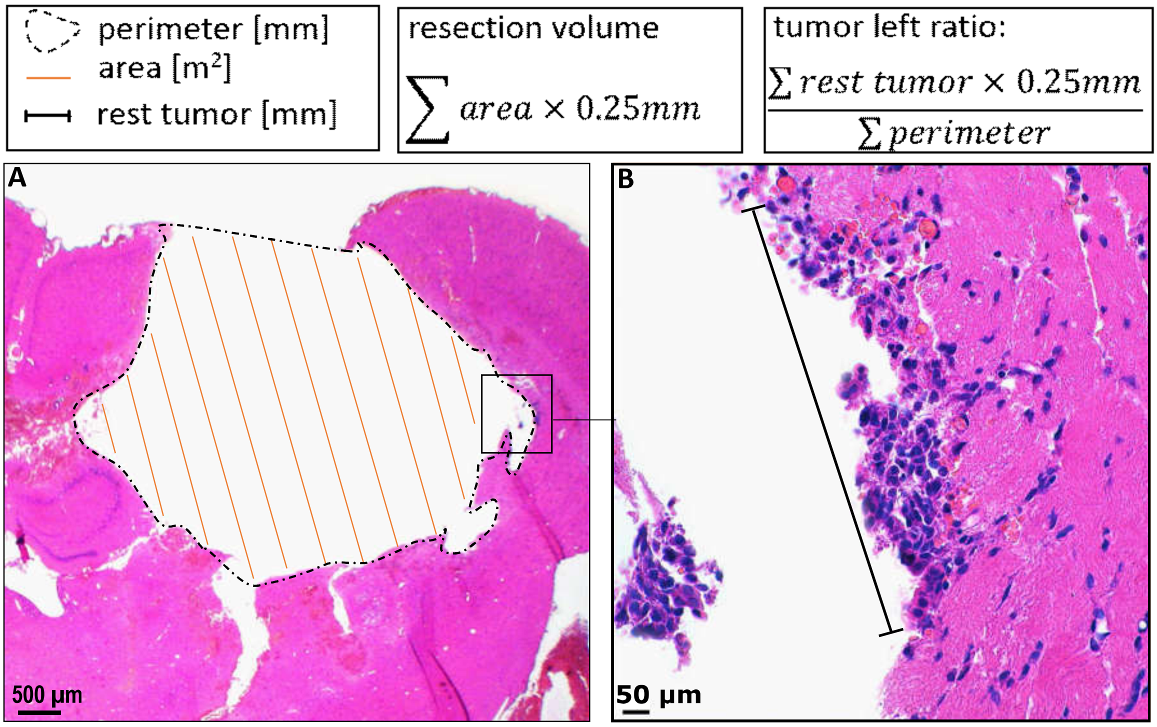

Figure 2.8: Calculation of the resection volume and the residual tumor ratio (source: own representation). The resection volume (A) and residual tumor in the resection zone (B) were determined using the Optima® 6.51 analysis program for image analysis. Each 4-µm-thick serial section (0.25-mm intervals) was examined individually for calculation. In order to calculate the resection volume (cavity), the resection areas were summated and multiplied by 0.25 mm. The "tumor left ratio" was calculated according to the following formula: [(summated rest tumor * 0.25 mm)/summated perimeter]. Only tumor tissue within the maximum depth of the CLSM GastroFlex™ (55–65 µm) was considered. A: Bar = 500 µm, B: Bar = 50 µm. *CLSM, confocal laser scanning microscopy.*

2.6.9 Studies on pig

One male pig (German breed) weighing 29 kg at the age of 4 months was used to investigate the use of CLSM for *in vivo* imaging of healthy, larger brain features. The pig as a model was used because of the similarities of its brain in terms of anatomy, histology, and vascularization with that of humans. The major advantage of the pig for neurosurgical research is the large size of its brain, allowing conventional surgery and imaging in a living model. The experiments were performed at the Institute for Neurosurgical Pathophysiology (Medical Center, Johannes Gutenberg University, Mainz, Germany).

2.6.10 Pig surgery and CLSM imaging

Anesthesia was induced via intramuscular injection of ketamine (15 mg/kg) and azaperone (3 mg/kg) followed by intravenous application of 10 mL thiopental-sodium (25 mg/mL; Trapanal®, Nycomed). Continuous intravenous application of thiopental (10–15 mg/kg bw/h) and piritramide (0.2–0.3 mg/kg bw/h) at a rate of 0.2–0.3 mg/kg bw/h-maintained sedation.

Body temperature was kept at homeostasis throughout the procedure with a heating pad (Homeothermic Blanket System; Harvard Apparatus, South Natick, MA, USA). The pig was intubated (Super-Safety-Clear, i.d./o.d. 6.0/5.5 mm, Teleflex, Ruesch, Germany) and mechanically ventilated (900 B; Siemens-Elema, Erlangen, Germany), while inspired oxygen (FiO_2) and end-tidal carbon dioxide ($etCO_2$) were continuously monitored (Capnomag Ultima; Datex Engstrom Division, UK).

The head was fixed in a stereotaxic frame, and craniotomy was performed to expose the brain surface by a veterinarian (Fig. 2.9). Healthy brain structures were imaged by gently pressing the GastroFlex^{TM} probe against the brain tissue. Both a topical application of one drop of ICG (0.5 mg/mL in NaCl) and an injection of 0.4 mg/kg ICG dissolved in NaCl were used to enhance tissue contrast. After CLSM imaging, the anesthetized pig was killed by lethal injection of potassium chloride for other laboratory purposes in accordance with national and international guidelines.

Figure 2.9: Setup pig surgery (source: own representation). One male pig weighing 29 kg at the age of 4 months (A) was used to investigate CLSM for *in vivo* imaging of healthy brain tissue. Craniotomy was performed in a stereotaxic frame (A) to remove the skull and gain access to the brain (B). Craniotomy was performed under a conventional light microscope (C). *CLSM, confocal laser scanning microscopy.*

3. Results

3.1 Distribution of primary CNS tumors

This section gives a descriptive overview of all examined tumor samples with the CLSM device. In addition, important prognostic factors are presented, such as the behavior of the tumor (benign or malignant), and the gender and age of the patient at the initial diagnosis.

3.1.1 Distribution by subtype, behavior, and gender

The distribution of all surgically treated and examined primary CNS tumors during the period January 2014–February 2016 at the Department of Neurosurgery of the Merheim, Hospital, Cologne, Germany, are illustrated in Figures 3.1 and 3.2. During the 2-year period, 317 primary CNS tumors were collected; metastases and other entities, such as abscesses, were excluded.

The rates of collected tumor samples were significantly higher ($p <= 0.01$) in men ($n = 162$) than in women ($n = 155$). Benign primary CNS tumors had a higher rate in females (56%) than in males (44%) due to a higher rate of benign meningiomas (31%). Pituitary adenomas were more common in males (74%) than in females (26%). Also, more males (62%) were treated for a glioblastoma (Fig. 3.1).

In total 170 benign primary CNS tumors were collected (Fig. 3.3). Meningiomas had the highest rate, with 125 cases. Thus, meningiomas were both the most common resected primary CNS tumors and the most common benign CNS tumors in the tumor sample collection. Only 8% of the resected meningiomas were malignant. Schwannomas were the second most common benign tumors (12%), followed by pituitary adenomas (11%). Rare primary benign CNS tumors (< 2%) included mixed choroid plexus papillomas, pilocytic astrocytomas, other nerve sheath tumors, epidermoid tumors, and hemangioblastomas (Fig. 3.3).

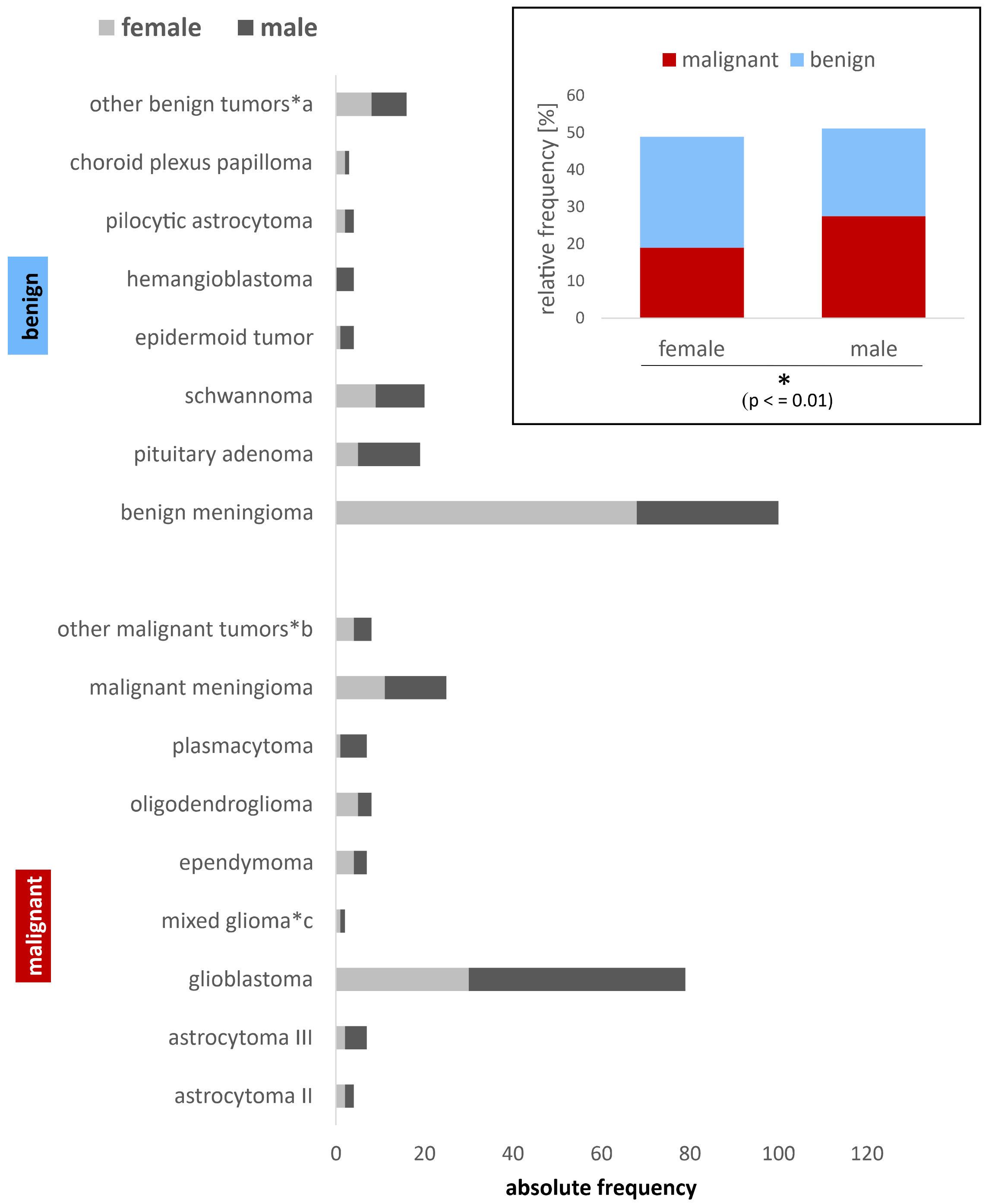

*a. includes neurofibromas, cavernomas, and gangliogliomas. *b. Includes gliosarcomas and other high-grade gliomas. *c. Includes anaplastic oligoastrocytomas

Figure 3.1: Absolute frequency of all examined primary CNS tumors (n = 317) by histopathological subtypes, behavior (malignant, benign), and gender, 2014–2016. *CNS, central nervous system.*

In total, 145 tumor samples were malignant primary CNS tumors. Of these, glioblastomas had the highest rate, with 80 cases (25%). The second most common malignant tumor was malignant meningiomas (17%), followed by oligodendrogliomas (6%), WHO grade III astrocytomas (5%), ependymomas (5%), and plasmacytomas (5%). Rare primary malignant CNS tumors ($< 2\%$) included diffuse astrocytomas and mixed gliomas (Fig. 3.4).

Gliomas represented approximately 35% of all resected primary CNS tumors. The distribution of gliomas by histology is illustrated in Figure 3.5. Glioblastomas made up over 71% of all gliomas, while mixed gliomas represented a minority of 2%. WHO grade I astrocytomas, the only benign gliomas, accounted for about 4% of all gliomas.

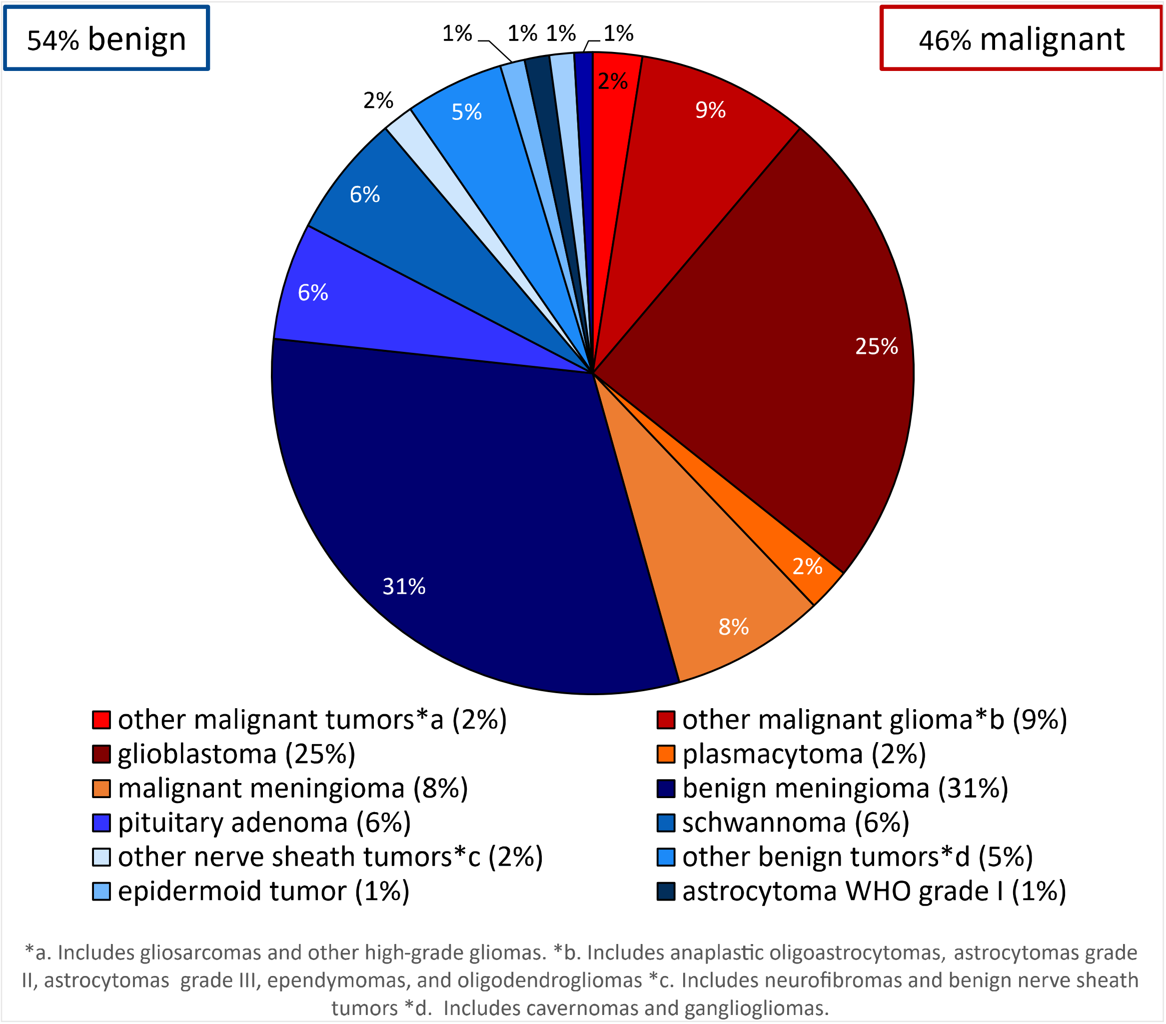

*a. Includes gliosarcomas and other high-grade gliomas. *b. Includes anaplastic oligoastrocytomas, astrocytomas grade II, astrocytomas grade III, ependymomas, and oligodendrogliomas *c. Includes neurofibromas and benign nerve sheath tumors *d. Includes cavernomas and gangliogliomas.

Figure 3.2: Relative frequency of all investigated primary CNS tumors by histopathological subtypes, 2014–2016. *CNS, central nervous system.*

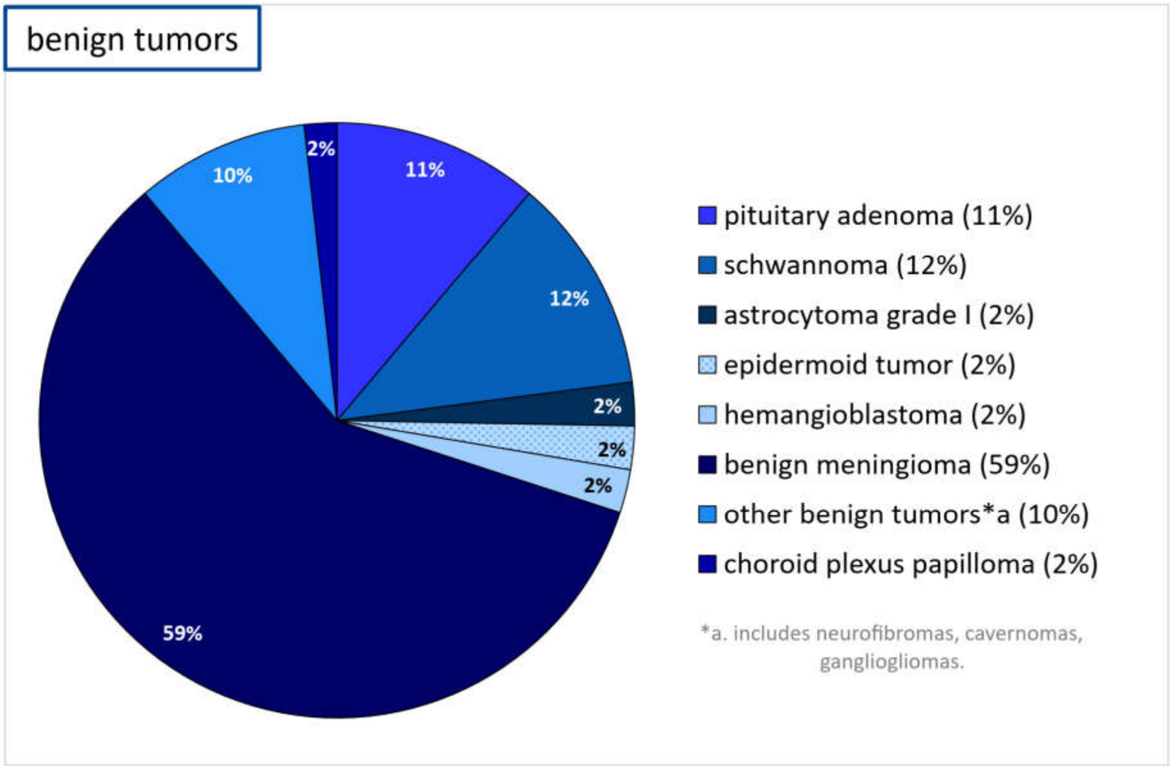

Figure 3.3: Relative frequency of all benign primary CNS tumors (n = 170) by histopathological subtypes, 2014–2016. *CNS, central nervous system.*

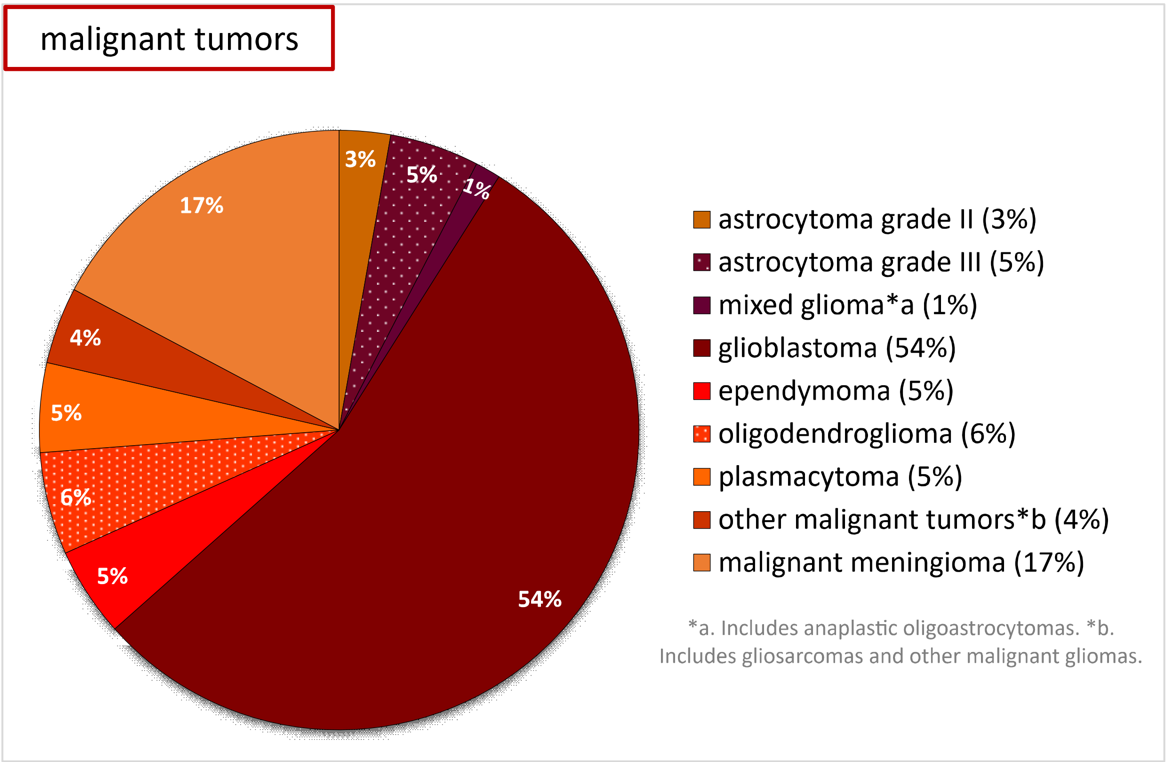

Figure 3.4: Relative frequency of all investigated malignant primary CNS tumors (n = 145) by histopathological subtypes, 2014–2017. *CNS, central nervous system.*

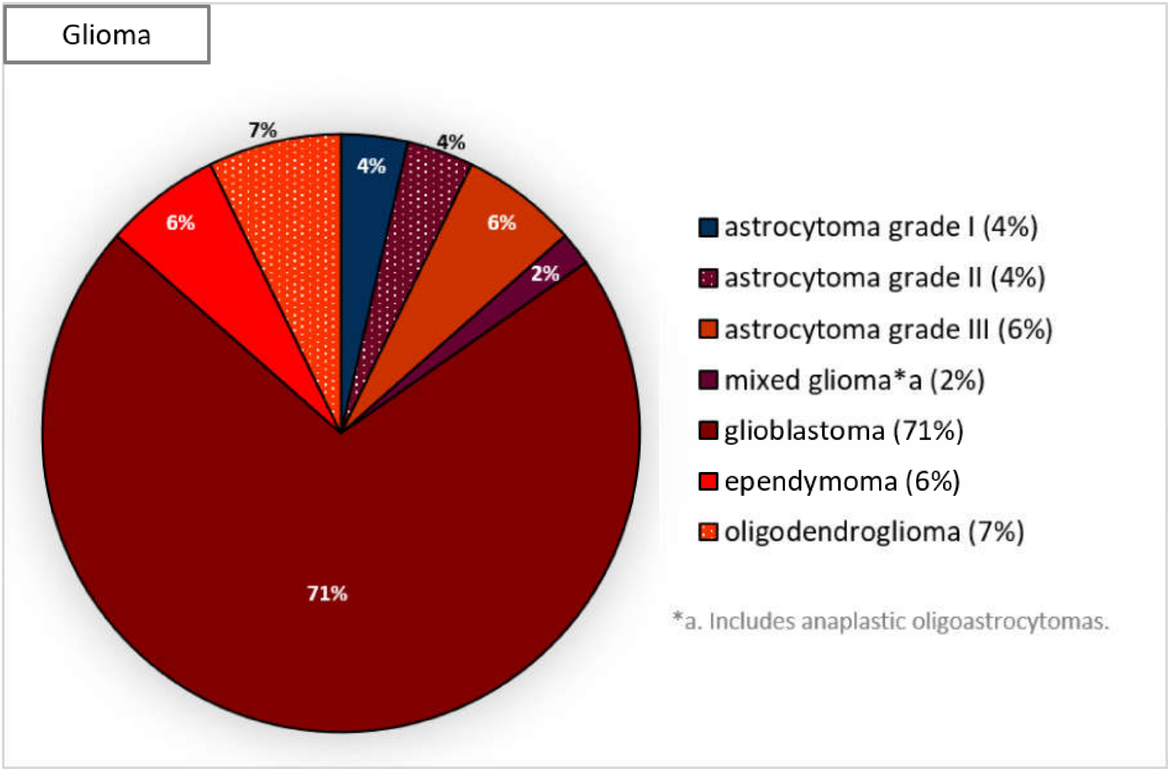

Figure 3.5: Relative frequency of all investigated gliomas (n = 111) subdivided by histopathological subtypes, 2014–2016.

3.1.2 Distribution by age and behavior

The overall median age at the first surgical treatment of a primary CNS tumor was 52 years. The histology-specific median ages ranged from 19 years (WHO grade I astrocytomas; Fig. 3.7) to 74 years (high-grade gliomas; Fig. 3.6). Overall, gliomas, except for glioblastomas and oligodendrogliomas, were surgical treated at younger median ages (WHO grade II astrocytomas, 29 years; WHO grade III astrocytomas, 38.8 years; ependymomas, 38 years; Fig. 3.6 and 3.7). Oligodendrogliomas and glioblastomas were on average first treated at older median ages (oligodendrogliomas, 53 years; glioblastomas, 68 years; Fig. 3.6). Patients with a malignant meningioma were on average younger at their surgical treatment (median age of 57 years; Fig. 3.6) than patients with a benign meningioma (median age of 63 years; Fig. 3.7).

The ages at the first surgical treatment of a glioblastoma were highly variable: the youngest patient was 28 years old, while the oldest patient was 88 years old. Similarly, the ages at the first treatment of a malignant meningioma were variable: the youngest patient was 27 years old, while the oldest patient was 73 years old (Fig. 3.6). The same applies to benign meningioma: the youngest patient was 27 years old, and the oldest patient was 90 years old at their first surgical treatment (Fig. 3.7).

The overall frequency of primary CNS tumors by age group and behavior is illustrated in Figure 3.8. The frequency rate for all primary CNS tumors was highest in the < 55–64 > year age group and lowest in the < 5–14 > year age group at the Merheim, Hospital. Among children, aged < 0–15 > years, the frequency of a CNS tumor was much lower than in adults (no pediatric department at the Merheim, Hospital). The number of malignant primary CNS tumors increased steadily with higher age until its peak in the < 65-74 > year age group, after which the number decreased. The frequency of benign primary CNS tumors was highest between 55 and 64 years and lowest between 85 and 94 years.

The relative frequency of the most common primary CNS tumors by age group and histology are presented in Figures 3.9 and 3.10. Frequency of glioblastomas and malignant meningiomas increased with higher age until peaking in the < 75–84 > year age group and < 65–74 > year age group, respectively. Ependymoma occurrence peaked at ages between 35 and 44 years. The number of oligodendrogliomas increased until ages 45–54 years and then steadily decreased until ages 75–84 years (Fig. 3.9).

Benign meningiomas peaked, like glioblastomas, in the < 75–84 > year age group. The number of benign pituitary adenomas and schwannomas also increased with higher ages, with a peak between the ages of 55 and 64 (Fig. 3.10).

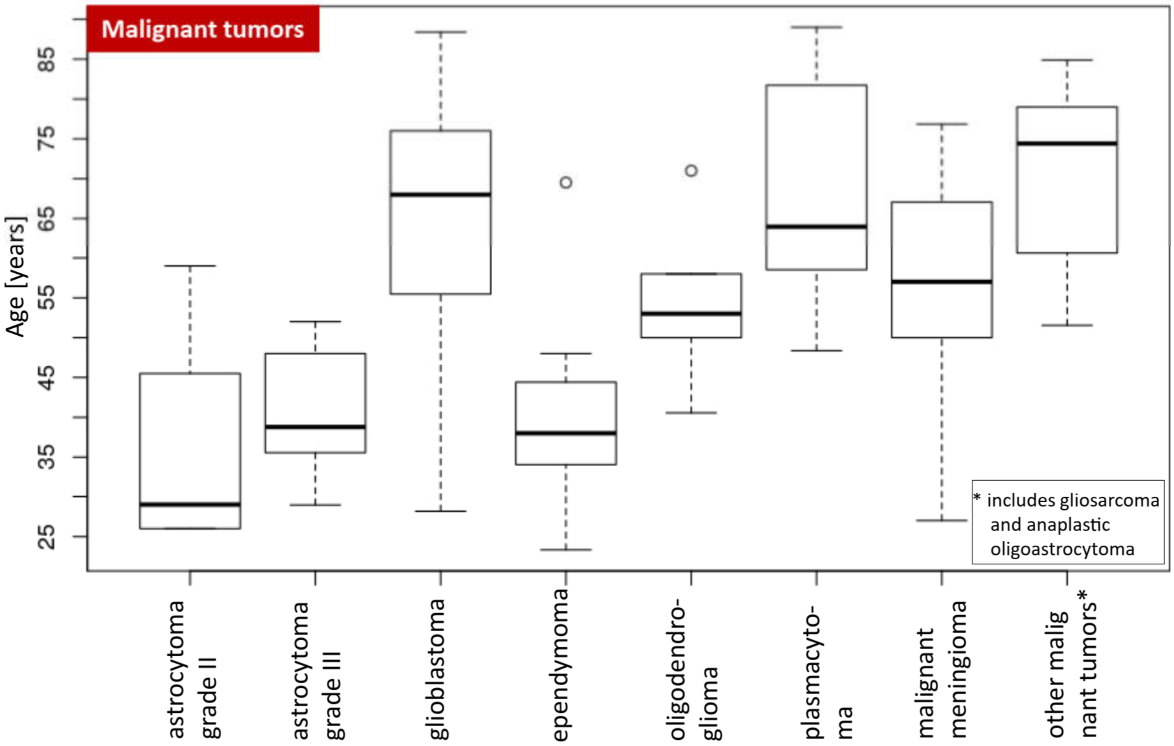

Figure 3.6: Boxplots regarding ages at diagnosis of a malignant primary CNS tumor. The distribution of patient ages at the first surgical treatment of a malignant primary CNS tumor during 2014–2016 at the Merheim, Hospital is presented. The boxplots indicate the median age, the 25% and 75% quantiles, and the maximum (greatest value, excluding outliers) and minimum (lowest value, excluding outliers) age in years for each tumor. The outliers are indicated as circles. *CNS, central nervous system.*

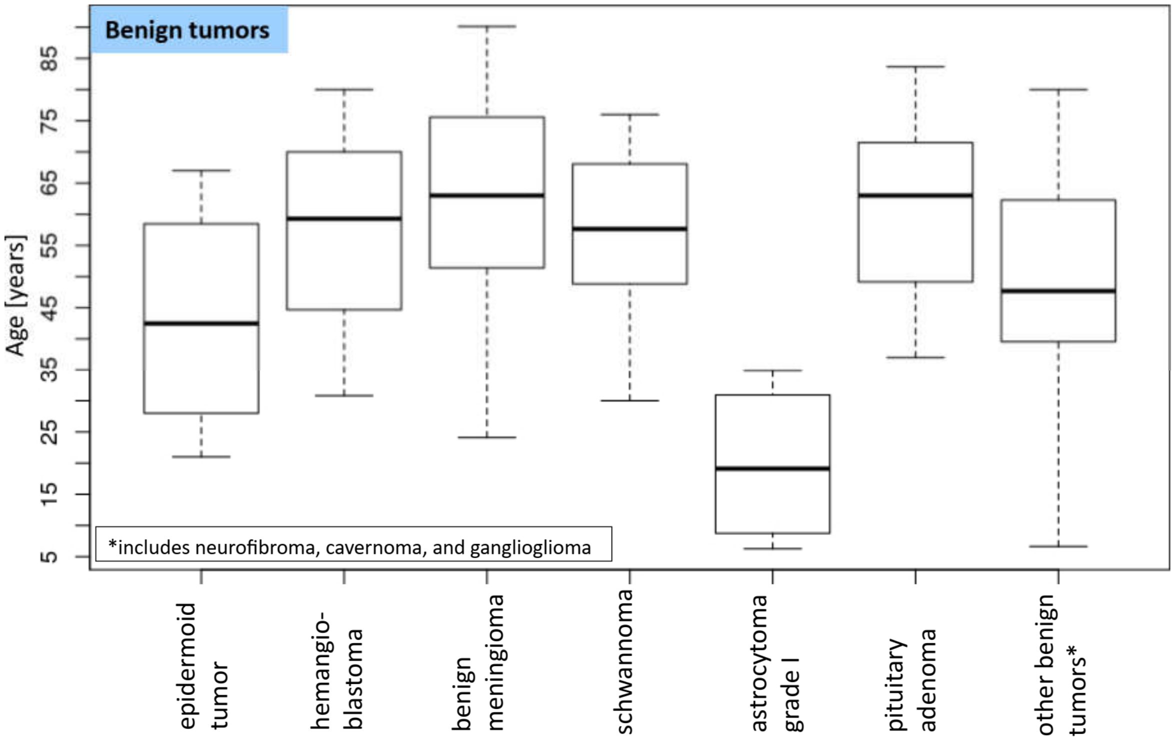

Figure 3.7: Boxplots regarding ages at first surgical treatment of a benign CNS tumor. The distribution of patient ages at diagnosis of a benign primary CNS tumor during 2014–2016 at the Merheim, Hospital is presented. The boxplots indicate the median age, the 25% and 75% quantiles, and the maximum (greatest value, excluding outliers) and minimum (lowest value, excluding outliers) age in years for each tumor. *CNS, central nervous system.*

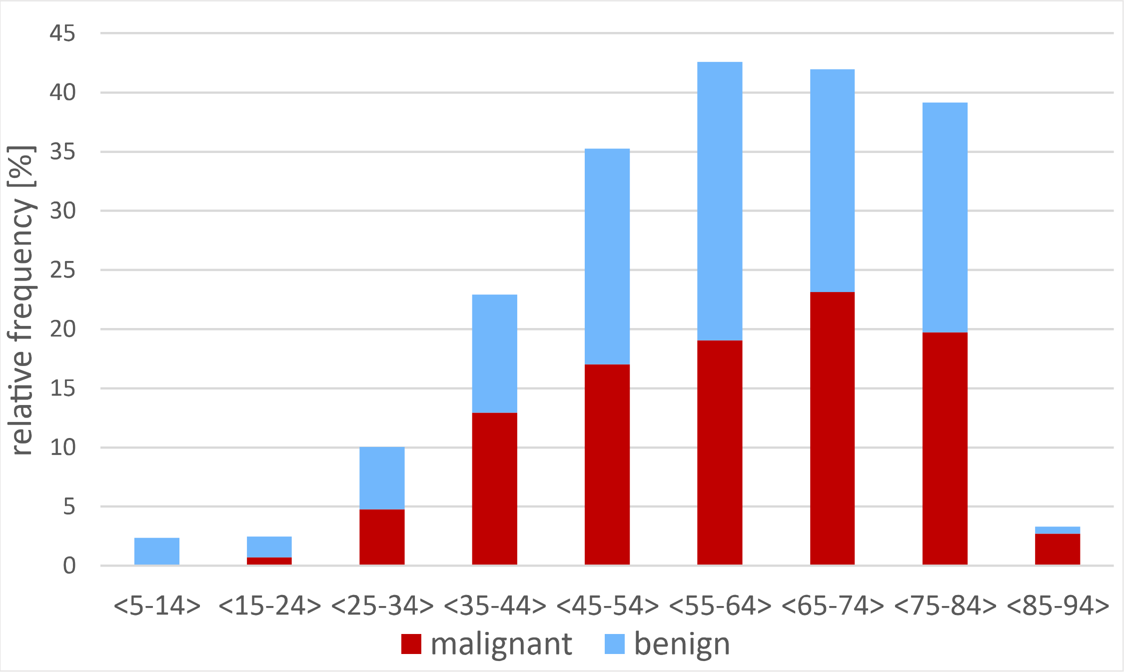

Figure 3.8: Relative frequency of primary CNS tumors by age and behavior (malignant, benign), 2014–2016. *CNS, central nervous system.*

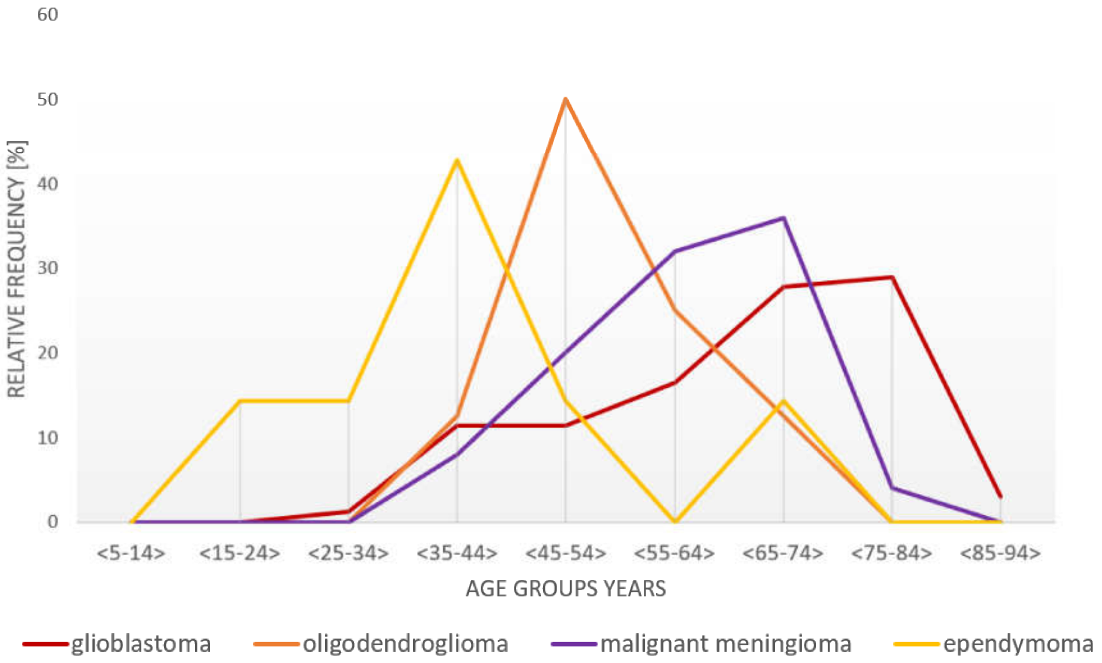

Figure 3.9: Age-adjusted frequency of the most common malignant primary CNS tumors by histology subtypes and age groups (age 5–94 years), 2014–2016. *CNS, central nervous system.*

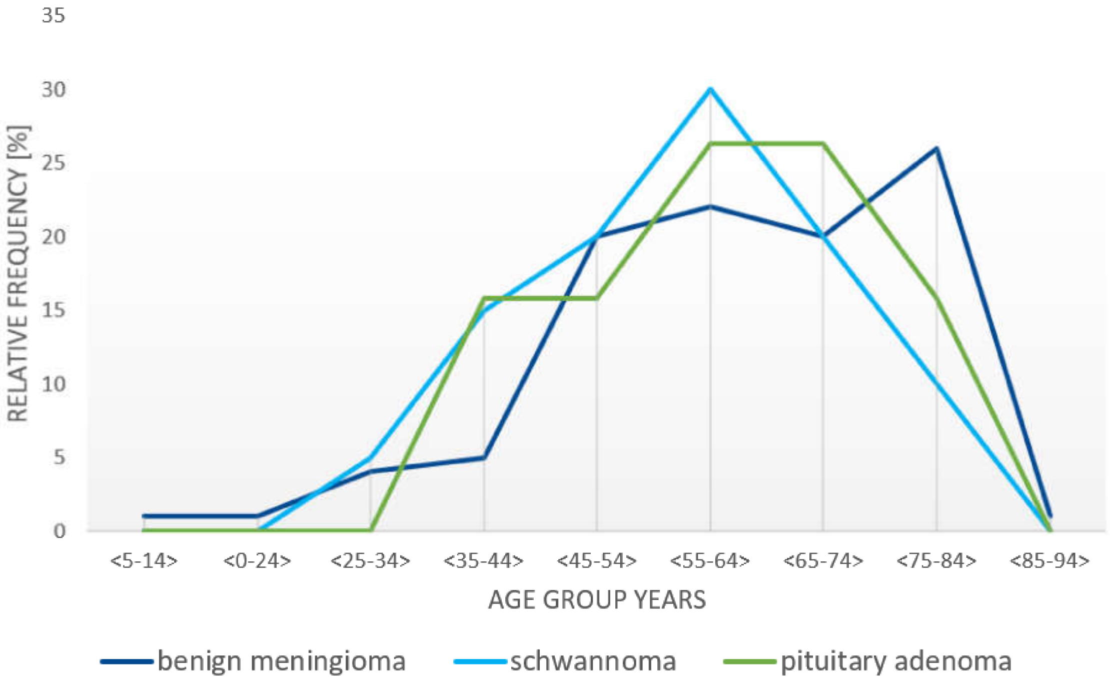

Figure 3.10: Age-adjusted frequency of the most common benign primary CNS tumors by histology subtypes and age groups (age 5–94 years), 2014–2016. *CNS, central nervous system.*

3.2 *Ex vivo* studies using the CLSM device at 488 nm excitation

3.2.1 Investigation of different CLSM Miniprobes™

Fresh oligodendroglioma specimens (randomly chosen; resected on the day of received Miniprobes™) were examined with the CystoFlex™ UHD, UroFlex™, and the GastroFlex™ probes to determine which would be more suitable for a neurosurgical application. *Ex vivo* imaging was performed with the CLSM system as described in Subsection 2.4.2. In all cases, AF was applied to enhance tissue contrast. Histopathological examination with H&E from the same specimen and ROI was performed as the gold standard.

All three probes visualized the typical round and uniform nuclei of oligodendrogliomas with high contrast, resembling the findings in traditional histology (Fig. 3.11). Since the UroFlex™ probe has a lower depth of observation range than the other probes, and the CystoFlex™ UHD probe is shorter in length (Table 2.4), the GastroFlex™ probe was chosen for all following studies.

3.2.2 Investigation of incubation times for tumor staining

The optimal concentrations of AF, AO, and CV for tissue staining are well established, but the incubation time protocols are variable in the literature. To find the optimal incubation time, a WHO grade I meningioma specimen was examined 1, 5, 10, and 30 min after topical application of AF, AO, and CV.

After topical application of AF and AO, tissues were stained immediately, and fluorescence was observed with CLSM. The best image was obtained after an incubation time of 1 min (Fig. 3.12 and 3.13). Both fluorophores stained the cell nuclei, providing contrast among the nuclei and cytoplasm and demonstrating different features, such as pleomorphism and an increased nuclear-to-cytoplasmic ratio. Psammoma bodies, round anuclear structures, were best seen after an incubation time of 1–5 min with AF and AO. After an incubation time of 10 min with one of the fluorophores, the fluorescence intensity was too bright to allow demarcation of tissue features (Fig. 3.12 and 3.13). Topical application of CV resulted in fluorescence of the cytoplasm with an optimal incubation time of 5–10 min. Longer or shorter incubation times resulted in a fluorescence intensity that was too low or high (Fig. 3.14).

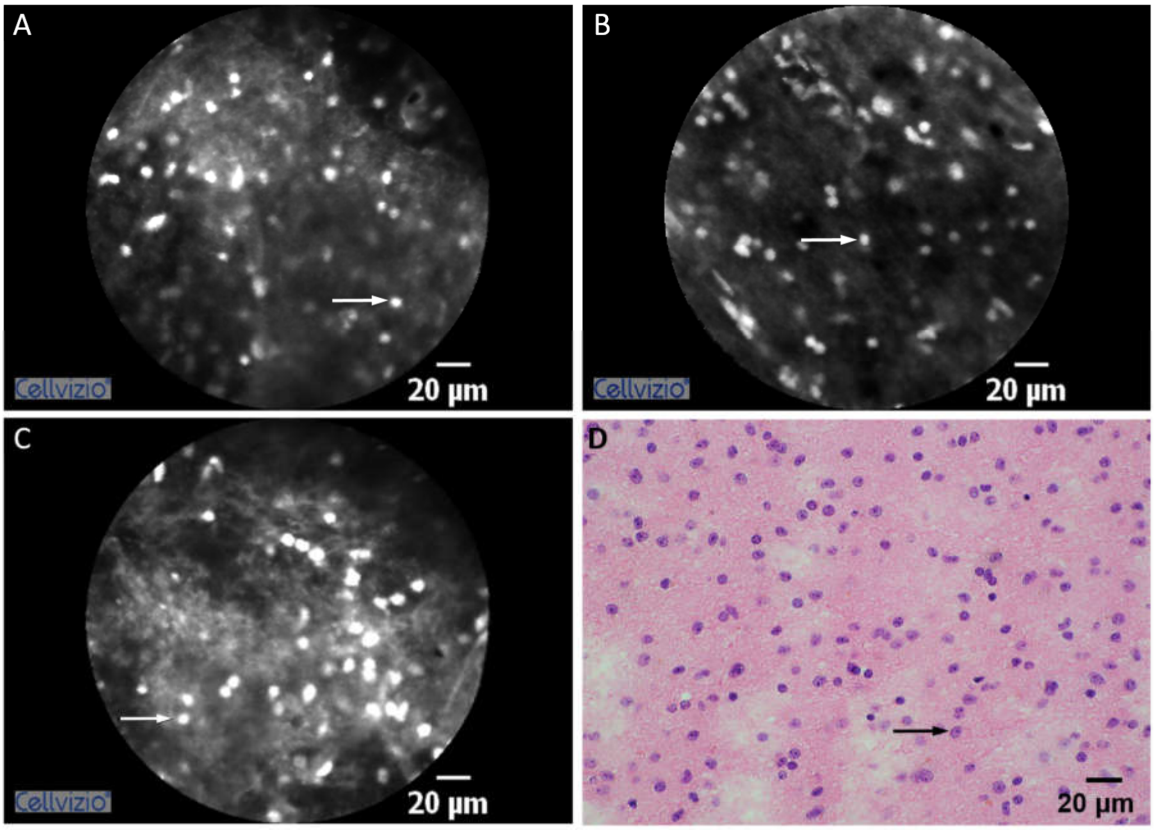

Figure 3.11: Investigation of CLSM Miniprobes™. Oligodendroglioma was examined using three different CLSM Miniprobes™. AF was applied as contrast agent. CystoFlex™ UHD probe (A), GastroFlex™ probe (B), and UroFlex™ probe (C) revealed the typical round and uniform nuclei (→) of the oligodendroglioma specimen, accordingly to the H&E stained section (D). Bars = 20 µm. *CLSM, confocal laser scanning microscopy; AF, acriflavine hydrochloride; H&E, hematoxylin and eosin.*

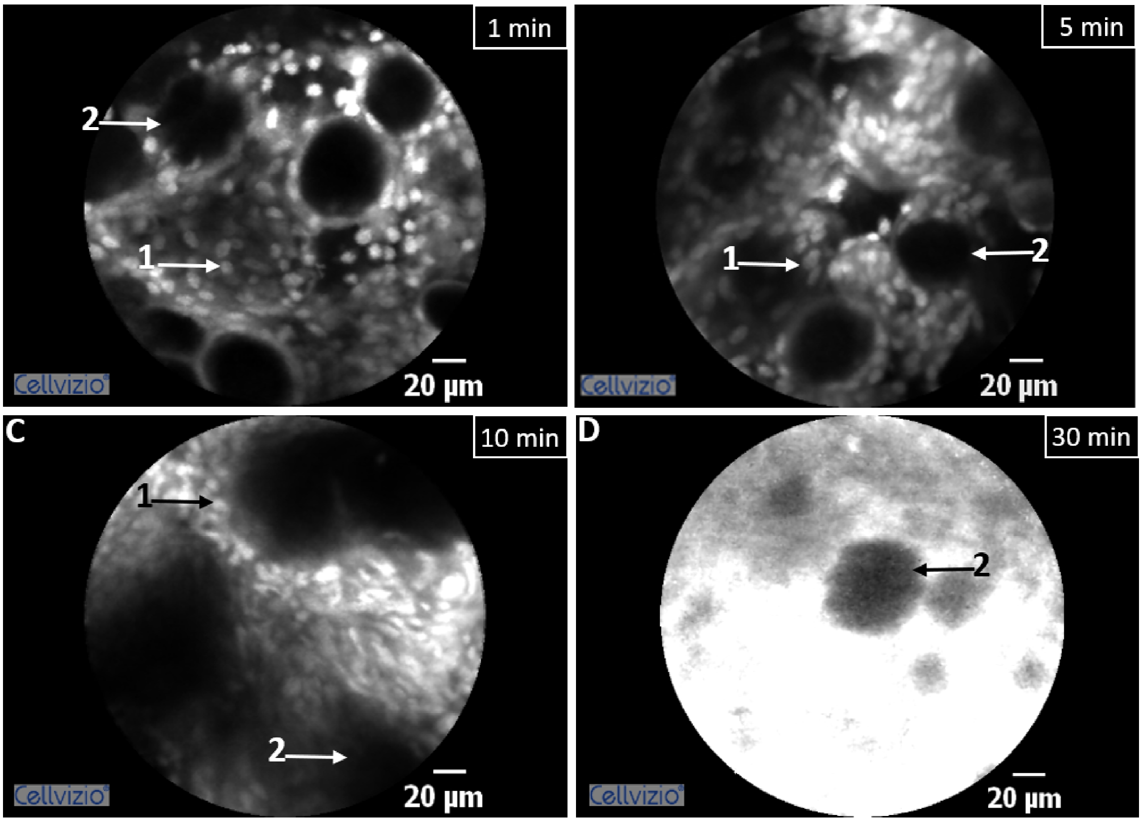

Figure 3.12: Incubation times of AF for tumor staining. CLSM imaging of WHO grade I meningioma allowed best cell nuclei detection after 1 min incubation with AF (A 1→). Psammoma bodies were best visible after an incubation of 1–5 min with AF (A, B 2→); at 10 min they appeared as indistinct structures (C, D 2→). After a 10 min incubation, the background noise was too high to detect cellular features (C, D). Bars = 20 µm. *AF, acriflavine hydrochloride; CLSM, confocal laser scanning microscopy; WHO, World Health Organisation.*

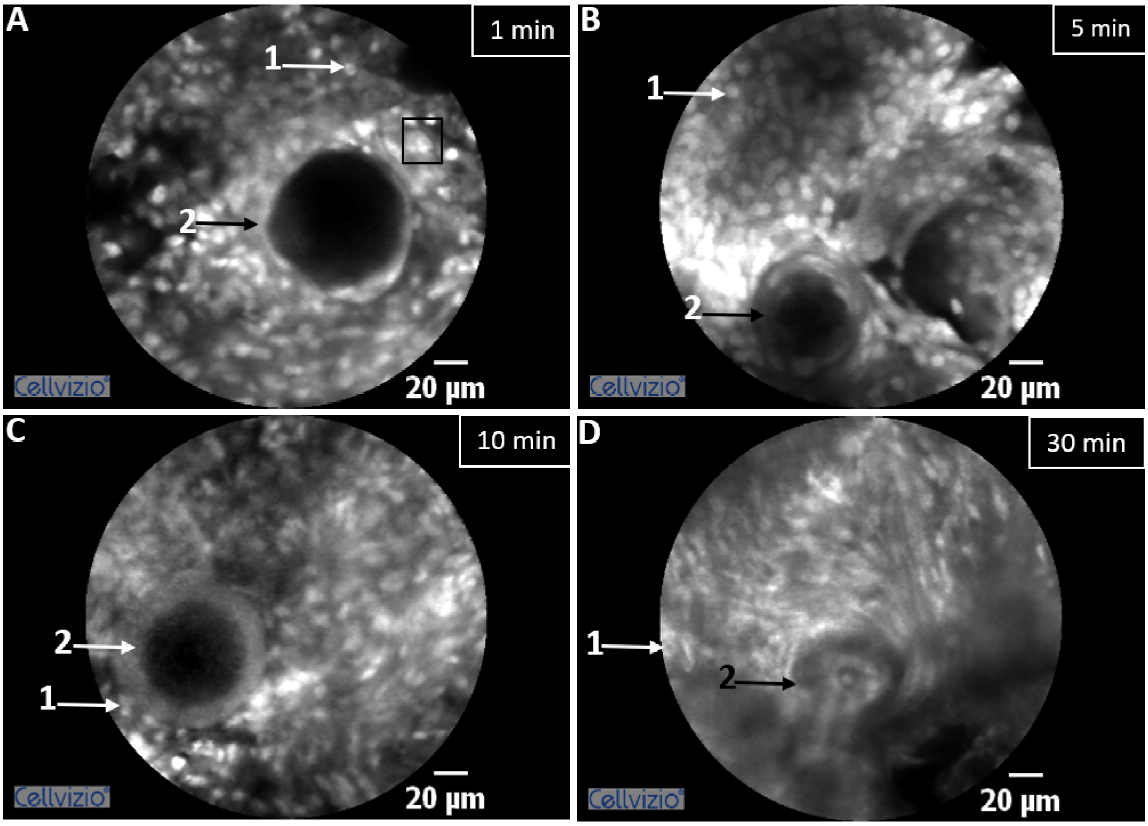

Figure 3.13: Incubation times of AO for tumor staining. A WHO grade I meningioma was examined 1, 5, 10, and 30 min after application of AO with CLSM. Pathological features such as pleomorphism (accentuation) and increased nuclear-to-cytoplasmic ratio were best detected after an incubation time between 1 and 5 min (A, B 1→). Psammoma bodies (2→) were clearly identified after an incubation time of 1, 5, and 10 min (A, B, C). Calcium deposits could also be seen in the psammoma bodies (B, C). After a 10 min incubation with AO, the background noise was too bright to detect cellular features (D). Bars = 20 µm. *AO, acridine orange; WHO, World Health Organization; CLSM, confocal laser scanning microscopy.*

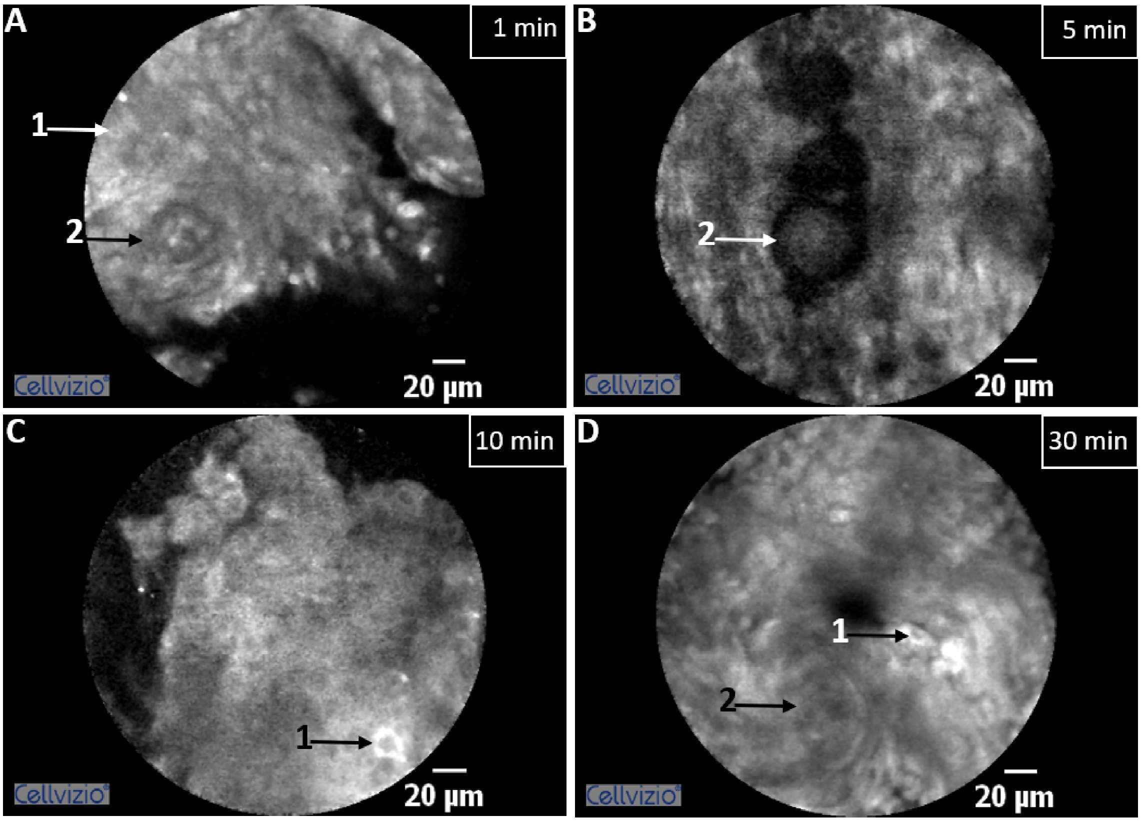

Figure 3.14: Incubation times of CV for tumor staining. A WHO grade I meningioma was examined 1, 5, 10, and 30 min after application of CV with CLSM. CV stained the cytoplasm with the cell nuclei visible as dark spots (A, C, D 1→). After an incubation of 1 min with CV, no clear cell structures could be detected due to a low fluorescence intensity (A). The best image was obtained after an incubation time of 10 min (C 1→). Psammoma bodies (2→) were clearly observed after an incubation time of 5 min with the dye (B). Overall, the resolution of all images was low (A–D). Bars = 20 µm. *CV, cresyl violet; WHO, World Health Organization; CLSM, confocal laser scanning microscopy.*

3.2.3 Investigations of contrast agents for tumor staining

Fresh biopsies of the CNS were collected from various patients of both genders and different ages. The different samples were analyzed before (native) and after staining with AF, AO, and CV. From the same ROI, traditional histology with H&E was performed for each sample as the gold standard. The average image quality was overall equal for all examined samples. However, the first images taken with CLSM were of inferior quality. Only representative images are presented below.

Natively

Imaging using CLSM without any contrast agent showed a slight autofluorescence of the biopsies. The autofluorescence was especially visible when the elastin and collagen fiber content was high, as seen in samples with high amounts of blood vessels, such as in hemangioblastomas (Fig. 3.15). In non-small cell lung adenocarcinomas (this chapter includes metastases, as only fresh specimens were examined, and these tumors were the most frequently resected ones), some autofluorescence could be detected in the cells (Fig. 3.17). Nonetheless, natively no exact diagnoses of the biopsies could be made except for epidermoid tumors (Fig. 3.18) and choroid plexus papillomas (Fig. 3.20).

Acriflavine hydrochloride and acridine orange

AF and AO rapidly stained the nuclei of the tumor cells. AF further stained the cell membrane and the extracellular matrix to a lesser extent, which sharply contrasted the cytoplasm. This allowed for a precise analysis of the cell volume, shift of nuclear-to-cytoplasmic ratio, and tissue architectures with CLSM.

AO, which stained only the cell nuclei, was more effective at demonstrating subcellular components, well visualized in the brain metastasis of a non-small cell lung adenocarcinoma, in which the big nucleus and its nucleoli were strongly visible (Fig. 3.17).

Endothelial cells on blood vessels were also stained by AF and AO, which, for example, allowed identification of hemangioblastomas. In addition to a prominent vasculature, hemangioblastomas were characterized by large stromal cells (Fig. 3.15).

Tumor features such as high cell density, pleomorphism, and necrosis were also identifiable after staining with AF and AO, as shown in the glioblastoma samples. Analysis of glioblastoma with AO also revealed perivascular growth of tumor cells on the blood vessels (Fig. 3.16).

Both dyes allowed a unique visualization of the crystal-like structure of the anuclear stratum corneum ("cell ghosts") of epidermoid tumors, which were detached from the epithelium in the H&E stained section (Fig. 3.18). Psammoma bodies in WHO grade I meningiomas were visualized, using CLSM, as globular, anuclear structures with excellent correlation to the staining with H&E (Fig. 3.19). CLSM images of choroid plexus papilloma stained either with AF or AO showed villous structures with an ordered flat layer of ependymal cells surrounding the fibrovascular cores, corresponding with the H&E findings (Fig. 3.20). In most cases, both dyes provided tissue features similar to those obtained through traditional histology (Fig. 3.20).

Cresyl violet

CV predominately stained the cytoplasm, causing the cell nuclei to appear as dark spots. This allowed assessment of the cell density, altered nuclear-to-cytoplasmic ratio, and information about the cell shape using CLSM. These highlights were especially informative in the diagnoses of glioblastomas (Fig. 3.16) and brain metastases of non-small cell lung adenocarcinomas (Fig. 3.17). Stained blood vessels were visible as big dark spots or as elongated structures, which could be precisely distinguished from the bright cytoplasm, as seen in the hemangioblastoma sample (Fig. 3.15). Analyses of epidermoid tumors with CV revealed the anuclear crystal-like structure of the "cell ghosts" almost identical to the results obtained with AF and AO (Fig. 3.18). Psammoma bodies in the WHO grade I meningioma sample were visualized as round and anuclear structures, but cellular features were hard to identify (Fig. 3.19). In the choroid plexus papilloma specimen, the abnormal villous structures were precisely defined, comparable to those revealed by the corresponding histology (Fig. 3.20). Compared to AF and AO, the fluorescence intensity of CV obtained by CLSM was weak.

Simultaneous use of the contrast agents

Furthermore, AF, AO, and CV were used, alone and simultaneously, to enhance tissue contrast in a pilocytic astrocytoma (WHO grade I) and compared to traditional histology. CV alone did not show any tumor features, due to low signal-to-noise ratio (not shown). Rosenthal fibers, a specific feature of pilocytic astrocytomas, were observed after all staining combinations and with AF and AO alone, corresponding with the H&E findings of the same ROI. The simultaneous use of AF or AO with CV also revealed that not all cell nuclei were stained by AF or AO, as only the cytoplasm was stained by CV in some cells (Fig. 3.21). Overall, the simultaneous use of the contrast agents did not aid in obtaining tumor information and was, therefore, not further tested.

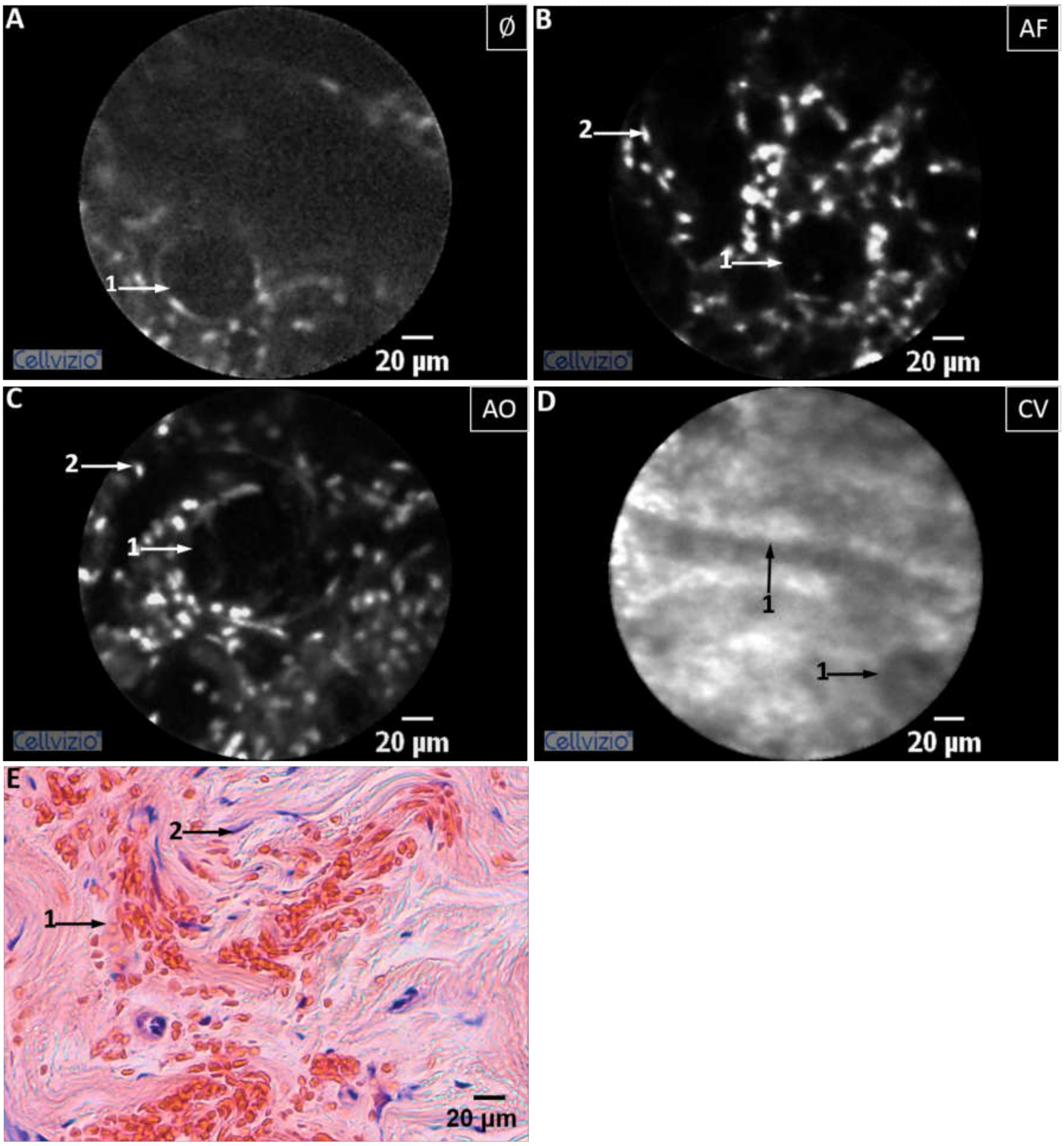

Figure 3.15: Analysis of hemangioblastoma. CLSM imaging showed a slight autofluorescence of the hemangioblastoma biopsy, especially around the blood vessels (A1→). Staining with AF (B) and AO (C) revealed a good visualization of the prominent vascular structures (1→) and of the stromal cells (2→), strongly mimicking the histopathological findings (E). CV staining showed blood vessels in both transverse and longitudinal orientation (D1→). Stromal cells were difficult to identify (D). Bars = 20 µm. *CLSM, confocal laser scanning microscopy; AF, acriflavine hydrochloride; AO, acridine orange; CV, cresyl violet.*

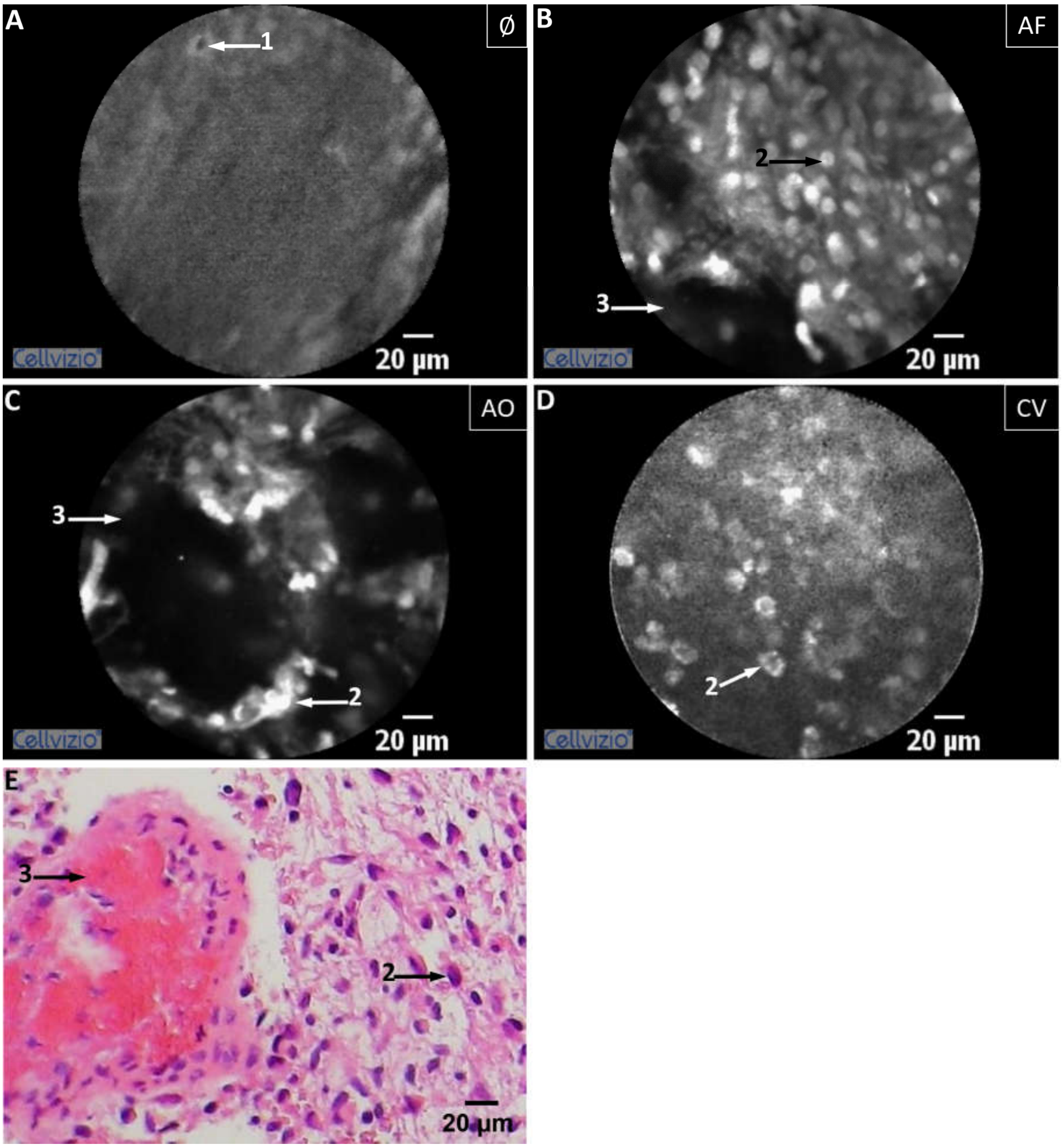

Figure 3.16: Analysis of glioblastoma. The CLSM images were obtained prior to staining (A) and after staining with AF (B), AO (C), and CV (D). Natively, neither cells nor necrosis could be identified, but a feature similar to microvascular proliferation was obtained (1→) with CLSM (A). AF and AO staining enabled a strong staining of the cell nuclei (B, C 2→), whereas CV stained the cytoplasm, with the cell nuclei showing as dark spots (D 2→). Analysis of glioblastoma with AO also revealed perivascular growth of tumor cells (C 2→) on the blood vessels (C 3→). AF and AO tissue staining resulted in CLSM images which were highly comparable to the histopathological gold standard with H&E (E). Bars = 20 µm. *AF, acriflavine hydrochloride; AO, acridine orange; CV, cresyl violet; CLSM, confocal laser scanning microscopy.*

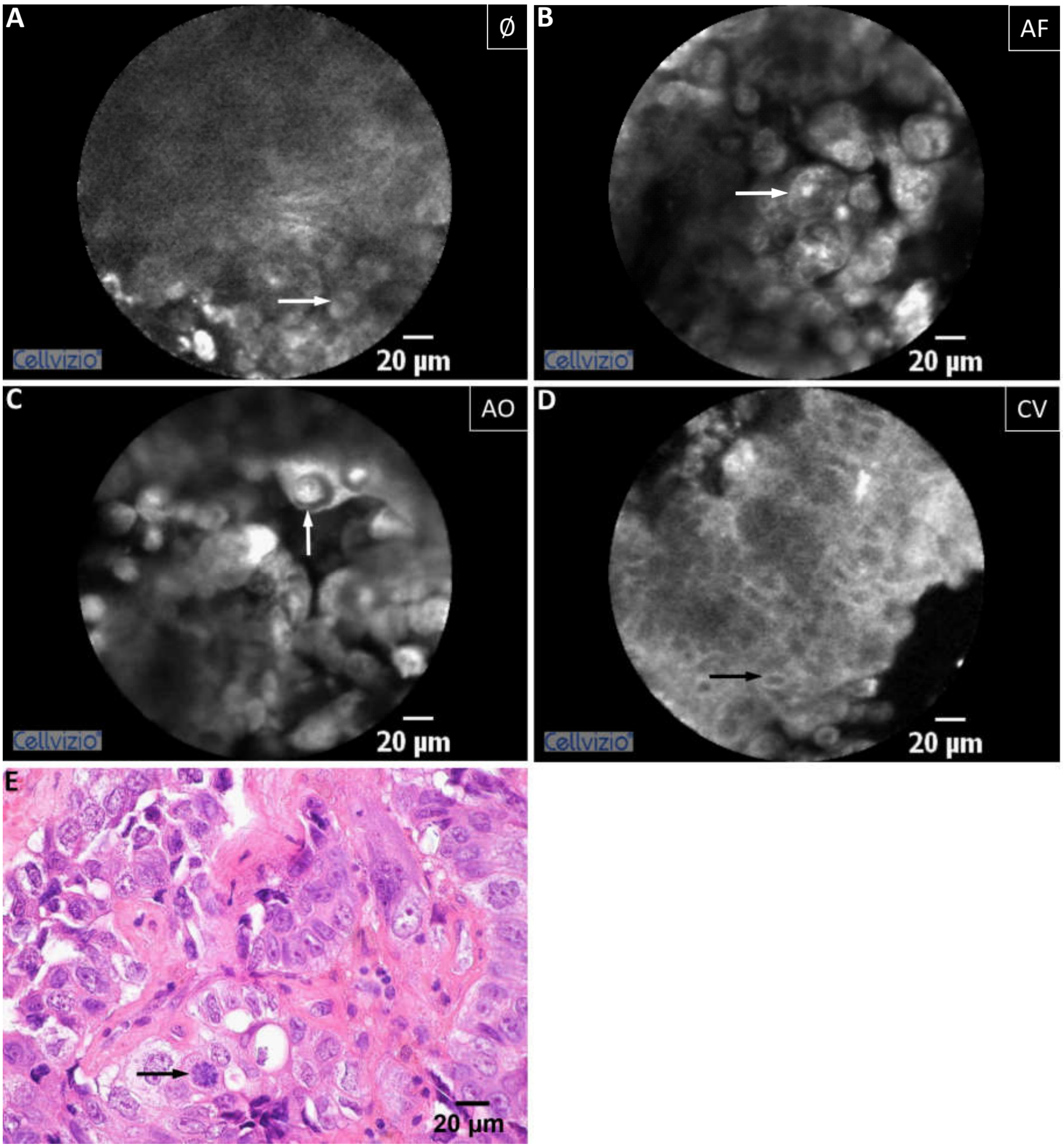

Figure 3.17: Analysis of a brain metastasis of a non-small cell lung adenocarcinoma. Representative images of a brain metastasis of a non-small cell lung adenocarcinoma obtained prior to staining (A) and after staining with AF (B), AO (C), CV (D), and H&E (E). Natively (A), some autofluorescence could be seen, but no clear structures were identified. Cell nuclei were partly visible (→). Staining with AF (B) and with AO (C) allowed a good estimation of the cell size, cell density, and atypia, revealing a high cell density with a round-to-fusiform shape and big nucleus (B, C →). The cell nuclei were also well visualized after staining with CV (D), where the unstained large nuclei were well demarcated from the bright cytoplasm (D →). High resemblance between CLSM images and H&E stained section (E) was found. Bars = 20 µm. *AF, acriflavine hydrochloride; AO, acridine orange; CV, cresyl violet; H&E, hematoxylin and eosin; CLSM, confocal laser scanning microscopy.*

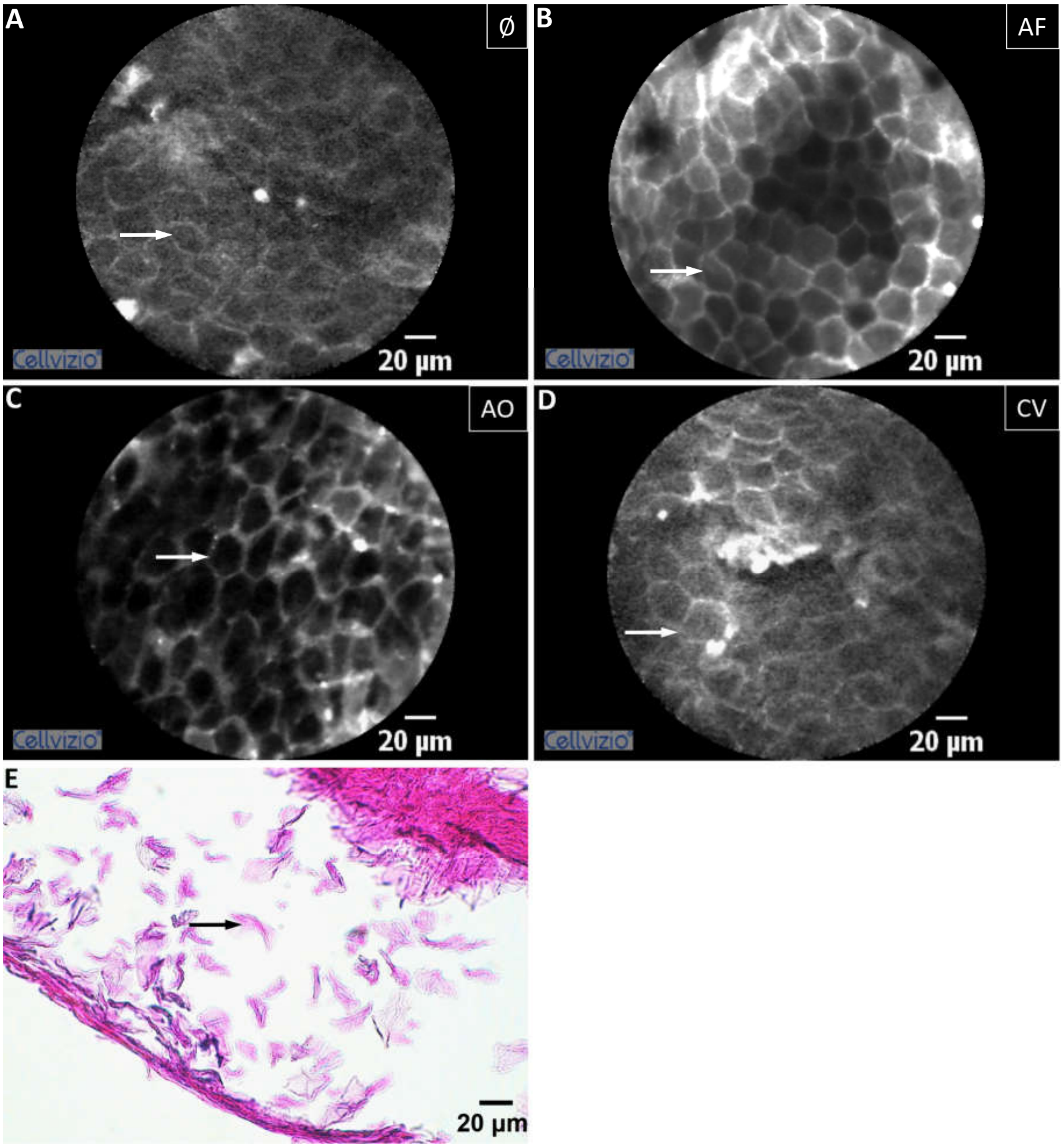

Figure 3.18: Analysis of epidermoid tumor. Representative CLSM images prior to staining (A) and after staining the tissue with AF (B), AO (C), and CV (D) revealed the anuclear crystal-like structure of the "cell ghosts" (→). The stratum corneum layer was detached from the epithelium in the corresponding H&E stained section (E→). Bars = 20 µm. *CLSM, confocal laser scanning microscopy; AF, acriflavine hydrochloride; AO, acridine orange; CV, cresyl violet; H&E, hematoxylin and eosin.*

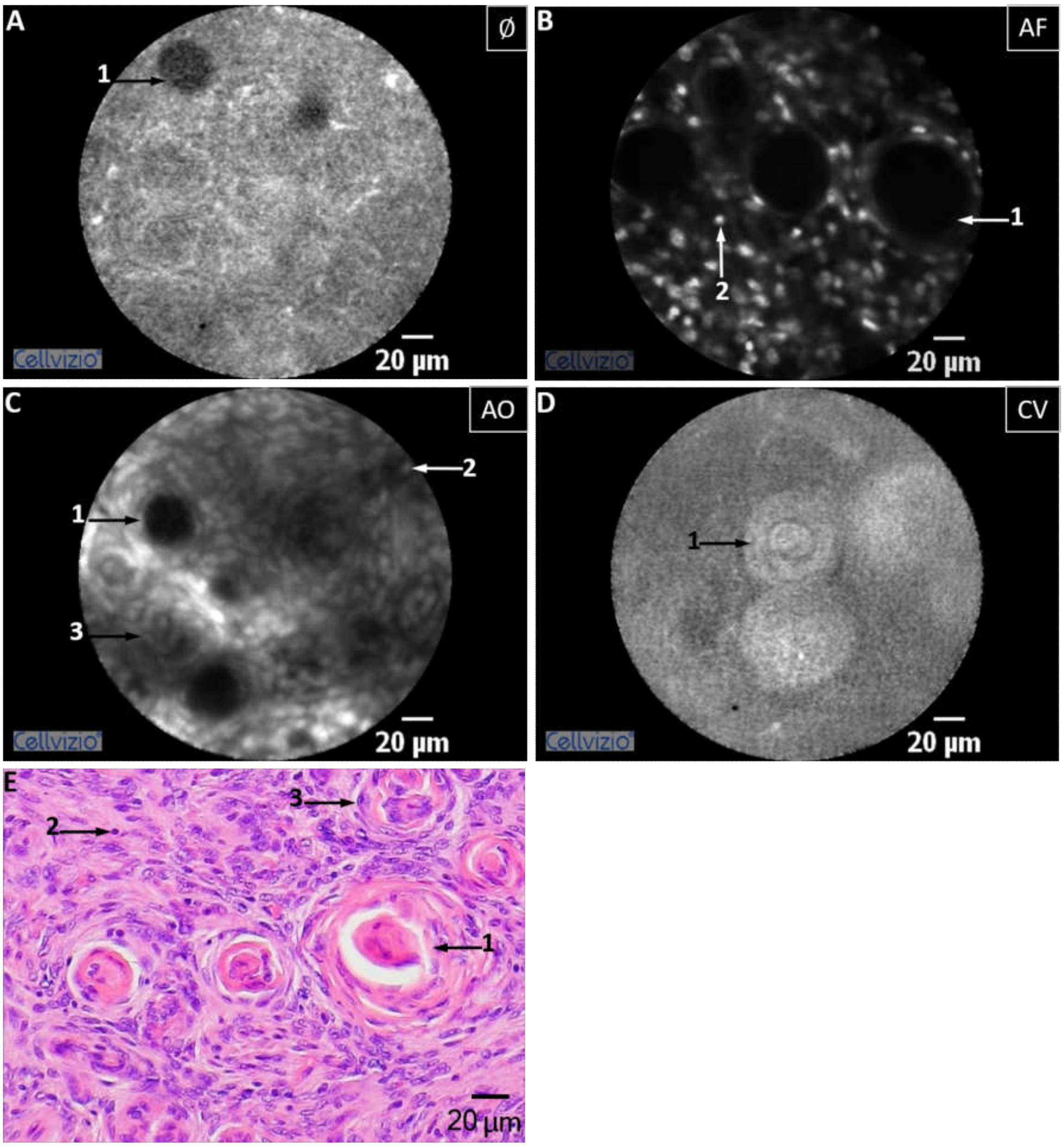

Figure 3.19: Analysis of WHO grade I meningioma. CLSM imaging demonstrated the characteristic psammoma bodies as round, anuclear structures (1→) natively (A) and after staining with AF (B), AO (C), and CV (D). Small to medium-sized cells with nuclei mostly of equal size and shape (2→) were observed after AF (B) and AO (C) staining. Focal whorls were visualized after AO (C 3→) and H&E staining (E 3→). High resemblance between CLSM images and traditional histology was especially found after AF staining (B, E). CV staining did not allow detection, using CLSM, of any cellular features (D). Bars = 20 µm. *WHO, World Health Organization; CLSM, confocal laser scanning microscopy; AF, acriflavine hydrochloride; AO, acridine orange; CV, cresyl violet; H&E, hematoxylin and eosin.*

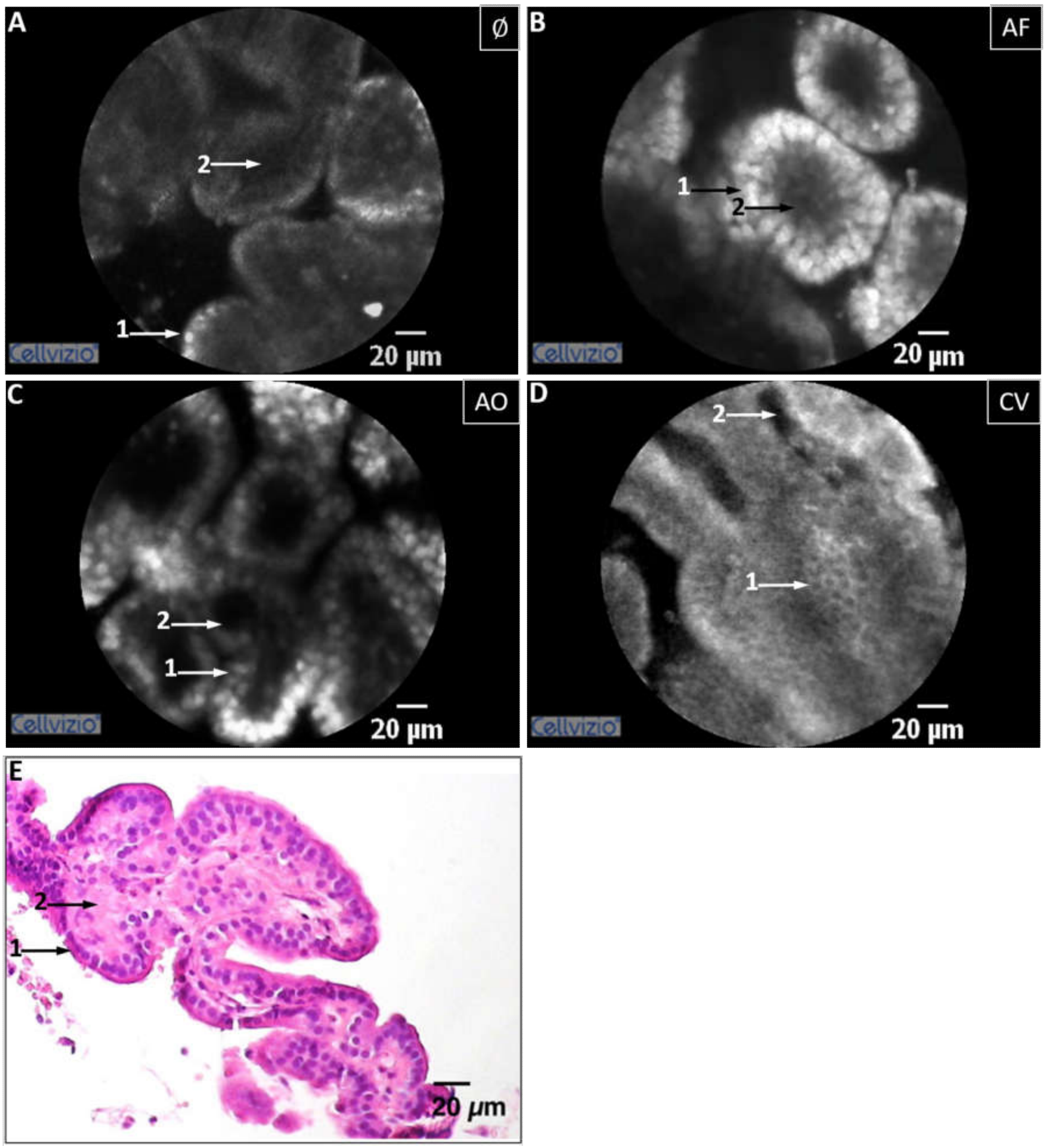

Figure 3.20: Analysis of choroid plexus papilloma. CLSM imaging showed natively (A) and after staining with AF (B), AO (C), and CV (D) a flatly arranged layer of neoplastic cells (1→) surrounding the fibrovascular cores (2→). An excellent correlation to the image obtained using H&E staining was found (E). Bars = 20 µm. *CLSM, confocal laser scanning microscopy; AF, acriflavine hydrochloride; AO, acridine orange; CV, cresyl violet; H&E, hematoxylin and eosin.*

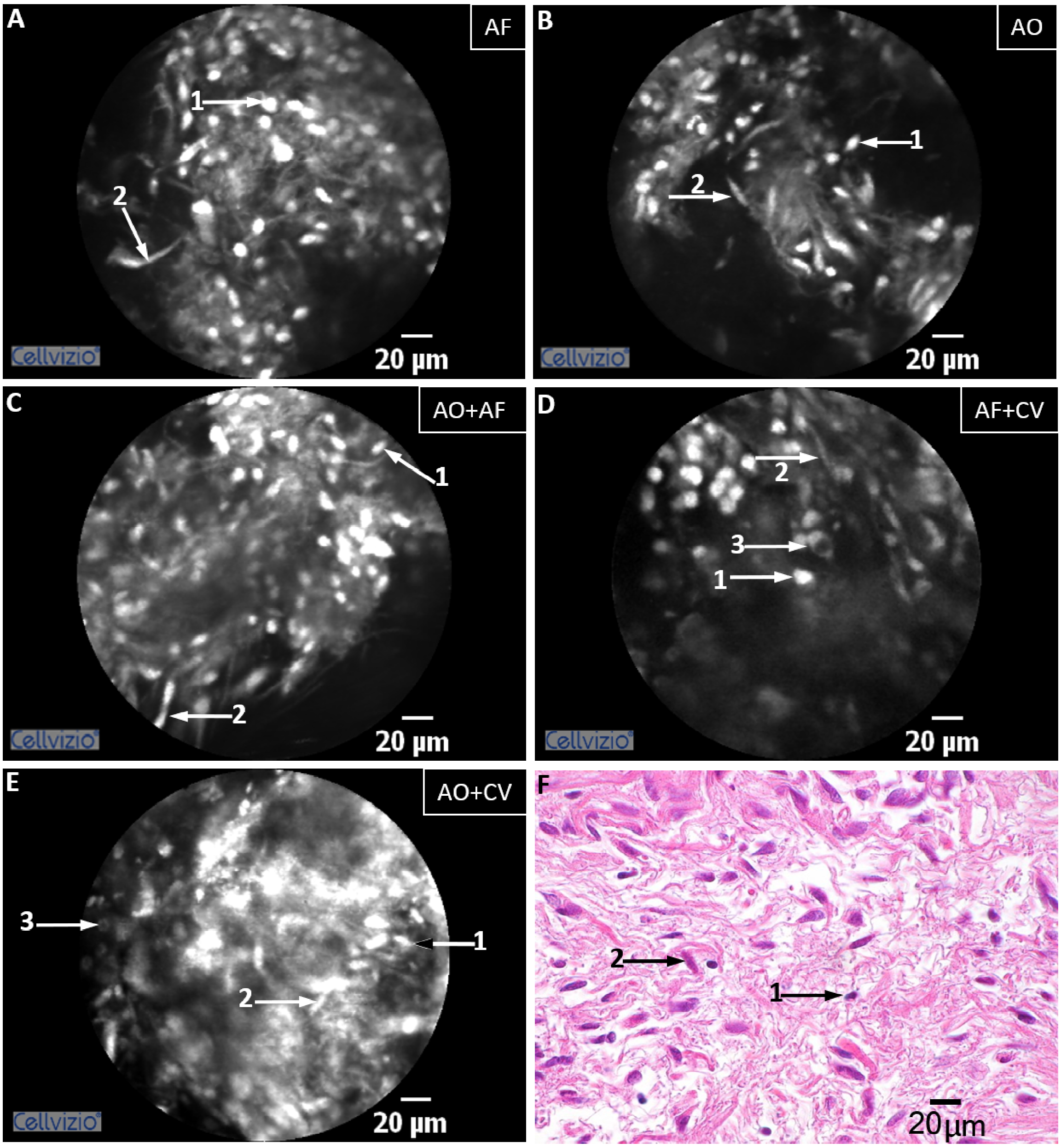

Figure 3.21: Analyses of pilocytic astrocytoma with different fluorophore combinations. The tumor was stained alone with AF (A) and AO (B), with AO and AF simultaneously (C), with AF and CV simultaneously (D), with AO and CV simultaneously (E), and with H&E (F). Cell nuclei were observed as bright spots in all CLSM images (A-E 1→). However, not all cell nuclei were stained by AO or by AF, as shown in the images D and E, in which only the cytoplasm was stained by CV in some cells (3→). Rosenthal fibers (2→), a specific feature of pilocytic astrocytomas, were observed after all staining combinations, corresponding with the H&E stained findings (F). Bars = 20 µm. *AF, acriflavine hydrochloride; AO, acridine orange; CV, cresyl violet; CLSM, confocal laser scanning microscopy; H&E, hematoxylin and eosin.*

3.2.4 Investigation of the food dyes

The food additives allura red AC, erythrosine, canthaxanthen, ponceau SX, and rubixanthin were investigated to examine tumor samples of the CNS, using CLSM. Of these, allura red AC, canthaxanthen, ponceau SX, and rubixanthin showed either no fluorescence or not enough to identify tissue features (data not shown). Erythrosine was the only tested food dye allowing tissue enhancement with CLSM.

- **Investigation on fibroblast cells**

First, the uptake of erythrosine in living fibroblast cells was demonstrated by a bench-top fluorescence microscope with blue laser illumination (Fig. 3.22). The uptake was analyzed after an incubation time of 0, 1, 5, 10, 30, 60, and 300 min as well as overnight. The results shown in Figure 3.22 illustrate the accumulation of erythrosine after 1 min, 300 min, and overnight, as there were no relevant differences between these incubation times. Topical administration of erythrosine readily stained the cytoplasm. The fluorescence intensity decreased after an incubation overnight (Fig. 3.22).

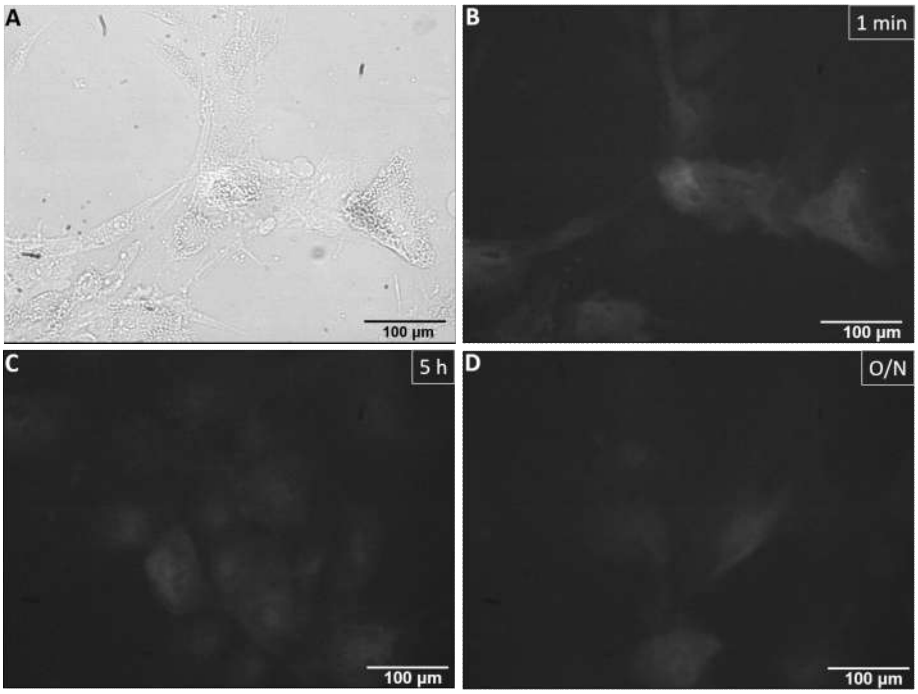

Figure 3.22: Erythrosine accumulation in fibroblast cells. Fibroblast cells were visualized by light microscopy (A) and by bench-top fluorescence microscopy with blue laser illumination (B–D). The accumulation of erythrosine after 1 min (B), 300 min (C), and overnight (O/N; D) are presented. Bars = 100 µm.

- **Investigation on WHO grade I meningioma**

Second, the most suitable concentration and incubation time of the food dye for the observations with the CLSM system were determined (Fig. 3.23). Therefore, different concentrations (0.5, 1.0, and 2.0 mg/mL) of erythrosine with different incubation times (1, 5, and 10 min) were investigated on a fresh WHO grade I meningioma sample. The used concentrations and resulting fluorescence intensity compared to the other contrast agents are presented in Table 3.1.

Psammoma bodies were clearly observed as round and anuclear structures, but other tumor features were hard to detect. Best resolution of the tumor tissue was acquired at a concentration of 1.0 mg/mL and an incubation time between 1 and 5 min, although there were no big differences to the other concentrations at the same incubation time (Fig. 3.23).

- **Investigation on further primary CNS tumors**

Third, the best parameters (1 min incubation with 1.0 mg/mL erythrosine) were then used to investigate erythrosine in staining further primary CNS tumors. In total, 20 samples of the CNS (5 glioblastomas, 5 oligodendrogliomas, 5 epidermoid tumors, and 5 schwannomas) were examined *ex vivo* after topical application of erythrosine under CLSM-488 nm. Representative images of each of the examined entities are presented in Figure 3.24.

CLSM imaging of erythrosine revealed immediately cytoplasm staining, showing the cell nuclei as small black dots as demonstrated in the **glioblastoma** sample. Here, erythrosine also showed staining of the abnormal blood vessel lumen (Fig. 3.24), but no clear tumor diagnosis could be made. CLSM real-time imaging of erythrosine-labeled **oligodendrogliomas** allowed visualization of the typical round and uniform nuclei, but more blurred than in the H&E stained section (Fig. 3.24). CLSM of **epidermoid tumors** revealed the anuclear crystal-like structures of the "cell ghosts", which were detached on the H&E stained section (Fig. 3.24). In the examination of **schwannomas**, areas with compact Schwann cells ("Antoni A" areas) and areas with looser stroma and fewer cells ("Antoni B areas") were hard to identify by CLSM, which again did not allow a clear diagnosis (Fig. 3.24). Altogether, erythrosine did not provide clear images, and important tumor features, such as mitoses and pleomorphism, could not be identified.

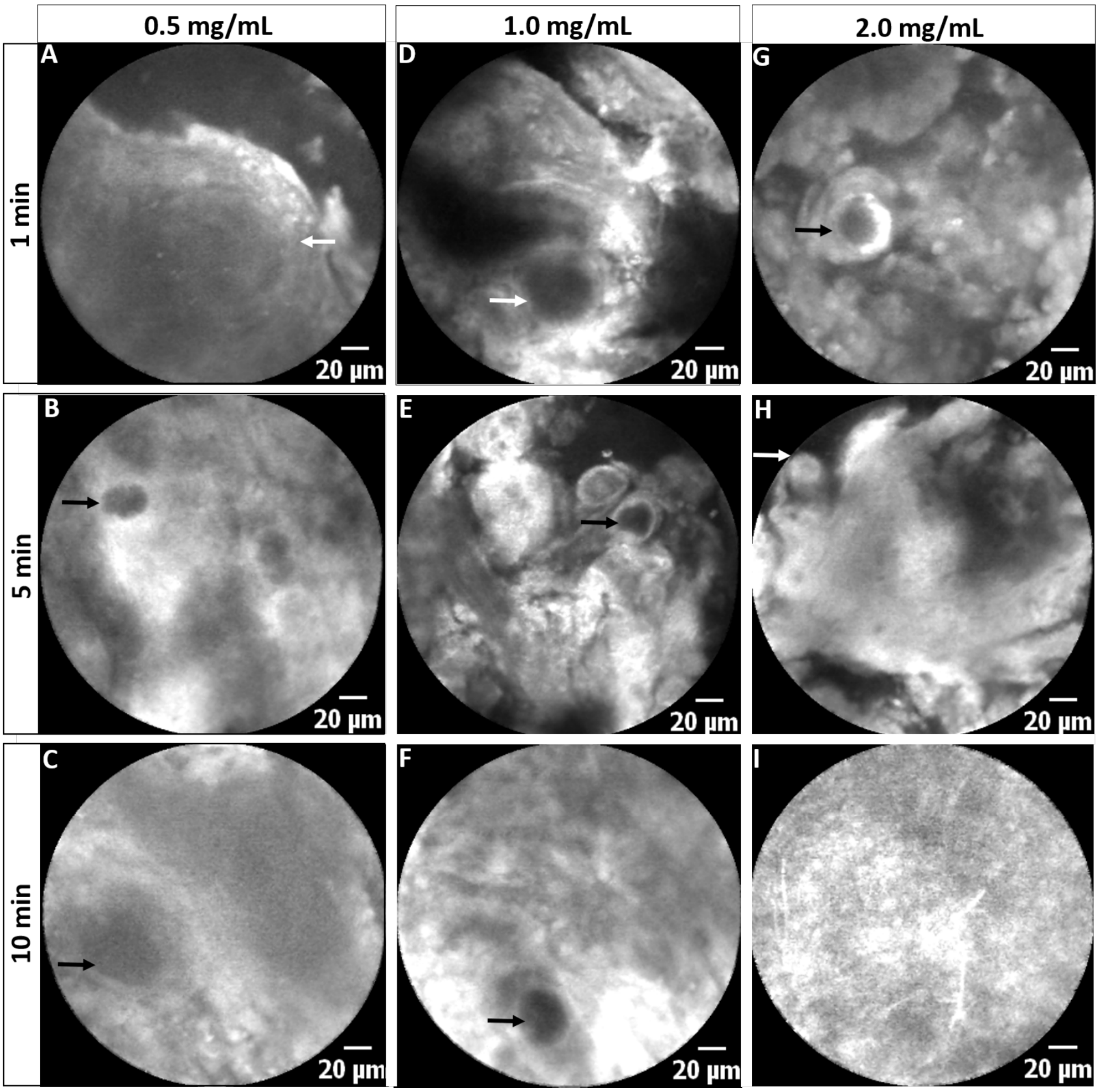

Figure 3.23: Investigation of erythrosine in tumor staining. WHO grade I meningioma specimens were stained with 0.5 mg/mL, 1.0 mg/mL, and 2.0 mg/mL erythrosine for 1, 5, and 10 min, respectively. Topical application of erythrosine enabled the visualization of psammoma bodies (→) at all concentrations, whereas cellular features were not clearly visible using CLSM. Best resolution of the tumor tissue was acquired at a concentration of 1.0 mg/mL and an incubation time between 1 and 5 min (D, E), although there were no big differences to the other concentrations at the same incubation time (A, B, G, H). After an incubation time of 10 min the background fluorescence was too bright (C, F, I) to distinguish any tissue features, especially at the highest concentration (I). Bars = 20 µm. *WHO, World Health Organization; CLSM, confocal laser scanning microscopy.*

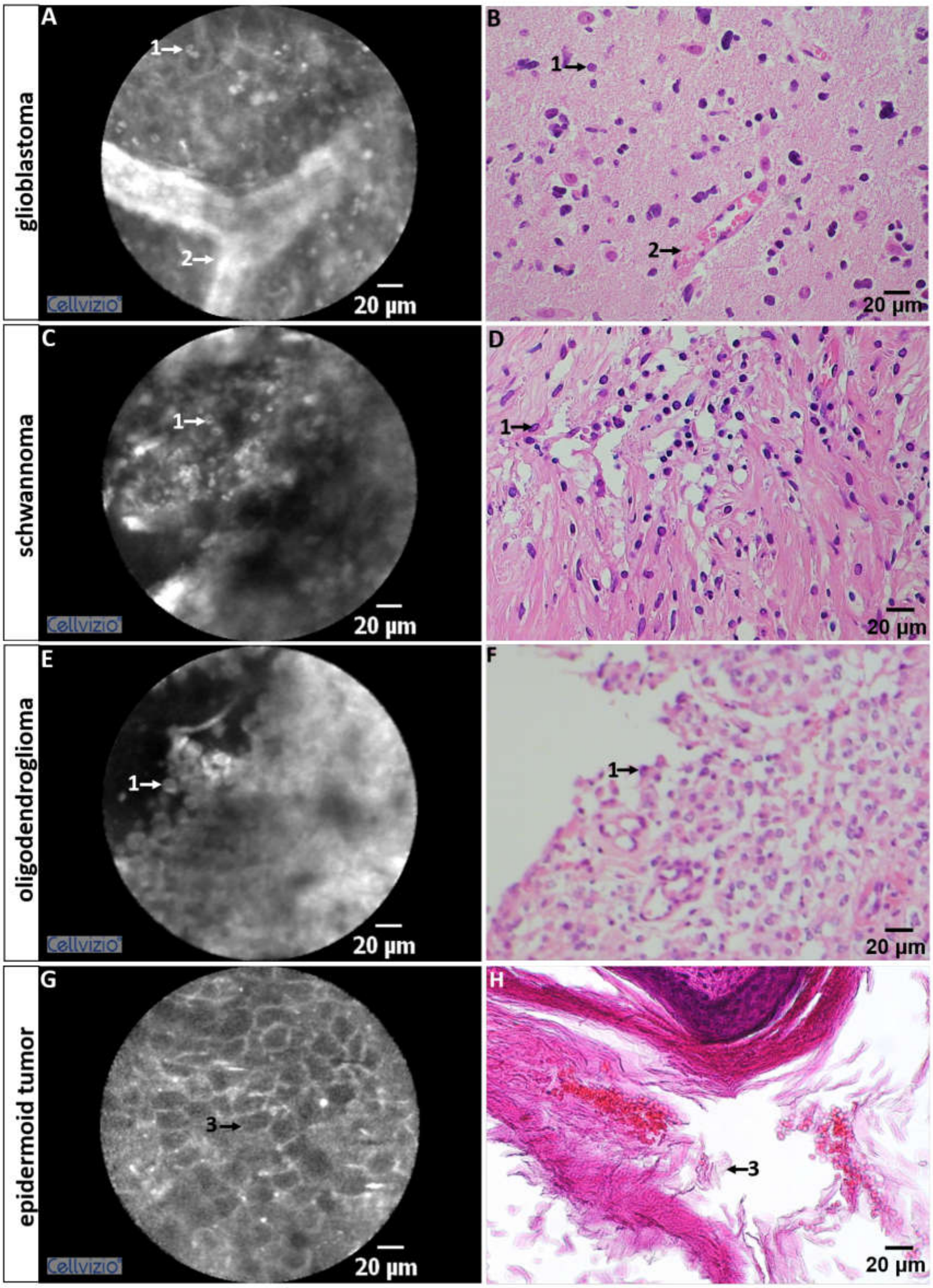

Figure 3.24: Investigation of erythrosine in CNS tumor staining compared to H&E. CLSM imaging of a glioblastoma sample showed nuclei of different size mimicking the histopathological findings (A, B 1→). Erythrosine also stained the lumen of the blood vessels (A 2→). Examination of schwannoma revealed medium-sized cells (E, F 1→), but "Antoni A" and "Antoni B" areas were hard to define. CLSM analysis of oligodendroglioma revealed round and uniform nuclei (E 1→), resembling the findings in histology (F 1→). CLSM imaging of an epidermoid tumor demonstrated the anuclear crystal-like structure of "cell ghosts" (G 3→), which were detached in the H&E stained section (H 3→). Bars = 20 µm. *CNS; central nervous system; H&E, hematoxylin and eosin; CLSM, confocal laser scanning microscopy.*

Table 3.1: Fluorophores and their fluorescence intensity.

Fluorophore	**Concentration**	**Cell permeability**	**Fluorescence intensity**
5-aminolevulinic acid	200 mg/kg	yes	-
Acridine orange	0.01 mg/mL	yes	+++
Acriflavine	0.01 mg/mL	yes	+++
Allura red AC	0.01–5 mg/mL	yes	-
Canthaxanthen	0.01–5 mg/mL	not visible	-
Cresyl violet	0.02 mg/mL	yes	+
Erythrosine	0.5 mg/mL	yes	+
Erythrosine	1.0 mg/mL	yes	+
Erythrosine	2.0 mg/mL	yes	++++
Fluorescein	0.01 mg/mL	no	++
Indocyanine green	0.5 mg/ml	yes	+++
Rubixanthin	0.01–5 mg/mL	not visible	-
Ponceau SX	0.01–5 mg/mL	not visible	-

*+ = poor; ++ = good; +++ = excellent; ++++ = too high; - = no signal

3.2.5 Investigation of CLSM in the diagnosis of primary CNS tumors

- **This section is based on the published paper:**

Daali, S., Javed, M., Altekoester, A.-K., Alhadi, I., Linxweiler, M., Bostelmann, R., Schlegel, J. & Charalampaki, P. (2016) Analysis of 258 Different Lesions of the Central Nervous System for Real Time Histological Diagnosis Using Confocal Laser Endomicroscopy. J Mult Scler (Foster City).

- **Only selected and independently made parts of the published paper are presented.**

The WHO grading scheme (Zülch, 1979; Louis et al., 2007; Louis et al., 2016) was used to interpret CLSM images of various CNS samples (n = 258). AF was applied to enhance tissue contrast because it had yielded the most detailed histopathological information in the previous work (see subsection 3.2.3). Only representative images are shown below. Tissue features obtained with CLSM are summarized and compared to the H&E stained findings in Table 3.2.

Non-neoplastic tissue

Non-neoplastic human tissues (n = 4) adjacent to tumor samples were also examined with CLSM and compared to traditional histology. Similarly to the H&E stained findings, cells with large nuclei, depicting neurons; cells with a small round shape, representing oligodendroglia cells; and cells with a round-to-oval nucleus with open chromatin and peripheral nucleoli, representing astrocytes, were identified (Fig. 3.25).

Neuroepithelial tumors

Glioblastoma: In total, 79 glioblastomas were examined using CLSM. Areas with high cell density and presence of necrosis were found in almost all samples via CLSM and H&E staining (Fig. 3.26 A, B). Necrosis was detected both with and without pseudopalisading, demonstrated as an accumulations of neoplastic cells around the central area of necrosis. Vascular proliferation was increased, but it was difficult to differentiate between glomeruloid and endothelial proliferation with CLSM. Additionally, anaplasia, pleomorphism, anisokaryosis were found in most samples. All examined glioblastomas showed an increased nuclear-to-cytoplasmic ratio. The cells were mainly spindle-shaped and the nuclei oval or elongated. In several nuclei, multiple nucleoli were visible (Fig. 3.26 A, B).

Oligodendroglioma: In total, 8 oligodendrogliomas were examined by CLSM and traditional histology. Characteristic features of WHO grade II oligodendrogliomas observable in all the samples were the round, monomorphic nuclei, corresponding to their traditional histology (Fig. 3.26 C, D). The cell density was very low. Microcysts were prominent in some of the examined oligodendrogliomas.

Three WHO grade III oligodendrogliomas were examined. In contrast to WHO grade II oligodendrogliomas, this tumor type had a higher cellular density and atypia, but also with a monomorphic cell distribution and round nuclei. Vascular proliferation was visible in all three samples, using CLSM. Mitoses were hard to detect with CLSM.

Ependymoma: In total, 7 ependymomas (WHO grade II) were examined using CLSM and traditional histology. In the CLSM images, perivascular pseudorosettes were identified in transversal and in longitudinal orientation, whereas in traditional histology, only the transversal orientation was visible (Fig. 3.26 E, F). Furthermore, a moderate cell density and small oval nuclei were found in the most samples. Microvascular proliferation and necrosis were detected on some CLSM images, also corresponding with the findings in histology.

Choroid plexus papilloma: Three choroid plexus papillomas were examined with CLSM and compared to traditional histology. CLSM images and H&E stained sections showed villous structures with an ordered flat layer of atypical ependymal cells surrounding the fibrovascular cores (Fig. 3.26 G, H). The epithelium and the irregular papillae of the tumor were immediately observed after AF staining with CLSM.

Cranial and paraspinal nerve tumors

Schwannoma: In total, 20 schwannomas were analyzed. CLSM imaging illustrated exclusively spindle-shaped Schwann cells corresponding with their traditional histology (Fig. 3.27 A, B). Furthermore, "Antoni A" areas with ordered, compact Schwann cells and Verocay bodies (anuclear zones between nuclear palisades), and "Antoni B" areas with a looser stroma and fewer cells were detected in some of the samples using CLSM. Only in the H&E stained sections were whorls found (Fig. 3.27 B).

Neurofibroma: Two neurofibromas were examined with CLSM and traditional histology. In both modalities, the tumor showed a medium cell density. The Schwann cells were characterized by elongated, curved nuclei without prominent nucleoli (Fig. 3.27 C, D).

Tumors of the sella region

Pituitary adenoma: In total, 19 pituitary adenomas were examined by CLSM and traditional histology. Typical characteristics of all samples were a monomorphic cell pattern and dense, round-to-ovoid nuclei (Fig. 3.28). Furthermore, a high cell density was observed in all samples. In one sample, cells arranged in clumps surrounded by a cell-free layer were found, which is unusual for this tumor type (Fig. 3.28).

Tumors of the meninges

WHO grade I meningioma

In total, 125 meningiomas of which 101 were WHO grade I, were analyzed using CLSM. The examination revealed histopathological features confirming the results on H&E stained sections. With CLSM, it was also possible to differentiate between the following different meningioma subtypes:

Psammomatous: Prominent psammoma bodies of different sizes were detected in all 14 psammomatous meningiomas (Fig. 3.29 A, B). In CLSM, psammoma bodies were observed as round, anuclear structures. Calcium deposits could be observed in only a few psammoma bodies, whereas in histology, calcifications could be found in almost all psammoma bodies (Fig. 3.29 A, B).

Meningothelial: In total, 62 meningothelial meningiomas were examined by CLSM and traditional histology. It was the most common subtype, characterized by whorls and syncytia of neoplastic cells. Psammoma bodies were occasionally detected. The cell nuclei were round or oval and had some nuclear pseudoinclusions (Fig. 3.29 C, D).

Transitional: In total, 6 transitional meningiomas were examined by CLSM and traditional histology. This subtype was characterized by prominent whorls and syncytial neoplastic cells. Psammoma bodies were also found in all examined samples on both image modalities (Fig. 3.29 E, F).

Angiomatous: In total, 7 angiomatous meningiomas were examined. This subtype was characterized by high vascularity which exceeded 50% of the total tumor area. Especially large vessels were found with CLSM and H&E staining on the samples. High cell density without mitotic activity was also a common feature found in this subtype

(Fig. 3.30 A, B).

Fibrous: In total, 12 fibrous meningiomas were examined by CLSM and traditional histology. This subtype was characterized by linear stromal calcifications and collagen content. The neoplastic cells were spindle-shaped with indistinct cell boundaries, as shown in CLSM and traditional histology (Fig. 3.30 C, D).

WHO grade II meningioma

Compared to WHO grade I meningiomas, WHO grade II meningiomas showed a high cellular density and increased nuclear-to-cytoplasmic ratio. No psammoma bodies were found (Fig. 3.31).

Atypical: In total, 16 atypical meningiomas were examined by CLSM and traditional histology. This subtype was characterized by a high cell density and some prominent nucleoli. The nuclear-to-cytoplasmic ratio was increased (Fig. 3.31 A, B).

Chordoid: In total, 8 chordoid meningiomas were examined by CLSM and traditional histology. Both approaches revealed meningothelial cells of medium size arranged in cords with a myxoid background. Some mitoses were detected in traditional histology but not in CLSM (Fig. 3.31 C, D).

Cavernoma

Five cavernomas were examined using CLSM and traditional histology. Medium cell density and pleomorphism around a malformed blood vessel were identified in CLSM (Fig. 3.32). The blood vessels were tightly juxtaposed. On the H&E stained section, abnormal blood vessels that had been hyalinized were visible. Due to a bruise of the H&E section, the blood vessels were blurred (Fig. 3.32).

Cysts and tumor-like lesions

Epidermoid tumor: In total, four epidermoid tumors were examined by CLSM and traditional histology. Histopathological analyses of epidermoid tumor specimens revealed mature epidermal cells with distinct granular layer. The epidermoid cyst's stratum corneum is excellently shown in both image modalities (Fig. 3.33). CLSM imaging showed a very bright granular layer of the epithelium due to the high content of stained nuclei by AF. H&E staining also allowed visualization of dystrophic calcification. The anuclear cell ghosts are visualized as crystal-like structures on the CLSM images, while they are detached on the H&E stained section (Fig. 3.33).

Tumors of the hematopoetic system

Plasmacytoma: In total, seven plasmacytomas were examined by CLSM and traditional histology. CLSM imaging revealed in four of the specimens, large round indefinable structures. In contrast, H&E staining revealed only normal sized atypical plasma cells with a high cell density (Fig. 3.34).

Statistical analysis

"Representative endomicroscopic images from $n = 258$ different human tissues were evaluated by four different participants (two surgeons and two neuropathologists) and accuracy was calculated. Astrocytic tumors WHO grades I-III (75%), glioblastomas (100%), ependymomas (75%), epidermoid tumors (50%), schwannomas (100%), meningiomas (100%), brain metastases from lung carcinoma (100%), brain metastases from rectum carcinoma (100%), choroid plexus papillomas (100%), pituitary adenomas (75%), neurofibromas (100%) were diagnosed with high accuracy. Overall correct detection rate was 88.64%." (Daali et al., 2016).

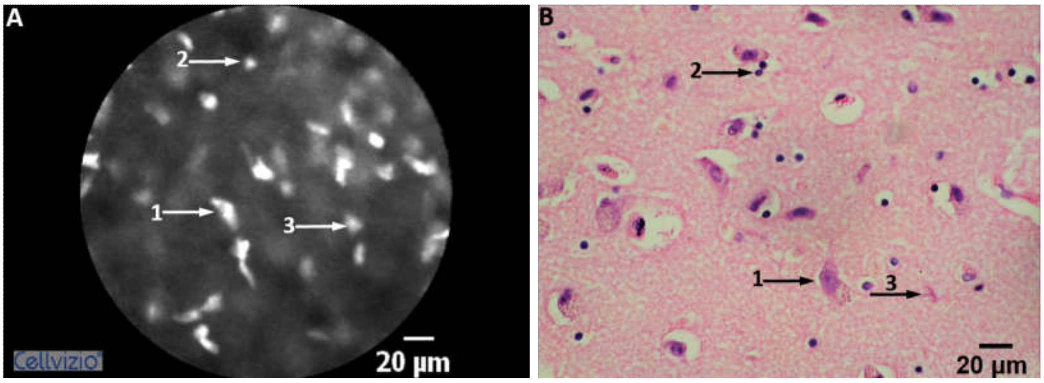

Figure 3.25: CLSM and histopathological examination of healthy cortex tissue. CLSM imaging of healthy human brain tissue with AF revealed neurons (1→), oligodendroglia cells (2→), and astrocytes (3→), mimicking the corresponding histopathological findings (B). Bars = 20 µm. *CLSM, confocal laser scanning microscopy; AF, acriflavine hydrochloride.*

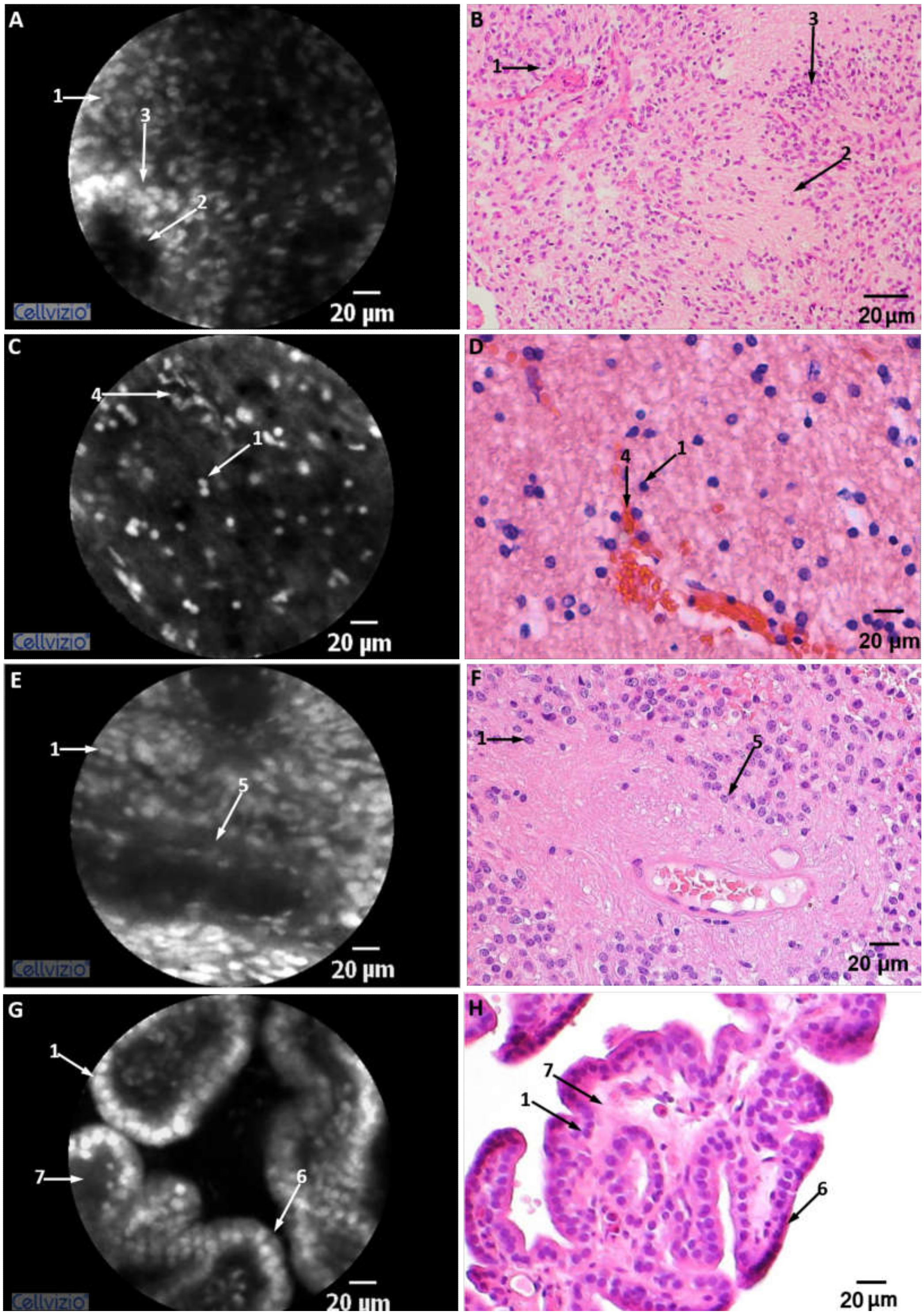

Figure 3.26: CLSM and histopathological examination of neuroepithelial tumors [modified from (Daali et al., 2016)]. Glioblastoma (A, B): Analysis revealed high cell density of neoplastic tumor cells (1→) and necrosis (2→) surrounded by pseudopalisading (3→). WHO grade II oligodendroglioma (C, D): Round uniform nuclei (1→) were typical characteristics of this tumor. The cell density was low. Vascular proliferation was also observed (4→). WHO grade II ependymoma (E, F): CLSM (E) and traditional histology (F) revealed small oval nuclei (1→) and perivascular pseudorosettes (5→). Choroid plexus papilloma (G, H): CLSM (G) obtained villous structures with an ordered flat layer of neoplastic cells (6→) surrounding the fibrovascular cores (7→), mimicking the histopathological findings (H). Bars = 20 µm. *CLSM, confocal laser scanning microscopy; WHO, world health organisation.*

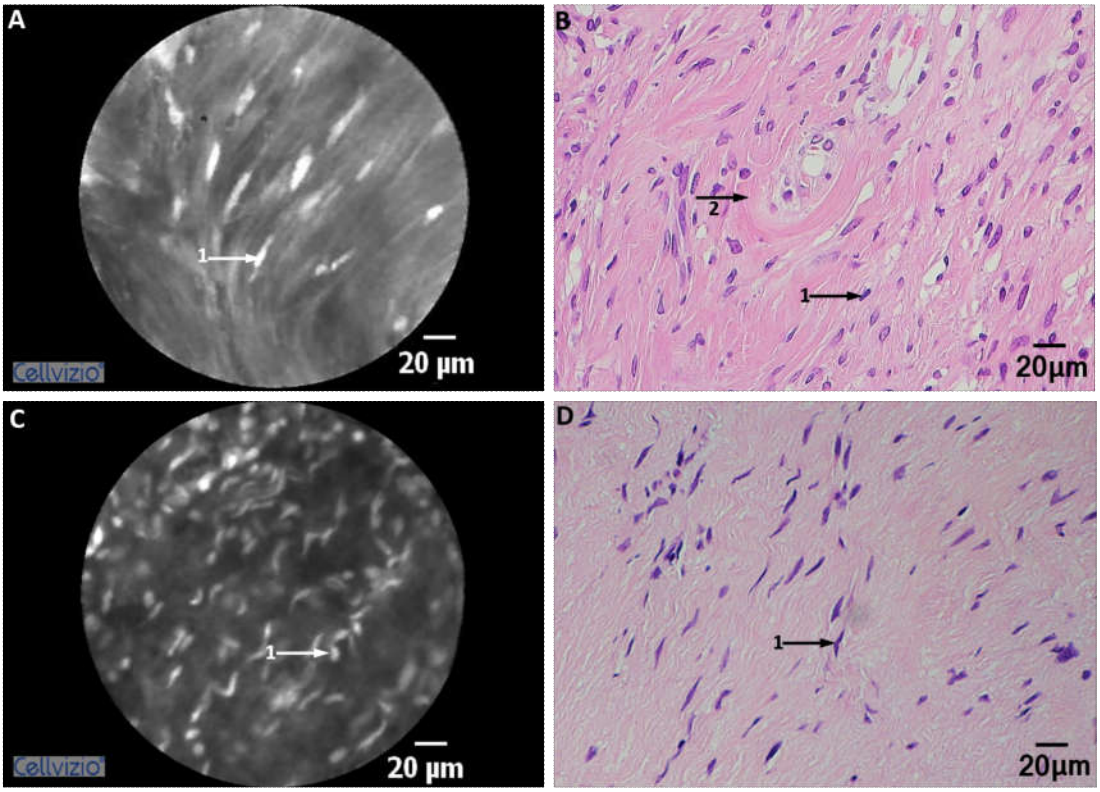

Figure 3.27: CLSM and histopathological examination of cranial and paraspinal nerve tumors [modified from (Daali et al., 2016)]. Schwannoma (A, B): "Antoni A" areas were characterized by a dense accumulation of spindle Schwann cells (1→) after staining with AF (A) and H&E (B). Whorls were found in the H&E stained section (B 2→). Neurofibroma (C, D): Examination of neurofibroma showed elongated, curved nuclei (1→) without prominent nucleoli. Bars = 20 µm. *CLSM, confocal laser scanning microscopy; AF, acriflavine hydrochloride; H&E, hematoxylin and eosin.*

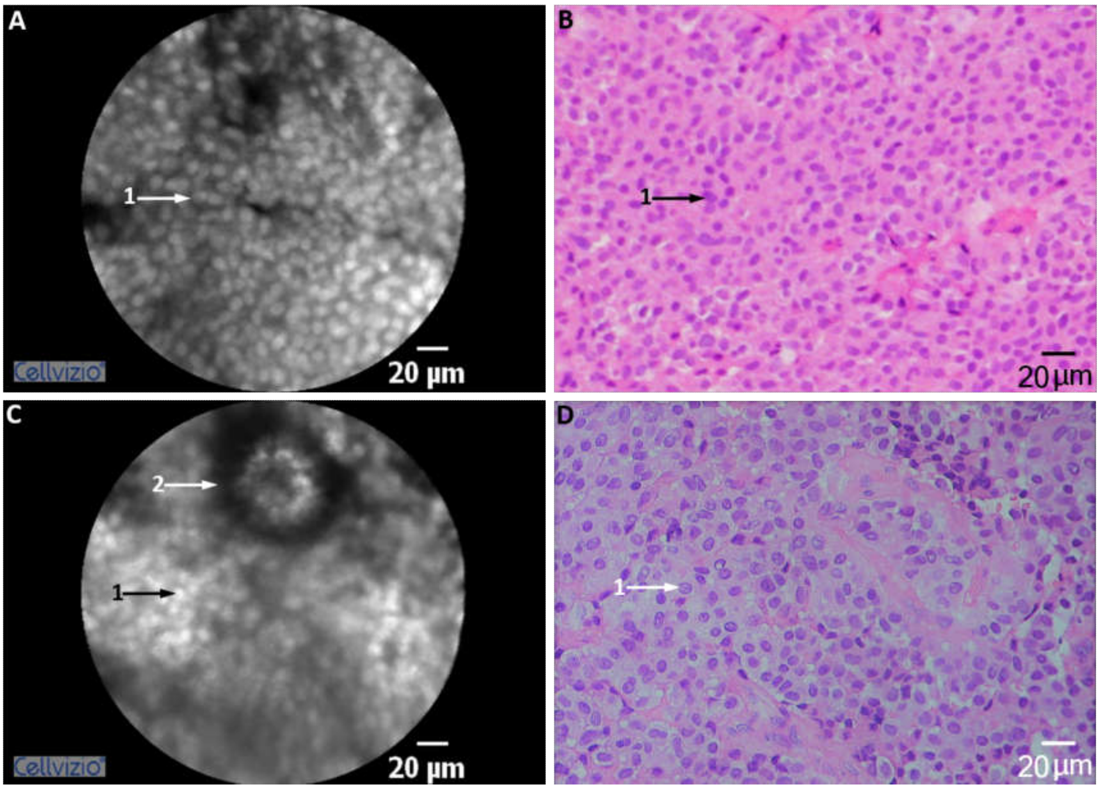

Figure 3.28: CLSM and histopathological examination of pituitary adenomas [modified from (Daali et al., 2016)]. The pituitary adenoma specimen showed high cell density with a monomorphic cellular appearance on both image modalities (A, B, D, D) but with a lower quality on the CLSM image (C). The nuclei were round to ovoid (1→). Cells arranged in clumps surrounded by a cell-free layer were also observed in one sample (C 2→). The macronodular pattern of the adenoma is unusual. Bars = 20 µm. *CLSM, confocal laser scanning microscopy.*

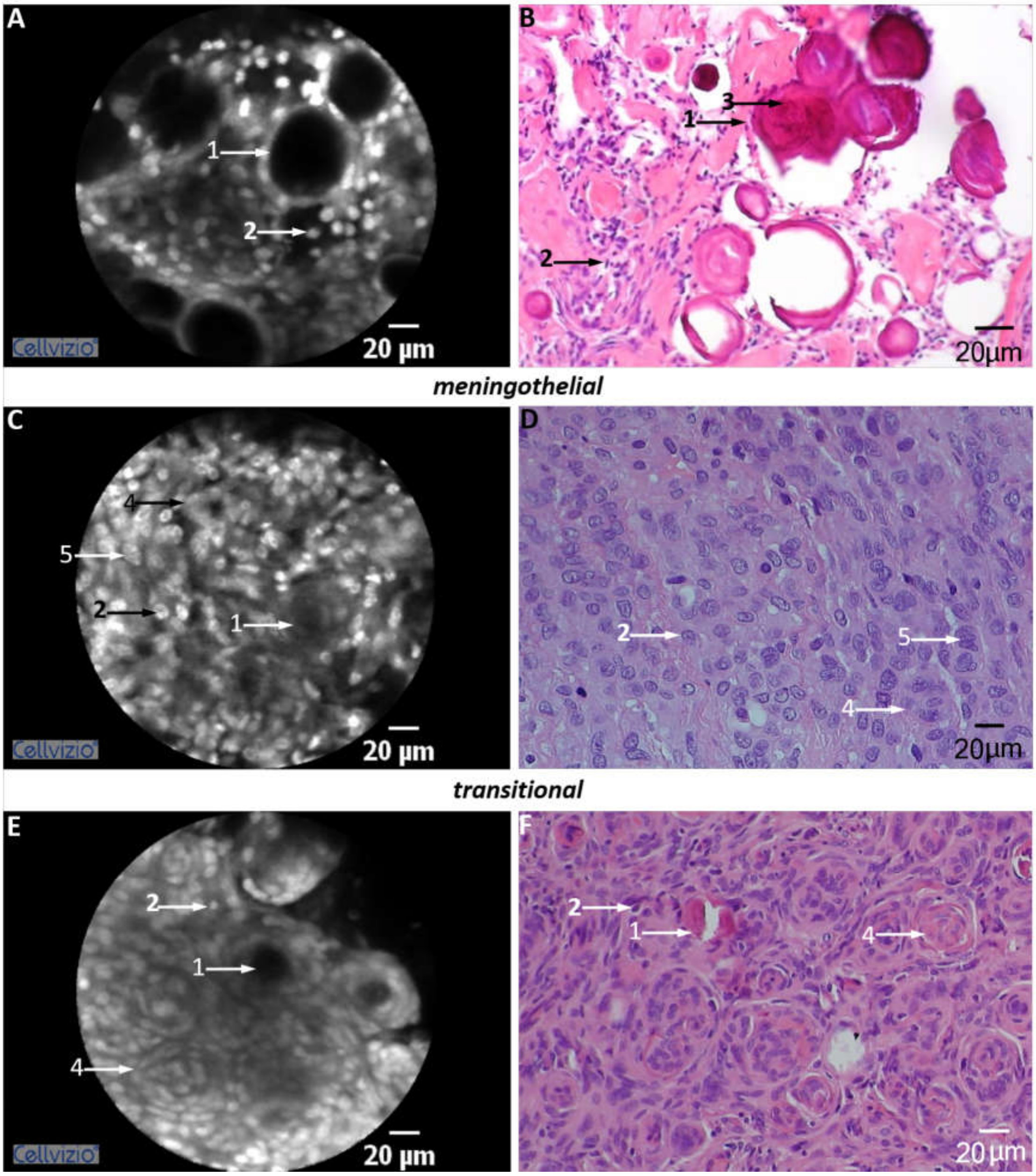

Figure 3.29: CLSM and histopathological examination of WHO grade I meningioma subtypes [modified from (Daali et al., 2016)]. Psammomatous (A, B): Both CLSM (A) and histology (B) showed prominent psammoma bodies of different sizes (1→). On the CLSM image, psammoma bodies were visible as round, anuclear structures (A 1→), whereas in histology, calcium deposits (B 3→) were found in almost all psammoma bodies (1→). Meningothelial (C, D): Whorls (4→) and syncytia of neoplastic cells (5→) were visible in CLSM (C) and histology (D). The uniform cell nuclei (2→) were round or oval. Transitional (E, F): Prominent whorls (4→) and high cell density (2→) without mitotic activity were detected in both image modalities. Psammoma bodies were also frequently detected (1→). Bars = 20 µm. *CLSM, confocal laser scanning microscopy; WHO, World Health Organization.*

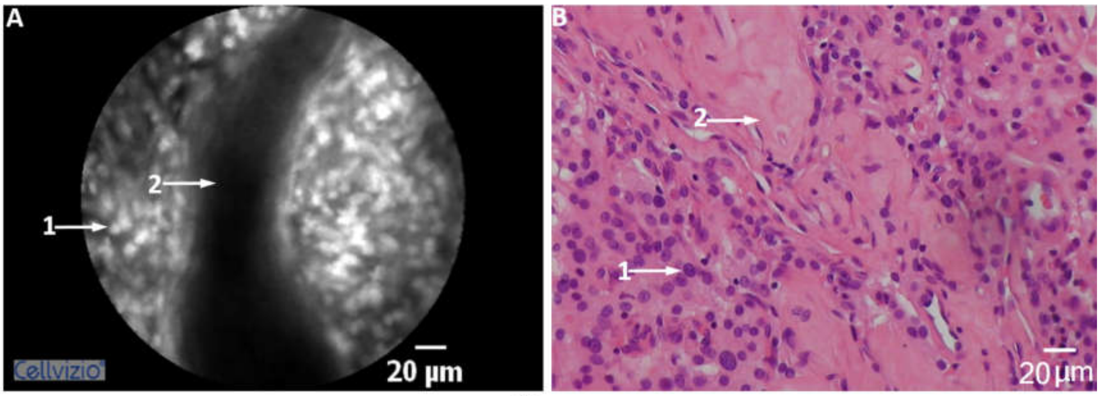

fibrous

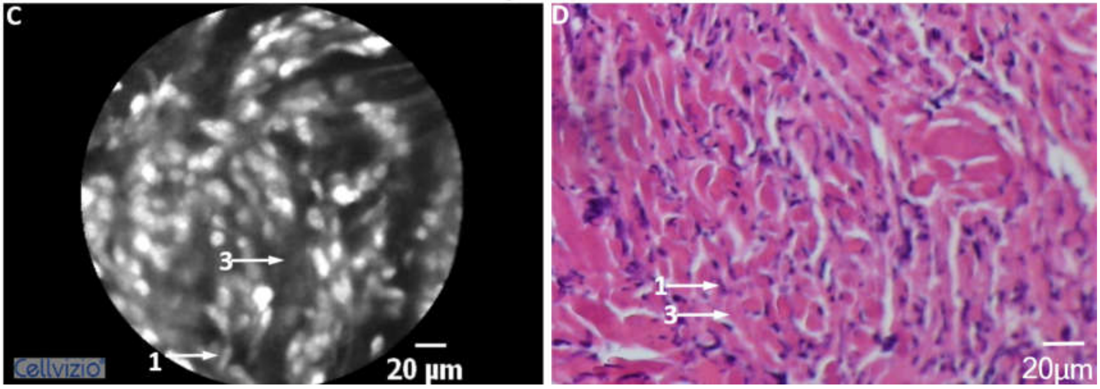

Figure 3.30: CLSM and histopathological examination of WHO grade I meningioma subtypes. Angiomatous (A, B): High cell density (1→) and large blood vessels (2→) were detected in both image modalities. Fibrous (C, D): CLSM (C) and histology (D) revealed high cell density aligned in streams. The cells were spindle-shaped (1→) and several linear stromal calcifications were visible (3→). Bars = 20 µm *CLSM, confocal laser scanning microscopy; WHO, World Health Organization.*

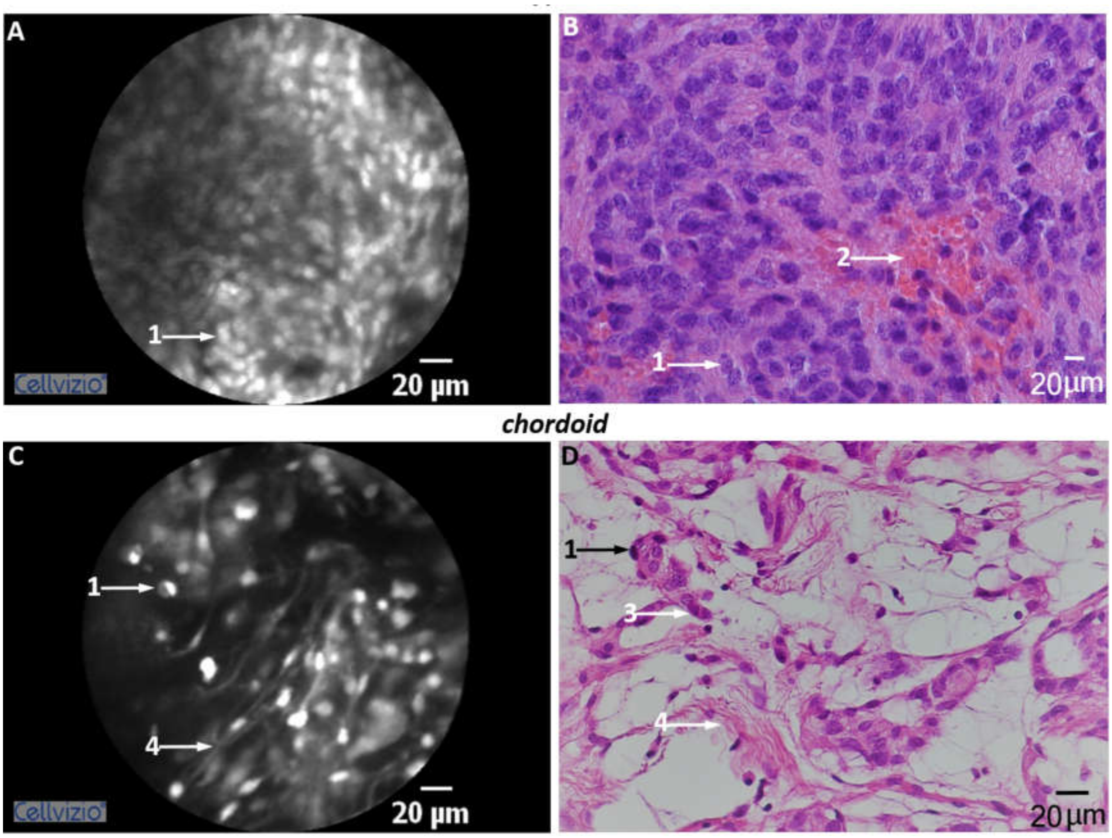

Figure 3.31: CLSM and histopathological examination of WHO grade II meningioma subtypes. Atypical (A, B): CLSM (A) and histology (B), showing high cell density (1→). In histology, some hemorrhages (B 2→) were stained. Chordoid (C, D): CLSM (C) and histology (D) revealed meningothelial cells of medium size (1→) arranged in cords with a myxoid background (4→). Some mitoses were detected in histology (D 3→). Bars = 20 µm. *CLSM, confocal laser scanning microscopy; WHO, World Health Organization.*

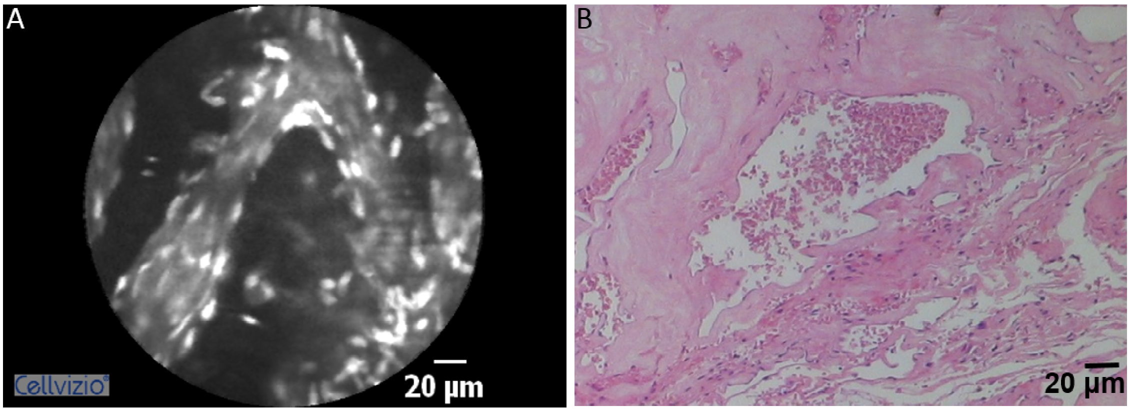

Figure 3.32: CLSM and histopathological examination of a cavernoma. CLSM imaging revealed a medium cell density as well as pleomorphism around a malformed blood vessel after AF staining (A). On histology, blurred convolute blood vessels are visible (B). Bars = 20 µm. *CLSM, confocal laser scanning microscopy; AF, acriflavine hydrochloride.*

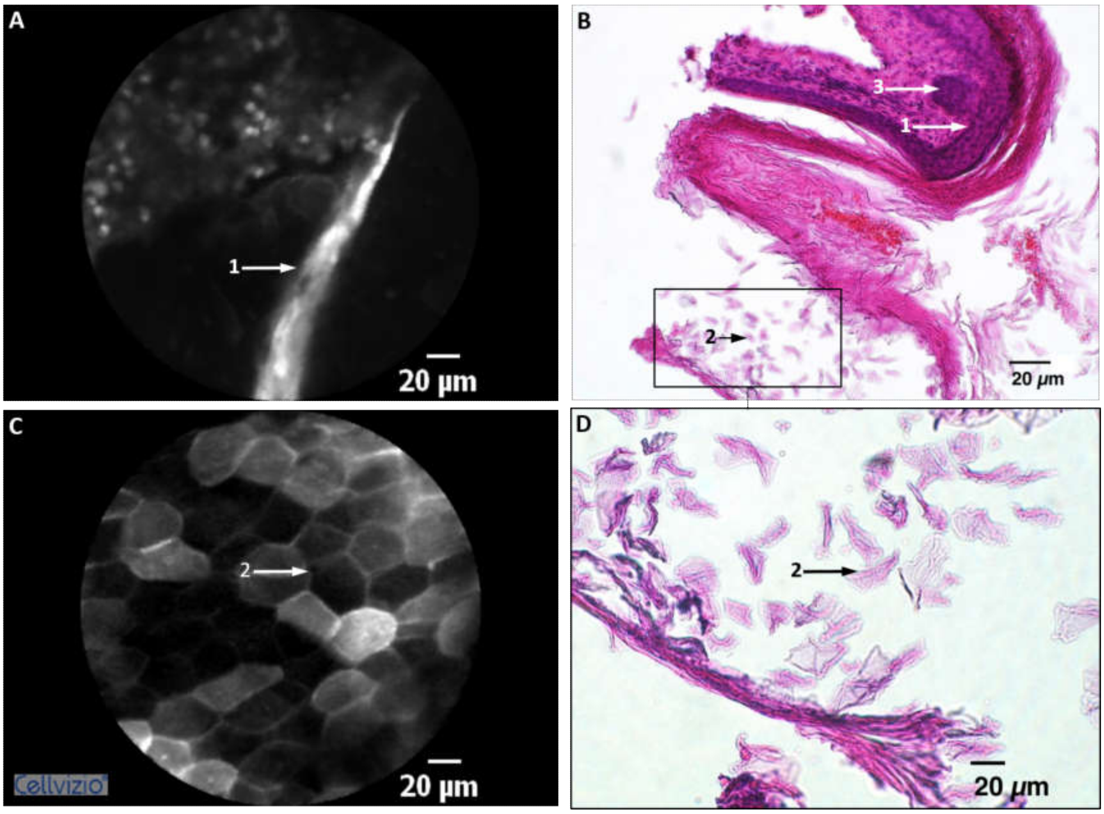

Figure 3.33: CLSM and histopathological examination of an epidermoid tumor [modified from (Daali et al., 2016)]. The stratum corneum was obtained by CLSM (A) and histology (B). The granular layer of the epithelium was very bright due to the high content of stained nuclei by AF (A 1→). In histology, dystrophic calcification is visible (B 3→). On the CLSM image, the crystal-like structure of anuclear squamous cells is shown (C 2→), while in the H&E stained section the "cell ghosts" were detached from the epithelium (B, D 2→). Bars = 20 µm. *CLSM, confocal laser scanning microscopy; AF, acriflavine hydrochloride; H&E, hematoxylin and eosin.*

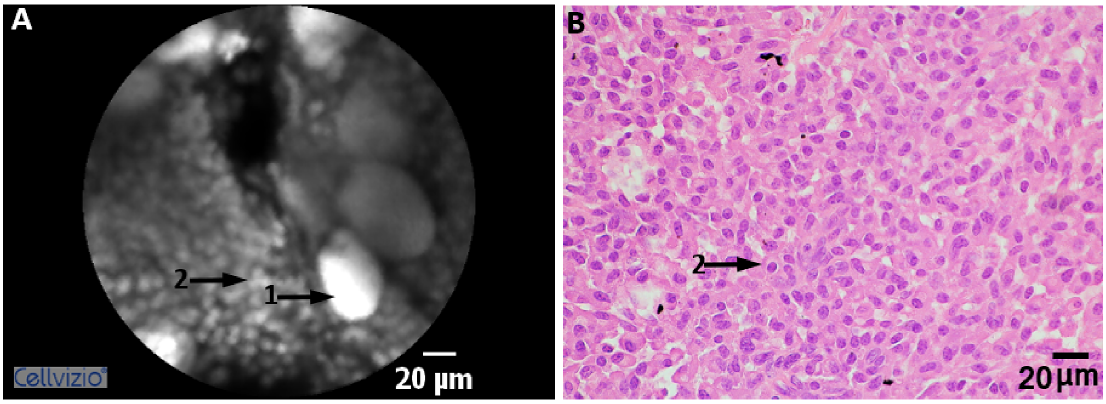

Figure 3.34: CLSM and histopathological examination of a plasmacytoma. After AF staining, large round structures were visible in CLSM (1→). On the H&E stained section (B), only the atypical plasma cells (2→) with a high cell density were observed. Bars = 20 µm. *CLSM, confocal laser scanning microscopy; AF, acriflavine hydrochloride; H&E, hematoxylin and eosin.*

Table 3.2: Comparison of cell features stained with AF and H&E (CLSM and traditional histology).

CNS lesion	Corresponding features	Only visible in CLSM	Only visible in histology
Non-neoplastic tissue	Clear cellular arrangement; nuclei of neurons, oligodendrocytes, and astrocytes	-	-
Pilocytic astrocytoma	Bipolar cells with elongated, hairlike processes arranged in bundles; Rosenthal fibers; cysts	-	-
Diffuse astrocytoma	Chiefly round, elongated cells; uneven cell distribution; vascular proliferation	-	-
Anaplastic astrocytoma	Increased cell density; diffusely distributed atypical cells; nuclear pleomorphism; mitoses; nuclei intercalations between axons; infiltration zones	-	-
Glioblastoma	High cell density; multinucleated cells; pleomorphic cells; increased nuclear-to-cytoplasm ratio; microvascular proliferation; necrosis; pseudopalisading	-	Mitoses
Choroid plexus papilloma	Villous structures; flat layer of increased ependymal cells	-	-
Ependymoma	Papillary tumor with perivascular pseudorosettes; low to medium cell density	Pseudorosettes in transversal and longitudinal orientation	Calcification

CNS lesion	**Corresponding features**	**Only visible in CLSM**	**Only visible in histology**
Oligoastrocytoma (WHO grade III)	High cell density; oval, uniformly shaped cells; nuclear pleomorphism	-	-
Oligodendroglioma (WHO grade II)	Low to medium cell density; round uniform nuclei	-	-
Oligodendroglioma (WHO grade III)	Higher cell density than in WHO grade II oligodendroglioma; round uniform nuclei	-	Mitoses
Neurofibroma	Low to medium cell density; spindle cells	-	Fibroblast cells; stromal mucin; collagen bundles; mast cells
Schwannoma	Compact Schwann cells; indistinct cytoplasm; "Antoni A": ordered cellular components; "Antoni B": looser stroma and fewer cells	-	Small necrosis; thick-walled blood vessels in "Antoni B" area
Cavernoma	High cell density; pleomorphism; high vascular malformations and spaces	-	-
Hemangioblastoma	Prominent pathological vasculature; nuclear pleomorphism; prominent nucleoli	-	-
Meningioma (WHO grade I)	psammoma bodies; whorls; syncytium	-	calcification in psammoma bodies

CNS lesion	**Corresponding features**	**Only visible in CLSM**	**Only visible in histology**
Meningioma (WHO grade II)	Increased cellular density and nuclear-to-cytoplasm ratio; no psammoma bodies	-	Fibrotic blood vessels; mitoses
Meningioma (WHO grade III)	-	Mitoses, anaplasia	
Plasmacytoma	Atypical plasma cells; high cell density	Large round structures	-
Pituitary adenoma	Monomorphic epithelial cells; dense, round-to-ovoid nuclei	Cells arranged in clumps surrounded by a cell-free layer	-
Epidermoid tumor	Mature keratinized squamous epithelium	-	-

CLSM, confocal laser scanning microscopy; AF, acriflavine hydrochloride; CNS, central nervous system; WHO, World Health Organisation.

3.2.6 Astrocytoma grading using CLSM and AF

Altogether, 29 astrocytic tumors were examined with CLSM after staining with AF, including 4 pilocytic astrocytomas (WHO grade I), 4 diffuse astrocytomas (WHO grade II), 9 anaplastic astrocytomas (WHO grade III), 2 anaplastic oligoastrocytomas (WHO grade III), and 10 glioblastomas (WHO grade IV). In the same ROI, traditional histology was performed as the gold standard. Representative images for each of the examined astrocytic tumors are presented in Figure 3.35.

In the CLSM images of **pilocytic astrocytomas**, bipolar cells with elongated, hair-like processes were visible, resembling the findings in traditional histology (Fig. 3.35 A, B). Moreover, thick, elongated bundles consistent with Rosenthal fibers were observed in both image modalities. A biphasic appearance with regions of loose cystic components and regions with compact cellular areas were also present. The nuclei were round and elongated. No mitotic figures or necrosis were found. Overall, a strong conformity to the H&E stained section was present (Fig. 3.35 A, B).

Diffuse astrocytomas showed an increased cellular density with moderate nuclear pleomorphism; nuclei were mostly elongated and irregular with distorted contours, as shown in both image modalities (Fig. 3.35 C, D). Additionally, perivascular aggregation was observed. Neither mitotic activity nor calcification were detected in CLSM and traditional histology.

CLSM imaging of **anaplastic astrocytomas** stained with AF revealed hypercellular collections of neoplastic astrocytes with excellent correlation to the findings in traditional histology (Fig. 3.35 E, F). Nuclei intercalating among axons were a common feature in diffuse astrocytomas and anaplastic astrocytomas. CLSM negative imaging (see subsection 2.4.2) also revealed occasional mitotic activity (Fig. 3.36).

CLSM examination of **anaplastic oligoastrocytomas** showed high cell density with oval, uniformly shaped cells and nuclear pleomorphism. Mitotic activity and foci of necrosis were increased (Fig. 3.36).

Glioblastomas CLSM examination showed high cell density, increased nuclear-to-cytoplasmic ratio, and necrosis as well as polymorphism, anaplasia, and anisokaryosis, resembling findings in traditional histology. Mainly spindle-shaped cells with either oval or elongated nuclei were observed by both *ex vivo* CLSM and traditional histology (Fig. 3.35 G, H). Moreover, several multiple distinct nucleoli were visible in the nuclei. Pseudopalisading and microvascular proliferations were only identified on the CLSM image (Fig. 3.35 G). Mitotic activity was increased (Fig. 3.36).

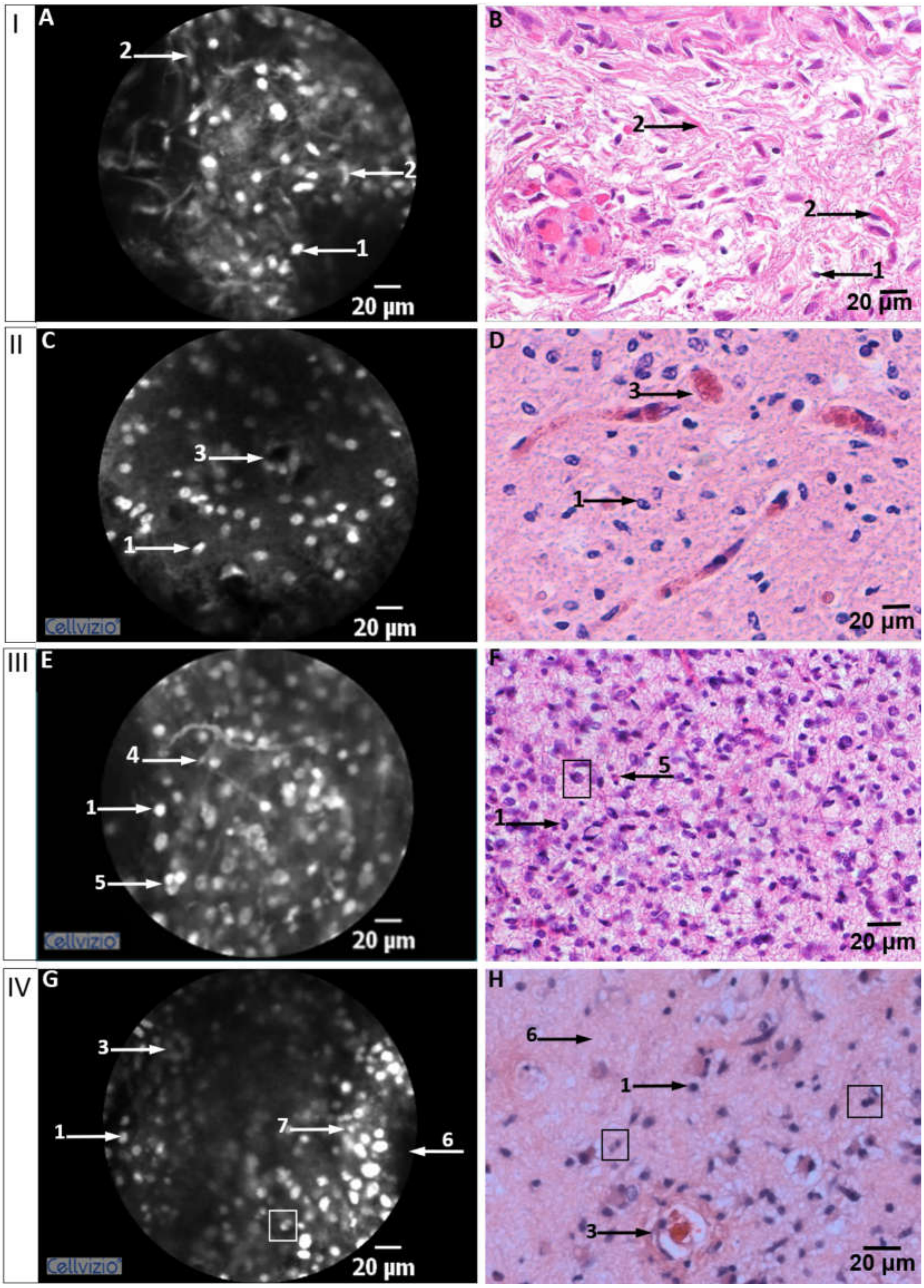

Figure 3.35: CLSM and histology of WHO grades I-IV astrocytomas. AF provided contrast of the nuclei (1→). WHO grade I (A, B): Thick, elongated bundles consistent with Rosenthal fibers were observed in CLSM and histology (2→). WHO grade II (C, D): Chiefly round, elongated cells (1→) displaying an uneven cell distribution and vascular proliferation were found in both image modalities (3→). WHO grade III (E, F): A higher cell density, and a greater cytological atypia (5→) were present compared to the lower-grade astrocytomas (A–E). Furthermore, mitoses were detected (F, accentuation). Nuclei intercalations between axons (4→) were only seen through CLSM (E). WHO grade IV (G, H): Necrosis (6→) and pseudopalisading (G 7→) were only observed in glioblastomas. Microvascular proliferation (3→) and mitoses (accentuation) were also found. Bars = 20 µm. *CLSM, confocal laser scanning microscopy; WHO, World Health Organization; AF, acriflavine hydrochloride.*

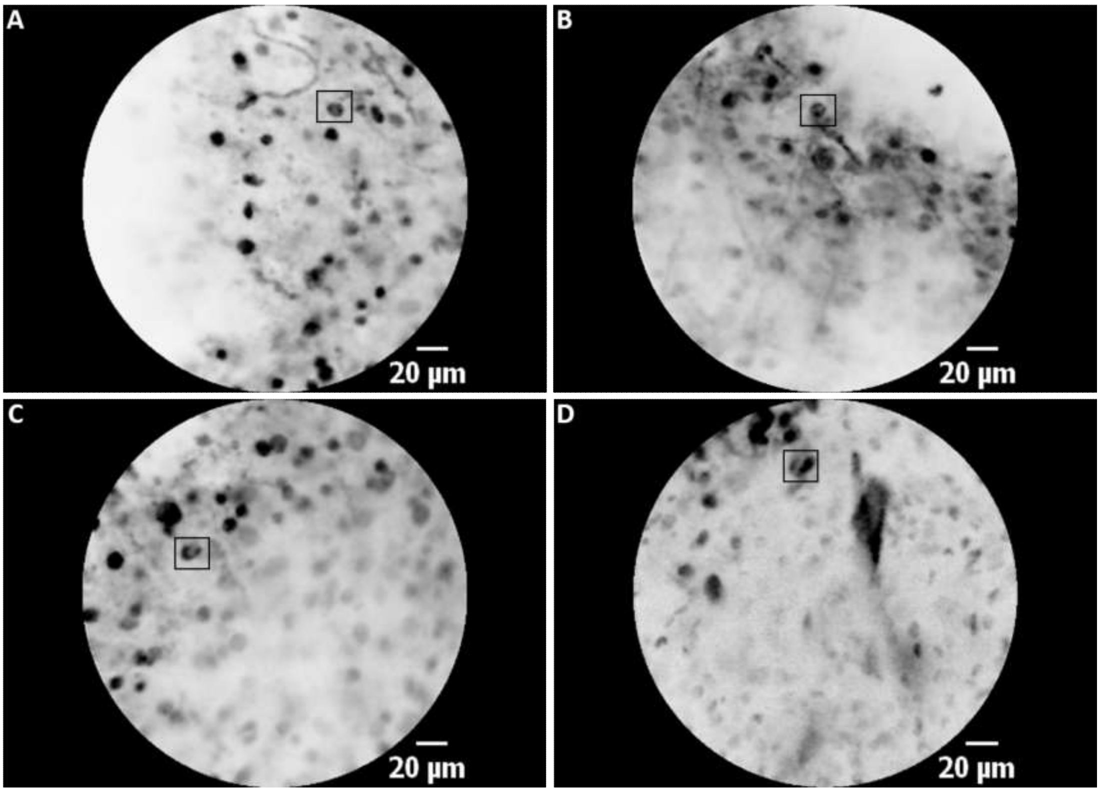

Figure 3.36: CLSM negative imaging of high-grade astrocytomas. CLSM negative imaging after AF staining of an anaplastic astrocytoma (A), an anaplastic oligoastrocytoma (B), and glioblastomas (C, D) revealed mitotic figures [box] showing the high WHO grades of these tumors. Bars = 20 µm. *CLSM, confocal laser scanning microscopy; WHO, World Health Organization; AF, acriflavine hydrochloride.*

Statistical analysis

In a blinded study, CLSM images (n = 27; 4 pilocytic astrocytomas, 4 diffuse astrocytomas, 9 anaplastic astrocytomas and 10 glioblastomas) obtained after CLSM examination with AF were evaluated by board-certified neuropathologists (n = 4). The accuracy was calculated using traditional histopathological diagnosis as the gold standard (see subsection **??**). Images of pilocytic astrocytoma (100%), diffuse astrocytoma (93.75%), and anaplastic astrocytoma (90%) were diagnosed with high accuracy. Glioblastoma images were recognized correctly in 75% of the cases. The percentage outcome was calculated from the multiple-choice result of all four pathologists. One neuropathologist was able to diagnose all entities correctly. Overall correct detection rate was 89.69%.

3.3 Examination of CNS tissue with ICG using the CLSM device at 780 nm excitation

A total of 20 biopsy samples of primary CNS tumors as well as healthy cerebral tissue attached to a tumor were collected from various patients of both genders and different ages. The samples (n = 20; 5 healthy tissues, 5 glioblastomas, 5 meningiomas, and 5 epidermoid tumors) were examined *ex vivo* after staining with ICG under CLSM-780 nm. Altogether, high-resolution images were obtained, showing detailed histopathological features comparable with traditional histology. Representative images for each of the examined entities are presented in Figure 3.37. The concentration used and the resulting fluorescence intensity compared to the other contrast agents are presented in Table 3.1.

Topical application of ICG readily stained the cytoplasm and allowed clear delineation of cellular and subcellular features, such as the nuclei, nucleoli, and atypia. CLSM images showed typical characteristics of **healthy brain tissues**, including clearly arranged astrocytes, resembling the findings in traditional histology of the same ROI (Fig. 3.37 A, B). In the **glioblastoma** samples, areas of hypercellularity, pleomorphism, and necrosis were found. Increased angiogenesis with perivascular clustering of tumor cells was observed by both *ex vivo* CLSM and histology. The nuclear-to-cytoplasmic ratio was increased. Furthermore, multinucleated cells and enlarged nuclei were a common feature in CLSM and traditional histology (Fig. 3.37 C, D). CLSM of **WHO grade I meningiomas** revealed psammoma bodies, which were visualized as globular, anuclear structures (Fig. 3.37 E, F). CLSM real-time imaging of ICG-labeled **epidermoid tumors** allowed visualization of the crystal-like structure of the cell ghosts, accordingly to the H&E stained section (Fig. 3.37 G, H).

Statistical analysis

In a blinded study, CLSM images (n = 20; 5 healthy tissues, 5 glioblastomas; 5 meningiomas, and 5 epidermoid tumors) obtained after CLSM examination with ICG were evaluated by neuropathologists (n = 4). The accuracy was then calculated using traditional histopathological diagnosis as the gold standard, as previously described in Subsection **??**. Glioblastomas (100%) and epidermoid tumors (100%) were all diagnosed correctly. Images of healthy cortex tissue (93.34%) and meningioma (93.34%) were also diagnosed with high accuracy. Overall correct detection rate was 96.67%.

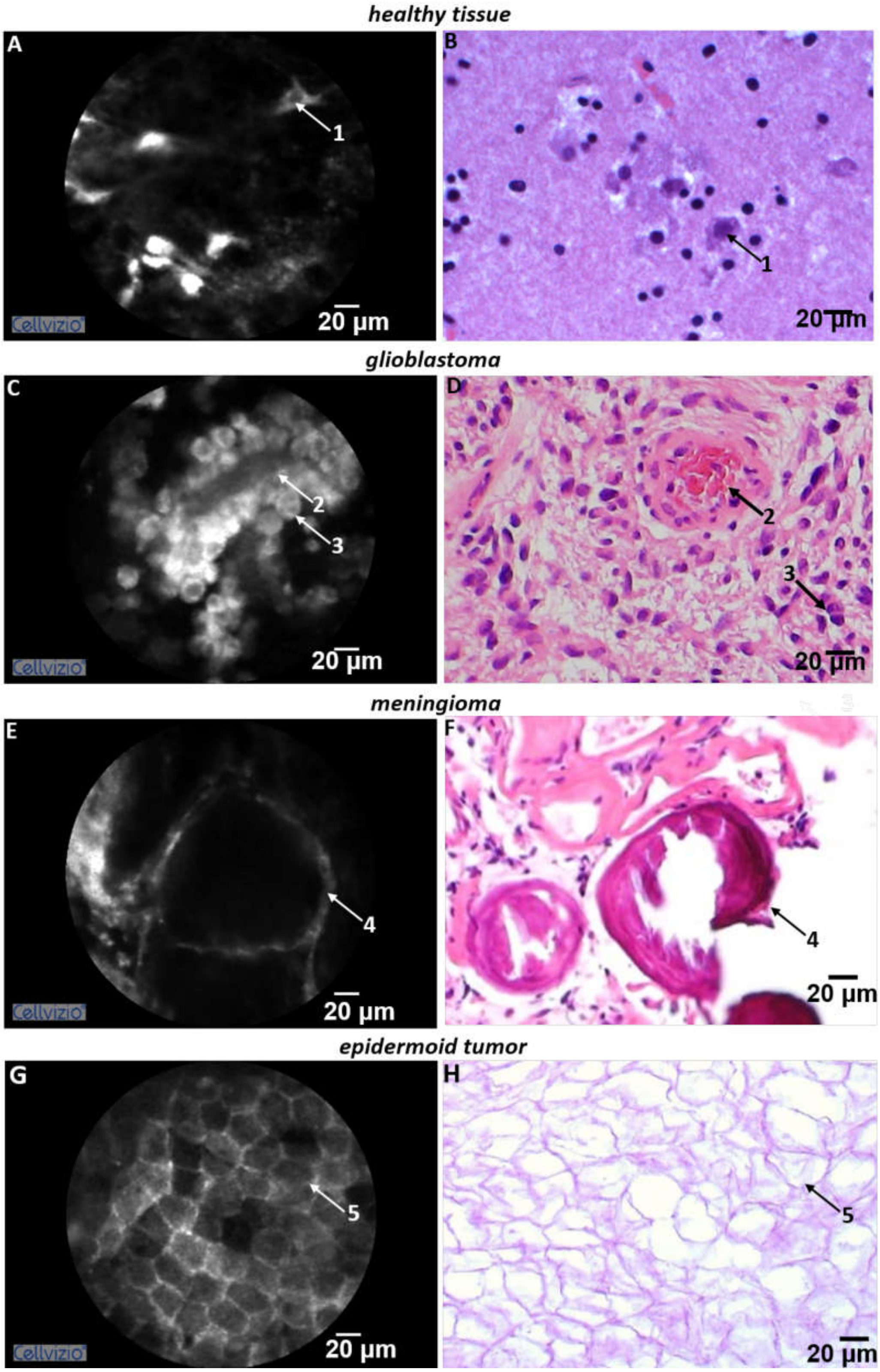

Figure 3.37: ***Ex vivo*** **examination with ICG and H&E.** Healthy tissue (A, B): CLSM (A) and histology (B) revealed clear cell structures of astrocytes (1→). Glioblastoma (C, D): CLSM (C) showed perivascular growth of tumor cells (2→), a high cell density, and the presence of multinucleated cells (3→), accordingly to the histology (D). Meningioma (E, F): Both CLSM (E) and histology (F) revealed a large psammoma body (4→). Epidermoid tumor (G, H): Anuclear crystal-like structures of the "cell ghosts" (5→) were observed by both approaches (G, H). Bars = 20 µm. *ICG, indocyanine green; H&E, hematoxylin and eosin; CLSM, confocal laser scanning microscopy.*

3.4 *In vivo* examination of brain tissue

3.4.1 Brain tumor resection assisted by intraoperative CLSM at 488 nm and 780 nm excitation

In order to evaluate CLSM and the contrast agents for an *in vivo* neurosurgical application, high-grade glioma resection was guided using intraoperative CLSM in rats implanted with C6 glioma cells. Routine surgical wide-field microscopy (OPMI Pentero®) with 5-ALA served as the optical gold standard. All animal studies were performed at the Institute for Neurosurgical Pathophysiology (Medical Center, Johannes Gutenberg University, Mainz, Germany).

CLSM discrimination between neoplastic and healthy rat brain tissues was primarily accomplished due to delineation of typical neoplastic features, such as hypercellularity and pleomorphism in the tumor tissue. Blood artifacts monitored with the CLSM device at 488 nm excitation were well differentiated from normal cells and were washed off using sodium chloride solution in order to avoid interference with resection.

AF: Brain tissue surface was readily stained with AF ($n = 5$). Nuclei appeared as bright spots, and staining of the cell membrane allowed a good impression of the cell volume. As the penetration of AF was limited to the surface of the brain (0–100 µm), a reapplication of AF was required during surgery.

Healthy tissue showed a clear cell distribution with a regular shape and size of the cells. Tumor tissue was characterized by high cell density and low cytoplasm (Fig. 3.38 A, B). Overall, staining with AF allowed a good differentiation between neoplastic and non-neoplastic tissues *in vivo*, resulting in a clear transition zone similar to that in the corresponding H&E stained section (Fig. 3.40 A, B).

Fluorescein sodium: In total, five rats exhibiting an allograft tumor were examined, using CLSM, after intravenous application of fluorescein. Almost immediately (a few seconds), blood vessels and capillaries could be seen (Fig. 3.38 C, D); after a few minutes (approximately 2 min), fluorescein could be detected inside the tumor tissue. The effect of the dye lasted up to 30 min.

Cells stood out as dark spots against the bright extracellular background. In healthy tissue, fluorescence was first seen only in the blood vessels (Fig. 3.38 C, D), but after 20 min some extravasation was observed. Tumor boundaries were clearly recognizable because of a greater cell concentration in the tumor area (Fig. 3.40 C, D). Tumor characteristics such as pleomorphism and mitotic activity were hard to identify. The red blood cells were not stained by fluorescein and appeared as moving black silhouettes in the lumen of the vessels.

Fluorescein sodium and AF: Concomitant use of fluorescein and AF (n = 5) did not aid in tissue information, as fluorescein fluorescence was very bright and masked the AF fluorescence in the tumor area (Fig. 3.39 A). In healthy tissues, AF fluorescence was clearly observed in the cell nuclei, whereas fluorescein was first only visible in the blood vessels (Fig. 3.39 B), allowing demarcation of healthy tissue from tumor tissue (Fig. 3.40 E, F).

ICG: Near-infrared CLSM with ICG fluorescence (n = 5) exhibited, due to cytoplasm staining, nuclear atypia, cellular pleomorphism, altered nuclear-to-cytoplasmic ratio, and high cell density in tumor tissue (Fig. 3.39 C). Healthy brain tissue clearly showed astrocytes and a clear cell arrangement with a low cell density (Fig. 3.39 D), which allowed for a clear differentiation to neoplastic tissue. Tumor margins were not clear lines due to an infiltrating growing pattern of the C6 glioma cell line (Fig. 3.40).

5-ALA: The fluorescence of PpIX could not be sufficiently detected by CLSM-488 nm (data not shown); therefore, the surgery was limited to two rats and no statistics were carried out.

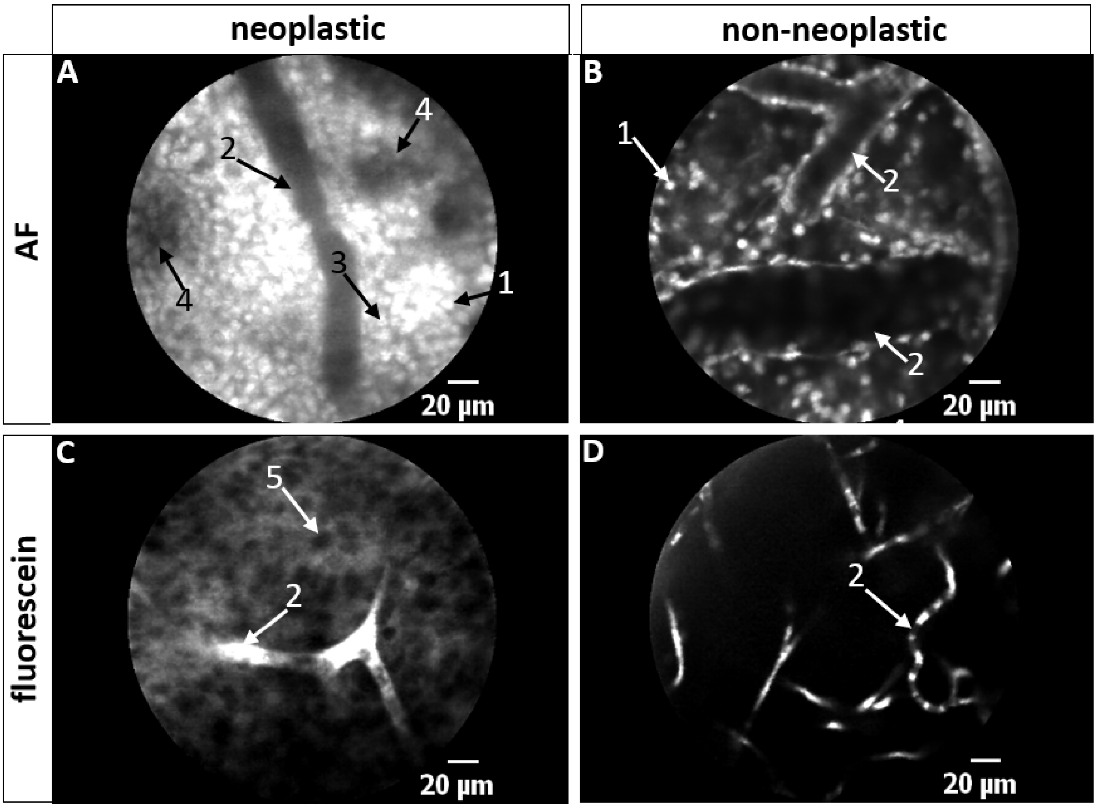

Figure 3.38: ***In vivo*** **CLSM imaging of AF and of fluorescein.** AF (A, B): AF nuclei staining (1→) allowed for the visualization of high cell density with an increased nuclear-to-cytoplasmic ratio (A) and a clear cell distribution in healthy brain tissue with CLSM (B). Blood vessels were not stained by topically applied AF (2→). Nuclei appeared to have an irregular size and shape (A 1→) with some prominent nucleoli (A 3→). Necrosis was also found in the tumor area (A 4→). Fluorescein (C, D): In tumor tissue, fluorescein revealed cells as dark, irregularly shaped spots (C 5→), due to an extracellular matrix staining after extravasation from the blood vessels (C 2→). In healthy tissue, capillaries contrasted sharply against the normal brain tissue (D 2→). The tissue was characterized by clear cell structures with a regular shape and size (B, D). Bars = 20 µm. *CLSM, confocal laser scanning microscopy; AF; acriflavine hydrochloride.*

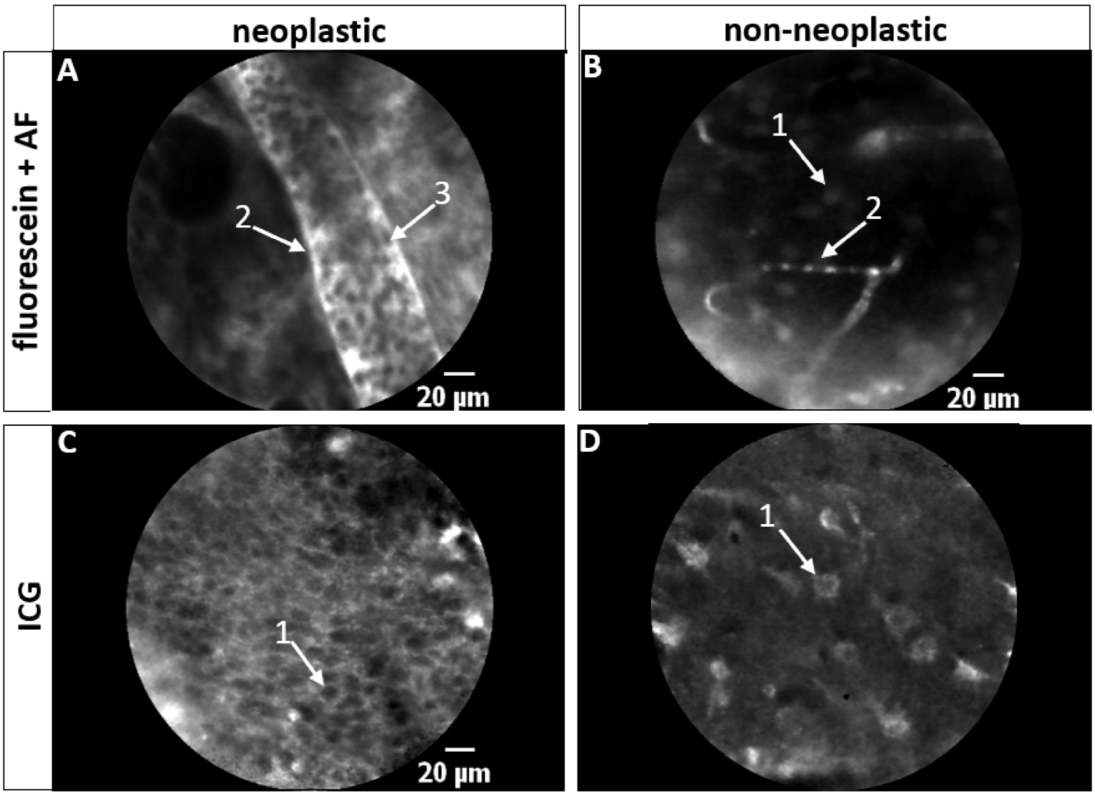

Figure 3.39: ***In vivo*** **CLSM imaging of AF + fluorescein and ICG**. Fluorescein + AF simultaneously (A, B): Fluorescein fluorescence was very bright and masked the AF fluorescence in the tumor area (A). Erythrocytes appeared as multiple non fluorescent silhouettes within the bright fluorescence of fluorescein (E 3→). In healthy tissues, cell nuclei were visible after staining with AF (B 1→), while fluorescein was retained in the blood vessels (B 2→). ICG (C, D): Topically applied ICG allowed the visualization of cytoplasm, against which the atypical nuclei stood out as dark spots (C 1→), showing a high cell density in tumor tissue (C) and well-defined cells in healthy tissue (D 1→). Overall, healthy tissue was characterized by clear cell structures with a regular shape and size (B, D). Bars = 20 µm. *CLSM, confocal laser scanning microscopy; AF; acriflavine hydrochloride; ICG, indocyanine green.*

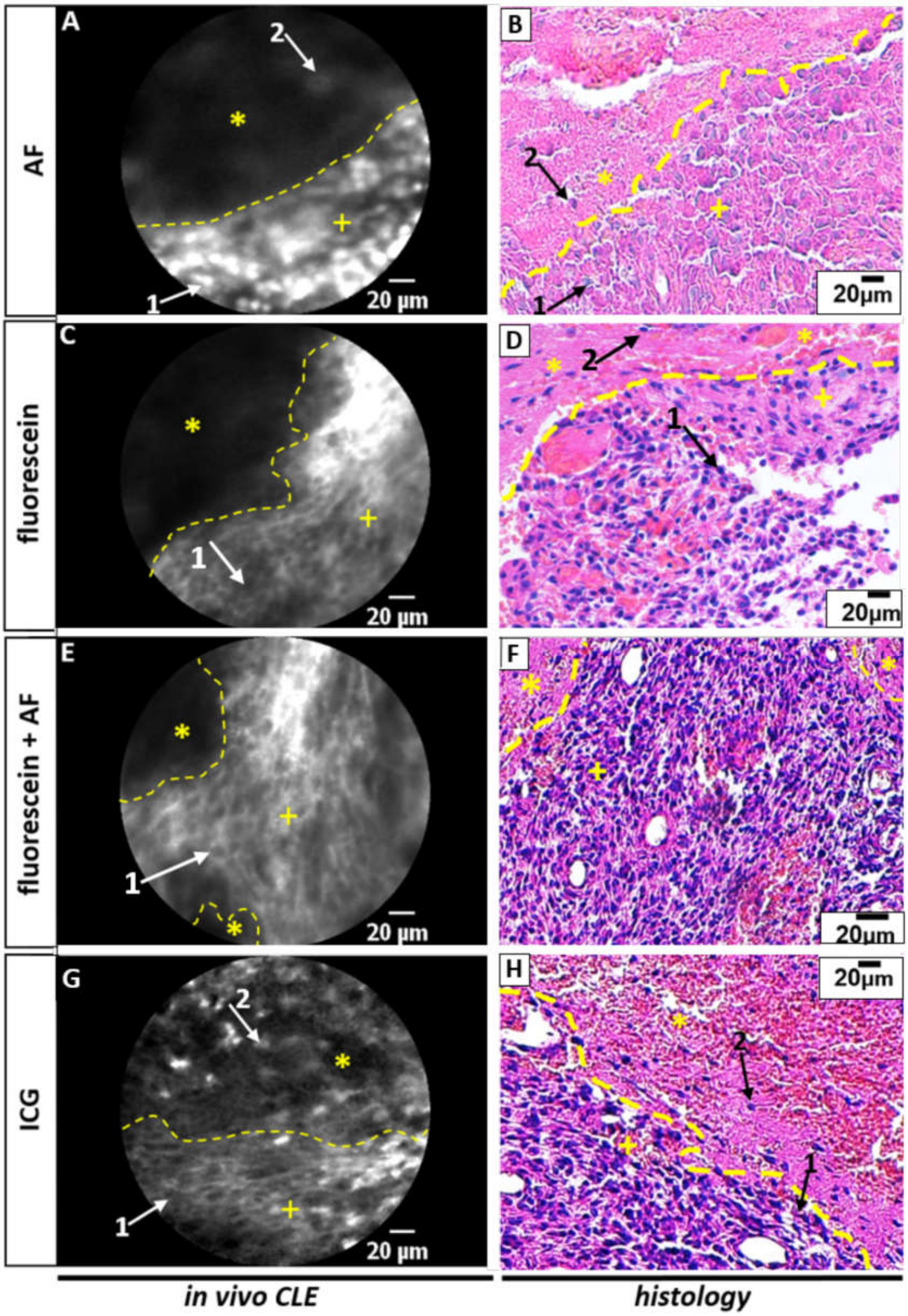

Figure 3.40: Examination of the tumor margins. Tumor margins (yellow dashed line) between non-neoplastic (asterisk) and neoplastic tissue (cross) could be observed based on higher cell density and cellular pleomorphism in tumor tissue, after staining with AF (A), fluorescein (C), fluorescein + AF (E), and ICG (G). AF (A) as well as ICG (G) staining allowed for visualization of neoplastic cells (1→) and healthy cells (2→), whereas fluorescein was not detected in healthy tissue (C, E). Overall, CLSM *in vivo* imaging revealed tumor margins comparable to those revealed by the corresponding histology (B, D, F, H). Both image approaches showed an indistinct transition zone. Bars = 20 µm. *CLSM, confocal laser scanning microscopy; AF; acriflavine hydrochloride; ICG, indocyanine green.*

3.4.2 Brain tumor resection assisted by OPMI Pentero®

5-ALA: As a control group, tumor tissues from five rats were resected without using CLSM. The resection was assisted by 5-ALA visualized by an OPMI Pentero®-400 nm surgical wide-field microscope, which is routinely used at the Merheim, Hospital for the resection of human glioblastomas. Tumor tissue showed an intense red fluorescent color after an incubation time of 3–5 h with 5-ALA. After resection of all stained tissue, tumor tissue (without any fluorescence) was still observed in the brains of two rats, which was later confirmed by histopathological examination (Fig. 40).

3.4.3 Histopathological analyses of the rat brain and the removed specimen

Overall, traditional histology served as the gold standard for diagnosis of the removed biopsies (during tumor surgery) and of the removed perfused brain (from each rat the brain was removed and completely examined by traditional histology as described in Subsection 2.6.7) to evaluate the resection outcome for each fluorescent agent as well as for the used microscope.

Histopathological analyses of the rat brains revealed migrating tumor cells all over the rat brain, especially in the ventricles and in the basal and/or inter-hemispheric arachnoid (Fig. 3.41). Since the maximum depth of the CLSM GastroFlex™ probe is 55–65 µm, cells located deeper than this range were impossible to detect with the CLSM approach. Therefore, for the calculation of the residual tumor area, tissues were only considered within this range (see subsection 2.6.8).

One example of a rat brain containing a high amount of residual tumor tissue in the range of CLSM is shown in Figure 3.41. Additionally, one example of a brain, with no apparent residual tumor within the range of CLSM, is presented in Figure 3.42. Histopathological sections of the resected biopsies are also demonstrated for each case (Fig. 3.41 and 3.42).

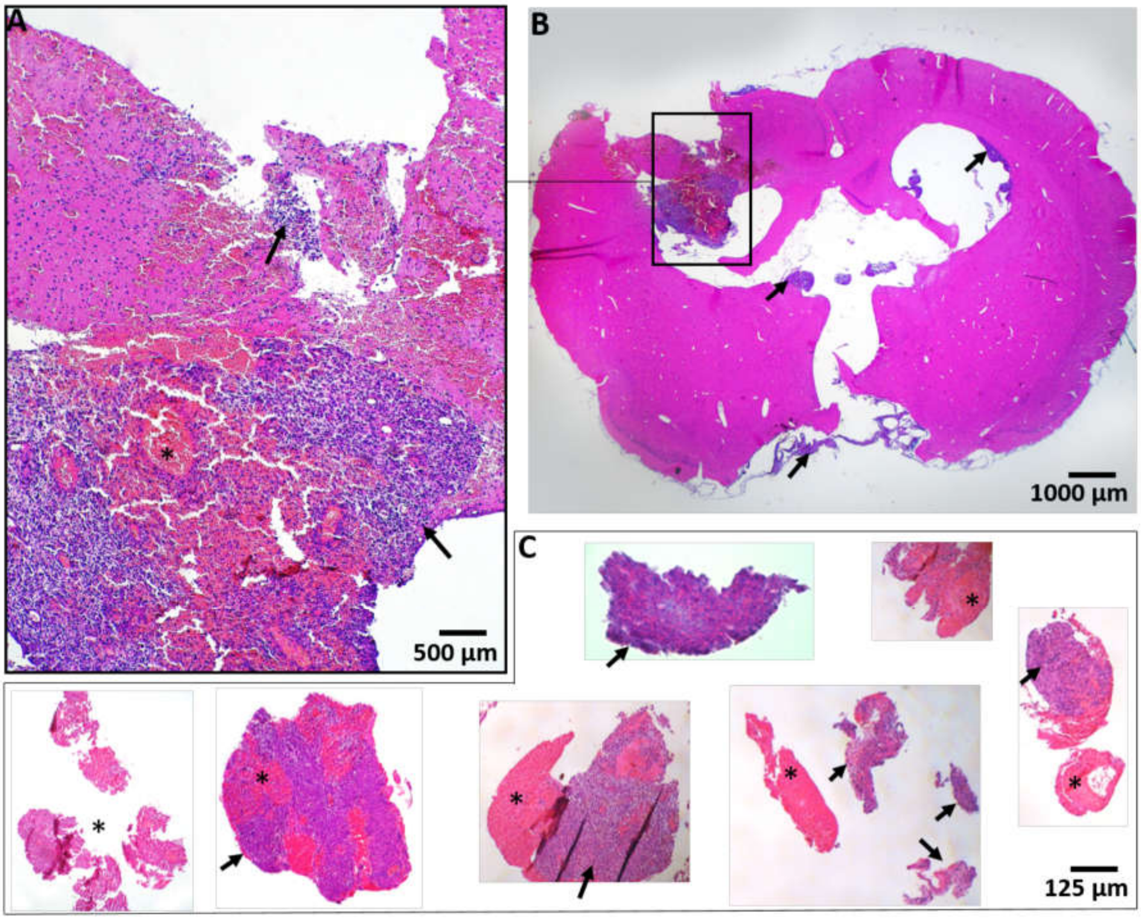

Figure 3.41: H&E stained sections of an incompletely removed tumor. Histopathological sections of both a removed brain (A, B) and its resected specimens during the surgery process are shown (C). Tumor tissue was found all over the resection zone (A). Histopathological examination also revealed migrating tumor cells all over the rat brain, including the opposite hemisphere (B). Especially the ventricles and basal and/or inter-hemispheric arachnoid were infiltrated by neoplastic cells (B →). The removed specimen (C) mainly contained tumor tissue (→) and hemorrhage (*). A: Bar = 500 µm, B: Bar = 1000 µm, C: Bar = 125 µm. *H&E, hematoxylin and eosin.*

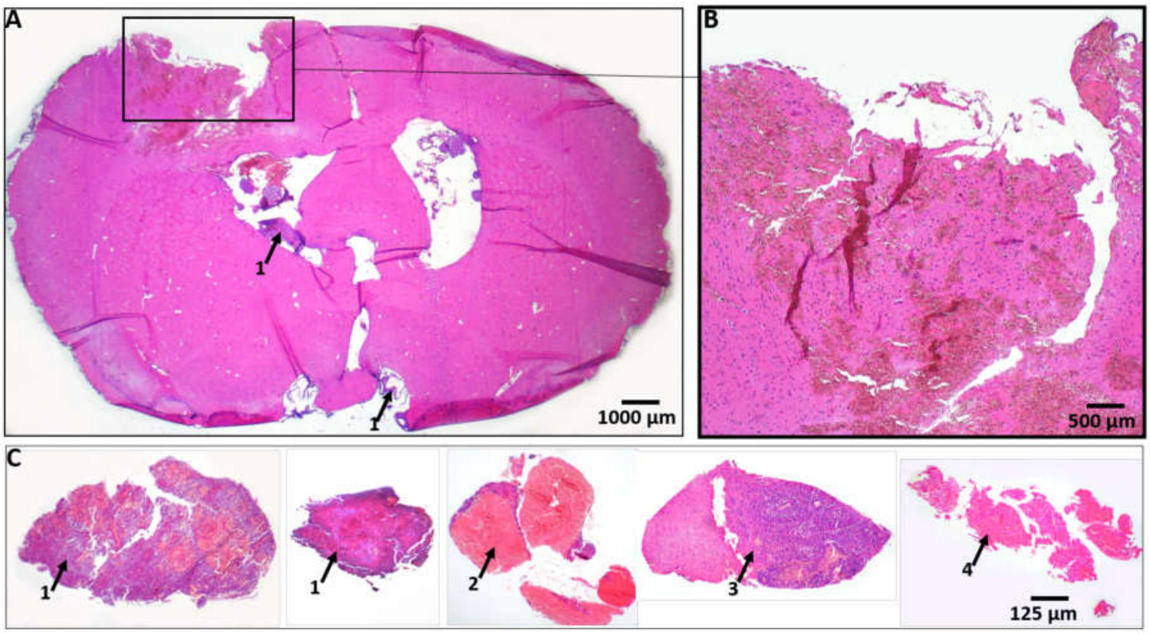

Figure 3.42: H&E stained sections of a sufficiently removed tumor. Histopathological sections of both a removed brain (A, B) and its resected tumor specimens during the surgery are shown (C). This example is considered as a "completely" resected tumor, as no tumor tissue was found in the resection cavity within the range of the probe (B). However, migrating tumor cells were found in the ventricles and in the basal and/or inter-hemispheric arachnoid (A 1→). The removed specimens (C) mainly contained neoplastic tissues (1→) and hemorrhage (2→), but transition zone (3→) and healthy tissue (4→) were also found. A: Bar = 500 µm, B: Bar = 1000 µm, C: Bar = 125 µm. *H&E, hematoxylin and eosin.*

The calculated mean residual tumor amount (within the range of the probe) and the mean resection volume for each rat group is shown in Figure 3.43. Overall, fluorescein-assisted surgery (n = 5), using the CLSM device at 488 nm excitation, had significantly (*) higher amounts of residual tumor tissue (average residual tumor ratio: 4.9%) compared to AF- (average residual tumor ratio: 0.8%) and to ICG-assisted surgery (average residual tumor ratio: 0.75%; Fig. 3.43). Additionally, the average resection volume was significantly larger in the fluorescein group than in the control group with 5-ALA. The simultaneous use of fluorescein and AF did not facilitate the resection of the tumor, since the brains showed a large mean amount of residual tumor tissue (average residual tumor ratio: 4.9%; Fig. 3.43). ICG tissue staining highlighted with CLSM-780 nm allowed for best resection results.

The control group using OPMI Pentero®-400 nm wide-field microscopy and 5-ALA as contrast agent had on average the largest tumor remains (3.7%). This group also had the smallest mean resection cavity compared to the other groups. One value in the control group was assessed as a statistical outlier (20 mm^2 remaining tumor tissue) and excluded in data analysis, but it was included in the regression analysis (Fig. 3.43).

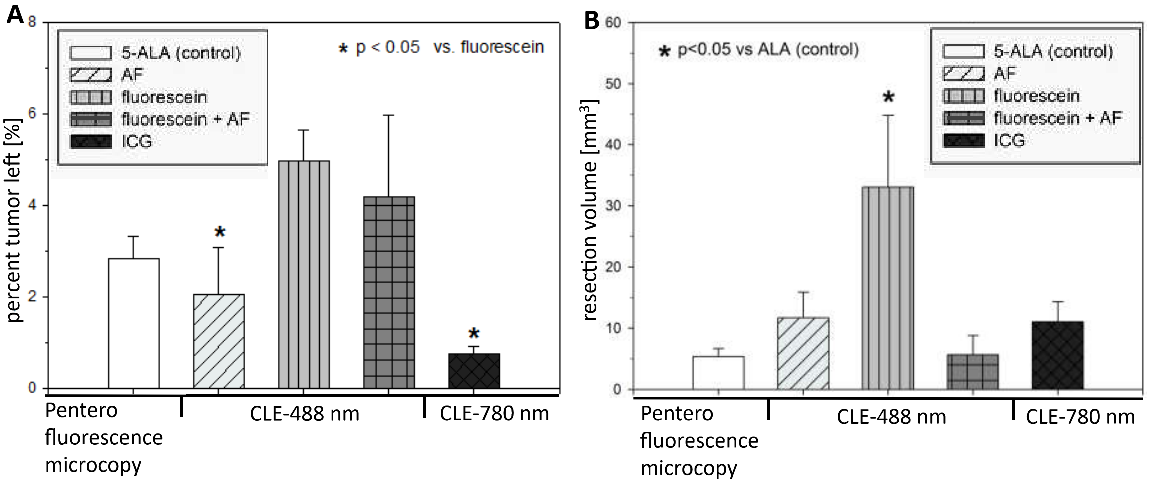

Figure 3.43: Resection outcome and resection cavity volume. Resection outcome assisted by CLSM-488 nm, by CLSM-780 nm and by OPMI Pentero®-400 nm fluorescence wide-field microscopy was compared (A). The resection volume gives an impression of how large the tumor was (B). Fluorescein-assisted surgery (n = 5): The rat brains composed significantly (*) higher tumor residues than the rat brains examined with AF and ICG (A). The average resection cavity (volume) was significantly larger than in the control group with 5-ALA (B). AF and fluorescein simultaneously (n = 5): The rat brains showed high amounts of residual tumor tissue (A). The average size of the resection cavity was small (B). AF-assisted surgery (n = 5): Histopathological analyses of the brain sections revealed a significantly lower average amount of residual tumor tissue in the resection cavity compared to fluorescein-assisted surgery (A). The average size of the resection cavity was small (B). 5-ALA-assisted surgery (n = 4): The control group, in which a wide-field fluorescence microscope was used as standard (OPMI Pentero®-400 nm), had on average the smallest resection cavity (B) but had on average the largest residual tumor tissue (A). One value in the control group was assessed as a statistical outlier and excluded in the data analysis. ICG-assisted surgery (n = 5): CLSM imaging of ICG provided the best resection results; it had on average the smallest amount of residual tumor tissue (A) and a medium-sized resection cavity (B). *CLSM, confocal laser scanning microscopy; AF; acriflavine hydrochloride; ICG, indocyanine green; 5-ALA, 5-aminolevulinic acid.*

Regression analyses

Regression analyses were carried out to better compare the resection outcomes assisted by wide-field microscopy or CLSM and to compare the staining abilities of the contrast agents. First, the correlation between the amount of healthy tissue in the biopsies and the remaining tumor tissue in the resection zone on the brain was estimated for each rat (Fig. 3.44). This correlation was examined to analyze if a safe resection combined with an extensive resection is possible using one of the approaches.

Neither wide-field microscopy (OPMI Pentero®-400 nm) and 5-ALA nor CLSM and fluorescein (Fig. 3.44) allowed for such an extensive and safe resection of the tumor. Moreover, the outlier in the 5-ALA control group had the largest total amount of remaining tumor (20 mm^2) in the resection cavity. Meanwhile, no healthy tissue was found in the resected biopsies. The surgery of the other rats from the 5-ALA group resulted in in a remainder of approximately 0.5%–1% of the tumor in the resection cavity, with no removal of healthy tissue during the surgery. However, this also means that no margins were found in any of the resected biopsies. A safe resection combined with an extensive resection was only achieved by CLSM-780 nm and ICG (Fig. 3.44).

Second, the correlation between the remaining tumor in the resection cavity and the resection volume was examined. This regression analysis was carried out to analyze if more residual tumor tissue was left when the tumor was large. A correlation was only found in the rat group with fluorescein and CLSM: the rats that were administered fluorescein for surgery had the largest average resection volume and the largest average residual tumor tissue (Fig. 3.44).

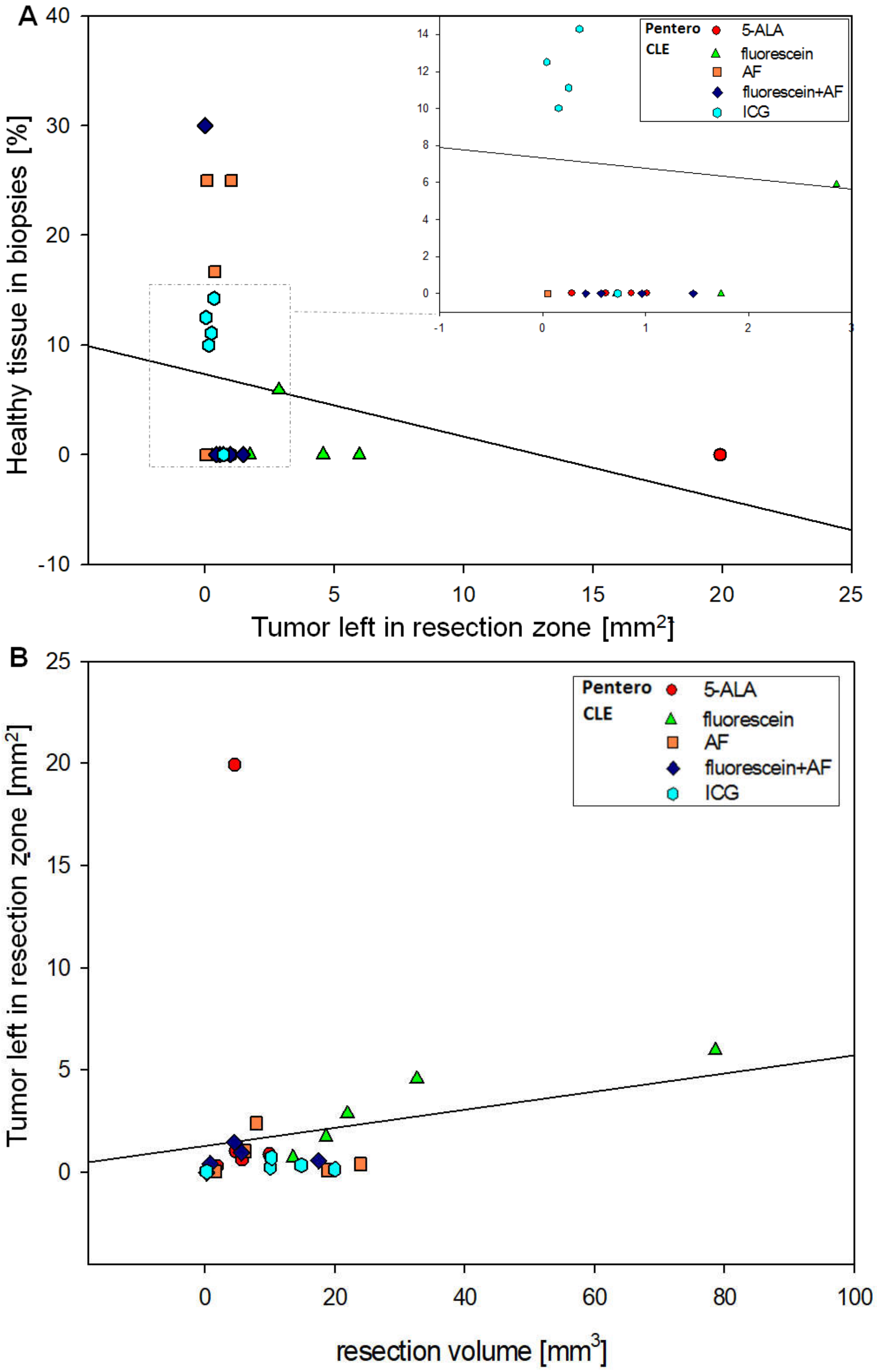

Figure 3.44: Regression analyses. Different correlations regarding the resection outcome assisted by CLSM-488 nm (AF and fluorescein), CLSM-780 nm (ICG), and by OPMI Pentero®-400 nm wide-field microscopy (5-ALA) were examined. The control group with 5-ALA (n = 5) had one outlier with more than 20 mm^2 remaining tumor tissue at the resection zone and no healthy tissue in the biopsies (A). CLSM imaging of ICG (n = 5) provided the best resection outcome (A). The rats that were administered fluorescein for surgery had the largest average resection volume and the largest amount of remaining tumor in the resection cavity (excluding the outlier; A). *CLSM, confocal laser scanning microscopy; AF; acriflavine hydrochloride; 5-ALA, 5-aminolevulinic acid; ICG, indocyanine green.*

3.4.4 *In vivo* examination of healthy brain tissue using CLSM at 780 nm excitation

In vivo examination of a pig brain allowed investigation of intraoperative CLSM in imaging larger, healthy brain structures. Topically and intravenously applied ICG were used for tissue contrast under CLSM-780 nm. Representative images of different brain structures are presented in Figures 3.45 and 3.46.

After craniotomy, the topical application of ICG revealed first the dura mater and then the pia mater in CLSM. The injection of ICG immediately provided physiological information, such as the blood flow through small capillaries and larger supplying vessels. After about 5 minutes, ICG was also visible in the cells, allowing differentiation of brain cells based on their typical shape, such as astrocytes, oligodendrocytes, microglia, and nerve cells, in the cerebral cortex. Likewise, fat tissue, and deeper brain structures, such as the choroid plexus, could be observed in real time. Since the field of view was very small, no exact regions of the brain could be identified.

Dura mater: The cerebral dura was the first examined tissue after craniotomy. In CLSM, collagenous connective tissue, blood vessel and a low amount of cells were visible.

Pia mater: CLSM examination exhibited collagenous connective tissue as well as a high number of blood vessels and cells.

Fat tissue: CLSM imaging revealed layers of adipose cells. The cells were characterized by a large size, in which the nuclei were visible on the corner of the cells.

Choroid plexus: CLSM allowed real-time imaging of the ependymal cell layer, which lined the ventricles. Moreover, CLSM images showed the typical villi structure of the choroid plexus.

Pyramidal cells: In CLSM, this type of neurons was clearly recognizable because of the conic shape of their cell body (soma). However, CLSM imaging did not allow to differentiate between dendrites and axons. Pyramidal cells were found all over the cerebral cortex.

Astrocytes: In CLSM, these cells were immediately identified due to their typical star shape. It was the most common cell type found in the cerebral cortex.

Oligodendrocytes: These cells were mostly detected close to nerve cells and were smaller than astrocytes. Oligodendrocytes were detected all over the cerebral cortex.

Microglia: Small cells, most likely microglia, were found isolated all over the examined brain tissue using CLSM.

Nerve cell: Nerve cells were observed as large structures surrounded by thick cell processes, most likely dendrites or axons.

Nerve fibers: Nerve fibers were seen in transversal and longitudinal orientation by intraoperative CLSM. In transversal orientation, the myelin sheath around the axons could be observed.

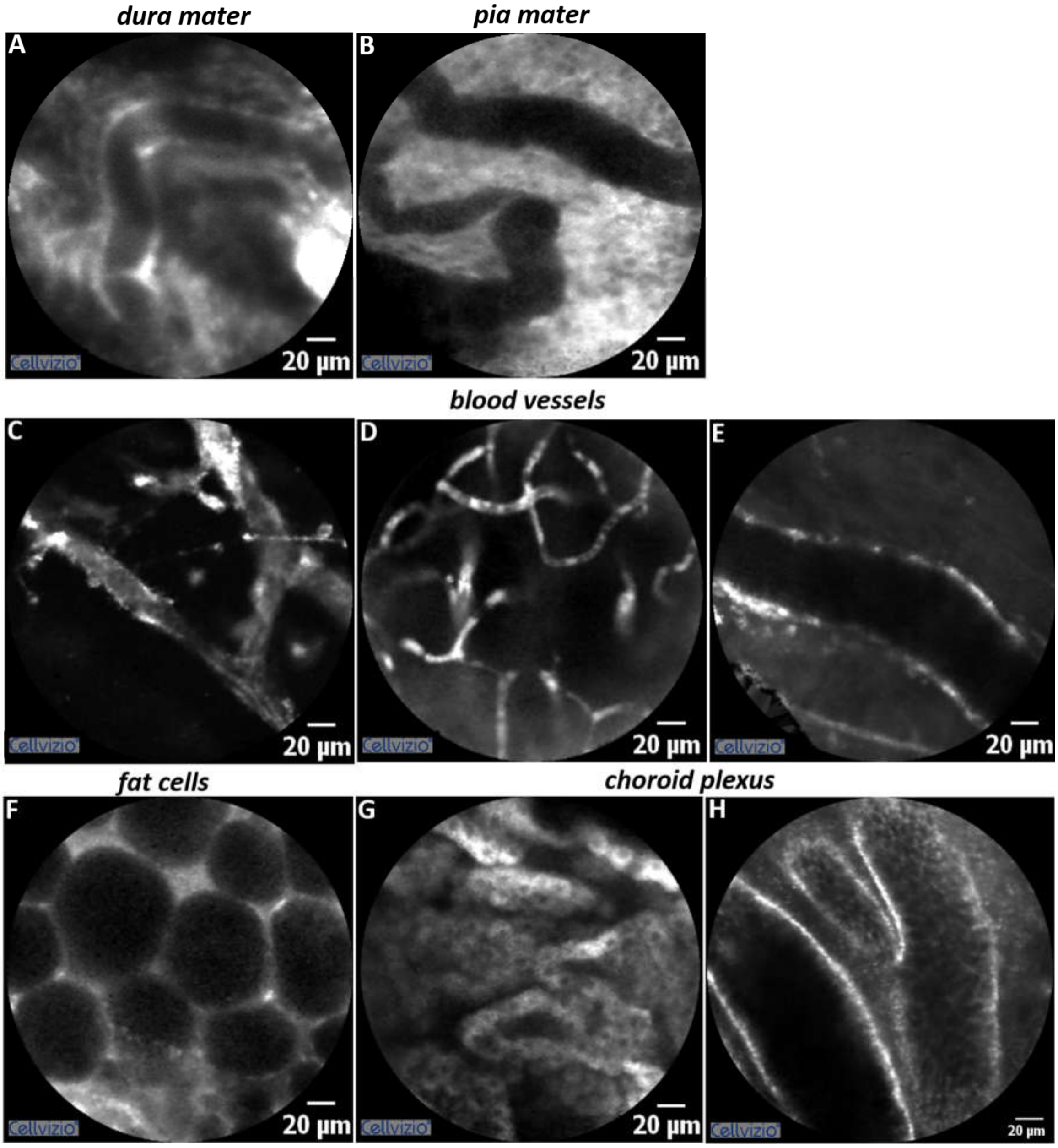

Figure 3.45: ***In vivo* CLSM imaging of healthy brain structures.** After ICG staining, CLSM examination revealed healthy brain structures in a pig, such as the dura mater (A), the pia mater (B), blood vessels (C, D), fat cells (F), and the choroid plexus (G, H). Bars = 20 µm. *CLSM, confocal laser scanning microscopy; ICG, indocyanine green.*

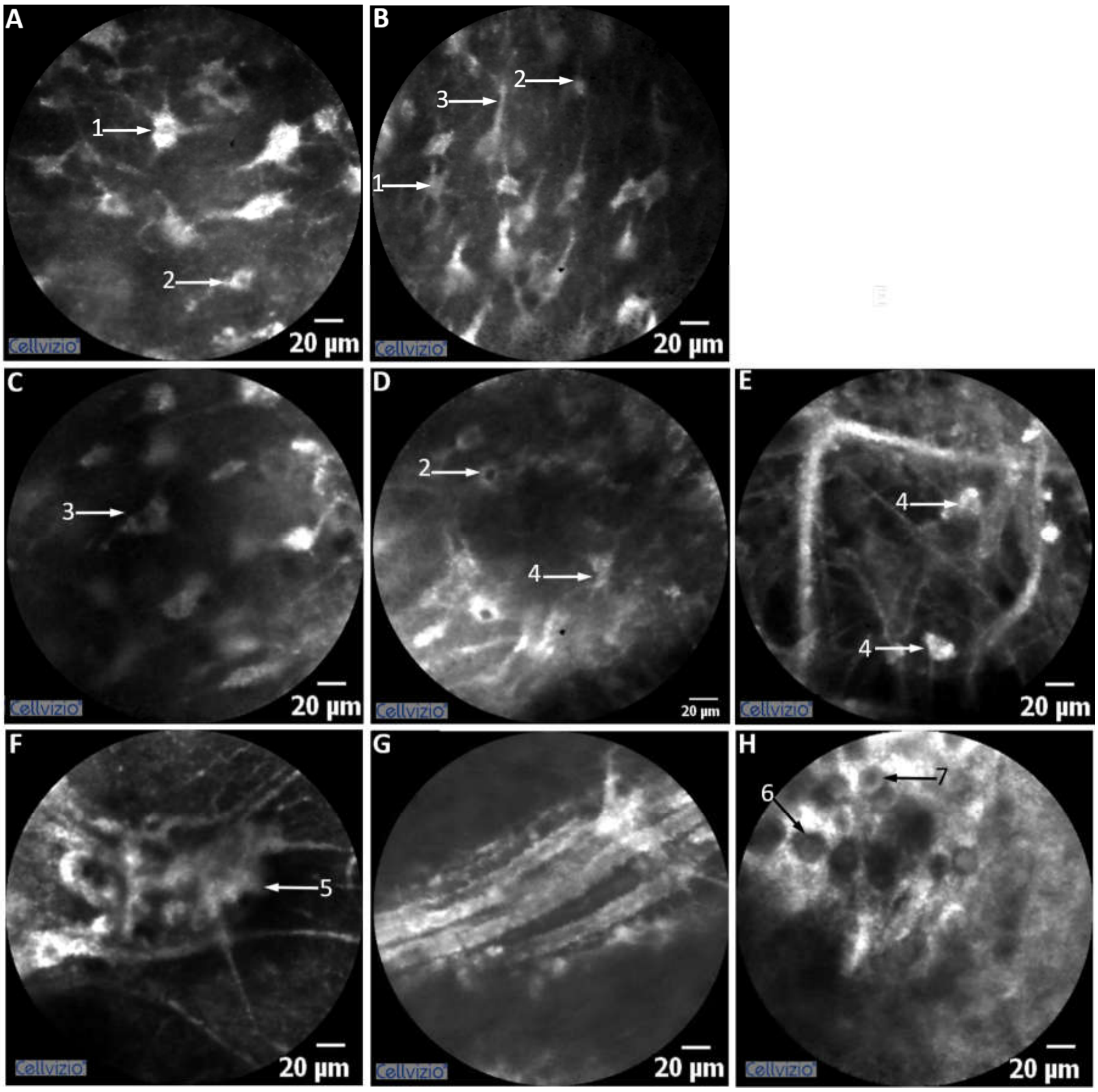

Figure 3.46: ***In vivo*** **CLSM imaging of healthy glia cells, nerve cells and nerve fibers.** ICG was applied to enhance tissue contrast. A: CLSM imaging revealed astrocytes, which were clearly recognized because of their stair shape (1→). In the same cerebral cortex tissue, small cells, most likely microglia, were found (2→). B, C: CLSM examination also exhibited pyramidal cells (B 3→). The pyramidal cells were characterized by a pyramidal shape of the cell body (C 3→). D, E: Glial cells, having a medium size and a lower amount of cell processes than in astrocytes, were identified as oligodendrocytes (4→). The cells were detected isolated (D 4→), but mostly close to nerve cells (E 4→). F: Nerve cells were recognized as large structures surrounded by thick cell processes (5→), most likely dendrites or axons. G, H: Nerve fibers were observed in transversal (G) and longitudinal orientation (H). The tranversal orientation of the nerve fibers (6→) also allowed to visualize the myelin sheath around the axons (7→). Bars = 20 µm. *CLSM, confocal laser scanning microscopy; ICG, indocyanine green.*

3.4.5 Artifacts during CLSM imaging

Investigation of CLSM imaging revealed also different "pitfalls." (Fig. 3.47). Motion artifacts were the most common cause of image impairment, caused by hands shaking while holding the very thin Miniprobe^{TM} (Fig. 2.1). Air bubbles were also a common cause for image impairments and were mistaken for histopathological features, such as psammoma bodies, at the beginning of the learning curve. Blood artifacts frequently interrupted the field of view but were well distinguishable from brain cells and washed off using physiological sodium chloride solution. A further pitfall was a broken Miniprobe^{TM} in the field of view, which made it difficult to properly visualize the tissue.

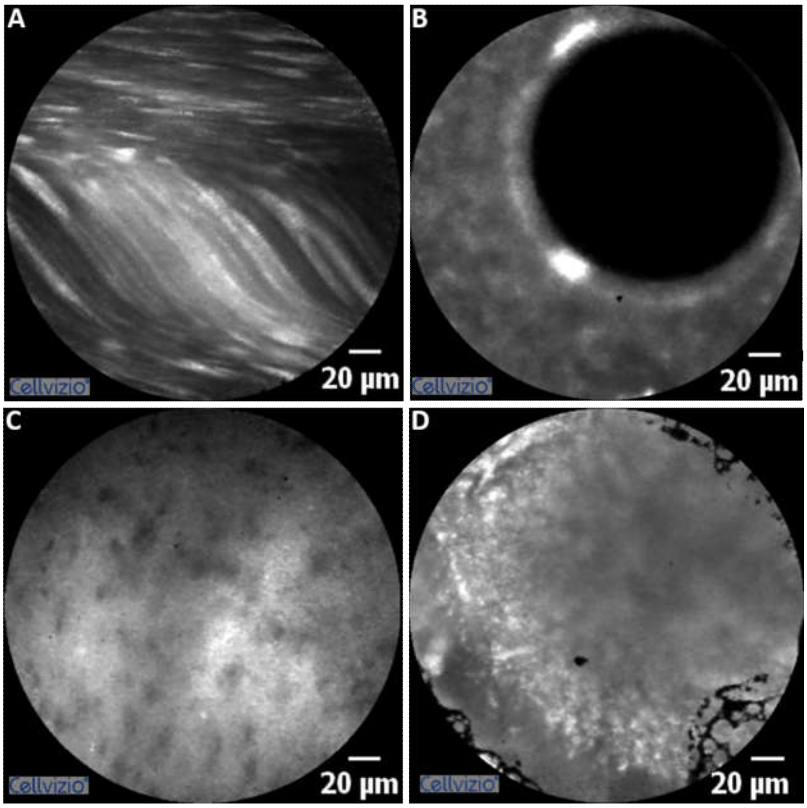

Figure 3.47: Artifacts during CLSM examination. Motion artifact (A), air bubble (B), blood artifacts (C), and damage to the probe (D) were common image impairments during CLSM imaging. Bars = 20 µm. *CLSM, confocal laser scanning microscoopy.*

4. Discussion

4.1 General aspects

This study demonstrates the potential of CLSM in the real-time visualization of histopathological features of different CNS lesions. The CLSM tool was easily introduced into the clinical routine, which allowed examination of biopsies in real time during the surgery process. Here, CLSM provided for the differentiation between healthy and tumorous tissue and for the identification of pathological entities of the CNS similar to the results of traditional histology of the same ROI, especially after staining with AF and ICG. Moreover, CLSM *in vivo* imaging of ICG in rats exhibiting gliomas allowed examination of tumor margins in real time and enabled better surgical outcomes than with wide-field visualization of 5-ALA-induced PpIX.

In neurosurgery, the risk of collateral damage to vital healthy tissue that is responsible for human key capabilities, such as motor function, speech, sensation, hearing, and memory, is a major concern (Nelson et al., 2013). On the other hand, Wood et al. reported in a study with 510 patients suffering from malignant cerebral gliomas that the amount of residual tumor is a significant prognostic factor for the overall survival time (Wood et al., 1988). Hence, to prevent a loss of brain function, neurosurgeons need to take utmost care when removing tumor tissue, at the same time removing as much of the tumor as possible to increase survival time and decrease intracranial pressure. However, finding a good balance between aggressive removal of tumor tissue and sparing of healthy important brain tissue, especially in the case of infiltrative tumors, is extremely challenging, as the surgical approaches currently available are not able to distinguish accurately between malignant and healthy tissue (Duffau, 2014). Thus, the tumor volume is often either overestimated or underestimated, based on the subjective assessment by the responsible neurosurgeons (Millgård et al., 2017).

To date, traditional histology is the only diagnostic method which can distinguish accurately between malignant and healthy tissue, but it is impractical for interactive guidance of resection due to a long processing time (Rees, 2011). For instance, when positive margins are postoperatively found during the final histopathological evaluation, the patient is forced to undergo a second surgery for removal of the residual margin, thus leading to an increase in healthcare costs, anesthesia, and the patient's risk of additional surgical complications (Shah, 2018).

CLSM, first introduced in 2004 in gastroenterology, is a promising tool to overcome these difficulties, as it allows *in vivo* high-resolution imaging of tissues in real time and on a cellular level (Kiesslich et al., 2004). In the field of neurosurgery, experience with CLSM is still rare, presumably due to a lack of contrast agents and Miniprobes^{TM} appropriate for a neurosurgical application.

Therefore, this research aimed to add information about the potential of CLSM in the real-time visualization, using various contrast agents, of the histopathological features of different neurosurgical lesions. In particular, the application of intraoperative CLSM devices at 488 nm and 780 nm excitation was investigated for *ex vivo* and *in vivo* imaging of primary CNS tumors and healthy tissues, following AF, AO, CV, erythrosine, fluorescein, 5-ALA, and ICG staining.

4.2 Analyses of primary CNS tumors: *ex vivo* study

The distribution of all resected and examined primary CNS tumors was evaluated during the period January 2014–February 2016 at the Department of Neurosurgery of Merheim Hospital, Cologne, Germany.

The statistical analyses were carried out to gain an overview of all resected primary CNS tumors in our hospital. The analyses showed that the overall distribution of the tumor types was similar to the literature data worldwide (Buckner et al., 2007; Das et al., 2000), which suggests that the presented data describes a sample that is representative for the analyzed tumor entities. The data shows the frequency of each tumor, the tumor's behavior (benign or malignant), and the gender and age of the patient at initial diagnosis, all of which are important prognostic factors (Gehan & Walker, 1977).

To avoid duplicates, recurrent tumors of a patient were not considered in the statistical analysis. This is one of the reasons why the total number of evaluated tumor samples was lower than the number of surgically treated tumors in our hospital. Furthermore, metastatic CNS tumors arising from non-CNS tumors, which represented one of the most frequently treated tumors in our hospital, were also excluded from the analysis.

Meningioma: Meningioma was the most common primary CNS tumor in the sample (37%) and accordingly the most frequently examined tumor using CLSM. CLSM examination allowed immediate diagnosis and also enabled distinction between the subtypes of WHO grade I meningiomas.

Meningiomas are also the most common form of primary CNS tumors in the US (Kohler et al., 2011; Ostrom et al., 2015; Ostrom et al., 2016), Australia (Das et al., 2000), China (Das et al., 2000) and Europe (Ferlay J, 2018). The high frequency of this tumor type makes it an interesting object of research. Most meningiomas are benign (WHO grade I) and separable from healthy tissue, but some infiltrate the brain and make a complete removal challenging (WHO grades II and III). In our hospital, 8% of meningiomas were malignant. According to literature data, approximately 5% of meningiomas are atypical or malignant (Das et al., 2000; Ostrom et al., 2015; Ostrom et al., 2016). Within 5 years after resection, the recurrence rate is currently 9%–20% in the case of WHO grade I, 29%–59% in the case of WHO grade II, and 60%–94% in the case of WHO grade III (Hortobagyi et al., 2016). Therefore, the aim of the surgical treatment of meningiomas is the complete resection of the tumor tissue (if possible) to reduce the risk of recurrence.

Intraoperative examination on a cellular level through CLSM may facilitate this goal. Additionally, CLSM may be interesting as an aid in the surgical treatment of meningiomas located close to critical brain regions, because of better optical distinction between neoplastic tissue, blood vessels, nerves, dura matter and other healthy brain structures on a cellular level.

Glioblastoma: Glioblastoma was the second most common primary CNS tumor and the most common primary malignant CNS tumor (54%) in our hospital. Therefore, it was the second-most examined tumor in this study. The incidence rate increased with the age of the patient, with a median age of 68 years at diagnosis, corresponding to findings all over the world (Ostrom et al., 2014; Visser et al., 2015). Due to an increase of life expectancy, the incidence rate of glioblastomas can also be expected to increase in the coming years. This will also increase the urgency for efficient diagnosis and treatment options. Thus, investigation of this tumor is of special relevance.

To date, treatment of glioblastomas is challenging due to their resistance to therapeutic interventions. Their infiltrating nature usually prevents a complete resection (Ohgaki et al., 2004; Adamson et al., 2010). Nonetheless, surgery is the initial therapeutic approach and remains a hallmark in the treatment, with the best prognosis; it increases patient survival from 4.7 months to 7–24 months (Wen & Kesari, 2008). The goal of glioblastoma surgery is a maximal safe removal of the tumor tissue. However, the balance between aggressive tumor removal and the sparing of healthy important brain tissue is especially critical here, due to the tumors' infiltrating of surrounding tissue. Hence, a cellular view of tissues could most likely increase the resection yield and improve the quality of the patient's life.

CLSM examination of 79 glioblastomas revealed the five WHO criteria for its diagnosis, namely cell density, cell pleomorphy, mitoses, microvascular proliferation, and pseudopalisades (Louis et al., 2007). Mitoses were often difficult to detect using the CLSM approach but are negligible features when the primary aim is to distinguish healthy and tumorous tissue, which was immediately possible with CLSM. Therefore, CLSM may be a promising tool for a more accurate extended surgical removal of infiltrative high-grade tumors.

Low-grade astrocytomas: CLSM examination also allowed differentiation between the lower-grade astrocytomas. Astrocytomas of WHO grade I (mainly pilocytic astrocytomas) and WHO grade II (diffuse astrocytomas) accounted for 4% of all examined tumors and were mostly diagnosed at younger ages (median age of 19 years and 29 years, respectively). Low-grade tumors grow, by definition, more slowly and are less aggressive, with a better survival prognosis, than high-grade tumors (Zülch, 1979; Louis et al., 2007; Louis et al., 2016). Nonetheless, astrocytomas of WHO grades I and II differ in their growing pattern and clinical behavior (Ajlan & Recht, 2014). WHO grade I astrocytomas have a promising prognosis of long-term progression-free survival after surgery (Louis et al., 2016) and were, therefore, considered as benign in the statistical study. In contrast, WHO grade II astrocytomas are infiltrative tumors with continuous growth (Zülch, 1979; Louis et al., 2016) and were, therefore, considered as malignant.

CLSM examination revealed, in WHO grade I astrocytomas, well-circumscribed lesions containing bipolar tumor cells with elongated, hairlike projections arranged in parallel bundles, accordingly to finding on traditional histology and the WHO grading scheme (Zülch, 1979; Louis et al., 2007). WHO grade II astrocytomas were characterized, using CLSM, by an increased cellular density of infiltrating, well-differentiated astrocytes, which allowed clear differentiation to WHO grade I and WHO grade III. WHO grade III astrocytomas had a higher cell density, and some mitotic activity could be detected after inverting the colors on the CLSM imaging program.

However, as the Merheim, Hospital, has no pediatric department, the absolute number of astrocytoma samples of WHO grades I and II (8 samples in total; 4 each) was insufficient to draw valid conclusions about the suitability of CLSM for their diagnosis. Therefore, CLSM features of a higher number of samples need to be investigated in future studies.

Benign CNS tumors: Choroid plexus papilloma, schwannoma, pituitary adenoma, hemangioblastoma, and epidermoid tumor are benign tumors of the CNS. Notwithstanding, some can be fatal because of progressive growth in the skull, or may cause additional health problems, such as increased intracranial pressure, mass effect, and focal or global neurological deficits (Aghi & Barker, 2006). Simultaneously, some are associated with various diseases or can progress to malignant forms. For this reason, an accurate diagnosis and treatment, even of benign tumors, can be crucial for the patient's survival and morbidity.

CLSM examination immediately demonstrated cellular characteristics similar to those revealed in the H&E stained sections of the same ROI: crypt structures in choroid plexus papillomas, spindle-shaped Schwann cells in schwannomas, monomorphic epithelial cells in pituitary adenomas, prominent pathological vasculature in hemangioblastomas, and "cell ghosts" in epidermoid tumors.

However, the small number of available tumor samples of these tumor types also precluded a valid assessment of the suitability and accuracy of CLSM as a diagnostic tool. The small number can be explained by their generally low incidence rate compared to meningiomas and glioblastomas and by the fact that patients with symptom-free and non-growing benign tumors usually do not undergo surgical treatment (Aghi & Barker, 2006). This also applies to malignant tumors found in critical regions of the brain and to tumors that have been diagnosed but not removed at the patient's request, which were often treated without surgery.

4.3 Contrast agents evaluated with CLSM

Fluorescence imaging is a valuable tool in the identification and resection of brain tumors, offering a generalized platform to guide and identify remnant tumor tissue, tumor borders, and healthy tissue (Zhao et al., 2013; Parrish-Novak et al., 2015). Major advantages of fluorescence over other imaging methods are the use of non-ionizing radiation, which makes it significantly safer than several traditional modalities (X-ray, CT, PET), and the ability to miniaturize the system components to achieve minimally invasive surgery.

However, suitable fluorescent dyes to stain human tissue *in vivo* are one of the greatest challenges when using fluorescence imaging in neurosurgery, especially due to strict FDA and EMA guidelines regarding limited research trials on their quality, safety, and efficacy (Schlosser et al., 2010; Whitson et al., 2011; Foersch et al., 2012; Wirth et al., 2012; Snuderl et al., 2013; Nguyen & Tsien, 2013). FDA- and EMA-approved fluorescent agents for human application are fluorescein sodium and ICG, but their use has been limited to clinical trials in neurosurgical oncology (Sanai et al., 2011b; Eschbacher et al., 2012; Nguyen & Tsien, 2013). In Europe, 5-ALA is the only permitted contrast agent for high-grade brain tumor imaging (EMA, 2018). In the US, 5-ALA is still awaiting approval by the FDA (Nguyen & Tsien, 2013).

4.3.1 5-ALA: *in vivo* study

In this study, 5-ALA was tested with the CLSM-488 nm approach, as Kim et al. showed further excitation spectra at 495 nm, 546 nm, and 625 nm beside the highest peak, at 405 nm, of 5-ALA-induced PpIX (Kim, 2010). It is the only fluorescent dye used which provides specific contrast in neoplastic cells and does not accumulate in healthy brain tissue (Stummer et al., 1998). However, PpIX fluorescence was also found in regions of gliosis and brain tissue altered with reactive astrocytes or invaded inflammatory cells (Stummer & Suero Molina, 2017).

In neurosurgery, 5-ALA is mostly used to enhance tissue contrast in high-grade gliomas, foremost glioblastomas. Most commonly, for wide-field microscopy detection, a dose of 20 mg/kg Gliolan®(5-ALA) is administered orally 2 to 4 hours before surgery. Peak PpIX production can be expected 6 to 8 hours after application, which should correspond to the tumor removal phase. The generated PpIX remains elevated for 12 hours (Stummer et al., 2003). In the rats treated with Gliolan®, the optimal peak was achieved after an incubation time of 5 hours. This was very time consuming and needed to be timed perfectly, in contrast to the other fluorescent dyes, which were used immediately in this study.

Experience with the use of CLSM in combination with 5-ALA is scarce. PpIX fluorescence in low-grade gliomas was examined by Sanai et al. using an Optiscan®-488 nm excitation device. The authors were able to detect PpIX fluorescence in all 10 patients, but the fluorescent signal was very low and offered little information about cellular features (Sanai et al., 2011). Further research on the fluorescent ability of PpIX to enhance contrast in gliomas was carried out by Martirosyan et al. in rats and mice. Although fluorescence was detected, it did not allow delineation of histopathological features comparable with that achieved with H&E staining (Martirosyan et al., 2014).

Consistent with these results, PpIX exhibited only weak fluorescence obtained with the Cellvizio®-488 nm excitation device in this study. It was possible neither to identify tumor boundaries nor to discriminate between healthy and tumorous tissue because of the faint fluorescent intensity resulting from a suboptimal excitation range. Thus, 5-ALA is not appropriate for use with the CLSM-488 nm device. In the future, with the application of more advanced CLSM devices with greater acquisition rates and wavelengths more adequate to the optimal excitation for PpIX (λ_{ex} of 405 nm), 5-ALA may improve *in vivo* tumor assessment not only macroscopically but also microscopically on a cellular level.

4.3.2 Fluorescein sodium: *in vivo* study

Fluorescein was investigated in this study because it is the most commonly used contrast agent combined with CLSM for gastrointestinal tissue imaging (Wallace et al., 2010). In 2004, Kiesslich and colleagues published the first clinical trial that evaluated the use of CLSM and intravenous fluorescein in patients during ongoing colonoscopy for the detection of neoplasm (Kiesslich et al., 2004). Following this, the same authors reported the first application of fluorescein-aided CLSM in the *in vivo* diagnosis of *Helicobacter pylori* infection (Kiesslich et al., 2005) and of pathologies such as Barrett's esophagus (Kiesslich et al., 2006). Furthermore, the safety of intraoperative CLSM in combination with fluorescein was demonstrated in 2272 patients in the diagnosis of gastrointestinal lesions (Wallace et al., 2010). Since then, CLSM with fluorescein contrast has been used extensively to detect neoplastic cells in various other clinical fields, such as in hepatology (Mennone & Nathanson, 2011), pulmonology (Fuchs et al., 2011), and urology, (Sonn et al., 2009) in preclinical and clinical studies.

In the field of neurosurgery, intravenous fluorescein for CLSM-based imaging was used for the first time in 2010 to examine gliomas in mice. The authors were able to distinguish *in vivo* between neoplastic and healthy tissue and to identify tumor margins and infiltrating tumor cells on a cellular level (Sankar et al., 2010). Similar results were obtained by Foersch et al., who applied CLSM for *in vivo* imaging of fluorescein in rats (Foersch et al., 2012). Finally, in 2011, Sanai and colleagues conducted the first human clinical trial of fluorescein-guided CLSM technology in 33 patients with brain tumors (Sanai et al., 2011a). The authors were able to detect vascular neoproliferation and tumor margins. However, since intravenous fluorescein stains both vasculature and the extracellular matrix but fails to stain nuclei, the evaluations of key histopathological features such as mitoses and pleomorphism were impossible, which made diagnosis of lesions challenging (Sanai et al., 2011a).

Similar results were obtained in this study. Fluorescein was well suited in visualizing general cytoarchitectural features as well as vessel density and shapes, but the lack of nuclei accentuation made it difficult to distinguish tumor areas reliably, which precluded a sufficient tumor resection in rats. Additionally, fluorescein-assisted surgery had its limitations in the subjective interpretation of fluorescence intensity that was low in areas with intact vasculature. The limitations of fluorescein could possibly be avoided by using FITC-dextran with a higher molecular weight, which would increase the specificity of fluorescent extravasation in the tumor area (Natarajan et al., 2017). However, neither the FDA nor the EMA have approved FITC-dextran for use in humans (Foersch et al., 2012). Thus, although successfully used in other clinical fields, fluorescein is not suggested for an application in neurosurgery with the CLSM approach.

4.3.3 Cresyl violet: *ex vivo* study

Another important contrast agent used in this study is CV. CV is often used to investigate the proportion of DNA and RNA molecules in nerve tissues, as its alkaline chemical properties enable staining of the acidic components of the neuronal cytoplasm (Pilati et al., 2008). CV is a nontoxic and clinically safe dye but is not approved by the FDA or EMA for human application (George & Meining, 2003; Goetz et al., 2009b). Nonetheless, in oncology, CV has been used in clinical studies for the staining of cervical lesions in gynecology and for the examination of suspicious lesions through chromoendoscopy in gastroenterology (Goetz et al., 2009).

In the present study, topically applied CV staining labeled the cytoplasm, allowing the cell nuclei to appear as dark spots. The staining enabled a more detailed visualization of capillaries and cellular structures compared to native imaging using CLSM. Unfortunately, technical limitations regarding the applicable wavelength for CV have been recognized. In particular, the ability to visualize tumor features such as cellular pleomorphism was limited due to faint fluorescence intensity. Therefore, CV was not considered in the resection trial with rats. In the future, with the application of advanced CLSM devices (currently in progress) exhibiting wavelengths similar to those of CV (λ_{ex} of 540 nm), CV may represent a suitable dye for intraoperative tissue examination in the neurosurgical operating theater.

4.3.4 Erythrosine B and other food dyes: *ex vivo* study

Erythrosine is a red xanthene dye approved by the FDA, by the Joint FAO/WHO Expert Committee on Food Additives (JECFA), and by the EU Scientific Committee for Food (SCF) for use as a color additive in foods, cosmetics, and pharmaceuticals (SCF, 1983; 1989; FDA, 1995; WHO, 1996; JECFA, 2006). It is water-soluble and has a 58% iodine content (Kobylewski & Jacobson, 2012), but it is considered safe for consumers when the daily acceptable intake of 0–0.1 mg/kg bw/day, with a maximum intake level of 200 mg/kg/day, or 75 mg/day for a child of 30 kg, is not exceeded (Gardner et al., 1987). Furthermore, Webb and colleagues demonstrated the metabolic stability of the food dye in rats; after application of 500 mg/kg bw erythrosine, the ingested amount was almost completely excreted via feces, with unchanged iodine content (Webb et al., 1962).

To the best of the author's knowledge, this study is the first to use food dyes as contrast agents to visualize CNS tumors with the CLSM approach. Of all investigated food dyes (allura red AC, canthaxanthin, ponceau SX, and rubixanthin), only erythrosine enhanced the tissue contrast obtained by CLSM. Erythrosine's value lies mainly in its ability to detect large features, such as blood vessels, which were immediately distinguishable from the surrounding tissue.

The main advantages of erythrosine compared to other fluorescent dyes not approved for surgical purposes are the following: (1) it is safe for an *in vivo* application, (2) it is approved by the FDA and SCF for usage as a food additive, and (3) it is already clinically approved for use in dentistry (Wood et al., 2006; Allaker & Douglas, 2009), thus facilitating its implementation in neurosurgical clinical practice. Unfortunately, staining with erythrosine, even with higher concentrations, did not yield consistently satisfactory results in tumor diagnoses compared to other stains, notably AF. Therefore, erythrosine, in combination with the current available CLSM devices, is not suggested for neurosurgical practice.

4.3.5 Acriflavine hydrochloride and acridine orange: *ex vivo* and *in vivo* studies

AF and AO were used in this study due to their appropriate wavelength with the CLSM device at 488 nm excitation. Furthermore, the yellow acridines show high fluorescence intensity and have been used in various clinical fields, such as a remedy for sleeping sickness, as a topical antiseptic, and as contrast agents in fluorescence and epifluorescence microscopy (Parng et al., 2004, Gruenwedel, 2003; Kawai et al., 2009; Kessel et al., 1991; Cossarizza et al., 1994; Poot & Pierce, 2001). In oncology, acridines have been used to detect high-grade, upper urinary tract and urothelial carcinoma cells *in vitro* (Li et al., 2014).

Combined with CLSM, AF has been used extensively in gastroenterology and pulmonology for the imaging of various tumors (Goetz et al., 2007; Haxel et al., 2010). AF staining enabled high sensitivity, specificity and accuracy in the tumor detection with CLSM, which were never below 70%, especially in the diagnosis of upper and lower gastrointestinal neoplasms (Polglase et al., 2005; Kiesslich et al., 2004; Meining et al., 2007). Concordantly, in the present study, CLSM imaging of topically applied AF enabled an 88.6% correct detection rate in predicting the tumor histology of the CNS biopsy. Similarly, Foersch and colleagues scored an 87.1% correct detection rate in the diagnosis of primary CNS tumors and metastases using CLSM (Foersch et al., 2010).

Overall, AF and AO staining of fresh tumor samples revealed excellent correlation to the H&E stained sections due to cell nucleus staining. Compared to traditional histology, CLSM was less labor-intensive and allowed faster visualization because of rapid uptake of AF/AO stain (approximately 1 min). Especially two confocal features were found to effectively differentiate neoplastic from non-neoplastic tissue after AF/AO staining similar to features of hematoxylin staining: (1) higher amount and alteration of cell nuclei (such as pleomorphism or increased nuclear-to-cytoplasm ratio) and (2) architectural disruption of cellular structures and pathological blood vessels.

In the *ex vivo* studies, AF yielded the most detailed histopathological information with the CLSM device at 488 nm excitation. Its ability to stain the cell membrane and extracellular matrix in a low amount, alongside its cell nucleus labeling, allowed a better evaluation of tumor cells than with AO, erythrosine and CV. Therefore, AF was chosen for the *ex vivo* assessment of the tumor grade, using CLSM-488 nm to differentiate between healthy and tumorous tissue and to define tumor features of various primary CNS samples. Moreover, in this study, AF was the only dye unapproved by the FDA/EMA for human application that was investigated *in vivo* in rats. Here, AF-based CLSM imaging allowed for a better resection rate of tumor tissue than 5-ALA-based fluorescence-guided surgery as the optical gold standard.

A drawback of this agent, besides concerns about carcinogenicity (Ferenc et al., 1999), was its limited tissue penetration, which resulted in the need to stain tissue repeatedly during the surgery process. All limitations are summarized in Section 4.7. Nonetheless, the advantage of AF outweigh its drawbacks. The high contrast of cellular details allowed for a fast tumor diagnosis and resection. Therefore, AF combined with CLSM is suggested for a rapid *ex vivo* examination of biopsies in the operating room.

4.3.6 Indocyanine green: *ex vivo* and *in vivo* studies

With the development of an near-infrared CLSM, ICG (λ_{ex} of 760–775 nm/λ_{em} of 835 nm) was first applied in the diagnosis of liver steatosis and fibrosis (Goetz et al., 2010). In neurosurgery, the CLSM device at 780 nm excitation and ICG as contrast agent were first investigated by Martirosyan and colleagues in murine glioma models, in which excellent results in the visualization of tumor tissue, transitional zones, and healthy brain tissue were reported (Martirosyan et al., 2011). Accordingly, Foersch et al. visualized, with a similar CLSM device, tumor regions as well as small intratumoral hemorrhages (Foersch et al., 2012). In contrast to the current study, both groups applied ICG intravenously, which resulted in ICG time dependency and low cellular resolution (Martirosyan et al., 2011, Foersch et al., 2012). Hence, the current study is the first one to investigate CLSM after a topical application of ICG.

The CLSM *in vivo* study provided high-resolution images of healthy and neoplastic tissue as well as of transition zones after application of ICG onto a rat brain, thus allowing better surgical results compared to the other contrast agents imaged with CLSM and to 5-ALA-based fluorescence-guided surgery. High sensitivity, long stability (up to 2 hours in tissues), ease of use, and lack of associated radiation exposure would make intraoperative CLSM with ICG a perfect tool for guiding intraoperative tumor resections in humans. Additionally, the correlation of ICG-based CLSM *ex vivo* imaging of human CNS tumors and H&E stained sections was excellent and allowed for high statistical accuracy of 96.67%, demonstrating the potential of CLSM for the intraoperative diagnosis of CNS lesions.

Moreover, multiple advantages could be shown of ICG-based fluorescence imaging using CLSM compared to wide-field visualization of 5-ALA-induced PpIX. First, its cell-based imaging allowed for a more precise resection of infiltrative tumor cells. Second, its applications could be expanded to low-grade gliomas and other CNS lesions. Third, its near-infrared fluorescence allowed deeper penetration without interference by blood artifacts.

Further studies should analyze the mechanism of how ICG enters the cells, as this may allow optimization of cell staining using ICG. Furthermore, the efficiency and suitability in clinical routines as well as the acute and long-term safety and tolerability should be investigated in the future.

Healthy brain: To apply CLSM as an adjunct to neurosurgical tumor resections, knowledge of CLSM features from healthy brain structures is required to distinguish them from neoplastic tissue. Therefore, ICG for CLSM-based imaging was applied to study *in vivo* healthy brain structures of a pig. Intraoperative CLSM demonstrated high-resolution histopathological features, such as astrocytes, oligodendrocytes, and pyramidal cells, as well as deeper brain structures, such as the choroid plexus. Nevertheless, to establish an accurate CLSM neuroanatomy atlas, it would be necessary to examine healthy brain structures from a whole human brain.

4.4 Grading of astrocytic tumors: *ex vivo* study

In the present study, the suitability of CLSM for diagnosis of astrocytic tumors and their grading is demonstrated. CLSM revealed cellular structures of all astrocytic tumors, such as high cell density, cell pleomorphism, microvascular hyperplasia, and pseudopalisading necrosis, according to the WHO grading system (Louis et al., 2016).

This enabled neuropathologists, who were blinded to the results of the traditional histology, to predict the correct WHO grade of various astocytomas with a diagnostic accuracy of 89.7%.

The specific grading of tumors is of high importance, as an incorrect grading can result in fatal consequences for the patient. For a correct diagnosis to be made, the biopsy has to contain the highest-grade component. This is, however, very difficult, since astrocytomas are heterogeneous, and parts of the same tumor often contain different grades in the frozen sections. Thus, it is possible that the highest-grade component is not present in the specimen sampled. A false interpretation of the tumor's grade could lead to an "undergrading" resulting in an "undertreatment" (e.g., surgery without radiographic follow-up). Similarly, an error causing an "overgrading" could lead to an "overtreatment" (e.g., chemoradiation of benign lesions). Both errors result in high risks for the patient's health (Chandrasoma et al., 1989; Glantz et al., 1991). Errors may also result from freezing artifacts, an incorrect interpretation, and/or the poor quality of the sample in frozen sections (Amraei et al., 2017). In contrast, CLSM is not affected by sampling errors, as it reveals histopathological features in real time, without the need for special sample preparation and thus allowing immediate diagnosis.

CLSM images enabled correct detection rates of 100% for pilocytic astrocytomas, 93.7% for diffuse astrocytomas, and 90% for anaplastic astrocytomas. For frozen section analysis, various studies have also evaluated the accuracy of the diagnosis of tumors. Most importantly, in the study conducted by Shrestha and colleagues on 90,000 entities, the authors showed a diagnostic accuracy of 98.52%, but tumors of different organs were evaluated here (Shrestha et al., 2009). CNS limited studies showed an accuracy of 77.9% in the diagnosis of 398 CNS lesions (Amraei et al., 2017), an accuracy of 85.7% in the diagnosis of 1000 CNS lesions (Oneson et al., 1989), and an accuracy of 96.6% in the diagnosis of 1,315 CNS lesions with an accuracy of 87.6% in the diagnosis of gliomas (Regragui et al., 2003). Overall, most mistakes were made on establishing the subtype or grade of astrocytomas, in particular high-grade astrocytomas were often mistaken as lower-grade astrocytomas (Amraei et al., 2017).

The same result was found in this study, the lowest diagnostic accuracy was made in the determination of glioblastomas. The correct detection rate here was only 75%, which is lower than that for frozen section analysis, which ranged between 78.4% and 95% (Mat Zin & Zulkarnain, 2019).

Since neither CLSM nor frozen analyses could provide a diagnostic accuracy of approximately 100%, the combination of both techniques, CLSM and frozen section analysis, is proposed. This may increase the diagnostic accuracy and support a safe tumor resection. For example, CLSM may be used first to scan the tissue for areas with the highest-grade components for a biopsy, and then frozen section analysis could be performed for final evaluation. However, the efficacy of the combination of these approaches needs to be proven first in preclinical and clinical studies.

Currently, immunohistochemistry (screening for molecular markers) is routinely performed for an accurate diagnosis of several primary CNS tumors and their subtypes. For instance, primary glioblastomas have no *idh* variations (mutations affecting codon 132 of the *idh1* gene or codon 172 of the *idh2* gene) compared to WHO grade II–III gliomas (diffuse astrocytoma, oligodendroglioma, oligoastrocytoma, anaplastic astrocytoma, anaplastic oligodendroglioma, and anaplastic oligoastrocytoma) and secondary glioblastomas, in which an *idh* variation occurs in approximately 80% of the cases (Balss et al., 2008). Hence, traditional histology and immunohistochemistry are indispensable for an accurate diagnosis and cannot be replaced by CLSM. Another possibility, other than the combination of frozen section analyses and CLSM, could be the combination of CLSM and immunohistochemistry (see subsection 4.8), which would close the gap between molecular examination and surgical microscopic imaging.

4.5 Comparison of CLSM and wide-field microscopy: *in vivo* study

To the best of the author's knowledge, this study was the first to evaluate the use of different fluorescent dyes in the CLSM approach as an adjunct to the resection of high-grade gliomas and to compare this approach to routine surgical wide-field microscopy with 5-ALA as the optical gold standard.

Both the intraoperative detection of tumor margins and the identification of neoplastic tissue and its infiltrating cells are two of the most demanding aspects of brain tumor surgery (Adamson et al., 2010). In this study, intraoperative CLSM was able to achieve both due to real-time high-resolution imaging of tumor features in rats, which enabled better resection result than with the optical visualization standard.

However, the tumors were not the same size although an equal amount of C6 glioma cells was implanted into the rats' brains. It would have been necessary to monitor the tumor size by MRI before surgery; this was, however, not possible at our institution. Nonetheless, to provide nearly the same conditions, four rats (one for each fluorescent agent: AF, AF + fluorescein, ICG, and 5-ALA as control) always received the C6 glioma cell implantation on the same day. Moreover, these rats were surgically treated on the same day to minimize performance differences.

During the surgery, each removed biopsy was collected to enable analysis by traditional histology to examine if and how much healthy tissue was removed. This was, however, not possible for all biopsies, as a few were too small for histopathological procedure. For the same reason, the margins could not always be identified in the biopsies. Thus, no exact conclusions about the precise resection of the tumor could be made by traditional histology.

The present study also pointed out that a complete resection of infiltrative tumor cells is impossible, even with an approach facilitating tumor resection on a cellular level. The intraoperative CLSM was investigated in C6 glioma formed in Sprague-Dawley rats by injection of C6 glioma cells. The C6 glioma cell line was first induced by Benda and colleagues by cloning brain tumors induced through N-nitrosomethylurea in Wistar Furth inbred rats. The cells have a high proliferation rate and are morphologically similar to human glioblastoma cells. They preferentially grow on blood vessels due to a high affinity for endothelial basement membranes, and they are highly invasive (Benda et., al 1968).

This could also be seen in the rat brain sections in this study: tumor cells invaded the whole rat brain, but especially the endothelial basement membranes and the perivascular spaces showed significant degrees of invasion. The infiltrating neoplastic cells were impossible to remove without killing the animal. Therefore, a brain was considered free from tumor cells when all tumor cells close to the bulk tumor within the range of the probe were removed (see subsection 2.6.8). This containment was necessary to allow comparison between the two image-guided technologies as well as between the contrast agents in their ability to facilitate glioma resection.

Best resection outcome was achieved by CLSM in combination with ICG as contrast agent. Nonetheless, for a better resection outcome of high-grade gliomas, a combination of macroscopic evaluation of 5-ALA using wide-field microscopy and a microscopic evaluation of ICG using CLSM are suggested. Because 5-ALA does not provide contrast enhancement in low-grade tumors, CLSM would generally constitute an important adjunct for extending tumor resection, especially to detect tumor residues at the final stage of surgery.

4.6 Advantages of CLSM

In the field of neurosurgery, CLSM may serve as a valuable adjunct to the current modalities due to a favorable combination of advantages found in this study.

- The miniaturization of the apparatus, as compared to the original bench-top confocal microscopes, allowed a portable use of CLSM suitable for application in clinical settings. It fitted in any operating room and could be easily integrated into the clinical workflow.
- Compared to intraoperative frozen section analyses, the entire lesion of the surgical cavity could be studied in real time, avoiding sampling errors and enabling faster tumor resection. As an example, in the present study, the total imaging time was approximately 10 min per rat. This was enough time to image a mean of 20 biopsy locations per animal. In comparison, the analysis of one biopsy by frozen section requires approximately 20 min for processing and interpretation. Thus, the number of biopsies may be decreased, and damage to healthy CNS structures may greatly be reduced by using CLSM. However, information about the entire surgical time on humans using CLSM-guided surgery compared to frozen section analysis is missing.
- CLSM *in vivo* imaging offered immediate visualization of transition zones as well as the behavior (malignant or benign) of brain tissue in rats. Gaining real-time insight into whether margins are free of tumor cells during the initial surgery could reduce the frequency of second surgeries and minimize both undertreatment and overtreatment of tumor patients. Thus, both better-quality treatment and cost savings to healthcare and insurance systems may be achievable.
- CLSM imaging provided cellular imaging of all primary CNS entities regardless of their grade, in contrast to wide-field visualization of 5-ALA-induced PpIX fluorescence, which enhance tissue contrast only in high-grade tumors.
- The real-time CLSM findings provided additional information compared to traditional histology, because it was possible to observe live cellular interaction over time. Thus, CLSM may help to better understand the development of tumors and provide novel cellular features of CNS tumor architecture. For example, in four plasmacytoma samples (57%), large oval structures were detected by CLSM, which are unusual for this tumor type and were not revealed by H&E staining of the same samples. Furthermore, in one pituitary adenoma sample, cell accumulation surrounded by a cell-free layer was found. The findings could not be explained by the responsible neuropathologists and need to be investigated in a larger number of samples.
- Because all data was digitally acquired and stored with the CLSM software, it was possible to review sequences multiple times. In the case of human surgery, a neuropathologist could review the images without delay and be involved in decisions during the surgery.

- The CLSM approach was easy to handle and required only minimal training with a short learning curve.

Nonetheless, CLSM is a diagnostic tool and not a therapeutic measure. As previously mentioned, CLSM should be used to enhance traditional histology, mapping and monitoring rather than replacing it. The simultaneous use of various visualization techniques during surgical resection may allow both a macroscopic and microscopic evaluation of suspect tissue while monitoring essential healthy neuronal structures at the same time. This may allow for a safer tumor resection with the best possible outcome for the patient.

4.7 General limitations and caveats of CLSM

A limitation of this study was the application of the contrast agents CV, AF, and AO, which are not approved by the FDA and EMA for an *in vivo* use in humans; further, hypothetical concerns have been raised about the risk of mutagenesis by AF and AO (Ferenc et al., 1999; Nguyen & Tsien, 2013). Despite this concern, AF has been used in several human clinical studies, primarily in Europe, and has shown no severe side effects combined with CLSM in gastroenterology and pulmonology (Goetz et al., 2007; Haxel et al., 2010). Furthermore, Lee et al. reported the antitumor effect of AF in cell culture and in an adenocarcinoma mouse model (Lee et al., 2014). Likewise, Shay et al. reported a slowing-down effect of AF on tumor progression in a mouse model of colorectal cancer (Shay et al., 2014). More recently, Mangraviti et al. demonstrated the potency of AF against brain tumors in a preclinical rat model. The *in vivo* application of AF provided a nearly 100% long-term survival. This was mainly achieved by an AF-induced inhibition of hypoxia-inducible factor 1 (HIF-1), which plays a critical role in cancer progression, tumor growth, and vascularization (Mangraviti et al., 2017). Moreover, AF has been used in patients for at least 5 months without major side effects (Wainwright, 2001). These reports support further clinical development and evaluation of AF's safety profile, and they may allow an *in vivo* brain application in future. Until then, AF can be applied as a rapid *ex vivo* stain in the operating room to examine biopsies in real time.

A further limitation of this study was that no postoperative performance status or other indicators of neurological morbidity were measured after surgical tumor treatment in rats. Therefore, additional studies regarding survival time and life quality after surgery with the CLSM approach are required, especially compared to other approved modalities, such as 5-ALA wide-field microscopy. Furthermore, additional studies with a higher number of animals and more CNS tumors are needed to verify the results of the rat trial.

A physical limitation of the CLSM device at 488 nm excitation was its excitation of red blood cells. This led to blood contamination of the entire imaging field, causing obscured tissue features on the CLSM images. The CLSM probe needed to be mechanically cleaned several times by elevating the probe from the tissue surface, which interrupted the imaging flow during the surgery. This could be avoided by the integration of an auto-irrigation mechanism similar to that used with the endoscope.

Motion artifacts introduced by the operator or by respiration of the animal were further common causes of image impairments. However, movements by the operator decreased with increasing practical experience using the CLSM device.

4.8 Future directions

This study describes the combination of CLSM and tumor-nonspecific dyes in the identification of cellular features of tumors and of healthy tissue. To identify and detect tumors more precisely, intraoperative CLSM combined with molecular imaging labels to target specific cancer biomarkers is suggested as the next step. This approach may also allow doctors the intraoperative visualization of the expression of molecular targets that influence the behavior of the tumor and its response to therapy in real time.

Molecular imaging probes that could be used with CLSM and have been already investigated in brain imaging fall into three categories: nanoparticles, antibodies, and peptides. Of these, "nanoparticles are organic or inorganic particles between 1 and 100 nm in size" (Ravichandran et al., 2016). They can be engineered to deliver a variety of small molecules, such as contrast agents and chemotherapy. Due to their small size, they are ideal for protein labeling through specific ligands on the particles (Sarin et al., 2008). In oncological research, nanoparticles have demonstrated that they provide intraoperative imaging of brain neoplasm and demarcate tumor boundaries (Arndt-Jovin et al., 2009; Orringer et al., 2009). However, nanoparticle strategies are still in their infancy and need further studies in clinical models to determine their safety profile and long-term effects before an implementation in neurosurgery is feasible.

In contrast, the concept of antibodies is supported by many clinical studies (van Dongen et al., 2007; Attarwala, 2010; Vacchelli et al., 2014). First and foremost, in the study by Keller et al., the authors used a prototype of a fluorescence colonoscopy to detect fluorescently labeled anti-CEA (carcinoembryonic antigen) antibodies in humans. The labeled monoclonal antibodies were sprayed onto the mucosa, and they allowed macroscopic detection in 19 of 25 carcinomas (Keller et al., 2002). This approach showed several advantages, such as high target specificity, slow extraction, and appropriate pharmacokinetic properties for imaging applications (van Dongen et al., 2007). Most importantly, the FDA has approved various labeled antibodies for diagnostic imaging of different cancer types (van Dongen et al., 2007).

In the field of neuro-oncology, a specific antibody was successfully developed in mice by Iqbal and colleagues. The authors evaluated single-domain antibodies specific to anti-insulin-like growth factor–binding protein 7 (IGFBP7), that accumulates in the basement membranes of glioblastoma vessels, but not in healthy vessels (Iqbal et al., 2010). Other promising fluorescence-labeled antibodies include those against epidermal growth factor receptor (EGFR), tumor necrosis factor (TNF), vascular endothelial growth factor-1 (VEGF-1), and insulin-like growth factor 1 receptor (IGF-1R), which were developed by different research groups (Wu & Olafsen, 2008; Foersch et al., 2010; Atreya et al., 2014; Dou et al., 2016). All these targets are overexpressed in tumor tissue and play an important role in cell growth pathways responsible for cell proliferation, migration, and/or neovascularization (Dou et al., 2016). Through the specific binding of the fluorescence-labeled antibodies to these targets, tumor tissue could be discriminated from healthy tissue using a regular confocal microscope or by spectrometry analyses (Wu & Olafsen, 2008; Foersch et al., 2010; Atreya et al., 2014; Dou et al., 2016). However, disadvantages of fluorescence-labeled antibodies were also identified, including a long half-life, low permeability, and, most importantly, risks of immunogenicity and toxicity (Burggraaf et al., 2015).

Alternatively, low-molecule-weight small peptides conjugated to fluorescent agents with a high affinity for an oncogene could be used. Such a peptide was successfully investigated by Burggraaf et al. in humans with colon cancer. The peptide was a small fluorescently labeled 26-amino acid cyclic agent (GE-137) with a high affinity for the *c-Met* gene, which is overexpressed in many cancer types, including malignant gliomas. GE-137 demonstrated a number of advantages over antibodies, including favorable pharmacokinetics and tissue distribution patterns, high permeability, flexibility in chemical modification, and, most importantly, a high safety profile in humans (Burggraaf et al., 2015).

Another promising example is integrin *avβ3*, which is highly expressed in tumor cells and tumor vessels but low in healthy cells. *In vivo* fluorescence imaging of integrin *avβ3* has been well studied in glioblastomas and medulloblastomas in various preclinical tumor models (Chen et al., 2004; Hsu et al., 2006; Huang et al., 2012). However, investigation in clinical studies in humans is required to prove its potential in a neurosurgical setting.

Overall, the combination of selective fluorescently labeled markers, targeted macroscopic image-guided surgery, and CLSM would represent a promising avenue for precise tumor detection. Moreover, CLSM *in vivo* imaging, in real time, of tumor markers' activity and their location changes over time would further promote the understanding of biological processes in tumors and may provide "on-the-spot" individualized therapy.

4.9 Conclusions

This study establishes CLSM as a feasible and reliable tool, not only in increasing the initial diagnosis yield but also in aiding the resection of tumors, especially in combination with ICG and AF. CLSM allowed clear differentiation between tumor and healthy tissue on a cellular level, making surgical margins more accurate than ever before. It was possible to scan a much larger area for tumor cells by using CLSM than would otherwise be possible via a biopsy, which further facilitated an extensive resection of the tumor. The utilization of CLSM in the operating room may improve the surgeon's intraoperative decisions more accurately and quickly, regarding the extent of resection and the functional preserving of brain tissues. Real-time telepathology with neuropathologists may further enhance neurosurgical decisions. Altogether, this could reduce operating time and anesthesia and minimize the need for a second surgery.

To establish this tool for use in neurosurgery, a more detailed CLSM atlas of both CNS tumors and healthy structures must be established in cooperation with experienced neuropathologists, and it must be integrated as a training program for doctors to gain the ability to interpret the *in vivo* CLSM images. The development of additional fluorophores suitable for *in vivo* use in humans, such as tumor-specific molecular probes, could further promote the use of CLSM in neurosurgery. In addition to advances in contrast, CLSM technology requires improvements facilitating deeper tissue imaging and detecting weak fluorescent signals. The aid of multiple laser lines and tunable emission filters in one CLSM device could detect multiple fluorophores and further increase the accuracy of fluorescence information. Finally, clinical trials with large patient cohorts are crucial to fully establish the role of CLSM in the neurosurgical operating room.

In conclusion, this study demonstrates CLSM, especially combined with ICG and AF, as an efficient approach to both increasing the diagnostic yield and extending the resection of tumors. In neurosurgical oncology, CLSM may reduce the risk of injury to eloquent tissue and detect *in vivo* brain invasion by tumor cells. Additionally, CLSM can be used intraoperatively to discriminate different CNS lesions, which may improve decisions during the surgery. Nonetheless, it is crucial to mention that the CLSM approach is still in its infancy, and several technical, training, logistic, and medico-legal issues need to be resolved before its clinical integration into neurosurgery can be achieved.

5. References

Ackerman, S. Discovering the Brain. Washington (DC): National Academies Press (US). (1992) 2, Major Structures and Functions of the Brain. Available from: https://www.ncbi.nlm.nih.gov/books/NBK234157/.

Adamson, D.C., Rasheed, B.A., McLendon, R.E. & Bigner, D.D. (2010) Central nervous system. Cancer biomarkers : section A of Disease markers, 9, 193-210.

Aghi, M. & Barker, F.G., 2nd (2006) Benign adult brain tumors: an evidence-based medicine review. Progress in neurological surgery, 19, 80-96.

Alattar, A. A., Carroll, K. T., Bryant, A. K., Hirshman, B., Joshi, R., Carter, B. S., . . . Chen, C. C. (2019). Prognostic Importance of Age, Tumor Location, and Tumor Grade in Grade II Astrocytomas: An Integrated Analysis of the Cancer Genome Atlas and the Surveillance, Epidemiology, and End Results Database. World Neurosurg, 121, e411-e418. doi:10.1016/j.wneu.2018.09.124.

Allaker, R.P. & Douglas, C.W. (2009) Novel anti-microbial therapies for dental plaque-related diseases. International journal of antimicrobial agents, 33, 8-13.

Allen, J.C., Siffert, J. & Hukin, J. (1998) Clinical manifestations of childhood ependymoma: a multitude of syndromes. Pediatric neurosurgery, 28, 49-55.

Amraei, R., Moradi, A., Zham, H., Ahadi, M., Baikpour, M. & Rakhshan, A. (2017) A Comparison between the Diagnostic Accuracy of Frozen Section and Permanent Section Analyses in Central Nervous System. Asian Pacific journal of cancer prevention : APJCP, 18, 659-666.

Arndt-Jovin, D.J., Kantelhardt, S.R., Caarls, W., de Vries, A.H., Giese, A. & Jovin Ast, T.M. (2009) Tumor-targeted quantum dots can help surgeons find tumor boundaries. IEEE transactions on nanobioscience, 8, 65-71.

Atreya, R., Neumann, H., Neufert, C., Waldner, M.J., Billmeier, U., Zopf, Y., Willma, M., App, C., Munster, T., Kessler, H. et al. (2014) In vivo imaging using fluorescent antibodies to tumor necrosis factor predicts therapeutic response in Crohn's disease.

Nature medicine, 20, 313-318.

Attarwala, H. (2010) Role of antibodies in cancer targeting. Journal of natural science, biology, and medicine, 1, 53-56.

Baek, H.Y., Lee, H.-J., Kim, J.M., Cho, S.-Y., Jeong, S. & Yoo, K.Y. (2015) Effects of intravenously administered indocyanine green on near-infrared cerebral oximetry and pulse oximetry readings. Korean J Anesthesiol, 68, 122-127.

Balss, J., Meyer, J., Mueller, W., Korshunov, A., Hartmann, C. & von Deimling, A. (2008) Analysis of the IDH1 codon 132 mutation in brain tumors. Acta neuropathologica, 116, 597-602.

Banks, W.A. (2009) Characteristics of compounds that cross the blood-brain barrier. BMC Neurol, 9 Suppl 1, S3.

Baron Nelson, M., Compton, P., Patel, S. K., Jacob, E., & Harper, R. (2013). Central nervous system injury and neurobiobehavioral function in children with brain tumors: a review of the literature. Cancer nursing, 36(2).

Bayer, S., Maier, A., Ostermeier, M. & Fahrig, R. (2017) Intraoperative Imaging Modalities and Compensation for Brain Shift in Tumor Resection Surgery. International journal of biomedical imaging, 2017, 6028645-6028645.

Behbahaninia, M., Martirosyan, N.L., Georges, J., Udovich, J.A., Kalani, M.Y., Feuerstein, B.G., Nakaji, P., Spetzler, R.F. & Preul, M.C. (2013) Intraoperative fluorescent imaging of intracranial tumors: a review. Clinical neurology and neurosurgery, 115, 517-528.

Bernas, T., Zarebski, M., Dobrucki, J.W. & Cook, P.R. (2004) Minimizing photobleaching during confocal microscopy of fluorescent probes bound to chromatin: role of anoxia and photon flux. Journal of microscopy, 215, 281-296.

Bloch, D.C., Oghalai, J.S., Jackler, R.K., Osofsky, M. & Pitts, L.H. (2004) The fate of the tumor remnant after less-than-complete acoustic neuroma resection. Otolaryngology–head and neck surgery : official journal of American Academy of Otolaryngology-Head and Neck Surgery, 130, 104-112.

Buchner, A.M. & Wallace, M.B. (2015) In-vivo microscopy in the diagnosis of intestinal neoplasia and inflammatory conditions. Histopathology, 66, 137-146.

Buckner, J.C., Brown, P.D., O'Neill, B.P., Meyer, F.B., Wetmore, C.J. & Uhm, J.H. (2007) Central nervous system tumors. Mayo Clinic proceedings, 82, 1271-1286.

Budczies, J., von Winterfeld, M., Klauschen, F., Bockmayr, M., Lennerz, J.K., Denkert, C., Wolf, T., Warth, A., Dietel, M., Anagnostopoulos, I., Weichert, W., Wittschieber, D. & Stenzinger, A. (2014) The landscape of metastatic progression patterns across major human cancers. Oncotarget, 6, 570-583.

Burggraaf, J., Kamerling, I.M.C., Gordon, P.B., Schrier, L., de Kam, M.L., Kales, A.J., Bendiksen, R., Indrevoll, B., Bjerke, R.M., Moestue, S.A. et al.(2015) Detection of colorectal polyps in humans using an intravenously administered fluorescent peptide targeted against c-Met. Nature medicine, 21, 955.

Carlson, K., Pavlova, I., Collier, T., Descour, M., Follen, M. & Richards-Kortum, R. (2005) Confocal microscopy: imaging cervical precancerous lesions. Gynecologic oncology, 99, S84-88.

Cartana, T., Saftoiu, A., Gruionu, L.G., Gheonea, D.I., Pirici, D., Georgescu, C.V., Ciocalteu, A. & Gruionu, G. (2012) Confocal laser endomicroscopy for the morphometric evaluation of microvessels in human colorectal cancer using targeted anti-CD31 antibodies. PloS one, 7, e52815.

Chai, Y.-H., Jung, S., Lee, J.-K., Kim, I.-Y., Jang, W.-Y., Moon, K.-S., Kim, J.-H., Lee, K.-H., Kim, S.-K. & Jung, T.-Y. (2017) Ependymomas: Prognostic Factors and Outcome Analysis in a Retrospective Series of 33 Patients. Brain tumor research and treatment, 5, 70-76.

Chaichana, K. L., Jusue-Torres, I., Lemos, A. M., Gokaslan, A., Cabrera-Aldana, E. E., Ashary, A., . . . Quinones-Hinojosa, A. (2014). The butterfly effect on glioblastoma: is volumetric extent of resection more effective than biopsy for these tumors? J Neurooncol, 120(3), 625-634. doi:10.1007/s11060-014-1597-9.

Chamberlain, M.C. (2003) Ependymomas. Current neurology and neuroscience reports, 3, 193-199.

Chandrasoma, P.T., Smith, M.M. & Apuzzo, M.L. (1989) Stereotactic biopsy in the diagnosis of brain masses: comparison of results of biopsy and resected surgical specimen. Neurosurgery, 24, 160-165.

Charalampaki, P., Javed, M., Daali, S., Heiroth, H.J., Igressa, A. & Weber, F. (2015) Confocal Laser Endomicroscopy for Real-time Histomorphological Diagnosis: Our Clinical Experience With 150 Brain and Spinal Tumor Cases. Neurosurgery, 62 Suppl 1, 171-176.

Chen, B., Wang, H., Ge, P., Zhao, J., Li, W., Gu, H., Wang, G., Luo, Y. & Chen, D. (2012) Gross total resection of glioma with the intraoperative fluorescence-guidance of fluorescein sodium. International journal of medical sciences, 9, 708-714.

Chen, X., Conti, P.S. & Moats, R.A. (2004) In vivo near-infrared fluorescence imaging of integrin alphavbeta3 in brain tumor xenografts. Cancer research, 64, 8009-8014.

Cohen, A. L., Holmen, S. L., & Colman, H. (2013). IDH1 and IDH2 mutations in gliomas. Current neurology and neuroscience reports, 13(5), 345-345. doi:10.1007/s11910-013-0345-4.

Coffey, R.J., Lunsford, L.D. & Taylor, F.H. (1988) Survival after stereotactic biopsy of malignant gliomas. Neurosurgery, 22, 465-473.

Colditz, M.J., Leyen, K. & Jeffree, R.L. (2012) Aminolevulinic acid (ALA)-protoporphyrin IX fluorescence guided tumour resection. Part 2: theoretical, biochemical and practical aspects. Journal of clinical neuroscience : official journal of the Neurosurgical Society of Australasia, 19, 1611-1616.

Cossarizza, A., Kalashnikova, G., Grassilli, E., Chiappelli, F., Salvioli, S., Capri, M., Barbieri, D., Troiano, L., Monti, D. & Franceschi, C. (1994) Mitochondrial modifications during rat thymocyte apoptosis: a study at the single cell level. Experimental cell research, 214, 323-330.

da Silva, C.E., da Silva, J.L. & da Silva, V.D. (2010) Use of sodium fluorescein in skull base tumors. Surgical neurology international, 1, 70.

Daali, S., Javed, M., Altekoester, A.-K., Alhadi, I., Linxweiler, M., Bostelmann, R., Schlegel, J. & Charalampaki, P. (2016) Analysis of 258 Different Lesions of the Central Nervous System for Real Time Histopathological Diagnosis Using Confocal Laser Endomicroscopy. J Mult Scler (Foster City).

Daneman, R. & Prat, A. (2015) The blood-brain barrier. Cold Spring Harbor perspectives in biology, 7, a020412-a020412.

Das, A., Chapman, C.A. & Yap, W.M. (2000) Histological subtypes of symptomatic central nervous system tumours in Singapore. Journal of neurology, neurosurgery, and psychiatry, 68, 372-374.

Deng, Q., Tian, Z., Sheng, W., Guo, H. & Dan, M.E. (2015) Surgical methods and efficacies for cervicothoracolumbar spinal schwannoma. Experimental and therapeutic medicine, 10, 2023-2028.

Devaux, B.C., O'Fallon, J.R. & Kelly, P.J. (1993) Resection, biopsy, and survival in malignant glial neoplasms. A retrospective study of clinical parameters, therapy, and outcome. Journal of neurosurgery, 78, 767-775.

Dou, X., Yan, J., Zhang, Y., Liu, P., Jiang, Y., Lv, S., Zeng, F., Chen, X., Wang, S., Zhanget et al. (2016) SPECT imaging of neuropilin receptor type-1 expression with 131I-labeled monoclonal antibody. International journal of oncology, 49, 961-970.

Drummen, G.P.C. (2012) Fluorescent probes and fluorescence (microscopy) techniques–illuminating biological and biomedical research. Molecules, 17.

Duffau, H. (2014) Preserving quality of life is not incompatible with increasing overall survival in diffuse low-grade glioma patients. Acta neurochirurgica.

Dziedzic, T. & Bernstein, M. (2014) Awake craniotomy for brain tumor: indications, technique and benefits. Expert Review of Neurotherapeutics, 14, 1405-1415.

Eschbacher, J., Martirosyan, N.L., Nakaji, P., Sanai, N., Preul, M.C., Smith, K.A., Coons, S.W. & Spetzler, R.F. (2012) In vivo intraoperative confocal microscopy for real-time histopathological imaging of brain tumors. Journal of neurosurgery, 116, 854-860.

Fass, L. (2008). Imaging and cancer: a review. Molecular oncology, 2(2), 115-152. doi:10.1016/j.molonc.2008.04.001.

FDA (1995) Food labeling: Reference Daily Intakes, Part II: Proposed rule. Fed Regist 59:427-432.

FDA (2018). "NDA/BLA Multi-Disciplinary Review and Evaluation". NDA 211580 505(b)(2)SPY AGENT Green, Indocyanine Green.
https://www.fda.gov/media/124115/download.com.

Fehlings, M.G., Nater, A., Zamorano, J.J., Tetreault, L.A., Varga, P.P., Gokaslan, Z.L., Boriani, S., Fisher, C.G., Rhines, L., Bettegowda, C. et al. (2016) Risk Factors for Recurrence of Surgically Treated Conventional Spinal Schwannomas: Analysis of 169 Patients From a Multicenter International Database. Spine, 41, 390-398.

Feindel, W., Yamamoto, Y.L. & Hodge, C.P. (1971) Red cerebral veins and the cerebral steal syndrome. Evidence from fluorescein angiography and microregional blood flow by radioisotopes during excision of an angioma. Journal of neurosurgery, 35, 167-179.

Fengqiang, L., Jiadong, Q. & Yi, L. (2008) Computer-assisted stereotactic neurosurgery with framework neurosurgery navigation. Clinical neurology and neurosurgery, 110, 696-700.

Ferenc, T., Janik-Spiechowicz, E., Bratkowska, W. & Denys, A. (1999) Mutagenic activity of 3,6-diamino-10-methyl-9,10-dihydroacridine in Salmonella typhimurium cells. International journal of occupational medicine and environmental health, 12, 67-72.

Ferlay J, S.I., Ervik M, Dikshit R, Eser S, Mathers C (2018) Cancer Incidence and

Mortality Worldwide: IARC CancerBase [Internet].

Foersch, S., Heimann, A., Ayyad, A., Spoden, G.A., Florin, L., Mpoukouvalas, K., Kiesslich, R., Kempski, O., Goetz, M. & Charalampaki, P. (2012) Confocal laser endomicroscopy for diagnosis and histomorphologic imaging of brain tumors in vivo. PloS one, 7, e41760.

Foersch, S., Kiesslich, R., Waldner, M.J., Delaney, P., Galle, P.R., Neurath, M.F. & Goetz, M. (2010) Molecular imaging of VEGF in gastrointestinal cancer in vivo using confocal laser endomicroscopy. Gut, 59, 1046-1055.

Foppiani, L., Ruelle, A., Cavazzani, P. & Del Monte, P. (2009) Hyperthyroidism unmasked several years after the medical and radiosurgical treatment of an invasive macroprolactinoma inducing hypopituitarism: a case report. Cases journal, 2, 6449.

Franklin, C.I. (1992) Does the extent of surgery make a difference in high grade malignant astrocytoma? Australasian radiology, 36, 44-47.

Fuchs, F.S., Zirlik, S., Hildner, K., Frieser, M., Ganslmayer, M., Schwarz, S., Uder, M. & Neurath, M.F. (2011) Fluorescein-aided confocal laser endomicroscopy of the lung. Respiration; international review of thoracic diseases, 81, 32-38.

Gardner, D.F., Utiger, R.D., Schwartz, S.L., Witorsch, P., Meyers, B., Braverman, L.E. & Witorsch, R.J. (1987) Effects of oral erythrosine (2’,4’,5’,7’-tetraiodofluorescein) on thyroid function in normal men. Toxicology and applied pharmacology, 91, 299-304.

Gehan, E.A. & Walker, M.D. (1977) Prognostic factors for patients with brain tumors. National Cancer Institute monograph, 46, 189-195.

George, M. & Meining, A. (2003) Cresyl violet as a fluorophore in confocal laser scanning microscopy for future in-vivo histopathology. Endoscopy, 35, 585-589.

Gessler, F., Zappi, J., Konczalla, J., Bernstock, J.D., Forster, M.-T., Wagner, M., Mittelbronn, M., Seifert, V. & Senft, C. (2017) Secondary Glioblastoma: Molecular and Clinical Factors That Affect Outcome After Malignant Progression of a Lower Grade Tumor. World neurosurgery, 102, 49-55.

Gibbs, S.L., Chen, B., O’Hara, J.A., Hoopes, P.J., Hasan, T. & Pogue, B.W. (2006) Protoporphyrin IX level correlates with number of mitochondria, but increase in production correlates with tumor cell size. Photochemistry and photobiology, 82, 1334-1341.

Gibson, S.L., Nguyen, M.L., Havens, J.J., Barbarin, A. & Hilf, R. (1999) Relationship of delta-aminolevulinic acid-induced protoporphyrin IX levels to mitochondrial content in neoplastic cells in vitro. Biochemical and biophysical research communications, 265, 315-321.

Glantz, M.J., Burger, P.C., Herndon, J.E., 2nd, Friedman, A.H., Cairncross, J.G., Vick, N.A. & Schold, S.C., Jr. (1991) Influence of the type of surgery on the histologic diagnosis in patients with anaplastic gliomas. Neurology, 41, 1741-1744.

Goetz, M., Deris, I., Vieth, M., Murr, E., Hoffman, A., Delaney, P., Galle, P.R., Neurath, M.F. & Kiesslich, R. (2010) Near-infrared confocal imaging during mini-laparoscopy: a novel rigid endomicroscope with increased imaging plane depth. Journal of hepatology, 53, 84-90.

Goetz, M., Memadathil, B., Biesterfeld, S., Schneider, C., Gregor, S., Galle, P.R., Neurath, M.F. & Kiesslich, R. (2007) In vivo subsurface morphological and functional cellular and subcellular imaging of the gastrointestinal tract with confocal mini-microscopy. World journal of gastroenterology, 13, 2160-2165.

Goetz, M., Toermer, T., Vieth, M., Dunbar, K., Hoffman, A., Galle, P.R., Neurath, M.F., Delaney, P. & Kiesslich, R. (2009) Simultaneous confocal laser endomicroscopy and chromoendoscopy with topical cresyl violet. Gastrointestinal Endoscopy, 70, 959-968.

Gopal, P., Parker, J.R., Debski, R. & Parker, J.C., Jr. (2008) Choroid plexus carcinoma. Archives of pathology & laboratory medicine, 132, 1350-1354.

Grimm, S.A. & Chamberlain, M.C. (2016) Anaplastic astrocytoma. CNS oncology, 5, 145-157.

Gruenwedel, D.W. (2003) NUCLEIC ACIDS | Properties and Determination. In Caballero, B. (ed) Encyclopedia of Food Sciences and Nutrition (Second Edition). Academic Press, Oxford, pp. 4147-4152.

Haglund, M.M., Berger, M.S. & Hochman, D.W. (1996) Enhanced optical imaging of human gliomas and tumor margins. Neurosurgery, 38, 308-317.

Hanel, R.A., Nakaji, P. & Spetzler, R.F. (2010) Use of microscope-integrated near-infrared indocyanine green videoangiography in the surgical treatment of spinal dural arteriovenous fistulae. Neurosurgery, 66, 978-984; discussion 984-975.

Hansen, D.A., Spence, A.M., Carski, T. & Berger, M.S. (1993) Indocyanine green (ICG) staining and demarcation of tumor margins in a rat glioma model. Surgical neurology, 40, 451-456.

Haxel, B.R., Goetz, M., Kiesslich, R. & Gosepath, J. (2010) Confocal endomicroscopy: a novel application for imaging of oral and oropharyngeal mucosa in human. European archives of oto-rhino-laryngology : official journal of the European Federation of Oto-Rhino-Laryngological Societies (EUFOS) : affiliated with the German Society for Oto-Rhino-Laryngology - Head and Neck Surgery, 267, 443-448.

He, L., Long, L. R., Antani, S., & Thoma, G. R. (2012). Histology image analysis for carcinoma detection and grading. Computer methods and programs in biomedicine, 107(3), 538-556. doi:10.1016/j.cmpb.2011.12.007.

Hirche, C., Dresel, S., Krempien, R. & Hunerbein, M. (2010) Sentinel node biopsy by indocyanine green retention fluorescence detection for inguinal lymph node staging of anal cancer: preliminary experience. Annals of surgical oncology, 17, 2357-2362.

Hojo, M., Arakawa, Y., Funaki, T., Yoshida, K., Kikuchi, T., Takagi, Y., Araki, Y., Ishii, A., Kunieda, T., Takahashi et al.(2014) Usefulness of tumor blood flow imaging by intraoperative indocyanine green videoangiography in hemangioblastoma surgery. World neurosurgery, 82, e495-501.

Hortobagyi, T., Bencze, J., Varkoly, G., Kouhsari, M.C. & Klekner, A. (2016) Meningioma recurrence. Open medicine (Warsaw, Poland), 11, 168-173.

Hsu, A.R., Hou, L.C., Veeravagu, A., Greve, J.M., Vogel, H., Tse, V. & Chen, X. (2006) In vivo near-infrared fluorescence imaging of integrin alphavbeta3 in an orthotopic glioblastoma model. Molecular imaging and biology : MIB : the official publication of the Academy of Molecular Imaging, 8, 315-323.

Huang, R., Vider, J., Kovar, J.L., Olive, D.M., Mellinghoff, I.K., Mayer-Kuckuk, P., Kircher, M.F. & Blasberg, R.G. (2012) Integrin αvβ3-targeted IRDye 800CW near-infrared imaging of glioblastoma. Clinical cancer research : an official journal of the American Association for Cancer Research, 18, 5731-5740.

Iacoangeli, M., Roselli, R., Prezioso, A., Scerrati, M. & Rossi, G.F. (1993) Staging of supratentorial hemispheric glioma using tumour extension, histopathological grade and extent of surgical resection. The British journal of surgery, 80, 1130-1133.

Ibrahim, G.M. & Bernstein, M. (2012) Awake craniotomy for supratentorial gliomas: why, when and how? CNS oncology, 1, 71-83.

Ichimura, K., Pearson, D.M., Kocialkowski, S., Backlund, L.M., Chan, R., Jones, D.T. & Collins, V.P. (2009) IDH1 mutations are present in the majority of common adult gliomas but rare in primary glioblastomas. Neuro Oncol, 11, 341-347.

Iqbal, U., Albaghdadi, H., Luo, Y., Arbabi, M., Desvaux, C., Veres, T., Stanimirovic, D. & Abulrob, A. (2010) Molecular imaging of glioblastoma multiforme using anti-insulin-like growth factor-binding protein-7 single-domain antibodies. British journal of cancer, 103, 1606-1616.

Jaafar, H. (2006) Intra-operative frozen section consultation: concepts, applications and limitations. The Malaysian journal of medical sciences : MJMS, 13, 4-12.

Jablonski, A. (1933) Efficiency of Anti-Stokes Fluorescence in Dyes. Nature, 131, 839-840.

Jaiswal, S., Vij, M., Mehrotra, A., Kumar, B., Nair, A., Jaiswal, A. K., . . . Jain, V. K. (2013). Choroid plexus tumors: A clinico-pathological and neuro-radiological study of 23 cases. Asian journal of neurosurgery, 8(1), 29-35. doi:10.4103/1793-5482.110277

Jameson, L.C., Janik, D.J. & Sloan, T.B. (2007) Electrophysiologic monitoring in neurosurgery. Anesthesiology clinics, 25, 605-630, x.

JECFA (2006) Combined compendium of food additive specifications-all specifications monographs from the 1st to the 65th meeting (1965-2005). FAO JECFA Monographs Series, No. 1, 1-3.

Jeibmann, A., Wrede, B., Peters, O., Wolff, J.E., Paulus, W. & Hasselblatt, M. (2007) Malignant progression in choroid plexus papillomas. Journal of neurosurgery, 107, 199-202.

Johnson, D.R., Brown, P.D., Galanis, E. & Hammack, J.E. (2012) Pilocytic astrocytoma survival in adults: analysis of the Surveillance, Epidemiology, and End Results Program of the National Cancer Institute. Journal of neuro-oncology, 108, 187-193.

Kaatsch, P., Rickert, C.H., Kuhl, J., Schuz, J. & Michaelis, J. (2001) Population-based epidemiologic data on brain tumors in German children. Cancer, 92, 3155-3164.

Kaminska, B., Czapski, B., Guzik, R., Król, S.K. & Gielniewski, B. (2019) Consequences of IDH1/2 Mutations in Gliomas and an Assessment of Inhibitors Targeting Mutated IDH Proteins. Molecules (Basel, Switzerland), 24, 968.

Kawai, M., Yamada, S., Ishidoshiro, A., Oyamada, Y., Ito, H. & Yamagishi, J. (2009) Cell-wall thickness: possible mechanism of acriflavine resistance in meticillin-resistant Staphylococcus aureus. Journal of medical microbiology, 58, 331-336.

Kelder, W., Nimura, H., Takahashi, N., Mitsumori, N., van Dam, G.M. & Yanaga, K. (2010) Sentinel node mapping with indocyanine green (ICG) and infrared ray detection in early gastric cancer: an accurate method that enables a limited lymphadenectomy. European journal of surgical oncology : the journal of the European Society of Surgical Oncology and the British Association of Surgical Oncology, 36, 552-558.

Keller, R., Winde, G., Terpe, H.J., Foerster, E.C. & Domschke, W. (2002) Fluorescence endoscopy using a fluorescein-labeled monoclonal antibody against carcinoembryonic antigen in patients with colorectal carcinoma and adenoma. Endoscopy, 34, 801-807.

Kessel, D., Beck, W.T., Kukuruga, D. & Schulz, V. (1991) Characterization of multidrug resistance by fluorescent dyes. Cancer research, 51, 4665-4670.

Khan, I., Saeed, K., & Khan, I. (2017). Nanoparticles: Properties, applications and toxicities. Arabian Journal of Chemistry.

Kiesslich, R., Burg, J., Vieth, M., Gnaendiger, J., Enders, M., Delaney, P., Polglase, A., McLaren, W., Janell, D., Thomas, S. et al. (2004) Confocal laser endoscopy for diagnosing intraepithelial neoplasias and colorectal cancer in vivo. Gastroenterology, 127, 706-713.

Kiesslich, R., Goetz, M., Burg, J., Stolte, M., Siegel, E., Maeurer, M.J., Thomas, S., Strand, D., Galle, P.R. & Neurath, M.F. (2005) Diagnosing Helicobacter pylori in vivo by confocal laser endoscopy. Gastroenterology, 128, 2119-2123.

Kiesslich, R., Gossner, L., Goetz, M., Dahlmann, A., Vieth, M., Stolte, M., Hoffman, A., Jung, M., Nafe, B., Galle, P.R. et al. (2006) In vivo histology of Barrett's esophagus and associated neoplasia by confocal laser endomicroscopy. Clinical gastroenterology and hepatology : the official clinical practice journal of the American Gastroenterological Association, 4, 979-987.

Kim, A.R., Mathieu; Dadani, Farhan N.; Wilson, Brian C. (2010 November-December) Topographic mapping of subsurface fluorescent structures in tissue using multiwavelength excitation. J Biomed Opt.

Kobylewski, S. & Jacobson, M.F. (2012) Toxicology of food dyes. International journal of occupational and environmental health, 18, 220-246.

Kohler, B.A., Ward, E., McCarthy, B.J., Schymura, M.J., Ries, L.A., Eheman, C., Jemal, A., Anderson, R.N., Ajani, U.A. & Edwards, B.K. (2011) Annual report to the nation on the status of cancer, 1975-2007, featuring tumors of the brain and other nervous system. Journal of the National Cancer Institute, 103, 714-736.

Kolodziej, A., Krajewski, W., Matuszewski, M. & Tupikowski, K. (2016) Review of current optical diagnostic techniques for non-muscle-invasive bladder cancer. Central European journal of urology, 69, 150-156.

Kopczak, A., Renner, U. & Karl Stalla, G. (2014) Advances in understanding pituitary tumors. F1000prime reports, 6, 5-5.

Kowalczuk, A., Macdonald, R.L., Amidei, C., Dohrmann, G., 3rd, Erickson, R.K., Hekmatpanah, J., Krauss, S., Krishnasamy, S., Masters, G., Mullan, S.F. et al.(1997) Quantitative imaging study of extent of surgical resection and prognosis of malignant astrocytomas. Neurosurgery, 41, 1028-1036; discussion 1036-1028.

Lacroix, M., Abi-Said, D., Fourney, D.R., Gokaslan, Z.L., Shi, W., DeMonte, F., Lang, F.F., McCutcheon, I.E., Hassenbusch, S.J., Holland, E. et al. (2001) A multivariate analysis of 416 patients with glioblastoma multiforme: prognosis, extent of resection, and survival. Journal of neurosurgery, 95, 190-198.

Lane, P.M., Lam, S., McWilliams, A., Leriche, J.C., Anderson, M.W. & Macaulay, C.E. (2009) Confocal fluorescence microendoscopy of bronchial epithelium. Journal of biomedical optics, 14, 024008.

Langen, K.-J., Drzezga, A. & Galldiks, N. (2018) Chapter 12 - Brain Tumors. In Beheshti, M., Langsteger, W., Rezaee, A. (eds) PET/CT in Cancer: An Interdisciplinary Approach to Individualized Imaging. Elsevier, pp. 235-254.

Lara-Velazquez, M., Al-Kharboosh, R., Jeanneret, S., Vazquez-Ramos, C., Mahato, D., Tavanaiepour, D., . . . Quinones-Hinojosa, A. (2017). Advances in Brain Tumor Surgery for Glioblastoma in Adults. Brain sciences, 7(12), 166.

Lee, C.J., Yue, C.H., Lin, Y.J., Lin, Y.Y., Kao, S.H., Liu, J.Y. & Chen, Y.H. (2014) Antitumor activity of acriflavine in lung adenocarcinoma cell line A549. Anticancer research, 34, 6467-6472.

Li, J., Zhang, Z., Wang, J., Zhang, C., Li, H. & Xu, Y. (2014) Urinary cytology with acridine orange fluorescence is highly valuable for predicting high-grade upper urinary tract urothelial carcinoma. International Journal of Clinical and Experimental Pathology, 7, 774-778.

Licha, K. (2002) Contrast Agents for Optical Imaging. In Krause, W. (ed) Contrast Agents II: Optical, Ultrasound, X-Ray and Radiopharmaceutical Imaging. Springer Berlin Heidelberg, Berlin, Heidelberg, pp. 1-29.

Linsler, S., Kraemer, D., Driess, C., Oertel, J., Kammers, K., Rahnenfuhrer, J., Ketter, R. & Urbschat, S. (2014) Molecular biological determinations of meningioma progression and recurrence. PloS one, 9, e94987.

Lippert, E. (1957) Elektrochem. 61:92-101.

Lohrke, J., Frenzel, T., Endrikat, J., Alves, F. C., Grist, T. M., Law, M., Pietsch, H. (2016). 25 Years of Contrast-Enhanced MRI: Developments, Current Challenges and Future Perspectives. Advances in therapy, 33(1), 1-28. doi:10.1007/s12325-015-0275-4.

Louis , D.N., O.H., Wiestle Otmar D., Cavenee Webster K. , Burger Peter C., Jouvet Anne , Scheithauer Bernd W. , and Kleihues Paul (2007) The 2007 WHO Classification of Tumours of the Central Nervous System. Acta Neuropathol., 114(2): 97–109.

Louis, D.N., Perry, A., Reifenberger, G., von Deimling, A., Figarella-Branger, D., Cavenee, W.K., Ohgaki, H., Wiestler, O.D., Kleihues, P. & Ellison, D.W. (2016) The 2016 World Health Organization Classification of Tumors of the Central Nervous System: a summary. Acta neuropathologica, 131, 803-820.

Machi, J., Oishi, A.J., Furumoto, N.L. & Oishi, R.H. (2004) Intraoperative ultrasound. The Surgical clinics of North America, 84, 1085-1111, vi-i.

Malmstrom, M.L., Karstensen, J.G., A, S.F., Riis, L.B., Gogenur, I. & Vilmann, P. (2014) [Confocal laser endomicroscopy is a new endoscopic technique for diagnosing colorectal neoplasia and inflammatory bowel disease.]. Ugeskr Laeger, 176.

Mangraviti, A., Raghavan, T., Volpin, F., Skuli, N., Gullotti, D., Zhou, J., Asnaghi, L., Sankey, E., Liu, A., Wang, Y. et al. (2017) HIF-1alpha- Targeting Acriflavine Provides Long Term Survival and Radiological Tumor Response in Brain Cancer Therapy. Scientific reports, 7, 14978.

Marbacher, S., Mendelowitsch, I., Gruter, B.E., Diepers, M., Remonda, L. & Fandino, J. (2018) Comparison of 3D intraoperative digital subtraction angiography and intraoperative indocyanine green video angiography during intracranial aneurysm surgery. Journal of neurosurgery, 1-8.

Markert, J. M. (2012). The role of early resection vs biopsy in the management of low-grade gliomas. Jama, 308(18), 1918-1919. doi:10.1001/jama.2012.14523Markert, J. M. (2012). The role of early resection vs biopsy in the management of low-grade gliomas. Jama, 308(18), 1918-1919. doi:10.1001/jama.2012.14523.

Martirosyan, N.L., Cavalcanti, D.D., Eschbacher, J.M., Delaney, P.M., Scheck, A.C., Abdelwahab, M.G., Nakaji, P., Spetzler, R.F. & Preul, M.C. (2011) Use of in vivo near-infrared laser confocal endomicroscopy with indocyanine green to detect the boundary of infiltrative tumor. Journal of neurosurgery, 115, 1131-1138.

Martirosyan, N.L., Georges, J., Eschbacher, J.M., Cavalcanti, D.D., Elhadi, A.M., Abdelwahab, M.G., Scheck, A.C., Nakaji, P., Spetzler, R.F. & Preul, M.C. (2014) Potential application of a handheld confocal endomicroscope imaging system using a variety of fluorophores in experimental gliomas and normal brain. Neurosurg Focus, 36, E16.

Mat Zin, A.A. & Zulkarnain, S. (2019) Diagnostic Accuracy of Cytology Smear and

Frozen Section in Glioma. Asian Pacific Journal of Cancer Prevention, 20, 321-325.

MaunaKeaTechnologies (2016) Cellvizio USER GUIDE CONFOCAL MINIPROBES™ FOR GASTRO-ENTEROLOGY. Gastro-enterology Confocal Miniprobes™ User Guide – Jan 2016 V 1.03.

Meining, A. (2009) Confocal Endomicroscopy. Gastrointestinal Endoscopy Clinics, 19, 629-635.

Meining, A., Saur, D., Bajbouj, M., Becker, V., Peltier, E., Hofler, H., von Weyhern, C.H., Schmid, R.M. & Prinz, C. (2007) In vivo histopathology for detection of gastrointestinal neoplasia with a portable, confocal miniprobe: an examiner blinded analysis. Clinical gastroenterology and hepatology : the official clinical practice journal of the American Gastroenterological Association, 5, 1261-1267.

Mennone, A. & Nathanson, M.H. (2011) Needle-based confocal laser endomicroscopy to assess liver histology in vivo. Gastrointestinal endoscopy, 73, 338-344.

Moore, G.E., Peyton, W.T. & et al. (1948) The clinical use of fluorescein in neurosurgery; the localization of brain tumors. Journal of neurosurgery, 5, 392-398.

Mesfin, F. & Al-Dhahir, M. (2017) Cancer, Brain, Gliomas StatPearls. StatPearls Publishing StatPearls Publishing LLC., Treasure Island (FL).

Millgard, L.S., Christina, D., Asgeir, S.J. & Ole, S. (2017) Accuracy of operating neurosurgeons' prediction of functional levels after intracranial tumor surgery. Journal of Neurosurgery JNS, 126, 1173-1180.

Minsky, M. (1988) Memoir on inventing the confocal scanning microscope. Scanning, 10, 128-138.

Mislow, J.M.K., Golby, A.J. & Black, P.M. (2009) Origins of intraoperative MRI. Neurosurgery clinics of North America, 20, 137-146.

Mitsui, T., Fujii, M., Tsuzaka, M., Hayashi, Y., Asahina, Y. & Wakabayashi, T. (2011) Skin shift and its effect on navigation accuracy in image-guided neurosurgery. Radiological physics and technology, 4, 37-42.

Miyata, S., Urabe, M., Gomi, A., Nagai, M., Yamaguchi, T., Tsukahara, T., Mizukami, H., Kume, A., Ozawa, K. & Watanabe, E. (2013) An R132H mutation in isocitrate dehydrogenase 1 enhances p21 expression and inhibits phosphorylation of retinoblastoma protein in glioma cells. Neurol Med Chir (Tokyo), 53, 645-654.

Mondal, S.B., Gao, S., Zhu, N., Liang, R., Gruev, V. & Achilefu, S. (2014) Real-time fluorescence image-guided oncologic surgery. Advances in cancer research, 124, 171-211.

Moore, G.E., Peyton, W.T. & et al. (1948) The clinical use of fluorescein in neurosurgery; the localization of brain tumors. Journal of neurosurgery, 5, 392-398.

Natarajan, R., Northrop, N. & Yamamoto, B. (2017) Fluorescein Isothiocyanate (FITC)-Dextran Extravasation as a Measure of Blood-Brain Barrier Permeability. Current protocols in neuroscience, 79, 9.58.51-59.58.15.

Nguyen, N.Q. & Leong, R.W. (2008) Current application of confocal endomicroscopy in gastrointestinal disorders. J Gastroenterol Hepatol, 23, 1483-1491.

Nguyen, Q.T. & Tsien, R.Y. (2013) Fluorescence-guided surgery with live molecular navigation–a new cutting edge. Nat Rev Cancer, 13, 653-662.

Oglat, A.A., Matjafri, M.Z., Suardi, N., Oqlat, M.A., Abdelrahman, M.A. & Oqlat, A.A. (2018) A Review of Medical Doppler Ultrasonography of Blood Flow in General and Especially in Common Carotid Artery. Journal of medical ultrasound, 26, 3-13.

Ohgaki, H., Dessen, P., Jourde, B., Horstmann, S., Nishikawa, T., Di Patre, P.L., Burkhard, C., Schuler, D., Probst-Hensch, N.M., Maiorka, P.C. et al. (2004) Genetic pathways to glioblastoma: a population-based study. Cancer research, 64, 6892-6899.

Ohgaki, H. & Kleihues, P. (2005) Population-based studies on incidence, survival rates, and genetic alterations in astrocytic and oligodendroglial gliomas. Journal of neuropathology and experimental neurology, 64, 479-489.

Ohnishi, S., Lomnes, S.J., Laurence, R.G., Gogbashian, A., Mariani, G. & Frangioni, J.V. (2005) Organic alternatives to quantum dots for intraoperative near-infrared fluorescent sentinel lymph node mapping. Molecular imaging, 4, 172-181.

Oneson, R.H., Minke, J.A. & Silverberg, S.G. (1989) Intraoperative pathologic consultation. An audit of 1,000 recent consecutive cases. The American journal of surgical pathology, 13, 237-243.

Orringer, D.A., Golby, A. & Jolesz, F. (2012) Neuronavigation in the surgical management of brain tumors: current and future trends. Expert review of medical devices, 9, 491-500.

Orringer, D.A., Koo, Y.-E.L., Chen, T., Kim, G., Hah, H.J., Xu, H., Wang, S., Keep, R., Philbert, M.A., Kopelman et al. (2009) In vitro characterization of a targeted, dye-loaded nanodevice for intraoperative tumor delineation. Neurosurgery, 64, 965-972.

Osterman, H., Schutz Geschwender, A. & Fluor, A. (2007) Seeing Beyond the Visible With IRDye ® Infrared Dyes.

Ostrom, Q.T., Gittleman, H., Fulop, J., Liu, M., Blanda, R., Kromer, C., Wolinsky, Y., Kruchko, C. & Barnholtz-Sloan, J.S. (2015) CBTRUS Statistical Report: Primary Brain and Central Nervous System Tumors Diagnosed in the United States in 2008-2012. Neuro Oncol, 17 Suppl 4, iv1-iv62.

Ostrom, Q.T., Gittleman, H., Liao, P., Rouse, C., Chen, Y., Dowling, J., Wolinsky, Y., Kruchko, C. & Barnholtz-Sloan, J. (2014) CBTRUS statistical report: primary brain and central nervous system tumors diagnosed in the United States in 2007-2011. Neuro-oncology, 16 Suppl 4, iv1-iv63.

Ostrom, Q.T., Gittleman, H., Xu, J., Kromer, C., Wolinsky, Y., Kruchko, C. & Barnholtz-Sloan, J.S. (2016) CBTRUS Statistical Report: Primary Brain and Other Central Nervous System Tumors Diagnosed in the United States in 2009-2013. Neuro-oncology, 18, v1-v75.

Ozdogan, S., Gergin, Y.E., Gergin, S., Senol, O., Tiryaki, M., Tatarli, N. & Hicdonmez, T. (2015) Choroid plexus carcinoma in adults: an extremely rare case. The Pan African medical journal, 20, 302.

Parng, C., Anderson, N., Ton, C. & McGrath, P. (2004) Zebrafish Apoptosis Assays for Drug Discovery Methods in Cell Biology. Academic Press, pp. 75-85.

Parney, I.F. & Berger, M.S. (2012) Chapter 15 - Principles of brain tumor surgery. In Aminoff, M.J., Boller, F., Swaab, D.F. (eds) Handbook of Clinical Neurology. Elsevier, pp. 187-213.

Parrish-Novak, J., Holland, E.C. & Olson, J.M. (2015) Image Guided Tumor Resection. Cancer journal (Sudbury, Mass.), 21, 206-212.

Peled, N., Wynes, M. W., Ikeda, N., Ohira, T., Yoshida, K., Qian, J., . . . Hirsch, F. R. (2013). Insulin-like growth factor-1 receptor (IGF-1R) as a biomarker for resistance to the tyrosine kinase inhibitor gefitinib in non-small cell lung cancer. Cell Oncol (Dordr), 36(4), 277-288. doi:10.1007/s13402-013-0133-9

Peng, Q., Warloe, T., Berg, K., Moan, J., Kongshaug, M., Giercksky, K.E. & Nesland, J.M. (1997) 5-Aminolevulinic acid-based photodynamic therapy. Clinical research and future challenges. Cancer, 79, 2282-2308.

Perkins, A. & Liu, G. (2016) Primary Brain Tumors in Adults: Diagnosis and Treatment. American family physician, 93, 211-217.

Petrovsky, A., Schellenberger, E., Josephson, L., Weissleder, R. & Bogdanov, A., Jr. (2003) Near-infrared fluorescent imaging of tumor apoptosis. Cancer research, 63, 1936-1942.

Pilati, N., Barker, M., Panteleimonitis, S., Donga, R. & Hamann, M. (2008) A rapid method combining Golgi and Nissl staining to study neuronal morphology and cytoarchitecture. The journal of histochemistry and cytochemistry : official journal of the Histochemistry Society, 56, 539-550.

Pogue, B.W., Gibbs-Strauss, S., Valdes, P.A., Samkoe, K., Roberts, D.W. & Paulsen, K.D. (2010) Review of Neurosurgical Fluorescence Imaging Methodologies. IEEE journal of selected topics in quantum electronics : a publication of the IEEE Lasers and Electro-optics Society, 16, 493-505.

Polglase, A.L., McLaren, W.J., Skinner, S.A., Kiesslich, R., Neurath, M.F. & Delaney, P.M. (2005) A fluorescence confocal endomicroscope for in vivo microscopy of the upper- and the lower-GI tract. Gastrointestinal endoscopy, 62, 686-695.

Polom, K., Murawa, D., Rho, Y.S., Nowaczyk, P., Hunerbein, M. & Murawa, P. (2011) Current trends and emerging future of indocyanine green usage in surgery and oncology: a literature review. Cancer, 117, 4812-4822.

Poot, M. & Pierce, R.H. (2001) Analysis of mitochondria by flow cytometry Methods in Cell Biology. Academic Press, pp. 117-128.

Preusser, M., Wohrer, A., Stary, S., Hoftberger, R., Streubel, B. & Hainfellner, J.A. (2011) Value and limitations of immunohistochemistry and gene sequencing for detection of the IDH1-R132H mutation in diffuse glioma biopsy specimens. Journal of neuropathology and experimental neurology, 70, 715-723.

Raj, V.S. & Lofton, L. (2013) Rehabilitation and treatment of spinal cord tumors. The journal of spinal cord medicine, 36, 4-11.

Ravichandran, S., Paluri, V., Kumar, G., Loganathan, K. & Kokati Venkata, B.R. (2016) A novel approach for the biosynthesis of silver oxide nanoparticles using aqueous leaf extract of Callistemon lanceolatus (Myrtaceae) and their therapeutic potential. Journal of Experimental Nanoscience, 11, 445-458.

Rees, J.H. (2011) Diagnosis and treatment in neuro-oncology: an oncological perspective. The British journal of radiology, 84 Spec No 2, S82-S89.

Regragui, A., Amarti Riffi, A., Maher, M., El Khamlichi, A. & Saidi, A. (2003) [Accuracy of intraoperative diagnosis in central nervous system tumors: report of 1315 cases]. Neuro-Chirurgie, 49, 67-72.

Riemenschneider, M.J., Perry, A. & Reifenberger, G. (2006) Histological classification and molecular genetics of meningiomas. The Lancet. Neurology, 5, 1045-1054.

Rizvi, S. A. A., & Saleh, A. M. (2018). Applications of nanoparticle systems in drug delivery technology. Saudi pharmaceutical journal : SPJ : the official publication of the Saudi Pharmaceutical Society, 26(1), 64-70. doi:10.1016/j.jsps.2017.10.012

Roth, J.G. & Elvidge, A.R. (1960) Glioblastoma multiforme: a clinical survey. Journal of neurosurgery, 17, 736-750.

Sahm, F., Capper, D., Jeibmann, A., Habel, A., Paulus, W., Troost, D. & von Deimling, A. (2012) Addressing diffuse glioma as a systemic brain disease with single-cell analysis. Archives of neurology, 69, 523-526.

Sanai, N. & Berger, M.S. (2008) Glioma extent of resection and its impact on patient outcome. Neurosurgery, 62, 753-764; discussion 264-756.

Sanai, N. & Berger, M.S. (2012) Recent surgical management of gliomas. Advances in experimental medicine and biology, 746, 12-25.

Sanai, N., Eschbacher, J., Hattendorf, G., Coons, S.W., Preul, M.C., Smith, K.A., Nakaji, P. & Spetzler, R.F. (2011a) Intraoperative confocal microscopy for brain tumors: a feasibility analysis in humans. Neurosurgery, 68, 282-290; discussion 290.

Sanai, N., Snyder, L.A., Honea, N.J., Coons, S.W., Eschbacher, J.M., Smith, K.A. & Spetzler, R.F. (2011b) Intraoperative confocal microscopy in the visualization of 5-aminolevulinic acid fluorescence in low-grade gliomas. Journal of neurosurgery, 115, 740-748.

Sankar, T., Delaney, P.M., Ryan, R.W., Eschbacher, J., Abdelwahab, M., Nakaji, P., Coons, S.W., Scheck, A.C., Smith, K.A., Spetzler, R.F. & Preul, M.C. (2010) Miniaturized handheld confocal microscopy for neurosurgery: results in an experimental glioblastoma model. Neurosurgery, 66, 410-417; discussion 417-418.

Sarin, H., Kanevsky, A.S., Wu, H., Brimacombe, K.R., Fung, S.H., Sousa, A.A., Auh, S., Wilson, C.M., Sharma, K., Aronova, M.A., Leapman, R.D., Griffiths, G.L. & Hall, M.D. (2008) Effective transvascular delivery of nanoparticles across the blood-brain tumor barrier into malignant glioma cells. Journal of translational medicine, 6, 80.

SCF (1983) Reports of the Scientific Comittee for Food (14th series).

SCF (1989) Reports of the Scientific Committee for Food (21st series).

Schlosser, H.G., Suess, O., Vajkoczy, P., van Landeghem, F.K., Zeitz, M. & Bojarski, C. (2010) Confocal neurolasermicroscopy in human brain - perspectives for neurosurgery on a cellular level (including additional comments to this article). Central European neurosurgery, 71, 13-19.

Schulz, A., Daali, S., Javed, M., Fuchs, P.C., Brockmann, M., Igressa, A. & Charalampaki, P. (2016) Presurgical mapping of basal cell carcinoma or squamous cell carcinoma by confocal laser endomicroscopy compared to traditional micrographic surgery: a single-centre prospective feasibility study. European journal of dermatology : EJD, 26, 572-579.

Schwartz, A., Wang, L., Early, E., Gaigalas, A., Zhang, Y.-Z., Marti, G.E. & Vogt, R.F. (2002) Quantitating Fluorescence Intensity from Fluorophore: The Definition of MESF Assignment. J Res Natl Inst Stand Technol, 107, 83-91.

Senft, C., Bink, A., Franz, K., Vatter, H., Gasser, T., & Seifert, V. (2011). Intraoperative MRI guidance and extent of resection in glioma surgery: a randomised, controlled trial. Lancet Oncol, 12(11), 997-1003. doi:10.1016/s1470-2045(11)70196-6

Seppala, M.T., Haltia, M.J., Sankila, R.J., Jaaskelainen, J.E. & Heiskanen, O. (1995) Long-term outcome after removal of spinal schwannoma: a clinicopathological study of 187 cases. Journal of neurosurgery, 83, 621-626.

Shah, A.K. (2018) Postoperative pathologic assessment of surgical margins in oral cancer: A contemporary review. Journal of oral and maxillofacial pathology : JOMFP, 22, 78-85.

Shaikh, N., Dixit, K., & Raizer, J. (2018). Recent advances in managing/understanding meningioma. F1000Research, 7, F1000 Faculty Rev-1490.

Shay, J.E., Imtiyaz, H.Z., Sivanand, S., Durham, A.C., Skuli, N., Hsu, S., Mucaj, V., Eisinger-Mathason, T.S., Krock, B.L., Giannoukos, D.N. & Simon, M.C. (2014) Inhibition of hypoxia-inducible factors limits tumor progression in a mouse model of colorectal cancer. Carcinogenesis, 35, 1067-1077.

Shibuya, M. (2015) Pathology and molecular genetics of meningioma: recent advances. Neurologia medico-chirurgica, 55, 14-27.

Shinoda, J., Yano, H., Yoshimura, S., Okumura, A., Kaku, Y., Iwama, T. & Sakai, N. (2003) Fluorescence-guided resection of glioblastoma multiforme by using high-dose fluorescein sodium. Technical note. Journal of neurosurgery, 99, 597-603.

Shinya, T., Nagamine, H., Sugawara, K.-I. & Ishiuchi, S. (2018) The usefulness of indocyanine green during surgery for hypervascular posterior fossa tumors. Surg Neurol Int, 9, 90-90.

Simpson, J.R., Horton, J., Scott, C., Curran, W.J., Rubin, P., Fischbach, J., Isaacson, S., Rotman, M., Asbell, S.O., Nelson, J.S. & et al. (1993) Influence of location and extent of surgical resection on survival of patients with glioblastoma multiforme:

results of three consecutive Radiation Therapy Oncology Group (RTOG) clinical trials. International journal of radiation oncology, biology, physics, 26, 239-244.

Snuderl, M., Wirth, D., Sheth, S.A., Bourne, S.K., Kwon, C.S., Ancukiewicz, M., Curry, W.T., Frosch, M.P. & Yaroslavsky, A.N. (2013) Dye-enhanced multimodal confocal imaging as a novel approach to intraoperative diagnosis of brain tumors. Brain pathology (Zurich, Switzerland), 23, 73-81.

Sonn, G.A., Jones, S.N., Tarin, T.V., Du, C.B., Mach, K.E., Jensen, K.C. & Liao, J.C. (2009) Optical biopsy of human bladder neoplasia with in vivo confocal laser endomicroscopy. The Journal of urology, 182, 1299-1305.

Stepp, H., Beck, T., Pongratz, T., Meinel, T., Kreth, F.W., Tonn, J. & Stummer, W. (2007) ALA and malignant glioma: fluorescence-guided resection and photodynamic treatment. Journal of environmental pathology, toxicology and oncology : official organ of the International Society for Environmental Toxicology and Cancer, 26, 157-164.

Stokes, G.G. (1852) On the change of refrangibility of light. Royal Society, 142, Issue.

Stummer, W. (2015) Fluorescein in brain metastasis and glioma surgery. Acta neurochirurgica, 157, 2199-2200.

Stummer, W., Novotny, A., Stepp, H., Goetz, C., Bise, K. & Reulen, H.J. (2000) Fluorescence-guided resection of glioblastoma multiforme by using 5-aminolevulinic acid-induced porphyrins: a prospective study in 52 consecutive patients. Journal of neurosurgery, 93, 1003-1013.

Stummer, W., Pichlmeier, U., Meinel, T., Wiestler, O.D., Zanella, F. & Reulen, H.J. (2006) Fluorescence-guided surgery with 5-aminolevulinic acid for resection of malignant glioma: a randomised controlled multicentre phase III trial. Lancet Oncol, 7, 392-401.

Stummer, W., Reulen, H.J., Novotny, A., Stepp, H. & Tonn, J.C. (2003) Fluorescence-guided resections of malignant gliomas–an overview. Acta neurochirurgica. Supplement, 88, 9-12.

Stummer, W., Stepp, H., Moller, G., Ehrhardt, A., Leonhard, M. & Reulen, H.J. (1998) Technical principles for protoporphyrin-IX-fluorescence guided microsurgical resection of malignant glioma tissue. Acta neurochirurgica, 140, 995-1000.

Stummer, W. & Suero Molina, E. (2017) Fluorescence Imaging/Agents in Tumor Resection. Neurosurgery Clinics of North America, 28, 569-583.

Sugden, J.K. (2004) Photochemistry of dyes and fluorochromes used in biology and medicine: some physicochemical background and current applications. Biotechnic &

histochemistry : official publication of the Biological Stain Commission, 79, 71-90.

Tagaya, N., Yamazaki, R., Nakagawa, A., Abe, A., Hamada, K., Kubota, K. & Oyama, T. (2008) Intraoperative identification of sentinel lymph nodes by near-infrared fluorescence imaging in patients with breast cancer. American journal of surgery, 195, 850-853.

Tan, J., Quinn, M.A., Pyman, J.M., Delaney, P.M. & McLaren, W.J. (2009) Detection of cervical intraepithelial neoplasia in vivo using confocal endomicroscopy. BJOG : an international journal of obstetrics and gynaecology, 116, 1663-1670.

Te Velde, E.A., Veerman, T., Subramaniam, V. & Ruers, T. (2010) The use of fluorescent dyes and probes in surgical oncology. European journal of surgical oncology : the journal of the European Society of Surgical Oncology and the British Association of Surgical Oncology, 36, 6-15.

Teixidor, P., Arraez, M.A., Villalba, G., Garcia, R., Tardaguila, M., Gonzalez, J.J., Rimbau, J., Vidal, X. & Montane, E. (2016) Safety and Efficacy of 5-Aminolevulinic Acid for High Grade Glioma in Usual Clinical Practice: A Prospective Cohort Study. PloS one, 11, e0149244.

The Alex Foundation (2007) Alex the African grey parrot and subject of landmark studies of bird intelligence dies at 31. The Alex Foundation, Waltham, MA.

Thiberville, L., Moreno-Swirc, S., Vercauteren, T., Peltier, E., Cave, C. & Bourg Heckly, G. (2007) In vivo imaging of the bronchial wall microstructure using fibered confocal fluorescence microscopy. American journal of respiratory and critical care medicine, 175, 22-31.

Thiberville, L., Salaun, M., Lachkar, S., Dominique, S., Moreno-Swirc, S., Vever-Bizet, C. & Bourg-Heckly, G. (2009) Confocal fluorescence endomicroscopy of the human airways. Proceedings of the American Thoracic Society, 6, 444-449.

Tofte, K., Berger, C., Torp, S.H. & Solheim, O. (2014) The diagnostic properties of frozen sections in suspected intracranial tumors: A study of 578 consecutive cases. Surg Neurol Int, 5, 170.

Trovato, C., Sonzogni, A., Ravizza, D., Fiori, G., Tamayo, D., De Roberto, G., de Leone, A., De Lisi, S. & Crosta, C. (2013) Confocal laser endomicroscopy for in vivo diagnosis of Barrett's oesophagus and associated neoplasia: a pilot study conducted in a single Italian centre. Dig Liver Dis, 45, 396-402.

Tsutsumi, Y., Fukuma, S., Tsuchiya, A., Ikenoue, T., Yamamoto, Y., Shimizu, S., Fukuhara, S. (2017). Computed tomography during initial management and mortality among hemodynamically unstable blunt trauma patients: a nationwide retrospective cohort study. Scandinavian journal of trauma, resuscitation and emergency medicine, 25(1), 74-74. doi:10.1186/s13049-017-0396-7

Vacchelli, E., Aranda, F., Eggermont, A., Galon, J., Sautes-Fridman, C., Zitvogel, L., Kroemer, G. & Galluzzi, L. (2014) Trial Watch: Tumor-targeting monoclonal antibodies in cancer therapy. Oncoimmunology, 3, e27048.

Valdes, P.A., Kim, A., Brantsch, M., Niu, C., Moses, Z.B., Tosteson, T.D., Wilson, B.C., Paulsen, K.D., Roberts, D.W. & Harris, B.T. (2011) delta-aminolevulinic acid-induced protoporphyrin IX concentration correlates with histopathologic markers of malignancy in human gliomas: the need for quantitative fluorescence-guided resection to identify regions of increasing malignancy. Neuro Oncol, 13, 846-856.

van Dongen, G.A., Visser, G.W., Lub-de Hooge, M.N., de Vries, E.G. & Perk, L.R. (2007) Immuno-PET: a navigator in monoclonal antibody development and applications. The oncologist, 12, 1379-1389.

Vigneswaran, K., Neill, S. & Hadjipanayis, C.G.J.A.o.T.M. (2015) Beyond the World Health Organization grading of infiltrating gliomas: advances in the molecular genetics of glioma classification. 2015, 3.

Visser, O., Ardanaz, E., Botta, L., Sant, M., Tavilla, A., Minicozzi, P., Hackl, M., Zielonke, N., Oberaigner, W., Van Eycken, E. et al. (2015) Survival of adults with primary malignant brain tumours in Europe; Results of the EUROCARE-5 study. European Journal of Cancer, 51, 2231-2241.

Vrouenraets, M.B., Visser, G.W., Snow, G.B. & van Dongen, G.A. (2003) Basic principles, applications in oncology and improved selectivity of photodynamic therapy. Anticancer research, 23, 505-522.

Wainwright, M. (2001) Acridine-a neglected antibacterial chromophore. The Journal of antimicrobial chemotherapy, 47, 1-13.

Wallace, M.B., Meining, A., Canto, M.I., Fockens, P., Miehlke, S., Roesch, T., Lightdale, C.J., Pohl, H., Carr-Locke, D., Lohr, M. et al. (2010) The safety of intravenous fluorescein for confocal laser endomicroscopy in the gastrointestinal tract. Alimentary pharmacology & therapeutics, 31, 548-552.

Webb, J.M., Fonda, M. & Brouwer, E.A. (1962) Metabolism and excretion patterns of fluorescein and certain halogenated fluorescein dyes in rats. The Journal of pharmacology and experimental therapeutics, 137, 141-147.

Weller, M., Cloughesy, T., Perry, J.R. & Wick, W. (2013) Standards of care for treatment of recurrent glioblastoma–are we there yet? Neuro Oncol, 15, 4-27.

Wen, P.Y. & Kesari, S. (2008) Malignant gliomas in adults. The New England journal of medicine, 359, 492-507.

Wesseling, P., van den Bent, M. & Perry, A. (2015) Oligodendroglioma: pathology, molecular mechanisms and markers. Acta neuropathologica, 129, 809-827.

Whitson, W.J., Valdes, P.A., Harris, B.T., Paulsen, K.D. & Roberts, D.W. (2011) Confocal microscopy for the histological fluorescence pattern of a recurrent atypical meningioma: case report. Neurosurgery, 68, E1768-1772; discussion E1772-1763.

WHO (1996) Trace Elements in Human Nutrition and Health. Geneva: WHO.

Wiesner, C., Jager, W., Salzer, A., Biesterfeld, S., Kiesslich, R., Hampel, C., Thuroff, J.W. & Goetz, M. (2011) Confocal laser endomicroscopy for the diagnosis of urothelial bladder neoplasia: a technology of the future? BJU international, 107, 399-403.

Wirth, D., Snuderl, M., Sheth, S., Kwon, C.S., Frosch, M.P., Curry, W. & Yaroslavsky, A.N. (2012) Identifying brain neoplasms using dye-enhanced multimodal confocal imaging. Journal of biomedical optics, 17, 026012.

Wolenski, J.S. & Julich, D. (2014) Fluorescence microscopy gets faster and clearer: roles of photochemistry and selective illumination. The Yale journal of biology and medicine, 87, 21-32.

Wood, J.R., Green, S.B. & Shapiro, W.R. (1988) The prognostic importance of tumor size in malignant gliomas: a computed tomographic scan study by the Brain Tumor Cooperative Group. Journal of clinical oncology : official journal of the American Society of Clinical Oncology, 6, 338-343.

Wood, S., Metcalf, D., Devine, D. & Robinson, C. (2006) Erythrosine is a potential photosensitizer for the photodynamic therapy of oral plaque biofilms. The Journal of antimicrobial chemotherapy, 57, 680-684.

Wrobel, C.J., Meltzer, H., Lamond, R. & Alksne, J.F. (1994) Intraoperative assessment of aneurysm clip placement by intravenous fluorescein angiography. Neurosurgery, 35, 970-973; discussion 973.

Wu, A.M. & Olafsen, T. (2008) Antibodies for molecular imaging of cancer. Cancer J, 14, 191-197.

Wu, J., Armstrong, T.S. & Gilbert, M.R. (2016) Biology and management of ependymomas. Neuro-oncology, 18, 902-913.

Yang, X., Palasuberniam, P., Kraus, D. & Chen, B. (2015) Aminolevulinic Acid-Based Tumor Detection and Therapy: Molecular Mechanisms and Strategies for Enhancement. Int J Mol Sci, 16, 25865-25880.

Yi, X., Wang, F., Qin, W., Yang, X. & Yuan, J. (2014) Near-infrared fluorescent probes in cancer imaging and therapy: an emerging field. Int J Nanomedicine, 9, 1347-1365.

Youssef, P.P., Schuette, A.J., Cawley, C.M. & Barrow, D.L. (2014) Advances in Surgical Approaches to Dural Fistulas. Neurosurgery, 74, S32-S41.

Zehri, A.H., Ramey, W., Georges, J.F., Mooney, M.A., Martirosyan, N.L., Preul, M.C. & Nakaji, P. (2014) Neurosurgical confocal endomicroscopy: A review of contrast agents, confocal systems, and future imaging modalities. Surg Neurol Int, 5, 60.

Zhang, J., Li, Y., Zhao, Y. & Qiao, J. (2018) CT and MRI of superficial solid tumors. Quantitative imaging in medicine and surgery, 8, 232-251.

Zhao, S., Wu, J., Wang, C., Liu, H., Dong, X., Shi, C., Shi, C., Liu, Y., Teng, L., Han, D. et al. (2013) Intraoperative fluorescence-guided resection of high-grade malignant gliomas using 5-aminolevulinic acid-induced porphyrins: a systematic review and meta-analysis of prospective studies. PloS one, 8, e63682.

Zülch, K.J. (1979) Histological typing of tumours of the central nervous system., World Health Organization, Geneva.

Zülch, K.J. (1980) Principles of the new World Health Organization (WHO) classification of brain tumors. Neuroradiology, 19, 59-66.

Image sources

Fig. 1.1: https://pixabay.com/de/vectors/anatomie-gehirn-querschnitt-kopf-2027131/ (Status: 8/10/2019). License: Pixabay License CCO (Free commercial use).

Fig. 1.2: https://pixabay.com/de/vectors/anatomie-gehirn-querschnitt-kopf-2027131/ (Status: 8/10/2019). License: Pixabay License CCO (Free commercial use).

Fig. 2.2: www.maunakeatech.com / (Status: 4/4/2016). The diagram is used with permission from Mauna Kea Technologies.

Figs. 3.26; 3.27; 3.28; 3.29; 3.33: Daali, S., Javed, M., Altekoester, A.-K., Alhadi, I., Linxweiler, M., Bostelmann, R., Schlegel, J. & Charalampaki, P. (2016) Analysis of 258 Different Lesions of the Central Nervous System for Real Time Histopathological Diagnosis Using Confocal Laser Endomicroscopy. J Mult Scler (Foster City).

Acknowledgements

First, I would like to thank my supervisor PD Dr. Hans-Jürgen Laws, without his agreement to supervise my dissertation, the present work could not have been done. I am very grateful for all his comments and support during preparation of the thesis.

Furthermore, I would like to thank my co-supervisor Prof. Dr. Laura Rose for the evaluation of my PhD thesis and being part of my thesis committee.

The experiments of this work were primarily conducted at the Institute of Neurosurgery, Mehrheim, Cologne supervised by Prof. Dr. Cleopatra Charalampaki and financed by Siemens AG. All other experiments were performed in cooperation at the Neurosurgical Pathophysiology, Johannes Gutenberg University, Mainz and at the Institute of Neuropathology of the Technical University, Munich. Here, I would like to express my gratitude for all my scientific supervisors, foremost Prof. Dr. Cleopatra Charalampaki, Dr. Axel Heimann, Prof. Dr. Oliver Kempski, and Prof. Dr. Jürgen Schlegel, who established access to the laboratory and research facilities, provided all the materials as well as the research knowledge I needed. I want to thank them for their valuable support, encouragement and insightful discussions during the time of my Ph.D.

I also would like to thank my lab members, Barbara and Anett for all the everyday help and support.

My sincere thanks also goes to Dr. Christian Queckenberg, Dr. Ann-Kristin Alteköster and Dr. John Sharenot for their immense knowledge and support during the writing process.

In addition, I would like to thank my friends and my sister, Nadia Daali, for having always an open ear, for supporting me during this time, and for all the fun in daily life.

Finally, my very special thanks go to my family, especially my parents, Aicha Ajim Daali und Hassan Daali, who have made my life possible so far, who have tirelessly strengthened and motivated me and to whom I dedicate this work.

Erklärung der Urheberschaft

„Ich versichere, dass ich die von mir vorgelegte Dissertation selbständig angefertigt, die benutzten Quellen und Hilfsmittel vollständig angegeben und die Stellen der Arbeit - einschließlich Tabellen, Karten und Abbildungen -, die anderen Werken im Wortlaut oder dem Sinn nach entnommen sind, in jedem Einzelfall als Entlehnung kenntlich gemacht habe; dass diese Dissertation noch keiner anderen Fakultät oder Universität zur Prüfung vorgelegen hat; dass sie - abgesehen von unten angegebenen Teilpublikationen - noch nicht veröffentlicht worden ist sowie, dass ich eine solche Veröffentlichung vor Abschluss des Promotionsverfahrens nicht vornehmen werde. Die Bestimmungen der Promotionsordnung sind mir bekannt.“

Bemerkung: Teile dieser Dissertation werden/können als Manuskript zusammengefasst und in nächster Zeit als Publikation in der Arbeitsgruppe Charalampaki / Kempski freigegeben werden.

Teilpublikationen

Charalampaki, P., Javed, M., Daali, S., Heiroth, H.J., Igressa, A. & Weber, F. (2015) Confocal Laser Endomicroscopy for Real-time Histomorphological Diagnosis: Our Clinical Experience With 150 Brain and Spinal Tumor Cases. Neurosurgery, 62 Suppl 1, 171-176.

Daali, S., Javed, M., Altekoester, A.-K., Alhadi, I., Linxweiler, M., Bostelmann, R., Schlegel, J. & Charalampaki, P. (2016) Analysis of 258 Different Lesions of the Central Nervous System for Real Time Histopathological Diagnosis Using Confocal Laser Endomicroscopy. J Mult Scler (Foster City).

Kamen, A., Sun, S., Wan, S., Kluckner, S., Chen, T., Gigler, A.M., Simon, E., Fleischer, M., Javed, M., Daali, S., Igressa, A. & Charalampaki, P. (2016) Automatic Tissue Differentiation Based on Confocal Endomicroscopic Images for Intraoperative Guidance in Neurosurgery. BioMed research international, 2016, 6183218.

Schulz, A., Daali, S., Javed, M., Fuchs, P.C., Brockmann, M., Igressa, A. & Charalampaki, P. (2016) Presurgical mapping of basal cell carcinoma or squamous cell carcinoma by confocal laser endomicroscopy compared to traditional micrographic surgery: a single-centre prospective feasibility study. European journal of dermatology : EJD, 26, 572-579.

Köln, den 21. August 2019 Samira Daali